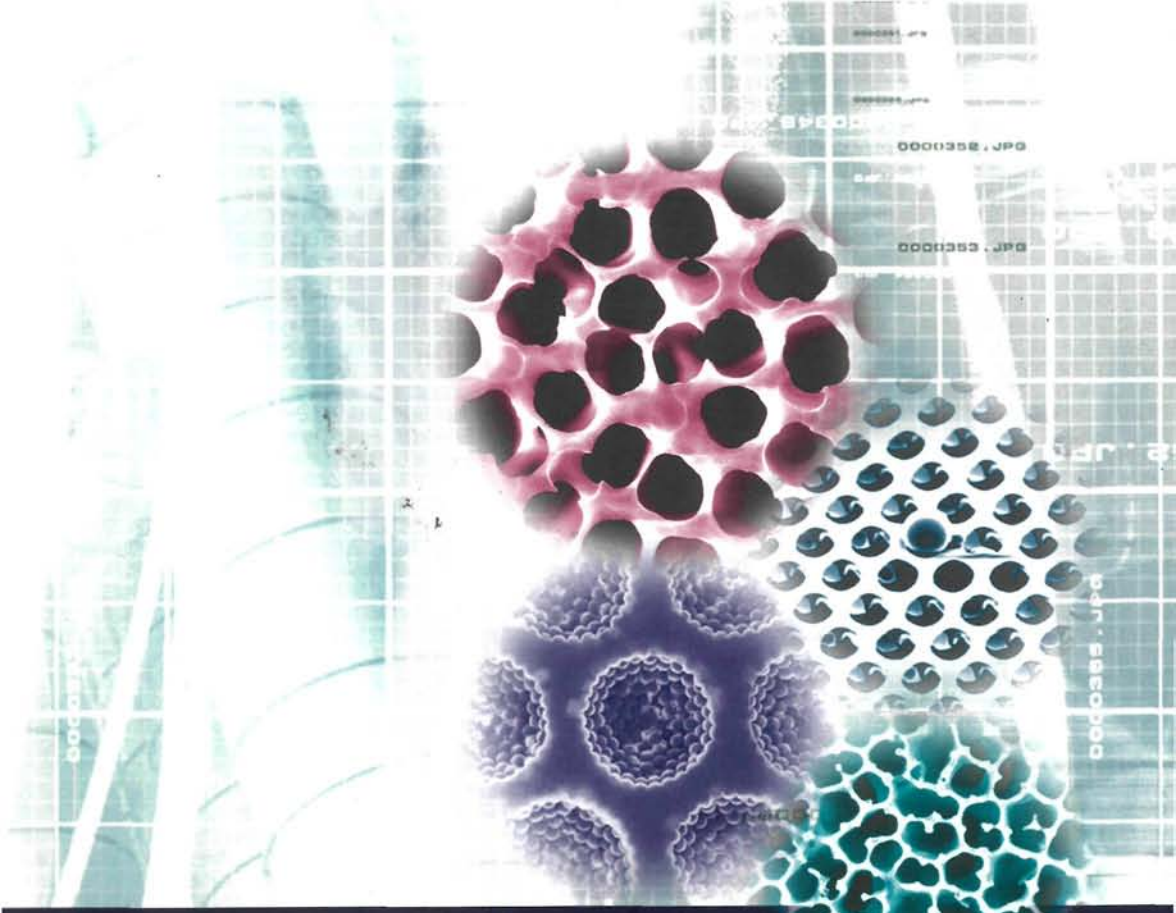

Proceedings of the Asian Symposium on Nanotechnology and Nanoscience 2002

AsiaNANO 2002

Editors

Masatsugu Shimomura & Teruya Ishihara

AsiaNANO 2002

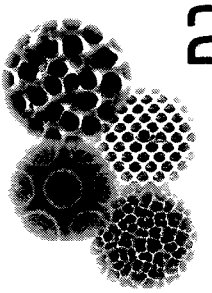

This page is intentionally left blank

Proceedings of the Asian Symposium on Nanotechnology and Nanoscience 2002

AsiaNANO 2002

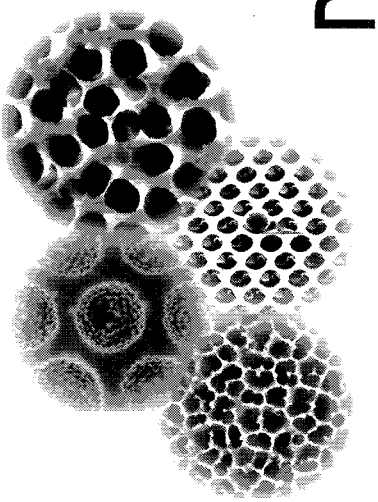

Editors

Masatsugu Shimomura
Hokkaido University, Japan

Teruya Ishihara
RIKEN, Japan

World Scientific

NEW JERSEY • LONDON • SINGAPORE • SHANGHAI • HONG KONG • TAIPEI • BANGALORE

Published by

World Scientific Publishing Co. Pte. Ltd.

5 Toh Tuck Link, Singapore 596224

USA office: Suite 202, 1060 Main Street, River Edge, NJ 07661

UK office: 57 Shelton Street, Covent Garden, London WC2H 9HE

British Library Cataloguing-in-Publication Data

A catalogue record for this book is available from the British Library.

AsiaNANO 2002

Proceedings of the Asian Symposium on Nanotechnology and Nanoscience 2002

ISBN 981-238-392-1

Printed in Singapore by Multiprint Services

CONTENTS

International Journal of Nanoscience, Vol. 1, Nos. 5 & 6 (2002) 375–381

CHARACTERISTICS AND MICROPATTERNING OF SPIN SELF-ASSEMBLED ULTRATHIN MULTILAYERS

KOOKHEON CHAR*, SANGCHEOL KIM, JINHAN CHO,
HIESANG SOHN, and HONGSEOK JANG

School of Chemical Engineering, Seoul National University
San 56-1, Shilim-dong, Kwanak-gu, Seoul, 151-744, Korea
**khchar@plaza.snu.ac.kr*

Received 27 November 2002
Revised 7 December 2002

A new method is introduced to build organic/organic multilayer films composed of cationic poly(allylamine hydrochloride) (PAH) and negatively-charged poly(sodium 4-styrenesulfonate) (PSS) using the spinning process. The adsorption process is governed by both the viscous force induced by fast solvent elimination and the electrostatic interaction between oppositely-charged species. On the other hand, the centrifugal and air shear forces applied by the spinning process enhance significantly the desorption of weakly-bound polyelectrolyte chains and also induce the planarization of the adsorbed polyelectrolyte layer. The surface of the multilayer films prepared with the spinning process is quite homogeneous and smooth. Also, a new approach to create multilayer ultrathin films with well-defined micropatterns in short process time is introduced. To achieve such micropatterns with high line resolution in organic multilayer films, microfluidic channels were combined with the convective self-assembly process employing both hydrogen bonding and electrostatic intermolecular interactions. As a next step, we extended the spin SA to the fabrication of multilayer micropatterns with vertical heterostructure.

Keywords: Spin self-assembly method; multilayer thin films; micropatterns; microfluidic channels; convective self-assembly.

1. Introduction

Fabrication of multilayer thin films have attracted much interest since they are of great use in thin film devices based on the electrochemical processes such as sensors, integrated optics, rectifiers, or light-emitting devices (LED).[1–5] For the applications of organic or organic/inorganic hybrid multilayer thin films to high performance devices, the internal structure of the films should be at the degree of high molecular order and the ability to pattern with at least micrometer-scale feature on the films are also required. Since the ionic layer-by-layer self-assembly (SA)

*Rm. 725, Bldg. 302, School of Chemical Engineering, Seoul National University, San 56-1, Shilim-dong, Kwanak-gu, Seoul, 151-744, Korea.

technique was introduced for the fabrication of polyelectrolyte multilayer, this self-assembling technique has been extended to conducting polymer composites, non-linear optical dyes, and the assembly of nanoparticles or biomolecular systems.[6–9] This layer-by-layer deposition by dipping method is principally governed by the self-diffusion of adsorbing polymer and the rearrangement on the surface and thus various experimental factors should be taken into account in order to obtain the uniform surface coverage of a polymer layer adsorbing onto a substrate: adsorption time, pH, concentration of polyelectrolyte and amount of added ionic salt. After the adsorption of a polyelectrolyte layer, thorough washing using pure solvent is required because the weakly-adsorbed polyelectrolyte chains increase significantly the surface roughness of the multilayer films.

Until now, several methods of multilayer patterning have been reported, including template-directed selective deposition with microcontact printing, electric field-directed deposition, and water-based subtractive patterning. In these methods, however, chemically-patterned templates should be prepared on the substrates because the adsorption process is based on the self-diffusion and rearrangement due to the interactions between adsorbing molecules and the patterned templates.

In present work, we describe the new spin self-assembly (SA) method as an alternative for producing well-organized multilayer films in short process time. Through the analyses by UV-vis spectroscopy and AFM, the multilayer thin films fabricated by the spin SA method were compared with those prepared by the conventional dipping method. We have also investigated the micropatterning of multilayers based on both hydrogen bonding and electrostatic intermolecular interactions. Furthermore, the obtained patterns were then used as templates to produce multilayer micropatterns with vertical heterostructure

2. Experimental

2.1. *Materials*

Poly(allylamine hydrochloride) (PAH, Mn = 50 000 ~ 65 000), poly(diallyldimethyl ammonium chloride) (PDAC, Mw = 100 000 ~ 200 000), poly(sodium 4-styrene-sulfonate) (PSS, MW = 70 000), poly(4-vinylpyridine) (PVP, Mw = 60 000) and poly(acrylic acid) (PAA, Mv ~ 450 000) were purchased from Aldrich and used without further purification. 16-mercaptohexadecanoic acid was obtained from Aldrich and used in absolute ethanol solution. Poly(dimethylsiloxane) (PDMS) and curing agent were purchased from Dow Corning.

2.2. *Multilayer preparation*

Quartz substrates for the deposition of polyelectrolytes were initially cleaned by ultrasonification in a hot mixture of H_2SO_4/H_2O_2 (7/3) for three hours. They were then heated in a mixture of $H_2O/H_2O_2/NH_3$ (5/1/1) at 80°C for 1 h, and then dried by N_2 gas purging. After this procedure, the substrates were negatively-charged

and used for the polyelectrolyte deposition starting with the cationic PAH. In the conventional layer-by-layer SA method, the substrates were immersed alternately in the cationic solution and in the anionic solution for 20 min for each deposition. After each deposition step, the surface of the self-assembled film was washed by dipping into the deionized water for 2 min and then blown dry with a stream of nitrogen. In the spin SA method, the deposition steps were carried out as follows: a few drops of polyelectrolyte solution were placed on the substrate and the substrate was then rotated at a fixed rotating speed (typically, 4000 rpm) for 8 to 15 s. After the deposition of each polyelectrolyte layer, the substrates were thoroughly rinsed twice with a plenty of deionized water. The spinning time and speed for the washing step were also identical to those for the layer deposition.

2.3. *Micropatterning of multilayers*

A silicon wafer was initially coated with a 1000 Å buffer layer of silicon oxide and followed by deposition of a 100 Å adhesive layer of titanium. A 1000 Å film of gold was then sputtered on the titanium surface. The COOH-terminated hydrophilic substrate was prepared by immersing the gold film into a 5 mM 16-mercaptohexadecanoic acid in absolute ethanol for 30 min. The multilayer deposition steps were carried out as follows: polymer solution was first allowed to fill the microfluidic channels, which were formed by the contact between a PDMS mold and a hydrophilic substrate, by the capillary pressure. The channel filling with a polymer solution also enables the polymer to adsorb onto the surface and the removal of residual solution is then carried out by the spinning process (typically, 6000 rpm for 2 min).

2.4. *Characterization*

The characteristics of multilayer films were analyzed by UV-vis spectrometer, atomic force microscope (AFM). An ellipsometer was also employed for the thickness measurement.

3. Results and Discussion

Figure 1 shows the difference in UV-vis absorbance of multilayer films prepared by both spin SA and dipping SA methods as a function of number of bilayers. Due to the contribution of the adsorbed PSS chains, the absorbance occurs at 225 nm in the UV region. The aqueous polyelectrolyte concentrations of PAH and PSS used in the two different deposition methods were all identical to be 10 mM (on the monomer unit basis). The dipping process was performed for an adsorption time of 20 min per layer in order to allow enough time for the saturated adsorption. In spin SA process, however, the amount of polymers adsorbed at each deposition step was found to be much larger. The film thickness per bilayer adsorbed by the dipping process and the spinning process was found to be about 4 Å and 24 Å, respectively, as determined from the ellipsometric measurement.

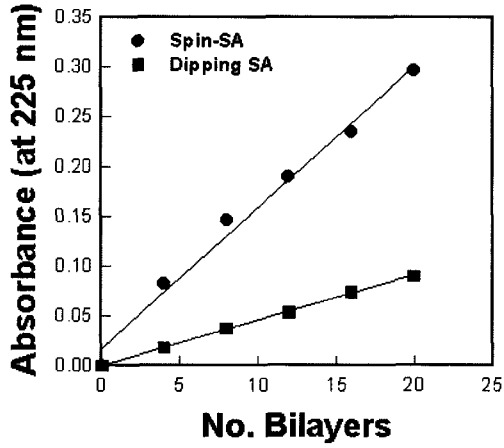

Fig. 1. Absorbance at 225 nm of PAH/PSS multilayers prepared by spin SA method and dipping SA method.

We also found that the spin SA method has a significant effect on the surface roughness of prepared multilayer films presumably due to the air shear force during the spinning process. In order to investigate this effect in detail, we measured the surface roughness of the self-assembled films using atomic force microscopy (AFM) in tapping mode as shown in Fig. 2. Although the flattened adsorption of a polyelectrolyte onto a substrate was obtained from a low ionic strength of the solution, the surface roughness of the dipping SA film composed of $(PAH/PSS)_{30}$ multilayer was measured to be about 8 Å.

On the other hand, the $(PAH/PSS)_{30}$ multilayer film prepared by the spin SA method shows a surface roughness of about 3 Å. These results are quite reproducible and clearly demonstrate that the air shear force imposed by the spinning process enhances significantly the surface planarization of the multilayer films. In addition, the surface roughness of about 3 Å and the bilayer thickness of 24 Å for the spinning process compared with 8 Å and 4 Å for the dipping process provides an indirect evidence that the internal structure of the spin SA films is highly ordered.[10]

To develop well-defined micropatterns of ultrathin multilayers in short process time, microfluidic channels were combined with the convective SA process (i.e., the self-assembling process in the presence of external flow) employing both electrostatic and hydrogen bonding intermolecular interactions.[11] The patterning is performed in two steps: polymer solution is first allowed to fill the microfluidic channels, which are formed by the contact between an elastomeric mold and a hydrophilic substrate, by the capillary pressure. The channel filling with a polymer solution also enables the polymer to adsorb onto the surface and the removal of residual polymer solution is then carried out by the spinning process.

The micropatterns of multilayer films with alternating PVP and PAA layers were prepared by the convective SA. As shown in Fig. 3, the micropatterns of ultrathin multilayers are significantly dependent on the solvent used. Micropatterns

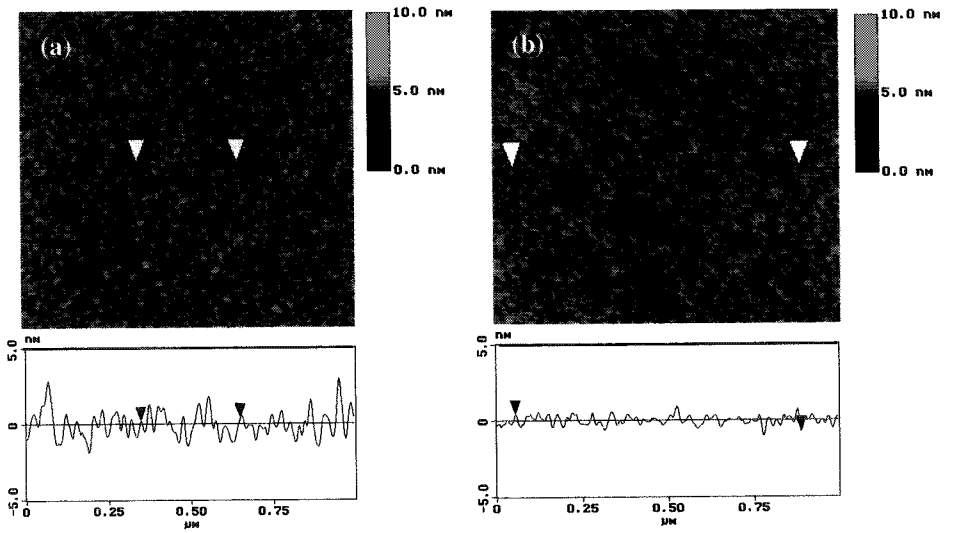

Fig. 2. Tapping mode AFM images of (a) a $(PAH/PSS)_{30}$ film prepared with the dipping SA and (b) a $(PAH/PSS)_{30}$ film fabricated with the spin SA.

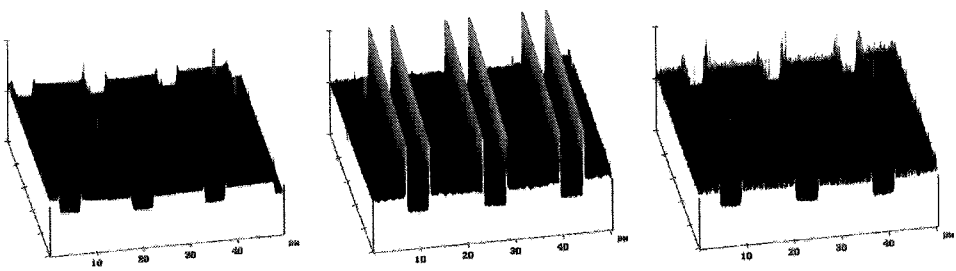

(a) (b) (c)

Fig. 3. AFM topography images of micropatterns of $(PVP/PAA)_5$ multilayers prepared with (a) DMF, (b) ethanol, and (c) ethanol/H_2O (9/1, v/v).

with sharp edge boundaries and small ridges were developed by using DMF as a solvent. For ethanol, high ridges are observed at the edges of the patterned lines, while the ridge was remarkably reduced by mixing ethanol with water. In previous works, the ridge formation phenomena were also observed in chemically-patterned films and were attributed to the retraction of a thin film of polymer from the resist alkanethiolate. However, in the case of the microfluidic channels employed in the present work, the ridge formation is due to the wetting of a solvent on the PDMS walls. It is consistent with the fact that the contact angle of ethanol on the PDMS is 31°, much lower than that of DMF (63°).

The alternate deposition of PDAC and PSS using the electrostatic intermolecular interactions was carried out by the spin SA on the patterned $(PVP/PAA)_5$

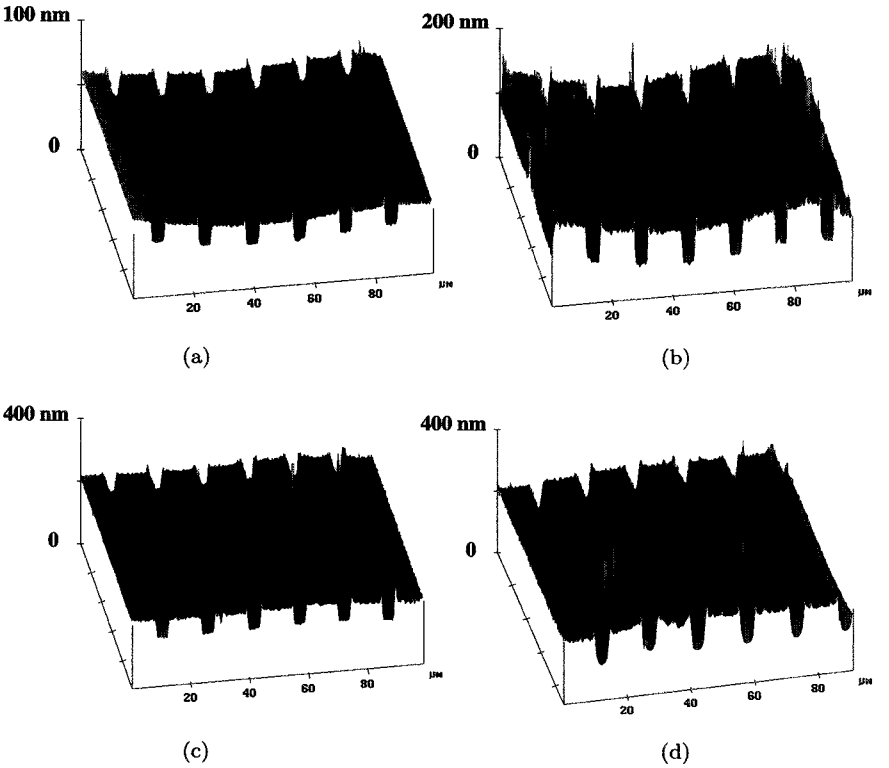

Fig. 4. Contact mode AFM images of patterned multilayer of $(PVP/PAA)_5(PDAC/PSS)_n$. (a) $n = 4$, (b) $n = 8$, (c) $n = 20$, and (d) $n = 40$.

multilayer template, initially prepared by using DMF as a solvent.[12] Carboxylate groups of PAA, an outmost layer of template, are partially ionized and thus allow the adsorption of cationic polyelectrolytes. The AFM topography images of 4, 8, 20, and 40 bilayers consisting of PDAC and PSS bilayers are shown in Fig. 4. The feature heights are 24, 30, 49, and 86 nm, respectively. These multilayer micropatterns with vertical heterostructure maintain high line resolution and small ridges. The surface of the micropatterns is also found to be quite homogeneous and smooth.

4. Conclusions

In summary, we have demonstrated for the first time that the spin SA process utilizing the centrifugal force, viscous force, air shear force and intermolecular interactions causes the adsorption, the rearrangement of polymer chains onto a substrate and the desorption of weakly-bound chains in a very short time of approximately 10 s. This new ultrathin film-forming process yields a highly-ordered internal structure far superior to the structure obtained by the conventional dipping SA process and it is much simpler and faster. It also allows us to precisely control and predict

the bilayer thickness as well as the surface roughness. The patterned multilayer films employing the hydrogen bonding and the electrostatic attractions can also be fabricated by the convective SA method combined with microfluidic channels. The well-defined micropatterns were obtained and then used as templates for the additional spin SA. Finally, the vertically heterostructural multilayer micropatterns with high line resolution and small ridges were produced.

Acknowledgments

This work was financially supported by the National Research Laboratory Program (Grant M1-0104-00-0191) and funded in part by the Ministry of Education through the Brain Korea 21 Program at Seoul National University.

References

1. P. K. Ho, J.-S. Kim, J. H. Burroughes, H. Becker, S. F. Y. Li, T. M. Brown, F. Cacialli, and R. H. Friend, *Nature* **404**, 481 (2000).
2. X. Zhang and J. Shen, *Adv. Mater.* **11**, 1139 (1999).
3. J. D. Mendelson, C. J. Barrett, V. V. Chan, A. J. Pal, A. M. Mayes, and M. F. Rubner, *Langmuir* **16**, 5017 (2000).
4. Laschewasky, E. Wischerhoff, M. Kauranen, and A. Persoons, *Macromolecules* **30**, 8304 (1997).
5. Y. He, S. Gong, R. Hattori, and J. Kanicki, *Appl. Phys. Lett.* **74**, 2265 (1999).
6. G. Decher, *Science* **277**, 1232 (1997).
7. K. M. Lenahan, Y. X. Wang, Y. J. Liu, R. O. Claus, J. R. Heflin, D. Marciu, and C. Figura, *Adv. Mater.* **10**, 853 (1998).
8. N. Kotov, I. Dekang, and J. H. Fendler, *J. Phys. Chem.* **99**, 13065 (1995).
9. Y. Lvov, K. Ariga, I. Ichinose, and T. Kunitake, *J. Am. Chem. Soc.* **117**, 6117 (1995).
10. J. Cho, K. Char, J. D. Hong, and K. B. Lee, *Adv. Mater.* **13**, 1076 (2001).
11. H. Jang, S. Kim, and K. Char, *Langmuir* **19**, 3094 (2003).
12. S. Kim, H. Jang, and K. Char, *Mol. Cryst. Liq. Cryst.*, submitted.

This page is intentionally left blank

International Journal of Nanoscience, Vol. 1, Nos. 5 & 6 (2002) 383–389

BIONANOMAGNET AND ITS APPLICATION

TADASHI MATSUNAGA and YOSHIKO OKAMURA
Department of Biotechnology
Tokyo University of Agriculture and Technology, 2-24-16
Naka-Cho, Koganei, Tokyo 184-8588, Japan

Received 27 November 2002

Magnetic bacteria synthesize intracellular magnets which are encapsulated by lipid bilayer membranes. Easy aqueous dispersion of bacterial magnetic particles (BMPs) enable development of highly sensitive chemiluminescence enzyme immunoassays by antibodies on BMP surfaces. We have reported a technique for preparing recombinant BMPs on which proteins were displayed by gene-fusion. We further applied such recombinant BMPs to biotechnologically-important issues, including novel bioassay platforms for medicine and environmental management.

Keywords: Bacterial magnetic particle (BMP); protein display; nanosized magnet.

1. Introduction

Nanotechnology has been identified as an area which will bring about new evolutions in materials, devices and processes. The challenges of nanobiotechnology entail manufacturing more sophisticated and highly efficient biosensors and biomaterials at the nanoscale level for use in interdisciplinary fields. Here, we introduce the molecular mechanism of bacterial magnetic particle (BMP) formation and the molecular architecture technique we have used for its application.

Magnetic bacteria have been isolated from freshwater and marine sediments, and are known to produce magnetite particles which are aligned in chains of around 20 particles per cell (Fig. 1(a)).[1–4] Bacterial magnetic particles (BMPs) are nanosize and disperse well in aqueous solution due to their stable lipid membranes (Fig. 1(b)).[5] On the basis of these properties, BMPs have been utilized in fluoroimmunoassays,[6–8] mRNA recovery[9] and as DNA carriers.[10] The use of magnetic particles in immunoassays enables the separation of bound and free analytes by applying a magnetic field. For example, proteins can be attached covalently to solid supports, such as magnetic particles, preventing the desorption of antibodies during assaying. Because these particles disperse evenly throughout the reaction mixture, they allow rapid reaction kinetics without the need for continuous mixing or shaking, enable coupling antibodies, and facilitate ease of use. Magnetic particles serve as both solid supports and a means of separation in the assay system.

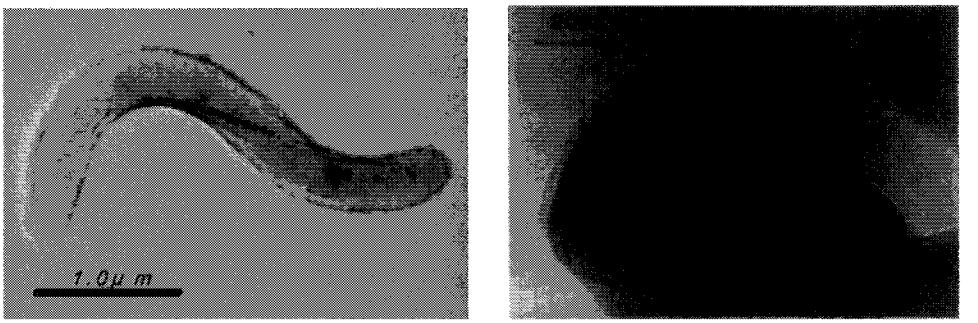

(a) (b)

Fig. 1. Transmission electron micrographs of (a) *Magnetospirillum magneticum* AMB-1 and (b) bacterial magnetic particle.

2. Genetic Analyses of *Magnetospirillum magneticum* AMB-1

Isolation and characterization of the genes that mediate magnetite formation in bacteria are prerequisite for determining the mechanisms of magnetic particle biosynthesis. In order to identify specific genes involved in magnetite synthesis, transposon mutagenesis has been conducted with strain AMB-1.[11] Numerous non-magnetic mutants have been successfully obtained and *magA* gene was subsequently isolated from one of the numerous mutants (strain NM5) by analyzing the transposon disrupted gene. The *magA* gene has homology with the Na^+/H^+ antiporter, *napA*, from *Enterococcus hirae*.[12] The iron uptake activity of MagA protein was determined using inverted vesicles prepared from fragmented membrane expressing MagA protein in *Escherichia coli*. An addition of ATP-initiated accumulation of

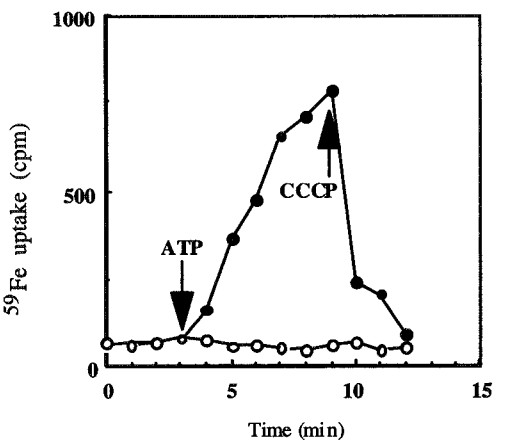

Fig. 2. Iron uptake into inverted vesicles. Arrowhead indicated the point of addition of ATP or CCCP. Symbols: the vesicles expressed MagA (•) and control vesicles (○).

ferrous ion in vesicles and the ion was released by addition of carbonyl cyanide m-chlorophenylhydrazone (CCCP) known as protonophore (Fig. 2).[13] The activity was also observed under artificial proton gradient without ATP. These results suggest that MagA protein is a proton-driving H^+/Fe(II) antiporter. Additionally, intracellular localization of the MagA protein was examined using a MagA-Luciferase fusion protein, indicating that MagA is localized on both the cytoplasmic and BMP membranes, where it appears to transport iron into BMP vesicles.[14] Therefore, MagA is considered to play an essential role in the bacterial formation of magnetite crystals.

Presupposing that proteins expressed on BMP membranes play a direct role in regulating magnetite crystallization, a number of distinct BMP-specific proteins have been identified. Protein fractions prepared from cellular and BMP membranes and cytoplasm were separated by SDS-polyacrylamide gel electrophoresis, revealing five specific proteins in BMP membrane fractions.[15] Utilizing 2D-electrophoresis, four of these proteins were separated for amino acid sequencing. On the basis of the *N*-terminal amino acid sequences determined, oligonucleotide primers were designed to perform polymerase chain reactions (PCR) to amplify DNA sequences of the target proteins. Subsequently, *mpsA* encoding a 36 kDa protein and *mms16* encoding a 16 kDa protein were isolated. DNA sequences of these two genes were analyzed and protein homology was examined. The amino acid sequence of MpsA was proven to be highly homologous with that of *E.coli* acetyl-CoA carboxylase.[16] Mms16 protein was found to be the most abundantly expressed one of the five BMP specific proteins and showed GTPase activity (Fig. 3).[17] Mms16 is a GTPase with properties similar to eukaryotic small GTPases which control priming and budding of trafficking vesicle. Thus, inhibition experiments on GTPase were conducted by using aluminum fluoride. AlF_4^- prevents BMP synthesis, suggesting that GTPase activity is required for BMP synthesis.[17] Thus, it has been shown that

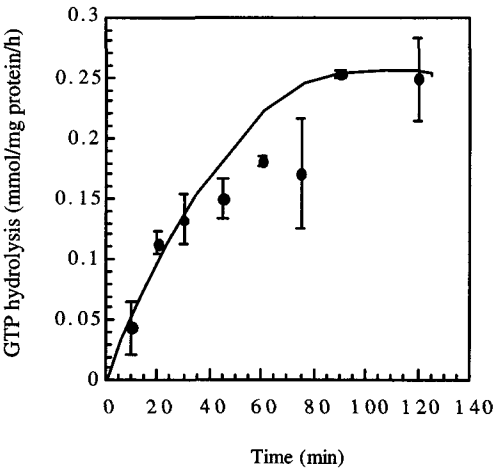

Fig. 3. Timecourse of GTP hydrolysis by purified Mms16.

magnetosomes arise through invagination of the cytoplasmic membrane and processes similar to those of eukar yotic vesicle formation.

3. Mechanism of BMP Formation

The BMP membrane is derived from the cytoplasmic membrane and formed through the invagination process. Transmission electron microscopy of *M.magnetotacticum* MS-1 reveals that BMP envelopes appear prior to the crystallization of magnetite.[18] The mechanism of envelope formation, however, still remains unclear. It is possible that magnetic bacteria have similar mechanisms of vesicle formation. Mms16 mediates the priming of invagination and MpsA mediates the acylation of Mms16 to anchor the BMP membrane. After formation of vesicle, moreover, MagA on BMP membrane transfers ferrous ions into intracellular vesicles (Fig. 4). Various

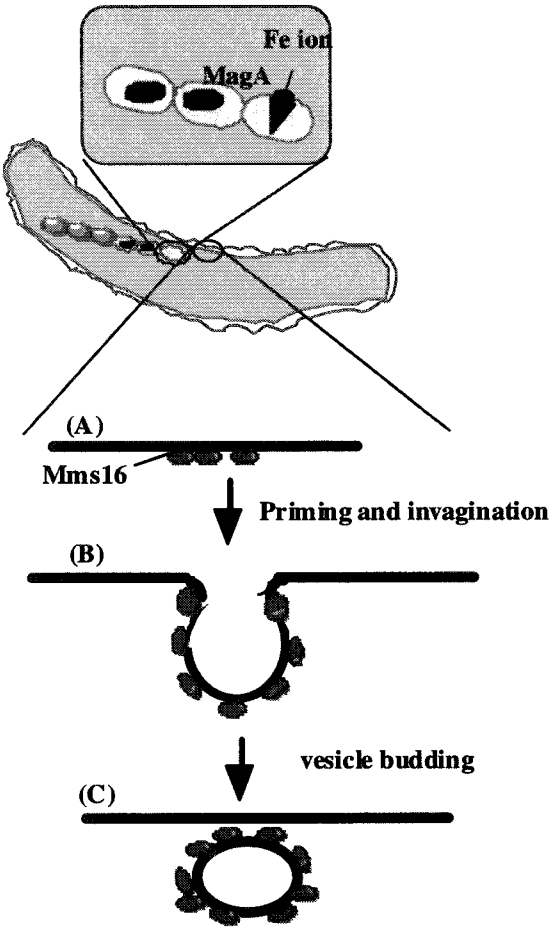

Fig. 4. Postulated mechanism of bacterial magnetic particle formation.

proteins associated with the BMP membrane may play functional roles involved in magnetite generation inside BMP envelopes. These include (1) the accumulation of supersaturating iron concentrations and maintenance of reductive conditions; and (2) the oxidation of iron to induce mineralization, or the partial reduction and dehydration of ferrihydrite to magnetite.

4. Molecular Architecture on BMP

MagA and Mms16 are all localized on the membranes of BMPs. These proteins could therefore be utilized as anchor proteins, allowing a variety of functional proteins to function on BMPs, i.e., enzymes or antibodies can be displayed on BMP membrane surfaces. For instance, employing the firefly luciferase *luc* gene, a *magA–luc* fusion gene was cloned into plasmid pRK415 and introduced into *M.magneticum* AMB-1 (Fig. 5).[14] Extracted BMPs from recombinant AMB-1 cells showed luciferase activity. In such a way, MagA protein acts as a workable anchor for the site-specific display of functional foreign proteins. Similarly, immunoglobulin (IgG) binding cell wall protein and protein A, were introduced to BMP membranes, using a *proteinA–magA* hybrid gene.[19] Using antibody bound proteinA–BMP complexes together with a chemiluminescence enzyme immunoassay, we have developed a rapid and highly sensitive diagnostic method for detecting human immunoglobin G (IgG).[20] Also, the feasibility of Mms16 as an anchor molecule was established by manifesting the estrogen receptor hormone binding domain (ERHBD) on BMP membranes. ERHBD–BMP complexes function as practical receptor binding assays for estrogen-like compounds. Upscale production of functionally-active antibodies or enzymes expressed on BMP membranes is effectively accomplished by fed-batch culturing techniques.[21] Furthermore, we constructed a high copy number plasmid pUMG in AMB-1 for a more efficient display of functional foreign proteins on BMP.[22]

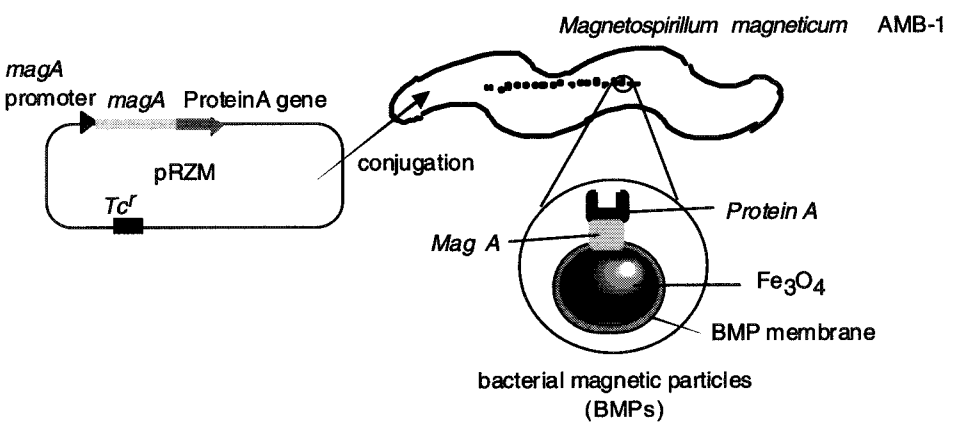

Fig. 5. Display of protein A onto bacterial magnetic particle using *magA* gene fusion.

5. Automization of Immunoassay Using BMPs

Functional uses of BMPs in immunoassay systems have been examined to detect various biological markers. The main advantage of using BMPs, compared with other conventional immunoassay methods, is the easy separation of membrane-bound and free fractions by applying a magnetic field. ProteinA–BMP complexes have viable applications in the detection of human IgG, insulin, HbA1 and glycated albumin from serum.[23] Antibodies conjugated with BMPs by chemical cross-linking methods are also valuable tools for detecting a wide variety of substances.

We have investigated various environmental pollutants, including endocrine disruptors, alkylphenol ethoxylates (APE), bisphenol A (BPA), and linear alkylbenzene sulfonates (LAS), using monoclonal antibodies immobilized on BMP and a fully-automated detection system. The automated sandwich immunoassay system developed comprises a reaction station, a tip rack, and an automated eight-channel pipet bearing a retractable magnet mounted close to the pipet tip and conterminous with a microtiter plate (96 wells). A single rack holds 8X3 tips for reaction. Our data show that this fully-automated system provides rapid detection (in 15 min), and efficiently determines concentrations of APE, BPA, and LAS with detection limits of 6.6 ppb, 0.023 ppt, and 35 ppt, respectively. The advantages afforded by this automated detection system should be practicable to other assay systems utilizing functional BMP.

6. Conclusion

In conclusion, BMP formation has been examined at the molecular level, although further studies are required to elucidate the whole mechanism of BMP formation and its highly-controlled biomineralization process. However, recent progress in molecular biology enables more highly-organized and systematic studies toward the elucidation of bacterial magnetite formation. In addition, improved analysis and identification of BMP specific factors will facilitate the use of biomineralization as a biomimetic technique for *in vitro* production of highly-controlled biocrystals.

References

1. R. P. Blakemore, *Science* **190**, 377 (1975).
2. T. Matsunaga, F. Tadokoro, and N. Nakamura, *IEEE Trans. Magn.* **26**, 1557 (1991).
3. T. Matsunaga, T. Sakaguchi, and F. Tadokoro, *Appl. Microbiol. Biotechnol.* **35**, 651 (1991).
4. T. Sakaguchi, J. G. Burgess, and T. Matsunaga, *Nature* **365**, 47 (1993).
5. D. L. Balkwill, D. Maratea, and R. P. Blakemore, *J. Bacteriol.* **141**, 1399 (1980).
6. N. Nakamura, K. Hashimoto, and T. Matsunaga, *Anal. Chem.* **63**, 268 (1991).
7. N. Nakamura, J. G. Burgess, K. Yagiuda, K. Kudo, S. Sakaguchi, and T. Matsunaga, *Anal. Chem.* **65**, 2036 (1993).
8. N. Nakamura and T. Matsunaga, *Anal. Chim. Acta* **281**, 585 (1993).
9. K. Sode, S. Kudo, T. Sakaguchi, N. Nakamura, and T. Matsunaga, *Biotechnol. Tech.* **7**, 688 (1993).

10. H. Takeyama, A. Yamazawa, C. Nakamura, and T. Matsunaga, *Biotechnol. Tech.* **9**, 355 (1995).
11. T. Matsunaga, C. Nakamura, J. G. Burgess, and K. Sode, *J. Bacteriol.* **174**, 2748 (1992).
12. D. Strausak, M. Waser, and M. Solioz, *J. Biol. Chem.* **268**, 26334 (1993).
13. C. Nakamura, J. G. Burgess, K. Sode, and T. Matsunaga, *J. Biol. Chem.* **270**, 28392 (1995).
14. C. Nakamura, T. Kikuchi, J. G. Burgess, and T. Matsunaga, *J. Biochem.* **118**, 23 (1995).
15. Y. Okamura, H. Takeyama, and T. Matsunaga, *Appl. Biochem. Biotech.* **84–86**, 441 (2000).
16. T. Matsunaga, N. Tsujimura, Y. Okamura, and H. Takeyama, *Biochem. Biophys. Res. Commun.* **268**, 932 (2000).
17. Y. Okamura, H. Takeyama, and T. Matsunaga, *J. Biol. Chem.* **276**, 48183 (2001).
18. Y. A. Gorby, T. J. Beveridge, and R. P. Blakemore, *J. Bacteriol.* **170**, 834 (1988).
19. T. Matsunaga, R. Sato, S. Kamiya, T. Tanaka, and H. Takeyama, *J. Magn. Magn. Mater.* **194**, 126 (1999).
20. T. Tanaka and T. Matsunaga, *Anal. Chem.* **72**, 3518 (2000).
21. C.-D. Yang, H. Takeyama, T. Tanaka, and T. Matsunaga, *Enz. Microb. Technol.* **29**, 13 (2001).
22. Y. Okamura, H. Takeyama, T. Sekine, T. Sakaguchi, A. T. Wahyudi, R. Sato, S. Kamiya, and T. Matsunaga, *Appl. Environ. Microbiol.*, submitted.
23. T. Tanaka and T. Matsunaga, *Biosens. & Bioelectron.* **16**, 1089 (2001).

This page is intentionally left blank

International Journal of Nanoscience, Vol. 1, Nos. 5 & 6 (2002) 391–395

EFFECT OF LIPID-PACKAGING ON THE CHARGE TRANSFER CHARACTERISTICS OF ONE-DIMENSIONAL, MIXED-VALENCE PLATINUM COMPLEXES

CHANG-SOO LEE, YASUHIRO HATANAKA, and NOBUO KIMIZUKA

Department of Chemistry and Biochemistry, Graduate School of Engineering
Kyushu University, Hakozaki 6-10-1, Higashi-ku
Fukuoka 812-8581, Japan

Received 27 November 2002

Lipid-packaged platinum complexes of $[Pt(en)_2][PtX_2(en)_2]$ (X = Cl, Br, I) are newly synthesized and their morphology and charge transfer (CT) absorption characteristics are compared in organic media. They show remarkably red-shifted CT absorption characteristics, which are ascribed to the significantly promoted exciton delocalization along the chains.

Keywords: Self-assembly; halogen-bridged mixed-valence complex; amphiphile.

1. Introduction

The synthesis of conjugated nanowires has been attracting much interests because of their potential applications in the future nanodevices. The next issues would involve control of their electronic states and fabrication of electrical nanocircuits by placing them at desired positions. The self-assembly approach may provide useful vehicles to manipulate such electronically-wired architectures. For this purpose, the design of conjugated nanowires that reversibly self-assemble from component molecules (or ions) in solution is of crucial importance. Inspired by the self-growth and self-restoration characteristics of biological neurons, we have developed a new family of self-assembling, soluble inorganic nanowires $[Pt(en)_2][PtCl_2(en)_2]$ (en; 1,2-diaminoethane) which is packaged by anionic amphiphiles.[1–8] We herein report the effect of lipid-packaging and bridging halogen atoms on their charge transfer absorption characteristics.

2. Materials and Methods

Amphiphile **1** was synthesized by BOP-Cl (N,N-Bis(2-oxo-3-oxazolidinyl)-phosphinic chloride)-catalyzed condensation of L-glutamate dialkyl ester and sulfoacetic acid. The structures of the intermediates and the final product were confirmed by thin layer chromatography, IR and NMR spectroscopies and elemental analysis. $[Pt^{II}(en)_2]X_2$, trans-$[Pt^{IV}X_2(en)_2]X_2$, and $[Pt(en)_2][PtX_2(en)_2](ClO_4)_4$ (X = Cl,

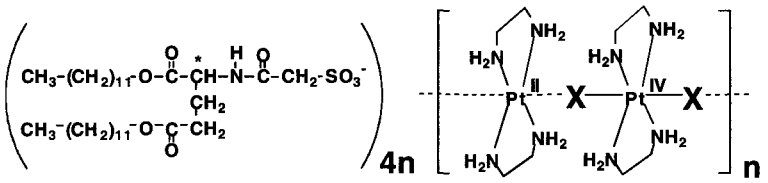

Br, I) were prepared according to the literature.[9] Aqueous dispersion of anionic amphiphile **1** (Na^+ salt, 10 mM, 20 mL) was prepared by ultrasonication (Branson Sonifier Model 185, sonic power 45 W, 5 min). It was added to equimolar solutions containing $[Pt(en)_2][PtX_2(en)_2](ClO_4)_4$ in deionized water ($[Pt]_{total}$ = 10 mM, 4 mL). When the bridged halogen ion is chloride, precipitate with deep purple color was immediately formed. On the other hand, indigo and dark blue precipitates were obtained for bromide and iodide complexes, respectively. These precipitates were collected by centrifugation, washed with pure water to remove sodium perchlorate, and were dried in vacuo. Elemental analysis, $[Pt(en)_2][PtCl_2(en)_2](\mathbf{1})_4$, calculated for $C_{132}H_{264}N_{12}O_{32}S_4Cl_2Pt_2$: C, 50.80; H, 8.53; N, 5.39%; found: C, 50.36; H, 8.60; N, 5.33%. $[Pt(en)_2][PtBr_2(en)_2](\mathbf{1})_4$, calculated for $C_{132}H_{264}N_{12}O_{32}S_4Br_2Pt_2$: C, 49.68; H, 8.40; N, 5.19%; found: C, 49.76; H, 8.51; N, 5.25%. $[Pt(en)_2][PtI_2(en)_2](\mathbf{1})_4$, calculated for $C_{132}H_{264}N_{12}O_{32}S_4I_2Pt_2$: C, 47.99; H, 8.05; N, 5.09%; found: C, 47.99; H, 8.05; N, 4.96%. These colored complexes were dissolved in dichloromethane (by hand-shaking) and in chlorocyclohexane (by ultrasonication for 5 min) and gave homogeneous dispersions. Transmission electron microscopy (TEM) was conducted on a Hitachi H-600 instrument (75 kV) without staining, and the specimens were prepared by dropping the dispersions on carbon-coated TEM grids at room temperature.

3. Results and Discussion

Quasi-one-dimensional, halogen-bridged mixed-valence metal complexes $[Pt(en)_2] \cdot [PtX_2(en)_2](ClO_4)_4$ display conjugated electronic states with strong intervalence charge transfer (CT, $Pt^{II}/Pt^{IV} \rightarrow Pt^{III}/Pt^{III}$) absorption.[10] These halogen-bridged chains have been available only as structural motifs in the bulk crystals, and they are dissociated into the component monomeric complexes in water. On the other hand, by substituting the perchlorate anions with anionic amphiphiles, the linear complexes become soluble in organic media due to the lipophilic nature of associating lipid molecules.[1–8]

When $[Pt_2(en)_2][Pt_2Cl_2(en)_2](\mathbf{1})_4$ and $[Pt_2(en)_2][Pt_2Br_2(en)_2](\mathbf{1})_4$ are dissolved in dichloromethane and in chlorocyclohexane (concentration, 0.6 unit mM, 1 unit = $[Pt_2(en)_2][Pt_2X_2(en)_2]$), they gave deep purple and indigo colors which are similar to those of the solid. These colors are ascribed to charge transfer (CT) absorption of the mixed valence complexes, and their maintenance in solution indicates that the halogen-bridged structures are preserved in these organic media. The iodine-

bridged complex $[Pt(en)_2][PtI_2(en)_2](\mathbf{1})_4$ also gave a pale-blue dispersion in chlorocyclohexane. On the other hand, when $[Pt(en)_2][PtI_2(en)_2](\mathbf{1})_4$ was dissolved in dichloromethane at room temperature, the color of the solid was immediately disappeared and a pale yellow solution was left. This yellow color is characteristic to the monomeric $PtI_2(en)_2$ complex, and it indicates that the complex is not maintained in dichloromethane. Thus, the iodine-bridged complex is highly lipophilic.

Figure 1 shows transmission electron microscopy of $[Pt(en)_2][PtX_2(en)_2](\mathbf{1})_4$ in chlorocyclohexane. As the samples are not stained, the dark portions in the pictures indicate the presence of $[Pt(en)_2][PtX_2(en)_2](\mathbf{1})_4$. Chloro-bridged complex $[Pt(en)_2][PtCl_2(en)_2](\mathbf{1})_4$ and bromo-bridged $[Pt(en)_2][PtBr_2(en)_2](\mathbf{1})_4$ displayed rectangular nanocrystals with widths of 200–300 nm and lengths of 500–1500 nm

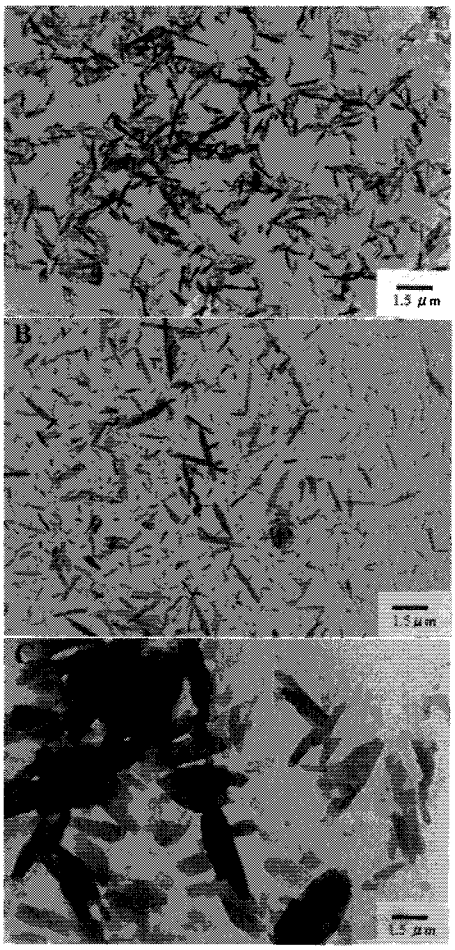

Fig. 1. TEM images of $[Pt(en)_2][PtX_2(en)_2](\mathbf{1})_4$ dropped from chlorocyclohexane dispersions (0.6 unit mM, 20°C). (A) X = Cl, (B) X = Br, and (C) X = I. Scale bar, 1.5 μm.

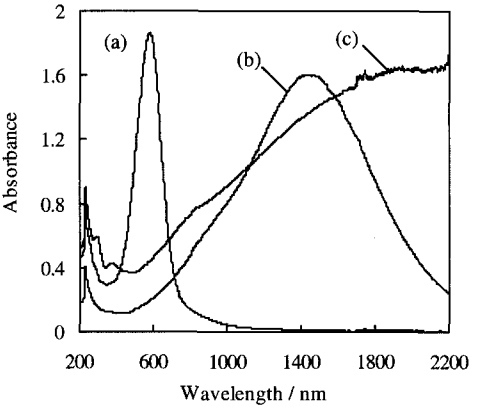

Fig. 2. Charge transfer absorption of $[Pt(en)_2][PtX_2(en)_2](\mathbf{1})_4$ in chloro-cyclohexane. (a) X = Cl, (b) X = Br, and (c) X = I. Temperature; 20°C, 0.6 unit mM, 1 mm cell.

(Figs. 1(A) and 1(B)). On the other hand, iodo-bridged complex gave plate-like microcrystals (Fig. 1(C)), and thus the solubility and morphology of the assembly is affected by the kind of bridging halogen ions.

Figure 2 shows UV-vis spectra of $[Pt(en)_2][PtX_2(en)_2](\mathbf{1})_4$ in chlorocyclohexane. $[Pt(en)_2][PtCl_2(en)_2](\mathbf{1})_4$ displays λ_{max} at 578 nm ((a), 2.15 eV, ε: 31 050 unit M^{-1} cm^{-1}) and $[Pt(en)_2][PtBr_2(en)_2](\mathbf{1})_4$ showed λ_{max} at 1426 nm ((b), 0.87 eV, ε: 26 769 unit M^{-1} cm^{-1}). The tendency that heavier halogen ions give red-shifted charge transfer absorption is also reported for the crystalline perchlorate complexes $[Pt(en)_2][PtX_2(en)_2](ClO_4)_4$ (Table 1).[11]

It is noteworthy that the CT absorption peaks observed for $[Pt(en)_2][PtX_2(en)_2](\mathbf{1})_4$ in chlorocyclohexane are significantly red-shifted compared to those observed for the crystalline $[Pt(en)_2][PtX_2(en)_2](ClO_4)_4$ (X = Cl; 2.72 eV, X = Br; 1.95 eV, Table 1). In addition, to our surprise, a continuous absorption which is extended from the ultraviolet to near infrared region is observed for $[Pt(en)_2][PtI_2(en)_2](\mathbf{1})_4$ (Fig. 2(c), band gap < 0.56 eV). Such continuous absorption indicates the presence of very small energy gap which is often observed for the doped, organic conductive polymers. Moreover, it is in remarkable contrast with the CT absorption of $[Pt(en)_2][PtI_2(en)_2](ClO_4)_4$, which only displays a sharp

Table 1. Comparison of charge transfer absorption maxima for platinum complexes.

X	$[Pt(en)_2][PtX_2(en)_2](ClO_4)_4^a$	$[Pt(en)_2][PtX_2(en)_2](\mathbf{1})_4$
Cl	456 nm (2.72 eV)	578 nm (2.15 eV)
Br	636 nm (1.95 eV)	1426 nm (0.87 eV)
I	905 nm (1.37 eV)	$\sim$ 2200 nm ($<$ 0.56 eV)

[a]Reflection spectral data for crystalline samples (taken from Ref. 11).

peak with much larger band gap (1.37 eV).[11] The CT excitation energy for the perchlorate complexes has been linearly correlated with the magnitude of off-center displacement of halogen ions between Pt^{II} and Pt^{IV}.[11] In the present lipid-packaged system, the densely-aligned sulfonate lipids would direct the electrostatically-bound $Pt(en)_2$ and $PtX_2(en)_2$ complexes to co-polymerize in higher density. It contracts the interplatinum (Pt^{II}-X-Pt^{IV}) distance, i.e. enhances the overlap between d_{z^2} and p-orbitals. This should promote the excitation delocalization along the chains, and the concomitant decrease in the LUMO–HOMO band gap may account for the observed red-shifted CT bands. The continuous CT absorption observed for the iodine-bridged complex is observed without doping and this unusual electronic property is not predictable from the conventional perchlorate complexes.

In conclusion, the lipid-packaged linear mixed-valence platinum complexes display significantly decreased LUMO–HOMO band gaps which are ascribable to the enhanced delocalization of the excitons. The amphiphiles not only gives the solubility to the linear metal complexes but also modulates their electronic states. The present finding can be generalized as a concept "supramolecular band gap engineering" and it would play a key role in the design and development of conjugated, inorganic–organic nanomaterials.

References

1. N. Kimizuka, *Adv. Mater.* **12**, 1461 (2000).
2. N. Kimizuka, N. Oda, and T. Kunitake, *Chem. Lett.*, 695 (1998).
3. N. Kimizuka, N. Oda, and T. Kunitake, *Inorg. Chem.* **39**, 2684 (2000).
4. N. Kimizuka, S.-H. Lee, and T. Kunitake, *Angew. Chem. Int. Ed.* **39**, 389 (2000).
5. N. Kimizuka, K, Yamada, and T. Kunitake, *Mol. Cryst. Liq. Cryst.* **342**, 103 (2000).
6. C.-S. Lee and N. Kimizuka, *Proc. Natl. Acad. Sci.* **99**, 4922 (2002).
7. N. Kimizuka, Y. Hatanaka, and T. Kunitake, *Advanced Macromolecular and Supramolecular Materials and Processes*, ed. K. Geckeler (Kluwer Academic Publishers), in press.
8. C.-S. Lee and N. Kimizuka, *Chem. Lett.*, 1252 (2002).
9. F. Basolo, J. C. Bailar, and B. R. Tarr, *J. Am. Chem. Soc.* **72**, 2433 (1950).
10. H. Okamoto and M. Yamashita, *Bull. Chem. Soc. Jpn.* **71**, 2023 (1998) and references therein.
11. Y. Wada, T. Mitani, M. Yamashita, and T. Koda, *J. Phys. Soc. Jpn.* **54**, 3143 (1985).

This page is intentionally left blank

International Journal of Nanoscience, Vol. 1, Nos. 5 & 6 (2002) 397–401

SELF-ORGANIZATION OF METAL NANOPARTICLES AND ITS APPLICATION TO SYNTHESES OF Pd/Ag/Rh TRIMETALLIC NANOPARTICLE CATALYSTS WITH TRIPLE CORE/SHELL STRUCTURES

NAOKI TOSHIMA, YUKIHIDE SHIRAISHI, TORU MATSUSHITA, HISAYOSHI MUKAI, and KAZUTAKA HIRAKAWA*

Department of Materials Science and Environmental Engineering
Tokyo University of Science, Yamaguchi
[*The former Science University of Tokyo in Yamaguchi*]
Onoda-shi Yamaguchi 756-0884, Japan

Received 27 November 2002
Revised 14 December 2002

Self-organization of metal nanoparticles, which is observed by mixing Ag nanoparticles and precious metal nanoparticles, is applied to the synthesis of Pd/Ag/Rh trimetallic nanoparticles having a Pd-core/Ag-interlayer/Rh-shell structure. These trimetallic nanoparticles work as a more active catalyst for hydrogenation of olefin than the corresponding monometallic and bimetallic nanoparticles.

Keywords: Metal nanoparticle; self-organization; core–shell structure; trimetallic nanoparticle; catalyst.

1. Introduction

Metal nanoparticles are considered as a building block of nano-organized systems, which may play an important role in nanotechnology.[1] Characteristic properties of metal nanoparticles are potentially useful for many applications such as optical, optoelectronic, magnetic, catalytic, and biological ones. On the other hand, self-organization of nanoparticles is one of the most interesting concepts, which can control the structure of nano-organized systems. The building and patterning of the nanoparticles into two- and three-dimensional organized structures by manipulation of individual units are often reported for an approach to realize nanodevices with unique optical or electro-optical properties. For these self-organization, the noncovalent interactions among the organic molecules surrounding the metal nanoparticles are important. Such interactions involve hydrogen bonding, π–π interaction, host–guest interactions, van der Waals forces, electrostatic forces,

*Present address: Radioisotope Center, School of Medicine, Mie University, Tsu, Mie 514-8507, Japan.

antibody–antigen recognition, and so on. However, few reports have been published on the interaction between different kinds of metal nanoparticles.[2,3]

In general, bimetallic nanoparticles can be prepared by simultaneous reduction of two kinds of metal ions by refluxing alcohol in the presence of protective reagents. The Pd/Pt bimetallic nanoparticles having a Pt-core/Pd-shell structure, synthesized by this method, is a typical example of core/shell-structured bimetallic nanoparticles.[4] This method can be applied to the synthesis of precious bimetallic nanoparticles.[5] In the simultaneous reduction method, the kinds of core and shell metals are decided by the nature of the metal and the reaction conditions. In the combination of Pd and Pt, for example, Pt atoms form the core and Pd atoms cover the core to form the shell. Thus, the bimetallic nanoparticles with a Pd-core/Pt-shell structure can be synthesized by stepwise reduction using sacrificial hydrogen.[6] By this method the bimetallic nanoparticles with any kind of core/shell structure can be prepared. Here we would like to report a new type of self-organization of two different kinds of metal nanoparticles, and its application to synthesis of Pd/Ag/Rh trimetallic nanoparticle catalysts with a triple core/shell structure.

2. Self-Organization of Metal Nanoparticles Forming Bimetallic Nanoparticles

Usually the mixtures of two kinds of dispersions of metal nanoparticles do not provide bimetallic nanoparticles, each particle is composed of two kinds of metal elements. However, the mixtures of colloidal dispersions of poly(*N*-vinyl-2-pyrrolidone) (PVP)-protected Ag nanoparticles and those of PVP-protected Rh nanoparticles can produce Ag/Rh bimetallic nanoparticles, in which Ag forms a core and Rh surrounds the Ag core to form a shell (cf. Fig. 1).[3] Formation of the Ag-core/Rh-shell structure was confirmed by the disappearance of the plasmon band in UV-vis spectra of the colloidal dispersion of Ag nanoparticles and the TEM observation including distribution analyses of elements with an EF-TEM apparatus (by Dr. S. Horiuchi at AIST). This interesting self-organization of metal nanoparticles in solution can be affected by a pair of metal elements and the kind of protective reagents. Although the mechanism of self-organization of metal

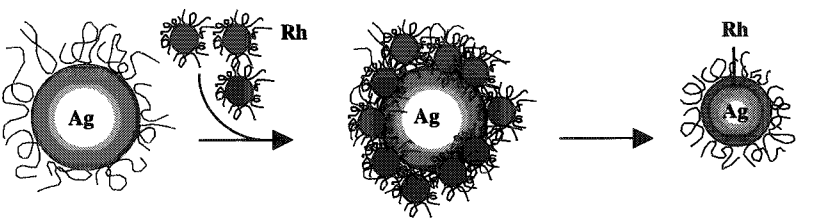

Fig. 1. Schematic illustration of self-organization of Ag and Rh nanoparticles to form Ag-core/Rh-shell bimetallic nanoparticles.

nanoparticles is not clear yet, the driving force of the formation of Ag/Rh bimetallic nanoparticles may be the larger binding energy between Ag and Rh atoms than between Rh atoms.

3. Design and Synthesis of Pd/Ag/Rh Trimetallic Nanoparticles with a Triple Core/Shell Structure

Bimetallic nanoparticles with a Pt-core/Pd-shell structure have much higher catalytic activity than Pt and Pd monometallic nanoparticles for partial hydrogenation of cyclooctadiene to cyclooctene. This is due to the electronic effect of Pt-core upon the electronic density of Pd-shell. Thus, the trimetallic nanoparticles with a Pd-core/Ag-interlayer/Rh-shell structure are expected to have a higher catalytic activity than the corresponding monometallic and bimetallic nanoparticles. However, the triple core/shell structure is not easily constructed. Simultaneous reduction, for example, does not produce the designed structure. The newly-discovered self-organization between Rh and Ag nanoparticles was applied to the synthesis of Pd/Ag/Rh trimetallic nanoparticles with a triple core/shell structure. At first Ag/Pd bimetallic nanoparticles with a Pd-core/Ag-shell structure were prepared by a stepwise reduction method using sacrificial hydrogen. Then, the colloidal dispersion of Pd-core/Ag-shell bimetallic nanoparticles were mixed with the colloidal dispersion of Rh nanoparticles. The time-dependant UV-vis spectra of the mixture of Pd/Ag bimetallic nanoparticles and Rh nanoparticles are shown in Fig. 2. Disappearance of the Ag plasmon absorption of Pd/Ag bimetallic nanoparticles suggests the covering of Pd/Ag bimetallic nanoparticles with Rh nanoparticles to

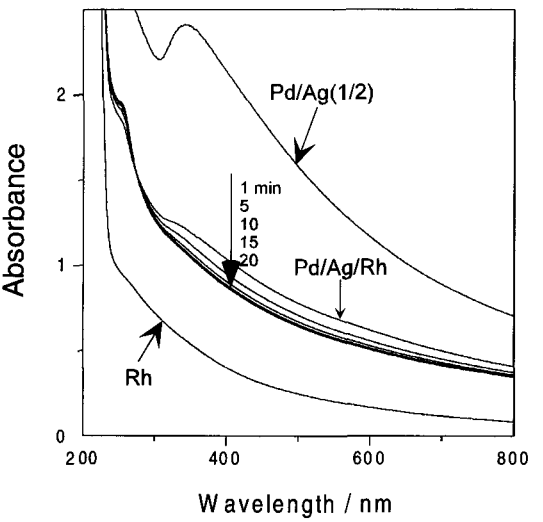

Fig. 2. UV-vis spectra of dispersions of Rh, Pd/Ag(1/2), and Pd/Ag/Rh trimetallic nanoparticles in 1, 5, 10, 15, and 20 min after mixing the dispersions of Rh and Pd/Ag(1/2) nanoparticles.

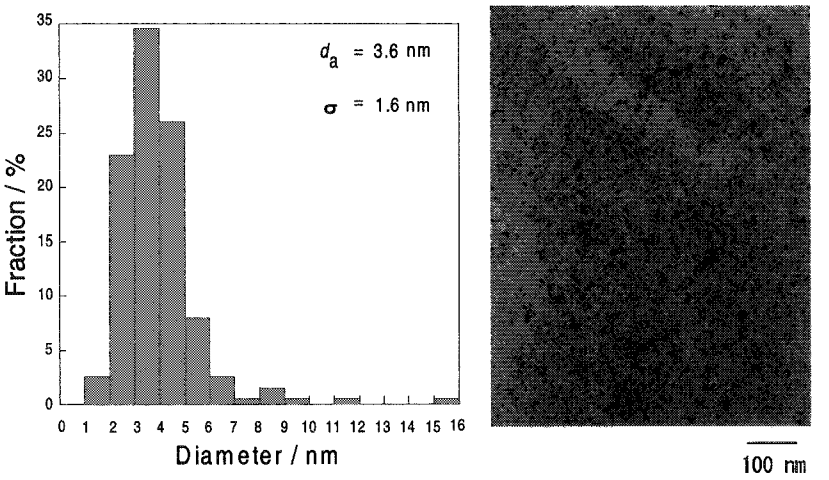

(a) (b)

Fig. 3. (a) The size distribution histogram and (b) TEM photograph of Pd/Ag/Rh(1/2/36 mol/mol/mol) trimetallic nanoparticles.

form a Pd-core/Ag-interlayer/Rh-shell structure. The TEM photograph (Fig. 3) of the trimetallic nanoparticles indicates the size of nanoparticles as an average diameter of 3.6 nm and a standard deviation of 1.6 nm.

4. Catalytic Activity of Pd/Ag/Rh Trimetallic Nanoparticles

The resulting Pd/Ag/Rh (1/2/36/mol/mol/mol) trimetallic nanoparticles with a triple core/shell structure was preliminarily applied to a catalyst for hydrogenation of methyl acrylate at 30°C under 1.01×10^5 Pa of hydrogen. The results are

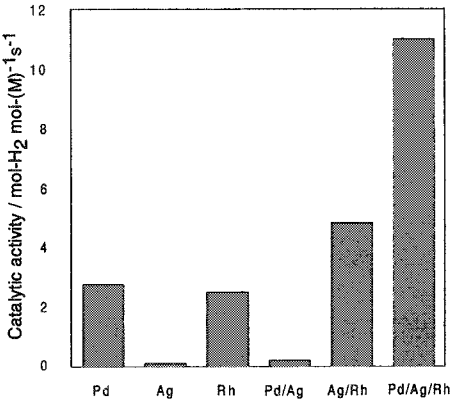

Fig. 4. Catalytic activity of Pd, Ag and Rh monometallic, Pd/Ag(1/2 mol/mol) and Ag/Rh(1/4 mol/mol) bimetallic, and Pd/Ag/Rh(1/2/36 mol/mol/mol) trimetallic nanoparticles.

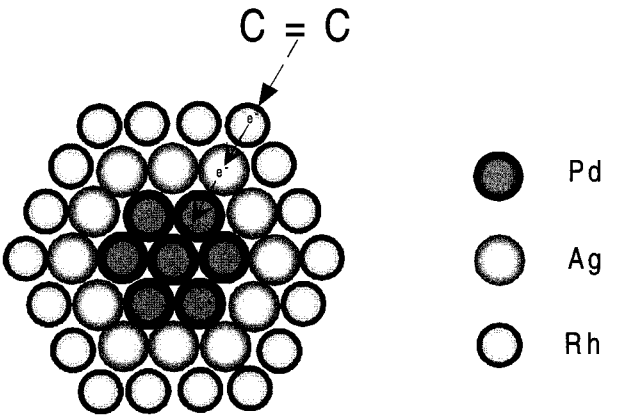

Fig. 5. Schematic illustration of enhancement of catalytic activity of surface Rh atoms in Pd/Ag/Rh trimetallic nanoparticles by sequential electron transfer.

summarized in Fig. 4. The Pd/Ag/Rh trimetallic nanoparticles have much higher catalytic activity than the corresponding monometallic and bimetallic nanoparticles examined. This is probably attributed to the sequential electronic effect of inner metals upon the surface Rh atoms, which is schematically shown in Fig. 5.

References

1. G. Schmid (ed.), *Clusters and Colloids: From Theory to Applications* (VCH, Weinheim, 1994).
2. T. Hashimoto, K. Saijo, M. Harada, and N. Toshima, *J. Chem. Phys.* **109**, 5627 (1998).
3. K. Hirakawa and N. Toshima, *Chem. Lett.* **32**(1), 78 (2003).
4. N. Toshima, T. Yonezawa, and K. Kushihashi, *J. Chem. Soc., Faraday Trans.* **89**, 2537 (1993).
5. N. Toshima, *Pure Appl. Chem.* **72**, 317 (2000).
6. Y. Wang and N. Toshima, *J. Phys. Chem. B* **101**, 5301 (1997).

This page is intentionally left blank

International Journal of Nanoscience, Vol. 1, Nos. 5 & 6 (2002) 403–407

LIPOPHILIC-FULLERENE DERIVATIVE MONOLAYERS AT THE AIR–WATER INTERFACE

J. S. KOO and K. SHIN*

Department of Materials Science and Engineering
KJIST, Kwangju, 500-712, Korea
**kwshin@kjist.ac.kr*

U. JENG and T.-L. LIN

Department of Engineering and System Science
National Tsing Hua University, Hsinchu 300, Taiwan

M. H. WU, Z. A. CHI, and M. C. SHIH

Department of Physics, National Chung-Hsin University, Tai-Chung 402, Taiwan

C.-H. HSU and H.-Y. LEE

Synchrotron Radiation Research Center, Hsinchu 300, Taiwan

L. Y. CHIANG

Center for Condensed Matter Sciences
National Taiwan University, Taipei 106, Taiwan

Received 27 November 2002
Revised 3 January 2003

Monolayers of a lipophilic C_{60}-derivative (FPTL) mixed in dipalmitoyl-phosphatidyl-choline (DPPC) have been studied by the Langmuir film balance technique and Brewster angle microscopy. Previous X-ray scattering studies showed that the FPTL molecules intercalated into the DPPC monolayers and modified the bending and compression modulus of the host DPPC membranes. Combined study of surface pressure–area isotherms and Brewster angle microscopy measurements clearly established that the liquid-condensed domain structures are strongly influenced by an addition of the fullerene bearing lipid molecules, where it caused smaller liquid-condensed domain structures.

Keywords: Lipophilic fullerene; Langmuir layer; Brewster angle microscopy.

1. Introduction

Largely motivated by biological model interfaces exhibiting various interactions with basic cell components, such as proteins, cells, and DNA, the preparation

*Corresponding author.

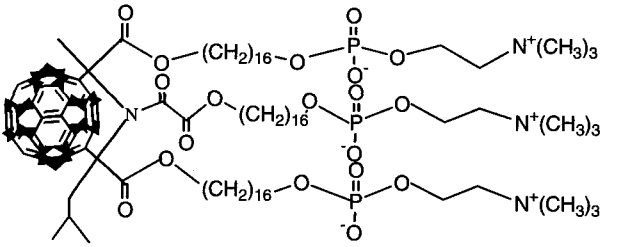

(a)

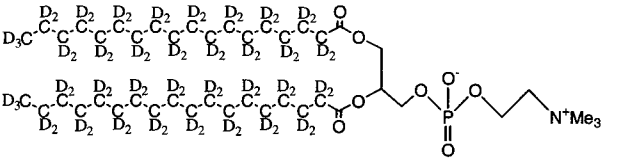

(b)

Fig. 1. Schematic molecular structure of (a) the lipophilic C_{60}, FPTL, and (b) d_{62}-DPPC, FPTL.

characterization of physical and chemical properties of phospholipid monolayers at the air/water interface have been attracting much interest.[1] Recently, in order to produce functionalized membranes, there are large activities in studying the interactions of lipid membranes with many different membrane intruders, for instances, peptides,[2] disacharides,[3] or enzymes,[4] etc. Although these intruders interact with lipid membranes for different purposes, such as attacking, protecting, or function attaching, a common preceding action is the binding to the lipid membranes. For the cell protecting effect, C_{60} has demonstrated an outstanding performance due to its capability of eliminating radicals in biosystems.[5] We have synthesized a lipophilic C_{60} derivative, FPTL, having three lipid-like tails chemically-bonded on one olefinic moiety of the C_{60} cage. As shown in Fig. 1, with the three lipid-like tails largely simulating the molecular structure of a phospholipid, dipalmitoylphosphatidylcholine (DPPC), the lipophilic-C_{60} is ready to incorporate into phospholipid membranes. The present study addresses in detail the structural effects in the presence of the FPTL molecules via the direct comparison of the DPPC and DPPC/FPTL mixture at the air/water interface using surface pressure–area (π–A) isotherms and the Brewster angle microscopy (BAM) techniques.

2. Experimental

Figure 1 shows the schematic view of the lipophilic C_{60}, FPTL, of a molecular weight M_w of 2178 and deuterated DPPC (d_{62}-DPPC, $M_w = 796$). The detailed synthesis route for FPTL will be reported elsewhere. The d_{62}-DPPC and d_{62}-DPPC/FPTL mixture (93.7:6.3 molar ratio) samples were spread on the water surface from

chloroform and 2:1 (v:v) benzene/chloroform mixture, respectively. For Langmuir experiments, a known volume (25–35 μL) of the spreading solution was added to the surface of Milli-Q water ($\gamma = 72.1$ dyne/cm^2) subphase using a Hamilton syringe. Surface pressure (π)–area (A) isotherms were then recorded at a compression rate of 105 cm^2/min using a Langmuir trough (KSV2000) with one moving barrier. The total compression area was 811.5 cm^2.

A commercial Brewster angle microscope (BAM2plus, NFT)[7] was used. It was mounted above the Langmuir trough to image the *in situ* domain morphology of the Langmuir layers during compression. P-polarized light from a 50 mW laser with a wavelength of 532 nm was reflected off the air/water interface with an angle of incidence close to the Brewster angle (53.1°) of the subphase, which is given by the Snell's law of refraction, $\tan(\theta) = n_{\text{water}}/n_{\text{air}}$, where n_i is the refractive index of a media i. A zooming microscope with a 10× objective was used with a lateral resolution of 2 μm.

3. Results and Discussion

The phase information of a Langmuir film is often determined by the analysis of surface pressure–area (π–A) isotherms. Figure 2 summarizes the π–A isotherms for compression–expansion cycles of the DPPC and DPPC/FPTL Langmuir films studied at 20.7°C. For the pure DPPC, the surface pressure first begins to rise moderately at the area (~90 Å^2/molecule), considered as the existence of a liquid expended (LE) phase, beyond which a well-defined plateau exists ($A \sim 65$ Å^2/molecule). Plateaus in the π–A isotherms are usually interpreted in terms of phase transitions in the film, and we can infer that liquid condensed (LC) domains are newly-formed and coexisted together with the LE phase as decreasing

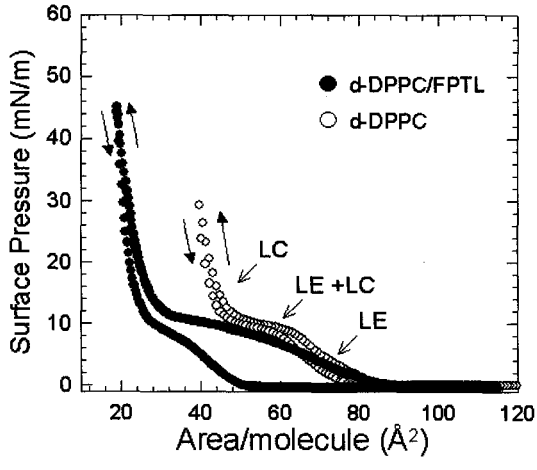

Fig. 2. Compression (arrow up) and expansion (arrow down) isotherm measured at 20°C for the d-DPPC and d-DPPC/FPTL.

area. There is the "second steep rise" in π at $A \sim 45$ Å^2/molecule, corresponding to the formation of a LC phase. On the other hand, when DPPC is mixed with 6.3 mol% of the FPTL molecules, the rise in LE becomes less steep and the onset for the plateau is not observed. Interestingly, the condensed phase (LC) is occurred at $A \sim 30$ Å^2/molecule, which is much smaller than that of the pure DPPC, indicating that the mixture layer is more compressible. Helm *et al.*[8] pointed that the compressibility of a phospholipid phase is influenced by a defect annealing and the deformation of solid domains. They reported that the spatial correlation range would be smaller if a phase becomes more compressible. This can be confirmed by BAM measurements when the domain sizes between the pure DPPC and the DPPC/FPTL mixture are compared.

The expanding curve for the DPPC/FPTL mixed layer shows a bigger hysteresis as compared to that for the pure DPPC case. The fact that the compressed films cannot return to the initial gas phase at large area, imply that the condensed DPPC/FPTL molecules are very cohesive and the molecule–molecule interaction is stronger than the molecule/water interaction.

Figure 3 depicts the BAM images for pure DPPC at different stages of compression. As reported previously by McConlogue and Vanderlick[9] and many others, the formation of multilobbed LC domains is clearly visualized. The LC domains having a characteristic chirality are covering the surface area upon compression (Figs. 3(b)–3(d)). In comparison, the domains of the DPPC/FTPL mixed layer shown in Fig. 4, are smaller ($\sim$ 15 μm in diameter) and have a widely dispersed

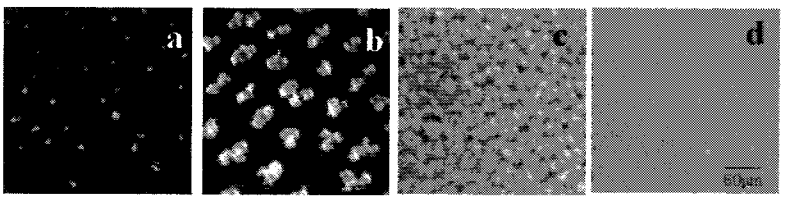

Fig. 3. Morphology of pure DPPC monolayer at various surface pressures visualized by BAM (a) $A \sim 72$ Å^2/molecule, (b) $A \sim 66$ Å^2/molecule, (c) $A \sim 50$ Å^2/molecule, and (d) $A \sim 42$ Å^2/molecule.

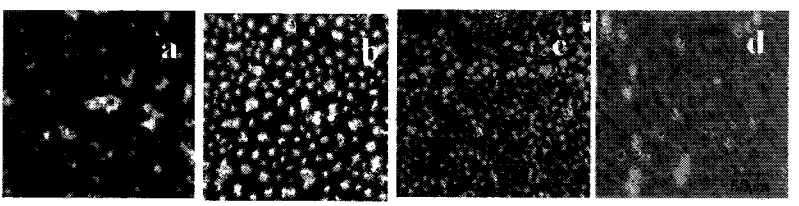

Fig. 4. Morphology of a mixed monolayer of DPPC/FTPL at various surface pressures visualized by BAM (a) $A \sim 90$ Å^2/molecule, (b) $A \sim 75$ Å^2/molecule, (c) $A \sim 48$ Å^2/molecule, and (d) $A \sim 32$ Å^2/molecule.

size distribution, which induced the dull isotherm without plateau. The smaller domain size indicates the reduced in-plane correlation of the domain molecules and may also be responsible for the higher compressibility. This is in agreement with our previous X-ray data.[6]

At small area, the DPPC/FTPL mixture at the LC phase (Fig. 4(d)) forms a smooth layer, which is also in good agreement with our previous AFM observations, which has less voids (defects) for the DPPC/FPTL LB films prepared in the LC phase (π = 30 mN/m) than that for pure DPPC LB films prepared under the same conditions. The presence of chirality for the DPPC/FTPL mixture is not clear due to the limited optical resolution. Nevertheless, BAM images evidently demonstrate that the LC domain structures are strongly influenced by the addition of the fullerene bearing lipid molecules.

In summary, the monolayers of a lipophilic C_{60}-derivative mixed in DPPC have been studied by the Langmuir film balance technique and BAM. The combined results confirmed that the liquid-condensed domain structures are strongly influenced by an addition of the fullerene bearing lipid molecules, where it caused smaller liquid-condensed domain structures.

Acknowledgments

The work was supported in part by the Korean Proton Accelerator User Program of KAPRA (K. Shin) and Brain Korea 21 program.

References

1. A. Baszkin (ed.), *Physical Chemistry of Biological Interfaces* (Marcel Dekker, New York, 2000).
2. M. H. Gaber, M. M. Ghanam, S. A. Ali, and W. A. Khalil, *Biophys. Chem.* **70**, 233 (1998).
3. T. Hasegawa, J. Nishijo, and J. Umemura, *J. Phys. Chem.* **102**, 8498 (1998).
4. U. Dahmen-Levison, G. Brezesinski, and H. Mohwald, *Thin Solid Films* **327**, 616 (1998).
5. I. C. Wang *et al.*, *J. Med. Chem.* **42**, 4614 (1999).
6. U. Jeug *et al.*, *Physica B*, submitted (2002).
7. C. Lheveder, J. Meunier, and S. Hónon, *Physical Chemistry of Biological Interfaces*, ed. A. Baszkin (Marcel Dekker, New York, 2000), p. 559.
8. C. A. Helm, H. Möhwald, K. Kjaer, and J. Als-Nielsen, *Biophys. J.* **52**, 381 (1987).
9. C. W. McConlogue and T. K. Vanderlick, *Langmuir* **14**, 6556 (1998).

This page is intentionally left blank

International Journal of Nanoscience, Vol. 1, Nos. 5 & 6 (2002) 409–414

NANOSTRUCTURED LB FILMS AND EMISSION LIGHT DUE TO MULTIPLE SURFACE PLASMON EXCITATIONS IN THE KRETSCHMANN CONFIGURATION

FUTAO KANEKO*, MITSURU TERAKADO, TOSHIHARU SATO,
HIROTSUGI HATAKEYAMA, WATARU SAITO,
KAZUNARI SHINBO, and KEIZO KATO

Department of Electrical and Electronic Engineering, Niigata University
Ikarashi 2-8050, Niigata 950-2181, Japan
**fkaneko@eng.niigata-u.ac.jp*

TAKASHI WAKAMATSU

Department of Electrical Engineering, Ibaraki National College of Technology
Nakane 866, Hitachinaka 312-8508, Japan

Received 27 November 2002
Revised 9 January 2003

Surface plasmon (SP) excitations have been investigated in the attenuated total reflection (ATR) Kretschmann configuration of prism/metal/Langmuir–Blodgett (LB) films containing dyes. The emission light through the prism was observed using direct irradiation of a laser beam from air to the LB films, i.e., reverse irradiation. The emission intensities depend on the emission angles through the prism, nanostructure of metal and LB films, dye molecules, separation between metal and dye molecules, interactions of dye molecules, etc. The spectra is strongly depended on the emission angles, and the emission light was caused by multiple SP excitations. Nanostructured devices of LB films using SP excitations are described.

Keywords: Surface plasmon excitation; reverse irradiation; Langmuir–Blodgett (LB) film.

1. Introduction

The attenuated total reflection (ATR) method using surface plasmon (SP) excitations, i.e., the surface plasmon resonance (SPR) method, is quite useful for the evaluation of ultrathin films and sensing.[1,2] The ATR measurements have reported the evaluate structure and dielectric properties of organic ultrathin films on metal thin films[2–4] and act as one of the sensing methods.[2,4] The ATR methods have also been investigated for device applications of organic ultrathin films, as a result of strong optical absorption and strong electric fields due to SP excitations.[6]

*Corresponding author.

Recently, emission light at a resonant angle region of SP excitations was observed through the prism in the ATR Kretschmann configuration, when metal ultrathin films on the prism or LB films on metal films were directly irradiated from air by a laser beam, i.e., by means of reverse irradiation.[7,8] The emission properties correspond to the resonant conditions of SPs in the Kretschmann configuration,[8–10] and the emission light was due to multiple SPs induced by excitation of dyes in the reverse irradiation.[8–10]

In this study, emission light properties due to multiple SP excitations have been investigated for various nanostructured LB films using the ATR method and the reverse irradiation.

2. Experimental

Arachidic acid (C20) Langmuir–Blodgett (LB) films and merocyanine (MC) LB films were deposited on microscopic cover glasses with vacuum evaporated metal thin films. The details of LB films have been reported elsewhere.[9] MC is one of the photosensitizing organic dyes that shows photoluminescence (PL). MC (NK2684) was purchased from Hayashibara biochemical Lab., Inc. C20 has no optical absorption and the thickness of the C20 monolayer was 2.76 nm.[3] The evaporated Ag and Al thin films with thickness of 50 nm and 15 nm, respectively, were used as the SP active layers.

Figures 1(a) and 1(b) show an ATR measuring system and the reverse irradiation method in the Kretschmann configuration, respectively. A complete description has been reported elsewhere.[9] In the ATR measurement, reflectance intensity to incident

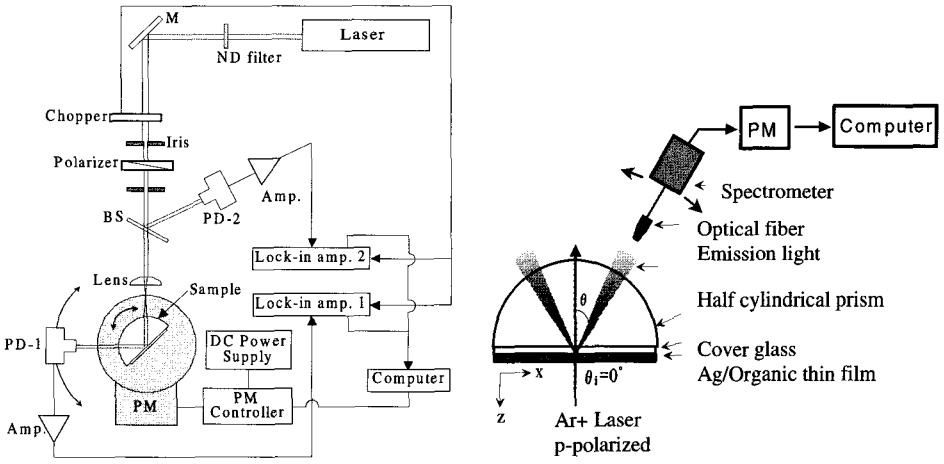

Fig. 1. (a) An ATR measuring system and (b) the reverse irradiation method in the Kretschmann configuration.

one was measured as a function of the incident angle, θ_i, of the laser beam. In this measurement, an Ar^+ laser (λ = 488.0 nm) was used. In the reverse irradiation method as shown in Fig. 1(b), samples were irradiated at the vertical incident angle by a p-polarized Ar^+ laser beam at 488 nm. The emission light through the prism was observed as a function of emission angle, θ_e.[8,9] Spectra of the emission light were measured with and without a sharp cut filter at about 520 nm at various emission angles.

3. Results and Discussion

Figures 2(a) and 2(b) show the ATR properties at 488 nm for Ag film: Ag/C20 (six layers)/MC (two layers) and Ag/C20 (six layers)/MC (eight layers) films; and for Al film: Al/C20 (five layers)/MC (two layers) and Al/C20 (five layers)/MC (eight

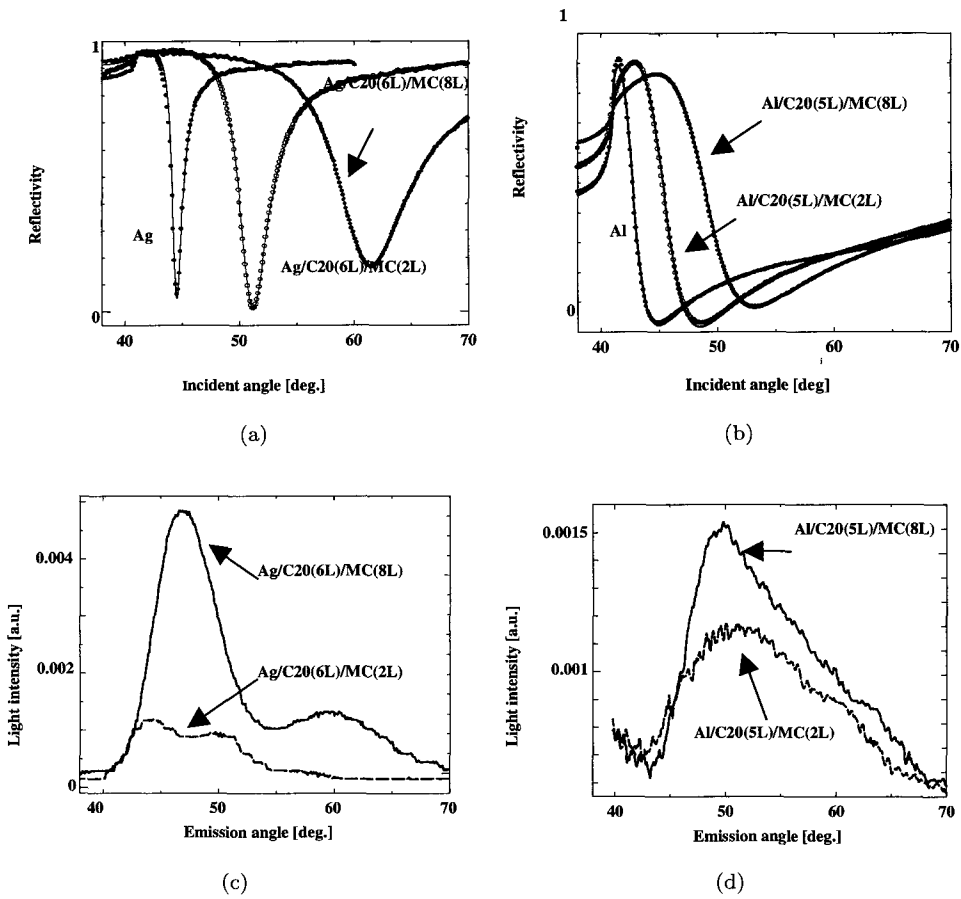

Fig. 2. (a) The ATR properties for Ag/C20/MC LB films and (b) for Al/C20/MC LB films, and the emission light through the prism in the reverse irradiation (c) for Ag/C20/MC LB films and (d) for Al/C20/MC LB films.

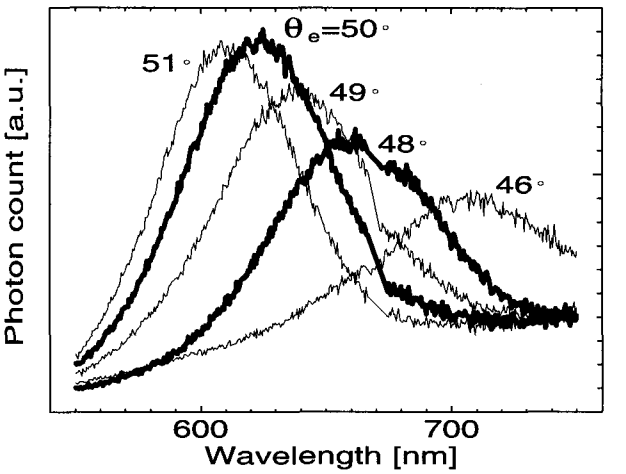

Fig. 3. The emission spectra at various emission angles in the reverse irradiation of a p-polarized laser beam at 488 nm for the Ag/C20 (two layers)/MC (16 layers) LB thin film.

layers) films. The difference between ATR properties for the LB films on Ag and Al was due to the dielectric properties of the metal thin films. The minima due to resonant excitations of SP were observed in the ATR properties. Figures 2(c) and 2(d) show emission light with a sharp cut filter at about 520 nm using the reverse irradiation at 488 nm. The emission peaks were observed at different angles from the resonant ones, and the emission spectra had the main peaks at about 600 nm that correspond to a photoluminescence (PL) peak of MC. The emission light from the LB films on Ag was larger than that on Al due to the roughness of the Ag thin films. The emission intensities increase with a larger quantity of MC dyes.

The emission spectra were also measured at various emission angles and strongly depended upon the angles.[8–10] Figure 3 shows an example of emission spectra at various emission angles in the reverse irradiation of a p-polarized laser beam at 488 nm for the Ag/C20 (two layers)/MC (16 layers) LB thin film. The emission properties corresponded to the resonant conditions of SPs in the Kretschmann configuration and was due to multiple SPs induced by excitation of dyes in the reverse irradiation.[8–10]

Figure 4 shows emission intensities for the Ag/C20/MC (four Layers)/C20 LB films when the separation between the Ag and the MC LB films was changed with C20 LB layers. The largest emission was observed with the separation of ten layers of the C20. It is tentatively estimated that small emissions are due to nonradiative energy transfer or charge transfer from the excited MC to the metal film in the small separations and due to smaller induced charges on the metal film in the large separations.[10]

Figure 5 shows a schematic diagram of the emission phenomenon due to multiple SP excitations.[10] It is evidenced that the SP emission phenomenon involves

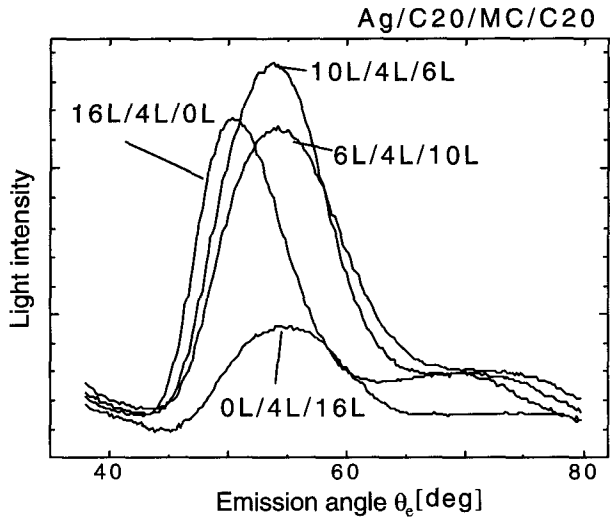

Fig. 4. Emission with various separations between the Ag and the MC in Ag/C20/MC/C20 LB films.

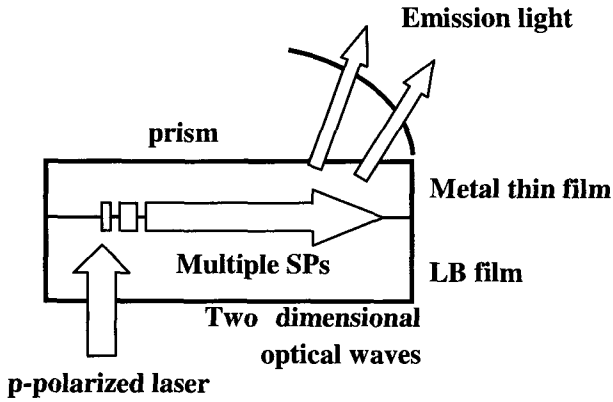

Fig. 5. A schematic diagram of the emission phenomenon due to multiple SP excitations.

the following processes: (1) multiple SPs are induced by the polarizations of excited organic dye molecules on metal thin films and/or by the surface roughness, (2) propagation on the metal surface, and (3) the propagating multiple SPs are converted into light that is emitted at the resonant SP conditions in the Kretschmann configuration due to the film properties and/or the roughness of the films.[8–10] This phenomenon will be used as a new sensing technique and may be used as devices for light emission of selectable colors as shown in Fig. 3, and for signal processing if some of the three processes can be controlled.[8–10]

4. Conclusions

The emission light through the prism due to multiple SP excitations has been investigated using the reverse irradiation. The emission light from the LB films on Ag was larger than that on Al. The emission also depended on the quantity of the MC dyes and the nanostructured separation between Ag and the dyes. It is evidenced that the phenomenon is useful for application to new nanostructured devices utilizing multiple SP excitations.

References

1. V. M. Agranovich and D. L. Mills (eds.), *Surface Polaritons* (North-Holland, Amsterdam, 1982).
2. W. Knoll, *Ann. Rev. Phys. Chem.* **49**, 569 (1998).
3. F. Kaneko, S. Honda, T. Fukami, K. Kato, T. Wakamatsu, K. Shinbo, and S. Kobayashi, *Thin Solid Films* **284–285**, 417 (1996).
4. A. Baba, F. Kaneko, K. Shinbo, K. Kato, S. Kobayashi, and T. Wakamatsu, *Jpn. J. Appl. Phys.* **37**, 2581 (1998).
5. K. Kato, C. M. Dooling, K. Shinbo, T. H. Richardson, F. Kaneko, R. Tregonning, M. O. Vysotsky, and C. A. Hunter, *Colloids and Surfaces A, Physicohem. and Eng. Aspects* **198–200**, 811 (2002).
6. K. Shinbo, T. Ebe, F. Kaneko, K. Kato, and T. Wakamatsu, *IEICE Trans. Electron.* **E83-C**, 1081 (2000).
7. I. Pockrand, A. Brillante, and D. Möbius, *Chem. Phys. Lett.* **69**, 499 (1980).
8. T. Nakano, T. Wakamatsu, H. Kobayashi, F. Kaneko, K. Shinbo, K. Kato, and T. Kawakami, *Mol. Cryst. Liq. Cryst.* **370**, 265 (2001).
9. T. Nakano, M. Terakado, K. Shinbo, K. Kato, F. Kaneko, T. Kawakami, and T. Wakamatsu, *Jpn. J. Appl. Phys.* **41**, 2774 (2002).
10. F. Kaneko, T. Sato, M. Terakado, T. Nakano, K. Shinbo, K. Kato, T. Wakamatsu, and R. C. Advincula, *2002 Solid State Devices and Materials*, Nagoya, Japan, C-5-3, September 2002.

International Journal of Nanoscience, Vol. 1, Nos. 5 & 6 (2002) 415–418

"HONEYCOMB FILMS": BIOINTERFACE FOR TISSUE ENGINEERING

TAKEHIRO NISHIKAWA, KEIKO ARAI, JUNKO HAYASHI, MASAHIKO HARA, and MASATSUGU SHIMOMURA*

Spatio-Temporal Function Materials Research Group
The Institute of Physical and Chemical Research (RIKEN)
Hirosawa 2-1, Wako, Saitama, 351-0198, Japan

Received 27 November 2002
Revised 18 December 2002

We report that tissue-like structure can be formed when cells are cultured on a microporous polymer film (honeycomb film). The honeycomb films were fabricated by applying a moist air to a spread polymer solution containing biodegradable polymers (poly(L-lactic acid) (PLLA) and poly(ε-caprolactone) (PCL)) and an amphiphilic polymer. Hepatocytes were cultured on a self-supporting honeycomb film of PLLA. The hepatocytes formed a single layer of columnar shape cells with a thickness of 20 μm. The tissue formation of hepatocytes was specifically occurred on the honeycomb film of PLLA and not on a flat film of PLLA. Three-dimensional tissue structures were formed, when cells were cultured on both sides of the self-supporting honeycomb film. Double layers of hepatocytes were obtained by the method. Striated tissues such as heart and blood vessel could be reconstructed by utilizing a stretched honeycomb film of PCL.

Keywords: Honeycomb film; biodegradable polymer; tissue engineering.

1. Introduction

The tissue engineering is a technology for reconstruction of living tissues. Various matrices such as gels and porous materials have been developed to realize ideal tissue formation.[1] Matrix surface, called "biointerface", is an important place where cells are initially attached, as the cell–matrix interaction significantly influences the subsequent cell–cell interactions.[2] In this sense, the biointerface should be designed to cause proper cell adhesion. It is well known that surface chemistry and surface morphology are two major points to note for the design of biointerface.[3–5] The biointerface in this paper is a microporous film of degradable polymers. Honeycomb films are microporous films of polymers, which are formed spontaneously by evaporating a polymer solution into a humid atmosphere.[6] We report the honeycomb films of degradable polymers, the control of cell spreading and the cell

*Nanotech Research Center, Research Institute for Electronic Science, Hokkaido University, N12W6, Sapporo, 060-0812 Japan.

alignment on the honeycomb films, and the application of the honeycomb films to three-dimensional cell culture system.

2. Self-Supporting Honeycomb Films for Cell Culture Substrates

Honeycomb films were fabricated by applying moist air to a spread polymer solution on the water surface.[7] Solutions containing 1 g/L of degradable polymers ((poly(L-lactic acid) (PLLA: Fig. 1(a)) and poly(ε-caprolactone) (PCL: Fig. 1(a)) and 0.1 g/L of an amphiphlic polymer (Fig. 1(a)) were prepared for the film fabrication. Benzene was utilized as a solvent for the amphiphilic polymer and PCL. Chloroform was utilized as a solvent for PLLA. One hundred μL of the polymer solution was spread onto the water surface in a ϕ9 cm petri-dish and evaporated by blowing the moist air at 1200 mL/min. The porous structure of the film results from a template, which consists of water microspheres and temporarily exists during the evaporation of polymer solution. Water microspheres are formed by the condensation of gaseous water at the air–polymer solution interface. Polymer dissolved in the solution is adsorbed into the interface between water and polymer solution. Water microspheres are prevented from collapse and fusion by the protecting layer of the polymer. The water microspheres form hexagonal array on the surface of polymer solution in self-organization process induced by capillary flow in the evaporating polymer solution. Honeycomb-like porous structure of polymer appears on a substrate after completing evaporation of water and organic solvent.

Figure 1(b) shows a SEM image of a honeycomb film of poly(L-lactic acid). This film has some structural features: (1) micropores with diameter of several micrometer, (2) hexagonal arrays of the micropores, (3) single layer of the array with several micrometer thickness. Although the honeycomb film exhibits the isotropic

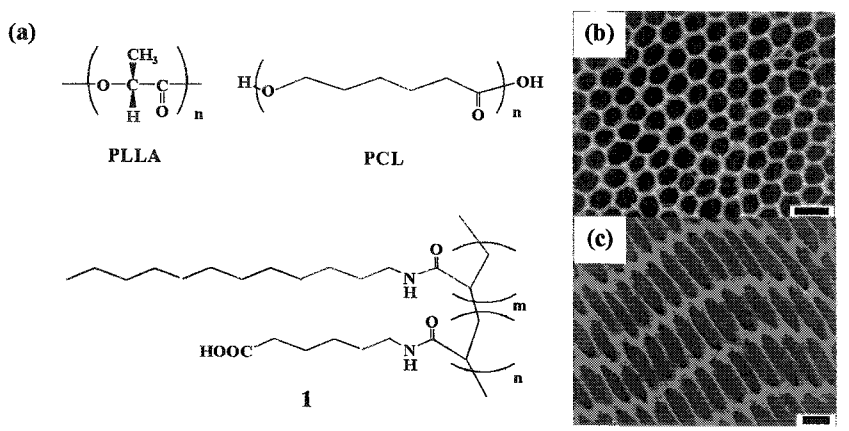

Fig. 1. (a) Polymers for the fabrication of honeycomb films. (b) Scanning electron microscope images of self-supporting honeycomb film of PLLA and (c) self-supporting stretched honeycomb film of PCL. Scale: 10 μm.

hexagonal pattern, a honeycomb film of a viscoelastic polymer can be stretched and anisotropic arrays of micropores can be formed. For the preparation of a viscoelastic honeycomb film, poly(ε-caprolactone), PCL was applied. The PCL exhibits viscoelastic property at around 20°C.[8] Therefore a self-supporting honeycomb film of PCL can be stretched at this temperature. After the uniaxial stretching, arrays of elongated micropores were observed in the stretched honeycomb film as shown in Fig. 1(c). The arrays of the stretched micropores are applicable to guiding cell alignment.

3. Three-Dimensional Culture System for Tissue Formation

The self-supporting honeycomb film is a two-sided substrate. Based on the feature of the honeycomb film, we expect that cells can be cultured on both sides of the film and they can contact with each other, laterally and vertically, through the micropores. In order to prove this hypothesis, various types of cells were cultured on both sides of a honeycomb film. At first, the heart muscle cells (cardiac myocytes (CMYs)) were cultured on both sides of a honeycomb film of PLLA. For comparison, an as-cast film of PCL was utilized for culture substrate of CMYs. Cardiac contraction was observed on the 7th day of the cultures. On the as-cast film, the contraction rhythm of CMYs was random. This indicates that cell–cell contact is insulated by the polymer film. On a honeycomb film, CMYs contracted in a synchronized rhythm. This suggests that the vertical contacts of the CMYs are achieved through the micropores of a honeycomb film.

The three-dimensional cell culture system can be applied to various cell types such as hepatocytes, endothelial cells, and smooth muscle cells. Figure 2(a) shows

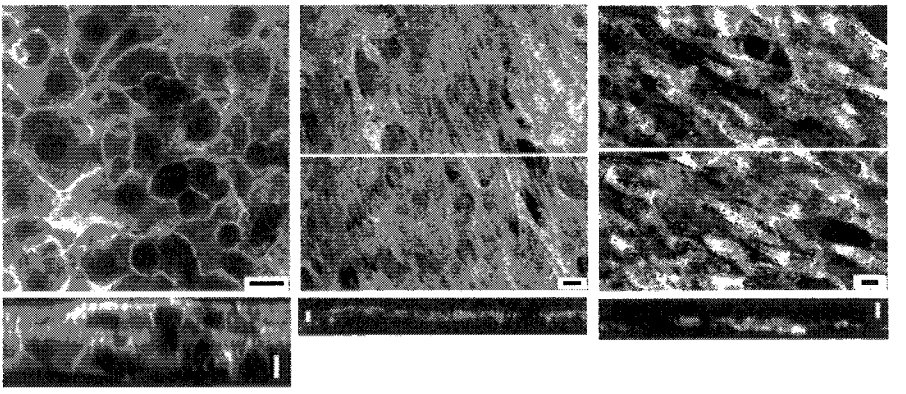

(a) (b) (c)

Fig. 2. Three-dimensional culture of (a) HEPs, (b) CMYs, and (c) ECs (bright) and SMCs (dark) by utilizing both sides of the porous films for cell attachment. The images were taken by confocal laser scanning microscopy. The cross-sectional images (bottom) were obtained along the line depicted on each X–Y plane image. Scale: 10 μm.

that liver HEPs form layer structure with a thickness of 20 μm at each side of a honeycomb film. The cellular aggregates of HEPs resemble the tissue structure of the liver *in vivo* where HEPs are adhered to the adjacent cells via cell adhesion proteins. The tissue formation of hepatocytes specifically occurred on the honeycomb film of PLLA and not on an as-cast film of PLLA. In the case of a stretched honeycomb film, CMYs are attached to both sides of the film and are aligned along the stretching direction of the honeycomb film (Fig. 2(b)). The co-culture system was also established by the culturing endothelial cells and the smooth muscle cells on a stretched honeycomb film. Figure 2(c) shows that each cell type was adhered separately onto each side of a stretched honeycomb film and are aligned along the arrays of micropores. Heterotypic cell–cell interaction are expected in the artificial multicellular tissue.

4. Conclusions

In the present study, we focused on the application of microporous films to the cell culture substrates for tissue engineering. The microporous films (honeycomb films) of degradable polymers were fabricated by evaporating a polymer solution into a humid atmosphere. Anisotropic arrays of micropores were formed by uniaxially stretching a honeycomb film of a viscoelastic polymer. The honeycomb films could be utilized for three-dimensional cell culture systems. The double-layered cellular aggregates were formed on the honeycomb films from the hepatocytes and cardiac myocytes respectively. The multicellular tissues like a blood vessel wall could also be reconstructed by co-culturing endothelial cells and smooth muscle cells on a stretched honeycomb film. The anisotropic arrays of the stretched micropores worked as a micropattern for guiding cell alignment. As a result, the cell culture on a self-supporting honeycomb film of a biodegradable polymer affects the basic cell behavior, such as cell adhesion, cell movement, and cell–cell interaction, and induces the self-organization of cells leading to tissue formation.

References

1. E. Bell, W. Saltzmann, J. Hubbel, R. Thomson, A. Shung, M. Yaszemski, and A. Mikos, *Principles of Tissue Engineering*, eds. R. Lanza, R. Langer, and J. Vacanti (Academic Press, 2000), pp. 181, 221, 237 and 251.
2. K. Dee, D. Puleo, and R. Bizios, *Biomaterials Today* **3**, 7 (2000).
3. K. McClary and D. Grainger, *Biomaterials* **20**, 2435 (1999).
4. D. Mooney, L. Hansen, J. Vacanti, R. Langer, S. Farmer, and D. Ingber, *J. Cell. Physiol.* **151**, 497 (1992).
5. A. Curtis and C. Wilkinson, *Biomaterials* **18**, 1573 (1997).
6. N. Maruyama, T. Koito, J. Nishida, T. Sawadaishi, X. Cieren, K. Ijiro, O. Karthaus, and M. Shimomura, *Thin Solid Films* **327–329**, 854 (1998).
7. T. Nishikawa, R. Ookura, J. Nishida, K. Arai, J. Hayashi, N. Kurono, T. Sawadaishi, M. Hara, and M. Shimomura, *Langmuir* **18**, 5734 (2002).
8. I. Engelberg and J. Kohn, *Biomaterials* **12**, 292 (1991).

International Journal of Nanoscience, Vol. 1, Nos. 5 & 6 (2002) 419–423

SURFACE STRUCTURE AND PROPERTIES OF MULTICOMPONENT MICROPATTERNED ORGANOSILANE MONOLAYERS PREPARED BY STEPWISE PHOTODECOMPOSITION AND CHEMISORPTION PROCESS

TOMOYUKI KOGA, MASAMICHI MORITA, HIROKI SAKATA, HIDEYUKI OTSUKA, and ATSUSHI TAKAHARA*

Institute for Fundamental Research of Organic Chemistry
Kyushu University, Hakozaki, Higashi-ku
Fukuoka 812-8581, Japan

Received 27 November 2002

Multicomponent micropatterned organosilane monolayers were successfully fabricated on Si substrate by stepwise vacuum ultraviolet-ray (VUV) photodecomposition and chemisorption process. The area-specific introduction of different organosilane molecules was confirmed by X-ray photoelectron spectroscopy (XPS). Atomic force microscopic (AFM) observation and lateral force microscopic (LFM) measurement revealed that the line-widths of the micropatterned surface corresponded to those of photomask. Micropatterning of the functional groups influenced the magnitudes of the surface free energy. The patterned surface was also applied for the site-specific polymerization and site-specific adsorption of microparticles.

Keywords: Organosilane; photodecomposition; surface nanostructure; surface properties.

1. Introduction

In order to fabricate micro- and nanodevices by the bottom–up approach, it requires building blocks with precisely controlled and tunable chemical composition, morphology and size virtually at will. Organosilane monolayers, which have surfaces terminated by various kinds of functional groups, are one of the candidates for the manipulation of physicochemical properties of solid surfaces.[1,2] Since organosilane monolayer is transparent against UV light, micropatterning employing vacuum ultraviolet (VUV)-ray photodecomposition process was proposed. By choosing 172 nm VUV-ray as an illumination source, a local photodecomposition of irradiated monolayer can be accomplished. In this study, micropatterned organosilane monolayers were prepared by a stepwise local photochemical decomposition and chemical vapor adsorption (CVA) process.[4–8] The multiphase surface obtained was thus characterized by various characterization techniques.

*Corresponding author.

2. Experimental

Octadecyltriethoxysilane (OTES), *N*-(2-aminoethyl)-3-aminopropylmethyldimethoxysilane (AEAPDMS) and (2-perfluorohexyl)ethyltriethoxysilane (FHETES) were employed as monolayer components. Si wafer substrates were photochemically cleaned by exposure for 3 min to vacuum ultraviolet-ray (VUV, λ = 172 nm) under 15 mmHg. The cleaned Si wafer substrates were immediately used for the preparation of OTES monolayer by chemical vapor adsorption method. Figure 1 outlines the steps for the fabrication of three-component micropatterned organosilane monolayers. The first step was the preparation of OTES-grafted Si substrates by CVA method.[5] Since VUV irradiation leads to excitation cleavage of C–C bonds, the irradiated parts becomes surface with Si–OH residues.[5] The OTES grafted Si-wafer was placed in an evacuated vacuum chamber. The sample was then covered with a photomask (20 mm × 20 mm square, 4 μm width Cr pattern, 2 μm slit with 20 mm line length) for irradiation (Fig. 1(b)). The sample was irradiated for 15 min with VUV light generated from an excimer lamp. In order to make sure the complete removal of the decomposed residue of organosilane monolayers, the patterned sample was sonicated for 10 min in ethanol and dried in vacuo. The second organosilane monolayer, FHETES, was then introduced into the first patterned surface by a similar method with alkylsilane (Fig. 1(d)).[8] The OTES/FHETES sample was then irradiated for 20 min with VUV, resulting in crossline micropatterns on the substrate's surfaces (Fig. 1(e)). The third organosilane monolayer, AEAPDMS, was finally introduced into the second-patterned substrate surfaces, again by the CVA method (Fig. 1(g)).[9]

Surface free energy of the monolayer was evaluated from the contact angles of the water and the methylene iodide droplets at 298 K based on Owens and Wendt's

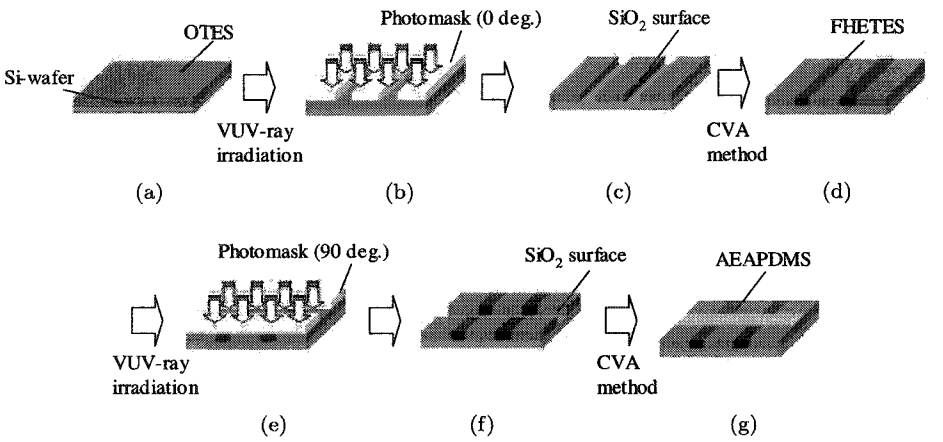

Fig. 1. Schematic representation of fabrication of three-component micropatterned organosilane monolayer.

method.[10] The stepwise fabrication of the three-component organosilane monolayer was confirmed by X-ray photoelectron spectroscopy (XPS). The emission angle of the photoelectrons was 45°. The surface nanostructure and frictional properties of the micropatterned monolayer were investigated by atomic force microscopic (AFM) observation and lateral force microscopic (LFM) measurement. AFM and LFM images were obtained under constant force mode in air at 300 K with 50–60% humidity, using a 100 μm × 100 μm scanner and Si_3N_4 tip on a triangle cantilever with a spring constant of 0.032 Nm^{-1}.

3. Results and Discussion

Surface chemical compositions of the micropatterned organosilane monolayers were characterized by XPS measurements. The OTES monolayer showed C_{1s}, O_{1s}, Si_{2s}, and Si_{2p} peaks at 285, 533, 151, and 100 eV, respectively. The OTES/FHETES patterned Si substrate clearly showed additional F_{1s} peak at 690 eV, while the OTES/FHETES/AEAPDMS grafted Si substrates showed further N_{1s} peak at 400 eV.[9] These results indicated that the three kinds of organosilane molecules were grafted on the substrate surfaces.

Changes of surface functional groups by micropatterning were also reflected in the magnitudes of surface free energy. The surface free energy of the OTES/FHETES micropatterned surface is smaller than that of the OTES monolayer surface; the decrease can be attributed to the introduction of fluoroalkyl group of FHETES, which is known to decrease surface free energy. On the other hand, the surface free energy, especially the polar component, increased after the grafting of AEAPDMS; this increase is attributed to the relatively high polarity of amino groups in the grafted AEAPDMS monolayers. From this stepwise change of surface free energy, it can be confirmed that the three-component organosilane surface has been micropatterned with highly hydrophobic, hydrophobic and hydrophilic areas.

Successful fabrication of a micropattern with three kinds of functional groups was confirmed by scanning force microscopic observation. Figures 2(a) and 2(b) show AFM and LFM images of a three-component micropatterned organosilane monolayer, respectively. These figures show lattice-like microstructures fabricated on the Si-wafer substrates. The widths of the fabricated FHETES and AEAPDMS lines were consistent with the widths of slits of the photomask. The height difference between the OTES and FHETES surfaces was ca. 1.4 nm. The height difference corresponds to the difference in the molecular length (ca. 1.3 nm) between OTES and FHETES. On the other hand, the height difference between the OTES and AEAPDMS surfaces was ca. 1.5 nm, corresponding to the difference in the molecular length (ca. 1.4 nm) between OTES and AEAPDMS. The origin of the contrast in the LFM image is explained by the difference in surface properties among three components, i.e., the chain rigidity, crystallinity, and the chemistry of terminal functional groups of the organosilane molecules.[2] The FHETES-grafted

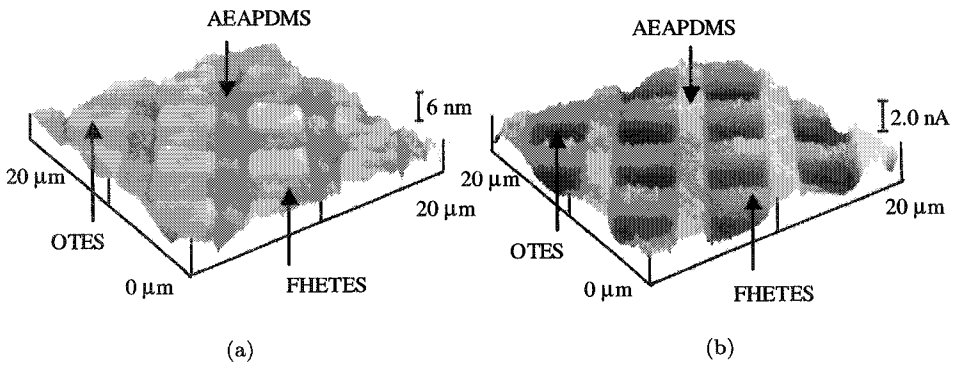

Fig. 2. (a) AFM and (b) LFM images of (OTES/FHETES/AEAPDMS) three-component micropatterned organosilane monolayer.

areas showed a higher magnitude of lateral force than that of OTES, owing to the larger shear strength of the rigid fluoroalkyl chain.[2,11,12] AEAPDMS-grafted areas are the brightest among the three components, because the terminal amino groups gave high lateral force due to the strong interaction between hydrophilic amino group and the Si–OH group of the surface of cantilever tip. The area ratio of the micropatterned monolayer is in accordance with that of the target value, i.e., the estimated area ratio of OTES/FHETES/AEAPDMS was 4/2/3.

The patterned surface was also applied for the site-specific polymerization and site-specific adsorption of microparticles. The (AEAPDMS/FHETES) patterned surface was immersed in the dispersion of SO_3H-modified polystyrene particle with 200 nm diameter. The microparticles were selectively adsorbed on the AEAPDMS phase.

Acknowledgments

This research was partially supported by Grant-in-Aid for scientific research No. 1200875189 and COE Research No. 08CE2005 from the Ministry of Education, Culture, Sports, Science and Technology, Japan and also by a grant from the Kawasaki Steel, 21st Century Foundation.

References

1. J. Sagiv, *J. Am. Chem. Soc.* **102**, 92 (1978).
2. K. Kojio, A. Takahara, and T. Kajiyama, *Langmuir* **16**, 9314 (2000).
3. J. M. Calvert and W. J. Dressick, *Jpn. J. Appl. Phys.* **32**, 5829 (1993).
4. H. Tada and H. Nagayama, *Langmuir* **10**, 1472 (1994).
5. H. Sugimura, K. Ushiyama, A. Hozumi, and O. Takai, *Langmuir* **16**, 885 (2000).
6. H. Sugimura, A. Hozumi, and O. Takai, *IEICE Trans. Electron.* **E83-C**, 1099 (2000).
7. A. E. Moser and C. J. Eckhardt, *Thin Solid Films* **382**, 202 (2001).
8. T. Koga, H. Otsuka, and A. Takahara, *Chem. Lett.*, 1196 (2002).
9. A. Hozumi, K. Ushiyama, H. Sugimura, and O. Takai, *Langmuir* **15**, 7600 (1999).

10. D. K. Owens and R. C. Wendt, *J. Appl. Polym. Sci.* **13**, 1741 (1969).
11. A. Takahara, K. Kojio, and T. Kajiyama, *Ultramicroscopy* **91**, 203 (2002).
12. A. Takahara, K. Kojio, S.-R. Ge, and T. Kajiyama, *ACS Symposium Series*, Vol. 694, *Scanning Probe Microscopy of Polymers*, Chap. 12 (ACS, 1998).

This page is intentionally left blank

International Journal of Nanoscience, Vol. 1, Nos. 5 & 6 (2002) 425–430

MECHANICAL PROPERTIES OF SURFACTANT-COATING CARBON NANOFIBER/EPOXY COMPOSITE

ZHE YING*, JIN-HONG DU, SHUO BAI, FENG LI,
CHANG LIU, and HUI-MING CHENG

Shenyang National Laboratory for Materials Science
Institute of Metal Research, Chinese Academy of Sciences
72 Wenhua Road, Shenyang 110016, China
**zying@imr.ac.cn*

Received 27 November 2002
Revised 24 December 2002

Carbon nanofibers (CNFs) were coated by surfactants of polyoxyetheylene alkyl ether (AEO_9, AEO_7) and polyvinyl alcohol (PVA 1799), respectively, after being mixed with surfactant aqueous solution and then treated with ultrasonication, high shear and magnetic stirring. The CNF/epoxy composites were prepared by mixing the surfactant coated CNFs with epoxy. Tensile strength, elastic modulus and ultimate strain of the composites were studied. The tensile strength and the ultimate strain of the composites were increased by 20% and 70%, respectively, after the CNFs were coated by surfactants. However, the elastic modulus of the composite will be lowered when the CNFs were treated by too high a concentration of surfactant solution.

Keywords: Carbon nanofibers; composites; surfactant; mechanical property.

1. Introduction

Due to their unique structure and extraordinary mechanical properties, carbon nanofibers (CNFs) are considered as a promising composite fillers and reinforcements.[1–4] CNF reinforced polymer composites have also attracted much research interest.[5–11] However, CNFs tend to agglomerate together and it is difficult to have them uniformly dispersed in the matrix, due to the strong interaction effect. Moreover, the interaction between the CNFs and the matrix is another important problem that need to be solved. Only when CNFs have strong interaction with polymer matrix, they can act as an effective reinforcing agent, which assures an effective transfer of the load from the polymer matrix to the CNFs when the composite is load-bearing. Presently, there are two main kinds of methods of surface treatment for CNFs employed to improve their interaction with the polymer matrix. One is surface functionalization[10]: some functional groups, which can improve the interaction between the CNF and the polymer matrix, are introduced into

*Corresponding author.

the surface of the CNFs; another method is to have the CNFs physically coated by some surfactants with interaction-improving groups. These two methods have achieved good results in the preparation of CNF/polymer composites. However, organic solvents are not suitable for mass application due to their high cost and harm.

In this paper, we chose several water-solvable surface-active resins and surfactants as the coating agents to prepare surfactant-coating CNFs. The CNF/epoxy composites were prepared, and their tensile properties were studied. The influence of surfactant-coating on the mechanical properties of the composites was investigated and discussed.

2. Experimental

In our experiment, carbon nanofibers were prepared by a floating catalyst method.[12] An SEM observation revealed that the average diameter of the CNFs was about 200 nm, and the purity was about 80%.

2.1. *Pre-treatment and surfactant coating of CNFs*

The CNFs were pulverized and annealed at 300°C under inert atmosphere for 2 h in order to remove organic materials introduced during preparation. The CNFs were then put into the aqueous solution of surfactants (AEO_7 and AEO_9), water-soluble resin (PVA 1799). A homogeneous suspension was obtained with magnetic stirring, ultrasonic and high shear stirring. Finally the coated CNFs were prepared by evaporating water in vacuum.

2.2. *Preparation of CNF/epoxy composites*

The surfactant-coating CNFs were mixed with epoxy resin (Bisphenol A-epichlorhydrine, hydroxylated polyamide), and stirred at 300 rpm for 1 h. The composite fluid was poured into a mold and vacuum degassed. The CNF/epoxy composite was cured for 4 h at 100°C.

2.3. *Tensile test*

The as-prepared composite with mold was cut into dumbbell-shaped samples. After the samples were annealed at 110°C for 10 h, the tensile test was performed with an Instron 1211 Elongation Analyzer at 10 mm/min at room temperature.

2.4. *SEM observations*

Surfactant-coating CNFs were observed by SEM and were analyzed by X-ray energy depressive spectroscopy (EDS). The fractural surface of CNF/epoxy composites and the interface between CNFs and epoxy matrix were also investigated.

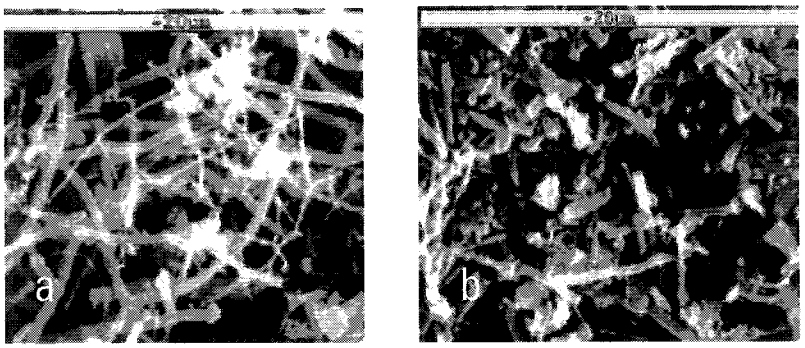

Fig. 1. SEM images of (a) CNFs and (b) surfactant AEO_7-coating CNFs.

3. Results and Discussion

3.1. *Mechanical properties of surfactant-coating CNF/epoxy composite*

SEM images of AEO_7-coating CNFs are shown in Fig. 1. We can see that the diameter of AEO_7-coating CNFs is larger than that of as-prepared CNFs. The EDS spectrum showed that the oxygen content of the coated CNFs is higher than that of CNFs, which may have been introduced by AEO_7. According to these results, we conclude that the CNFs have been effectively coated by AEO_7. The results for AEO_9 and PVA 1799 are similar.

Tensile properties of the surfactant-coating CNF/epoxy composite are shown in Fig. 2 and Table 1. Tensile strength of the composites can be improved up to about 20% by using the surfactant-coating CNFs, and the ultimate strain can be improved by as much as 60%. The functional mechanism of the surfactants may be these surfactants have hydrophilic segment as well as hydrophobic segment, the hydrophobic segment would wind around the surface of CNFs, while the hydrophilic ones

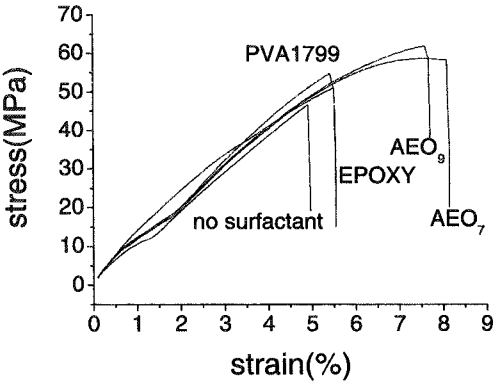

Fig. 2. Stress–strain curves for different surfactant-coating CNF/epoxy composite.

Table 1. Tensile properties of different surfactant-coating CNF/epoxy composite.

CNF content (Wt %)	Surfactant	Tensile strength (MPa)	Elastic modulus (MPa)	Ultimate strain (%)
0	—	52	1177	5.90
2	—	46	1175	5.08
2	PVA(1799)	55	1348	5.78
2	AEO_9	62	1385	8.04
2	AEO_7	58	1337	7.73

distribute outside of the CNFs and form hydrogen bonding with epoxy,[8] which is in favor of the dispersion of CNFs among epoxy matrix and improve the interfacial behavior. As a result, the load can be effectively transferred onto the CNFs when the composite is load-bearing. For AEO_7 and AEO_9, the hydrophobic segment is alkyl (mostly dodecyl), the hydrophilic segment is polyoxyethylene and hydroxy. The alkyl has strong interfacial bonding with CNFs, and the hydroxy and polyoxyethylene had strong interfacial bonding with epoxy. So AEO_7 and AEO_9 worked as reinforcement agent of the interfacial bonding of CNFs and epoxy. For PVA, the hydrophobic segment is polyethylene chain with hydroxy, and the hydrophilic is hydroxy. So PVA has an effect analogous to polyoxyethylene alkyl ether. However, there are many hydroxys on polyethylene chain, the hydrophobic properties of the polyethylene chain was weaker than that of the alkyl. So AEO_7 (or AEO_9) should have stronger interfacial bonding effect than for PVA 1799. Figure 3 shows the fractural surfaces of CNF (with and without surfactant-coating)/epoxy composites. In the case of the CNFs are not coated by surfactant, many CNFs were pulled out from epoxy matrix and slick ducks were left; when the CNFs are coated, the broken CNFs can be observed. These results indicate that the interfacial bonding between the coated CNFs and the epoxy is strong, while that between the uncoated CNFs and the epoxy is weak.

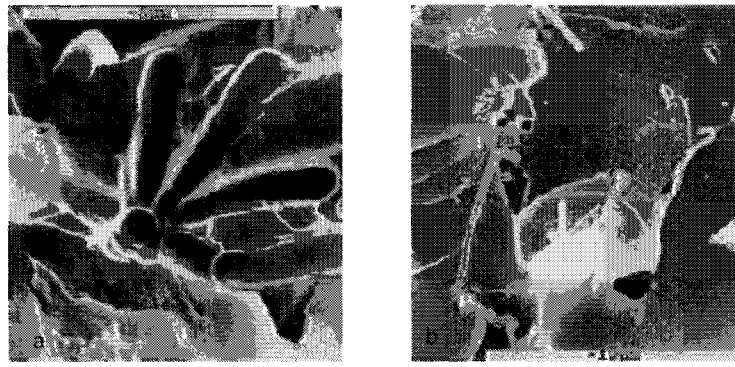

Fig. 3. SEM images of fracture surface of (a) CNF/epoxy composite and (b) surfactant-coating CNF/epoxy composite.

Table 2. Tensile properties for CNF/epoxy composites with different ratio of surfactant to CNFs.

Weight ratio of surfactant: CNF	Tensile strength (MPa)	Elastic modulus (MPa)	Ultimate strain (%)
0:1	46	1175	5.08
0.5:1	62	1385	8.04
1:1	61	1039	8.70

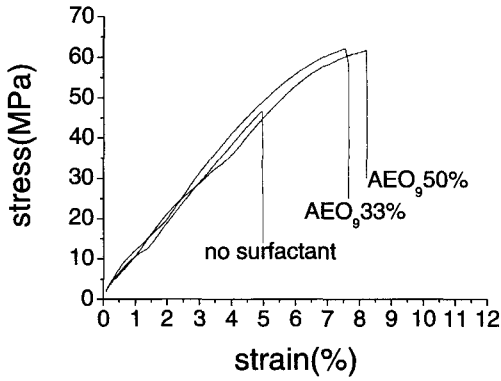

Fig. 4. Stress–strain curves of the composites with different surfactant contents.

3.2. *Effect of the surfactant concentration on the tensile properties of the CNF/epoxy composite*

Two AEO_9 concentrations were employed to evaluate the surfactant concentration effect. The tensile results of the composites obtained are listed in Table 2 and Fig. 4. It is showed that with the increase in the AEO_9 concentration, the tensile strength does not increase, apart from the increase in the elongation. There is a noticeable decrease in elastic modulus due to the surplus surfactant acted as the plasticizer of the epoxy matrix. The plasticizers will dilute polymer matrix and the weaker interaction between polymer chains, so the elastic modulus of polymer matrix was decreased. Therefore, a suitable concentration of surfactants is important to improve the overall mechanical properties of CNF/epoxy composites.

4. Conclusion

Three kinds of surfactants (PVA 1799, AEO_7 and AEO_9) were coated on the surface of CNFs, and then surfactant-coating CNF/epoxy composites were fabricated. The surfactants can be effectively coated on the CNFs thus enhance the interfacial bonding between the CNFs and the polymer matrix. The max increase of the tensile strength and the ultimate strain of the composites were increased by 20% and 70%, respectively, as compared with the composites reinforced by as-prepared CNFs. When the percentage of the added surfactants is too high, the surplus surfactant

acted as plasticizer and lowered the elastic modulus of the composites. Moreover, AEO_9 seems to be the most effective surfactant to improve the tensile properties of CNF/epoxy composites.

Acknowledgments

This work was supported by the National Natural Science Foundation of China (Nos. 50025204 and 50102007) and by Chinese Academy of Sciences.

References

1. Z. Jin, W. Sun, G. Xu, S. H. Goh, and W. Ji, *Chem. Phys. Lett.* **318**, 505 (2000).
2. D. Qian, E. C. Dickey, R. Andrews, and T. Rantell, *Appl. Phys. Lett.* **76**(20), 2868 (2000).
3. A. Peigney, E. Flahart, C. H. Laurent, F. Chastel, and A. Rousset, *Chem. Phys. Lett.* **52**, 20 (2002).
4. C. L. Xu, B. Q. Wei, R. Z. Ma, J. Liang, X. K. Ma, and D. H. Wu, *Carbon* **37**, 855 (1999).
5. M. S. P. Shaffer and A. H. Windle, *Adv. Mater.* **11**, 937 (1999).
6. L. Jin, C. Bower, and O. Zhou, *Appl. Phys. Lett.* **73**, 1197 (1998).
7. C. Bower, R. Rosen, L. Jin, J. Han, and O. Zhou, *Appl. Phys. Lett.* **74**, 3317 (1999).
8. X. G. Gong, J. Liu, S. Baskaran, R. D. Voise, and J. S. Young, *Chem. Mater.* **12**, 1049 (2000).
9. R. Haggenmueller, H. H. Gommans, A. G. Rinzler, and J. E. Fischer, *Chem. Phys. Lett.* **330**, 219 (2000).
10. K. Lozano and E. V. Barrera, *J. Appl. Polym. Sci.* **79**, 125 (2001).
11. A. Rodney, J. David, M. Mickael, and R. Terry, *Macromol. Mater. Eng.* **287**, 395 (2002).
12. Y. Y. Fan, H. M. Cheng, Y. L. Wei, G. Su, and Z. H. Shen, *Carbon* **38**(6), 921 (2000).

International Journal of Nanoscience, Vol. 1, Nos. 5 & 6 (2002) 431–436

HIGH DENSITY DIAMOND WHISKER FABRICATION AND SUPPRESSION OF SECONDARY ELECTRON EMISSION BY WHISKERS

D. JEON* and S. W. LEE

Department of Physics, Myong Ji University
San 38-2 Namdong Yongin Kyunggi-do, Seoul 449-728, Korea
**jeon@mju.ac.kr*

Y. J. BAIK

Thin Film Technology Center
Korea Institute of Science and Technology, P.O. Box 131
Cheongryang, Seoul 130-650, Korea

Received 27 November 2002
Revised 19 December 2002

Diamond whiskers were formed by etching diamond thin films using metal clusters as a shadow mask, which were deposited on the diamond film before or during etching. The whiskers were as thin as 100 nm and the density was as high as $10^{10}/\text{cm}^2$. The secondary electron emission yield of the diamond whiskers was significantly reduced as compared to the initial diamond film. The decrease in the yield was more significant if the primary electrons were impinged in parallel direction with the whiskers. We suggest that absorption of the secondary electrons in the narrow gap between the whiskers was the reason for the decreased yield.

Keywords: Diamond; whisker; field emission; secondary electron emission; etching.

1. Introduction

Secondary electrons are emitted when primary particles bombard a material. The secondary electron emission (SEE) yield depends on several factors. For example, if the electron–electron interaction is weak as in the wide band-gap materials, more secondary electrons can reach the surface to escape to vacuum. This is why diamond shows high SEE yield. The reported values of SEE yield of diamond show a large variance due to the different chemical status of carbon atoms on the diamond surface. The chemical states and the morphology of a material is an important parameter determining the SEE yield,[1] which is actually the operational principle of a scanning electron microscope. We report here that the secondary electron

*Corresponding author.

emission from diamond is significantly reduced by forming whiskers on the surface. We suggest that the decreased emission is due to the trap of the emitted electrons inside the narrow holes between the whiskers.

2. Experimental

Polycrystalline diamond films were prepared on a Si substrate using hot filament chemical-vapor-deposition method. 2% methane and 98% hydrogen gas were blown into the chamber to maintain 60 Torr pressure. The Si substrate was kept at 950°C using hot filaments positioned 2 cm above the substrate. The diamond films grown were 3 μm thick. The average sheet resistance of the films was around $0.2 \times 10^6\ \Omega/\square$.

The plasma etching forming whiskers was performed using radio frequency (RF) discharge of dry air. The RF power was 300 W and the airflow was controlled to keep the chamber pressure at 25 mTorr. The self-bias voltage to the substrate was typically -180 V. After the plasma etching, the samples were washed in acid solution to remove metal clusters adsorbed during the etching process. The acid treatment is also known to remove nondiamond substance and hydrogen from the surface.[2]

The SEE was measured by bombarding the samples with primary electrons of varying energies at different incident angles. The primary electron beam diameter was 2 mm and the current was 0.3 μA. The sample current was measured and converted to the SEE yield using the relation, *primary current + sample current = secondary current.*

3. Results and Discussions

Figure 1(a) shows a scanning electron micrograph (SEM) of the initial diamond film grown on a Si wafer. Figure 1(b) shows the whiskers after plasma etching process, and Fig. 1(c) shows whiskers after washing in acid to remove metal clusters deposited on the diamond during etching. The diamond whiskers shown in Fig. 1(c) are as tall as the thickness of the initial diamond film. Photoemission measurement showed that the metal clusters on the whiskers were Mo, which we believe was originated from the sputtering of the Mo substrate holder during etching. The different etching rates between the diamond and Mo, the angle dependence of the etching rate, and the positive bias voltage applied to the substrate were the reasons for the formation of the high-density diamond whiskers.[3,4] This process of whisker formation is illustrated in Fig. 2.

The SEE yield depends on the degree of electron–electron interaction and the surface barrier height. The SEE also depends on the surface morphology because the escape probability of the secondary electrons depends on the distance to reach the surface. To study how whisker morphology affected the SEE yield, we prepared diamond whiskers of different heights by varying the etching time. Figure 3(a) shows the initial diamond film before etching, and the whiskers shown in Figs. 3(b)–3(d) are roughly 200 nm, 400 nm, and 600 nm long, respectively.

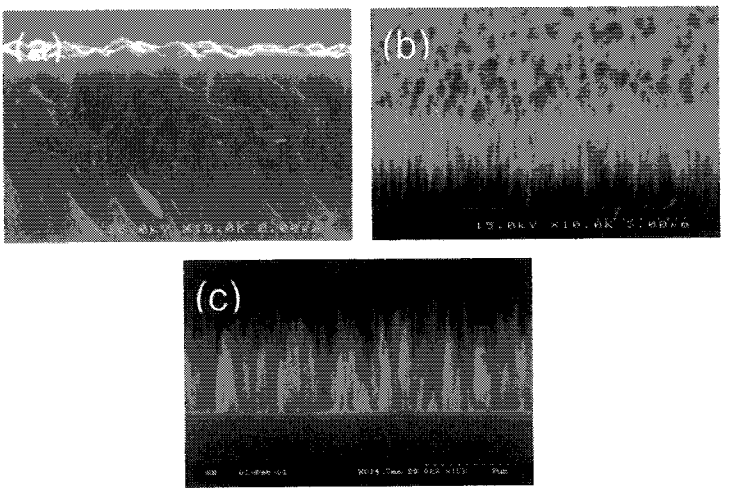

Fig. 1. The diamond whiskers were formed by air–plasma etching of polycrystalline diamond thin film grown by chemical vapor deposition on a Si substrate. The SEM micrographs of (a) the initial diamond film, (b) whiskers before washing the metal clusters, and (c) whiskers after washing away the metal clusters were shown.

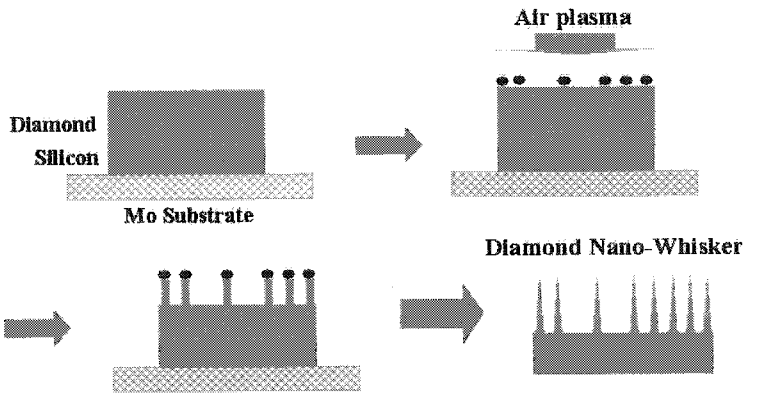

Fig. 2. Schematic process of the whisker formation. Metal clusters deposited onto the diamond during etching play a role of etch-resistant mask.

Figures 4(a)–4(d) represent SEE yields obtained from the samples shown in Figs. 3(a)–3(d), respectively. The yield from the initial diamond film is larger when the primary electron impinging direction is vicinal to the substrate surface because in this case the distance for the secondary electrons to escape to vacuum is short.[1] The maximum yield for the normal primary electron impinging direction occurs when the energy of the primary electrons is around 500 eV. With 60° direction, it occurs when the energy is around 1000 eV. The yields for normal, 20°, and 40° directions are similar due to the bumpy surface of the granular diamond film. When the whiskers are about 200 nm long, the SEE yield has decreased significantly

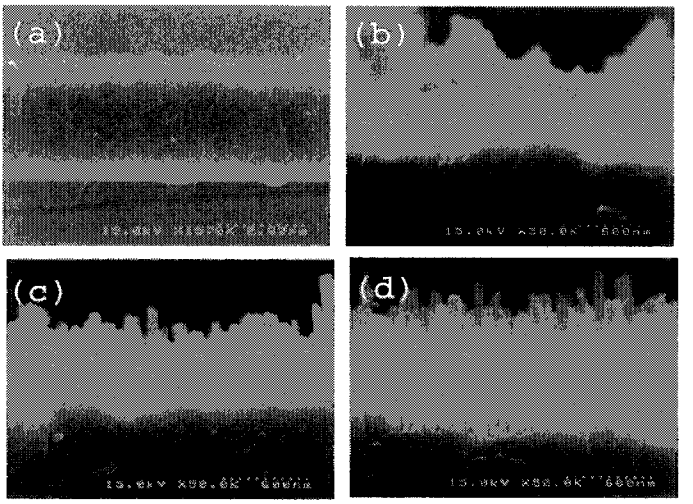

Fig. 3. (a) SEM micrograph of the cross-section of the initial diamond film. (b)–(d) Diamond whiskers of increasing lengths by air–plasma etching for increasing time.

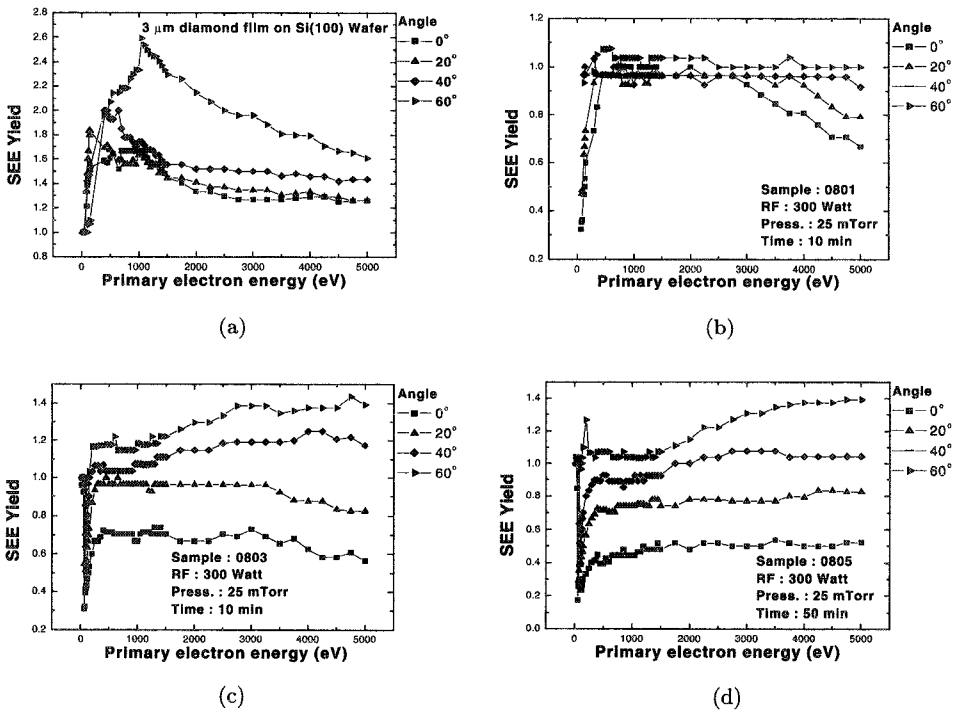

Fig. 4. SEE yield from diamond and diamond whisker samples for different incident angles of the primary electrons. The yields (a)–(d) were obtained from the samples shown in Figs. 3(a)–3(d), respectively.

for all primary electron incident angles, as shown in Fig. 4(b). For normal and 20° directions, the yields decrease after passing the maximum, for the increasing primary electron energy, but for 40° and 60°, the yields stay constant. When the whiskers are 400 nm long, the yields for normal and 20° decreased more as compared to 200 nm whiskers and stay constant for high primary electron energy [Fig. 4(c)]. The trend that SEE yield stay more or less constant at high primary electron energy for all primary electron impinging direction is repeated for 600 nm-long whiskers shown in Fig. 3(d).

For the primary electrons impinging from the direction normal to the surface, small fraction of the primary electrons hit the tip of the whiskers. Majority of the primary electrons will hit the side of the whiskers or the bottom of the hollow holes, and thus the secondary electrons have to travel a long distance to escape out of the whiskers. Since many secondary electrons will be recaptured before they escape, because their energy is low, the SEE yield of the whiskers is smaller than that of the bulk.

For bulk material, the SEE yield becomes maximum when the penetration depth of the primary electrons is approximately equal to the escape depth of the secondary electrons.[5] This is because when the primary electron energy is low, secondary electrons are produced close to the surface but the quantity is small, and when the primary electron energy is high, larger number of electrons are scattered but the scattered electrons have to travel greater distance before escaping to vacuum. As the primary electron energy increases the latter effect becomes significant and the SEE yield start to decreases. For the case of whiskers, the situation is different. If the primary electron energy is high, they can pass more whiskers before they are stopped. Since the secondary electrons can escape through the sidewall of the thin whiskers, the distance to the surface is not a limiting factor. Once the secondary electrons escape, they still have to travel up the hollow holes between the whiskers before they escape from the whiskers. This limits the SEE yield for whiskers. The SEE yield data obtained from long whiskers, depicted in Fig. 4(d), show that, different from the case of bulk materials, the yield almost saturates at high primary electron energy.

4. Summary

We have studied the secondary electron emission from diamond whiskers. Whiskers on the diamond surface significantly suppressed the secondary yield due to the trap of the emitted electrons inside the hollow holes between the whiskers. For the primary electrons impinge at the glazing angle, the yield increased with the primary energy because the primary electrons could pass more whiskers.

Acknowledgment

This work was supported by the Korea Science and Engineering Foundation under Grant No. R01-2000-000-00033-3 (2002).

References

1. N. Kotera, T. Kishida, and H. Suga, *Scanning Microscopy Supplement* **4**, 111 (1990).
2. A. Shih, J. Yater, P. Pehrsson, J. Butler, C. Hor, and R. Abrams, *J. Appl. Phys.* **82**, 1860 (1997).
3. R. Behrisch (ed.), *Sputtering by Particle Bombardment II* (Springer-Verlag, Berlin, 1983).
4. E.-S. Baik, Y.-J. Baik, S. W. Lee, and D. Jeon, *Thin Solid Films* **377–378**, 295 (2000).
5. A. Shih, J. Yater, C. Hor, and R. Abrams, *Appl. Surf. Sci.* **111**, 251 (1997).

International Journal of Nanoscience, Vol. 1, Nos. 5 & 6 (2002) 437–441

PREPARATION OF CUBE-SHAPED CdS NANOPARTICLES BY SONOCHEMICAL METHOD

HUI WANG*, YINONG LU†, and JUNJIE ZHU*,‡

*Laboratory of Mesoscopic Materials Science, Department of Chemistry
Nanjing University, Nanjing, 210093, P. R. China
†College of Materials Science and Engineering
Nanjing University of Technology, Nanjing, 210009, P. R. China
‡jjzhu@nju.edu.cn

Received 26 November 2002
Revised 24 December 2002

Cube-shaped CdS nanoparticles have been successfully prepared by a sonochemical method in an oil-in-water microemulsion. The product was characterized by using techniques including X-ray powder diffraction, high-resolution transmission electron microscopy, energy-dispersive X-ray analysis and UV-visible absorption spectroscopy. This microemulsion system in the presence of high-intensity ultrasound irradiation provides special conditions for the nucleation and growth of the CdS nanoparticles.

Keywords: CdS; nanoparticles; sonochemistry; microemulsion; cube-shaped.

There has been increasing interest in the preparation and characterization of chalcogenides due to their important physical and chemical properties.[1] Among the chalcogenides, CdS is one of the most attractive semiconducting materials owing to its special properties and wide application in various fields, especially in photoconducting cells. It is known that the chemical and physical properties of nanosized semiconductors depend on their size and morphology. Therefore, control over both size and morphology has become the focus of interest of many synthetic chemists and materials scientists. In the past few years, nanocrystalline CdS with various morphologies including spherical nanoballs,[2] nanorods or nanowires,[3] nanoribbons,[4] hollow spheres,[5] and peanut-like particles[6] have been successfully synthesized via several novel synthetic routes. However, up to now, designing new strategies for the fabrication of cube-shaped CdS nanoparticles still remains a great challenge.

Currently, ultrasound irradiation offers a very attractive method for the preparation of nanosized materials and has shown very rapid growth in its application to materials science due to its unique reaction effects and its ability to induce the formation of novel materials with unusual properties.[7] It has been reported that exposing an aqueous solution containing cadmium salts and sodium thiosulfate will lead to the formation of spherical CdS nanoparticles.[8] Sonochemical preparations of spherical assemblies composed of CdS spherical particles in

CS_2-water-ethylenediamine (CWE) system[9] have also been recently reported. Herein, we design a new strategy to prepare cube-shaped CdS nanoparticles sonochemically in a microemulsion. To the best of our knowledge, the preparation of cube-shaped CdS nanoparticles has never been reported before.

In a typical procedure, 5 mL sulfur-toluene solution (STS) was mixed with 95 mL aqueous solution containing 0.005 mol cadmium chloride ($CdCl_2$), 0.4 g sodium dodecyl sulfate (SDS) and 5 mL ethylenediamine. STS was prepared by stirring 1.0 g sulfur powder in 50 mL toluene at ca. 313 K till the sulfur powder was completely dissolved. Then the mixtures were exposed to ultrasound irradiation under ambient air for 30 min. Ultrasound irradiation was accomplished with a high-intensity ultrasound probe (Xinzhi Co., China; JY92-2D; 0.6 cm-diameter; Ti-horn, 20 kHz, 60 W/cm^2) immersed directly in the reaction solution. The sonication was conducted without cooling so that a temperature of about 333 K was reached at the end of the reactions. When the reactions finished, a yellow precipitate occurred. The precipitate was separated by centrifugation, washed with distilled water, absolute ethanol and acetone in sequence, and dried in air at room temperature. The final products were characterized by using techniques including X-ray powder diffraction (XPRD), high-resolution transmission electron microscopy (HRTEM), energy-dispersive X-ray analysis (EDAX) and UV-visible absorption spectroscopy. The XPRD analysis was performed by Shimadzu XD-3A X-ray diffractometer with graphite monochromatized $Cu_{K\alpha}$ radiation (λ = 0.15418 nm). The HRTEM images were obtained by employing a JEOL-2010 high-resolution transmission electron microscope with a 200 kV accelerating voltage. EDAX measurements were performed by employing the PV9100 instrument. Ruili UV-2400 photospectrometer was used to record the UV-visible absorption spectrum of the as-prepared particles.

The morphology and structure of the as-prepared CdS nanoparticles were characterized by HRTEM. The HRTEM images (Figs. 1(A)–1(C)) reveal that the product is composed of cube-shaped nanoparticles with 3–6 nm in size. Though they are agglomerated, cubic morphology and hexagonal lattice fringes can be clearly seen. Figure 1(D) provides further insight into the structure of an individual CdS nanoparticle. It is obvious that this particle crystallizes in a hexagonal structure with cell constant $a = b = 0.41$ nm, as measured directly in Fig. 1(D). The spaces of lattice planes are close to those obtained from the bulk CdS crystals. The XPRD pattern of the product (Fig. 2) provides further evidence to its crystalline structure. All the diffraction peaks can be indexed to be a pure hexagonal phase for CdS. The intensities and positions of the peaks are in good agreement with the literature values.[10] The average size of the as-prepared CdS nanoparticles is estimated to be 5 nm according to the Debye–Scherrer formula.[11] The product is also characterized by EDAX measurements for evaluation of their composition and purity. The EDAX results reveal that the as-prepared CdS has high purity and the Cd:S ratio is calculated to be approximately 1:1.

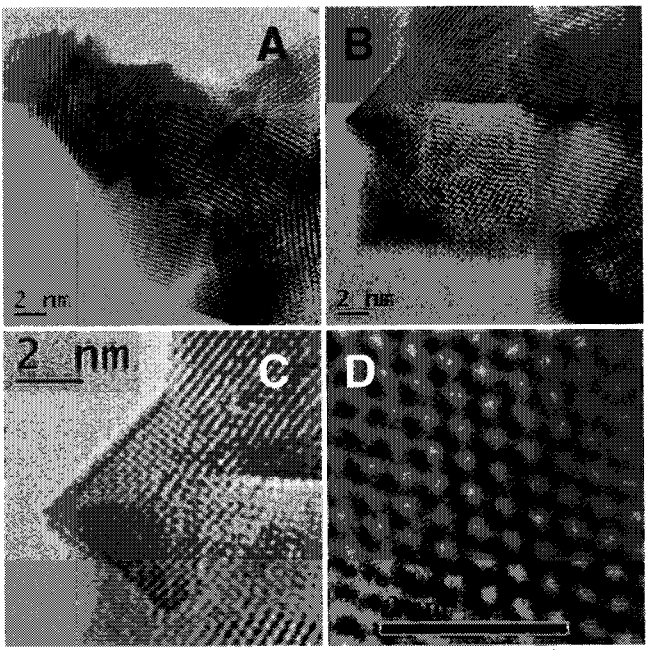

Fig. 1. HRTEM images of the as-prepared CdS nanoparticles.

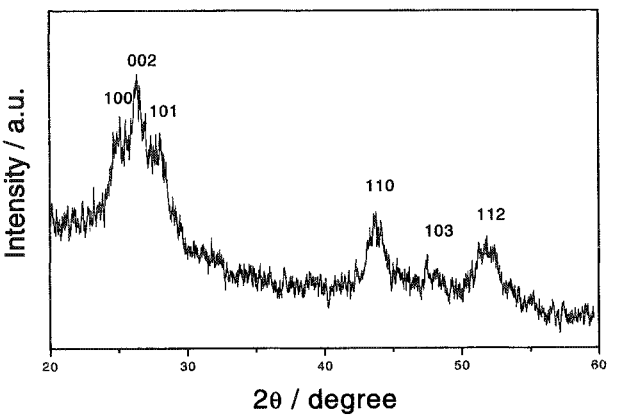

Fig. 2. XPRD pattern of the as-prepared CdS nanoparticles.

Figure 3 shows the UV-visible absorption spectrum of the as-prepared CdS nanoparticles dispersed homogeneously in ethanol solution (the concentration is 0.10 mg/mL). The maximum at about 475 nm is assigned to the optical transition of the first excited state.[3] The absorption edge of CdS is blue-shifted from the absorption edge of the bulk CdS (512 nm), indicating the presence of quantum size effects in this sample. The blue-shift of the absorption peak is attributed to the

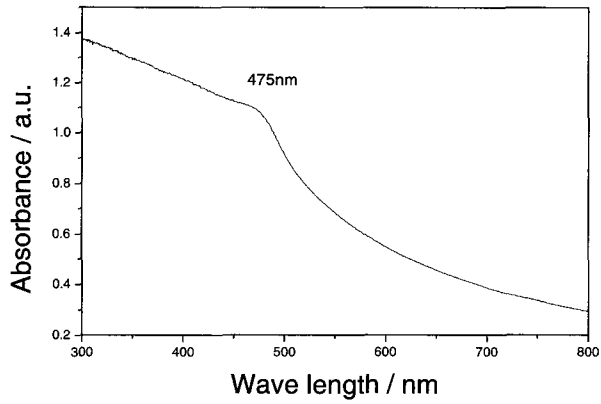

Fig. 3. UV-vis absorption spectrum of the as-prepared CdS nanoparticles.

increase of the band-gap of the nanoparticles, which indicates the size quantum effects.

The present synthetic design was motivated by the known simple interaction between sulfur and ethylenediamine,[12] but it provided special conditions for the formation and growth of the sulfide nanoparticles in such a microemulsion system in the presence of high-intensity ultrasound irradiation. Sulfur-toluene solution (STS) was chosen as the sulfur source. When STS was mixed with water, a liquid–liquid heterogeneous system was formed. Sulfur powder was dissolved in toluene, the oil phase, and $[Cd(en)x]^{2+}$, and excessive ethylenediamine was in the water phase. The cavitation behavior of ultrasound irradiation can lead to extraction, mixed phase reactions and emulsification in such a liquid–liquid heterogeneous system. Thus, an o/w microemulsion of toluene-in-water formed under ultrasound irradiation. Toluene droplets became homogenized and sulfur began to react with ethylenediamine at the oil–water interface to give H_2S. Then the released H_2S combined with $[Cd(en)x]^{2+}$ to form CdS nuclei in the water phase. SDS played a critical role in this process. It not only promoted the formation of the microemulsion as the oil droplet stabilizer, but also provided the sites for the reactions by bridging the oil–water interface. The details of the formation of cube-shaped CdS nanoparticles in such a microemulsion under ultrasound irradiation is still under study.

In summary, a novel sonochemical method for the preparation of cube-shaped CdS nanoparticles in a microemulsion has been successfully established. It may be extended to the preparation of some other chalcogenide nanoparticles and provides a promising way to produce nanoparticles with cubic morphology.

Acknowledgments

This work is supported by the National Natural Science Foundation of China (Grant Nos. 50072006 and 90206037) and the Jiangsu Advanced Science and Technology Program (BG 2001039).

References

1. N. Heron, J. C. Calabrese, W. E. Farneth, and Y. Wang, *Science* **259**, 1426 (1993); A. Henglein, *Chem. Rev.* **89**, 1861 (1989); C. Kaito, Y. Saito, and K. Fujita, *J. Cryst. Growth* **94**, 967 (1989); R. F. Service, *Science* **271**, 920 (1996).
2. C. Y. Wang, X. Mo, Y. Zhou, Y. R. Zhu, H. T. Liu, and Z. Y. Chen, *J. Mater. Chem.* **10**, 607 (2000); C. B. Murray, D. J. Norris, and M. G. Bawendi, *J. Am. Chem. Soc.* **115**, 8706 (1993).
3. C. C. Chen, C. Y. Chao, and Z. H. Lang, *Chem. Mater.* **12**, 1516 (2000); P. Yan, Y. Xie, Y. T. Qian, and X. M. Liu, *Chem. Commun.*, 1293 (1999); B. A. Simmons, S. Li, V. T. John, G. L. McPherson, A. Bose, W. Zhou, and J. He, *Nano Lett.* **2**, 263 (2002).
4. J. J. Zhu, H. Wang, J. M. Zhu, and J. Wang, *Mater. Sci. Eng. B* **94**, 136 (2002).
5. J. X. Huang, Y. Xie, B. Li, Y. Liu, Y. T. Qian, and S. Y. Zhang, *Adv. Mater.* **12**, 808 (2000).
6. Y. Xie, J. X. Huang, B. Li, Y. Liu, and Y. T. Qian, *Adv. Mater.* **12**, 1523 (2000).
7. K. S. Suslick, *Ultrasound: Its Chemical, Physical and Biological Effects* (VCH, Weinhein, Germany, 1988).
8. G. Z. Wang, W. Chen, C. H. Liang, Y. W. Wang, G. W. Meng, and L. D. Zhang, *Inorg. Chem. Commun.* **4**, 208 (2001).
9. J. X. Huang, Y. Xie, B. Li, Y. Liu, J. Lu, and Y. T. Qian, *J. Colloid Interface Sci.* **236**, 382 (2001).
10. JCPDS, File No. 41-1049.
11. H. Klug and L. Alexander, *X-Ray Diffraction Procedures* (Wiley, New York, 1962).
12. P. Dubois, J. P. Lelieur, and G. Lepoutre, *Inorg. Chem.* **28**, 195 (1989); G. Henshaw, I. P. Parkin, and G. A. Shaw, *Chem. Commun.*, 1095 (1996); G. Henshaw, I. P. Parkin, and G. A. Shaw, *J. Chem. Soc. Dalton Trans.*, 231 (1997).

This page is intentionally left blank

International Journal of Nanoscience, Vol. 1, Nos. 5 & 6 (2002) 443–447

XANES STUDY OF COPPER NANOPARTICLES IN THE ELECTROCHEMICAL REACTION OF Li WITH CuO

HYUN CHUL CHOI, YOUNG MEE JUNG, and SEUNG BIN KIM*

Department of Chemistry, Pohang University of Science and Technology
San 31, Hyojadong, Namgu, Pohang 790-784, Republic of Korea
**sbkim@postech.edu*

Received 27 November 2002

The electrochemical insertion–deinsertion of lithium into CuO electrode was examined by Cu K-edge X-ray absorption near edge structure (XANES) during the first electrochemical cycle. The XANES spectra in the Li_xCuO (x: lithium content) system reveal that the initial insertion of lithium leads to the reduction of the Cu^{2+} in the pristine CuO to form the reduced nanosized Cu metal. In the successive deinsertion of lithium, the reduced Cu particles changed partially to the phase of Cu_2O.

Keywords: XANES; nanoparticles; CuO.

1. Introduction

Recently the formation and characterization of metal nanoclusters, which are formed by the electrochemical reaction of lithium with the metal oxide, has been intensively studied in a lithium/metal oxide cell.[1–3] However, the electrochemical behavior of the metal oxide is still not fully understood. The discharge (insertion) reaction can be described as a formal displacement reaction: $2Li + MO \rightarrow Li_2O + M$, where MO is the metal oxides such as CuO, CoO, and MnO_2. Among them, CuO has drawn great attention due to the high theoretical capacity (0.67 Ah/g and 4.26 Ah/cm^3). Its large capacity leads to Li/CuO primary cells were produced on an industrial scale, and many discharge reaction mechanism have since been proposed.[3–8] Based on these characterization results, Ikeda and Narukawa reported that discharge reaction proceeds according to the following reaction: $CuO + 2Li \rightarrow Cu + Li_2O$.[5] In contrast, Matsuda *et al.* suggested CuO to be reduced stepwise: $CuO \rightarrow Cu_2O \rightarrow Cu$.[6] Bates and Jumel claimed that the discharge mechanism first involve the insertion of lithium into CuO lattice and then forms both Cu_2O and Li_2O.[7] Novak suggested the electrochemical insertion of the lithium into the CuO according to the following reaction: $CuO + xe^- + xLi^+ \rightarrow Li_xCuO$ $(0 < x < 2)$.[8]

*Corresponding author.

It is expected that the insertion–deinsertion reaction of lithium into the CuO electrode induces local structural and electronic perturbations of the materials, which can affect the oxidation state of the copper ion. X-ray absorption near edge structure (XANES) is known to provide valuable information about the local structural parameters such as the oxidation state of the chemical species, site symmetry, and covalent bond strength of X-ray absorbing atoms.[9] For these reasons, X-ray absorption spectroscopy has recently begun to be used as an ideal tool in the investigation of the electronic and structural properties of metal oxides in the materials science. The objective of the present study is to elucidate the mechanism of the lithium reaction with CuO from the viewpoint of the local geometric and electronic structures of Cu atoms. To achieve this objective, systems of formula Li_xCuO, where x is the lithium content, were analyzed by means of XANES during the first cycle. We found that lithium insertion is accompanied by the formation of metallic Cu nanoclusters, which are partially oxidized to Cu_2O after the first cycle.

2. Experimental

2.1. *Electrochemical experiments*

Electrochemical behavior of CuO was investigated in lithium cells. Slurries were prepared that consisted of 80 wt% CuO powder (Aldrich, 99%), 10 wt% acetylene black, and 10 wt% polyvinylidene fluoride (PVdF) dissolved in 1-methyl-2-pyrrolidinone. Electrodes were made by coating the slurry onto an aluminum foil substrate. Test cells were fabricated with these electrodes, metallic Li anodes, and polypropylene separators (Celgard 2400) in a glove box filled with Ar gas. 1.0 M solution of $LiPF_6$ in ethylene carbonate-diethyl carbonate (1:1 by volume) was used as the electrolyte. Cell performance was evaluated by galvanostatically discharging and charging the cell at a constant current density of 0.5 mA/cm^2 in the voltage range 0.1–3.2 V at room temperature with a WBCS 3000 battery tester system (Won A Tech Corp, Korea). The lithium content (x) is calculated from the amount of electricity that has passed through the electrode.

2.2. *XANES measurements*

The Cu K-edge X-ray absorption spectra were recorded using the BL3C1 beam line at the Pohang Light Source (PLS) with a ring current of 120 $\sim$ 170 mA at 2.5 GeV. A Si(111) monochromator crystal was used with detuning to 85% in intensity to eliminate high-order harmonics. Data were collected in transmission mode using gas-filled ionization chambers (85% nitrogen, 15% argon) as detectors. Energy calibration was carried out for all measurements using Cu foil placed in front of the third ion chamber. The XANES data analysis was carried out using the standard procedure.[9]

3. Results and Discussion

Normalized Cu K-edge XANES spectra of the Li_xCuO system in the first cycle are shown in Fig. 1 with some reference materials. Because the XANES spectra are very sensitive to the electronic structure of the X-ray absorbing atom, XANES spectra can be used for identifying chemical species. The first absorption peak on the absorption edge of pristine CuO at $\sim$ 8985 eV and pure Cu foil at $\sim$ 8980 eV is the 1s-4p+ shakedown transition which arises from a strong ligand to metal charge transfer induced by core–hole creation.[10] The absorption peak at $\sim$ 8982 eV appearing in pristine Cu_2O, is regarded as characteristic of a two-fold linear coordination for the absorbing Cu atom.[11] The main peak around the 8992 eV is due to the electric dipole-allowed transition of a 1s core electron to an unoccupied 4p bound state that appears in all Cu compounds. In comparison to the pristine CuO, the XANES spectra for the electrochemical insertion of lithium change significantly and the shift of Cu K-edge energy occurs with the increase of the x value. The main features observed at lithiated CuO electrodes show a greater resemblance to the feature of Cu foil than that of pristine Cu_2O. This indicates that the electrochemical insertion of lithium leads to the reduced Cu^0 state, and consequently the gradual formation of Cu clusters. However, even at the highest insertion of lithium ($x = 2.24$) its spectral feature is not exactly that of the reference spectrum of Cu foil. This difference can be explained by previous reports.[1,3]

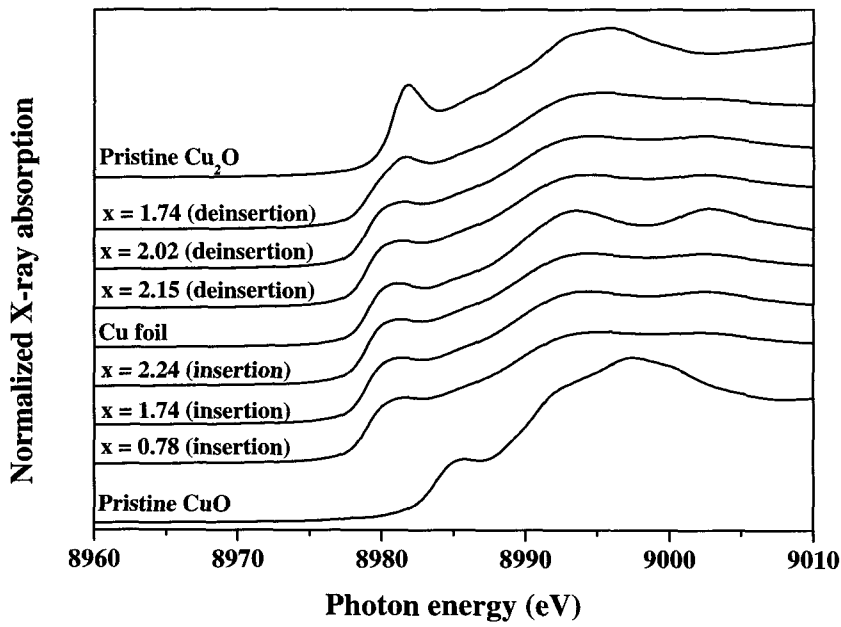

Fig. 1. Normalized Cu K-edge XANES spectra for the first cycle. The lithium content (x in Li_xCuO) is indicated in the figure.

Recently, our group reported the comparison of the XANES spectra between bulk Co metal and nanosized Co powder (approximately 7 nm).[1] The XANES spectrum of the bulk Co metal showed a more intense feature than that of the nanosized Co powder due to the size effect. As the particle size decreases, the surface-to-volume ratio increases with a consequent increase in the fraction of Co atoms in distorted environments at the surface. Grugeon *et al.* have suggested that the insertion of lithium into copper oxides (Cu_2O and CuO) leads the formation of Cu nanograins dispersed in the Li_2O matrix by using transmission electron microscopy (TEM) and X-ray diffraction (XRD) results.[3] In the present study, therefore, the difference between the spectra of the fully lithiated Li_xCuO and the pure reference Cu foil can be attributed to the structural difference between the pure Cu in the reference foil and the Cu in the nanoscale clusters in the Li_2O phase, the spectral feature of which is modified by the surface effect between the Cu cluster and Li_2O phase.

In the deinsertion process, the main spectral feature of lithiated electrodes at $x = 2.15$ and 2.02 show no noticeable variation compared with those of pure Cu foil. However, the Cu K-edge energy of Li_xCuO ($x = 1.74$) obtained during the 3.2 V charging step shifts to the vicinity of the pristine Cu_2O. This result indicates that the following charging process converts Cu nanograins into Cu_2O. The further study strengthens the following conclusion: the linear combination fitting was performed on the lithiated electrode ($x = 1.74$) using reference spectra of Cu foil and Cu_2O (figure is not shown). An excellent fit could be obtained for a lithiated electrode containing 43.5% Cu_2O and 56.5% Cu. The XANES results suggest that CuO is fully reduced to the Cu nanocluster and that the resulting metallic copper does partially reoxidized to Cu_2O and not to CuO during the first insertion–deinsertion process.

4. Conclusion

The reduction mechanism of the CuO/Li cell was investigated using Cu K-edge X-ray absorption spectroscopy. The XANES spectra show marked variations over the first electrochemical cycle. The initial insertion of lithium leads to the reduction of the Cu^{2+} in the pristine CuO to form the reduced metallic Cu nanoclusters. The nanosized Cu evolves gradually with a well-separated distribution in the Li_2O matrix. In the successive deinsertions of lithium, the reduced Cu nanoparticles change partially to Cu_2O particles. The nature of the formation of Cu_2O will be the subject of further studies. The results suggest that X-ray absorption spectroscopy is a valuable tool in the study of nanoparticles in materials science.

Acknowledgments

The present study was supported in part by the Korea Research Foundation (KRF-2002-015-CP0164). We are also grateful to the authorities in charge of the Pohang Light Source (PLS) for X-ray absorption measurements.

References

1. H. C. Choi, S. Y. Lee, S. B. Kim, M. G. Kim, M. K. Lee, H. J. Shin, and J. S. Lee, *J. Phys. Chem. B* **106**, 9252 (2002).
2. H. C. Choi, Y. M. Jung, I. Noda, and S. B. Kim, *J. Phys. Chem. B*, accepted paper.
3. S. Grugeon, S. Laruelle, R. Herrera-Urbina, L. Dupont, P. Poizot, and J.-M. Tarascon, *J. Electrochem. Soc.* **148**, A285 (2001).
4. P. Podhajecky and B. Scrosati, *J. Power Sources* **16**, 309 (1985).
5. H. Ikeda and S. Narukawa, *J. Power Sources* **9**, 329 (1983).
6. Y. Matsuda, K. Teraji, and Y. Takasu, *Denki Kagaku* **44**, 363 (1976).
7. R. Bates and Y. Jumel, *Lithium Batteries* (Academic Press, New York, 1983), p. 89.
8. P. Novak, *Electrochim. Acta* **30**, 1687 (1985).
9. B. K. Teo, *EXAFS: Basic Principles and Data Analysis* (Springer-Verlag, Berlin, 1986).
10. M. Giorgetti, S. Mukerjee, S. Passerini, J. McBreen, and W. H. Smyrl, *J. Electrochem. Soc.* **148**, A768 (2001).
11. K. V. R. Rao and K. B. Garg, *Physica C* **178**, 352 (1991).

This page is intentionally left blank

International Journal of Nanoscience, Vol. 1, Nos. 5 & 6 (2002) 449–453

SELF-ASSEMBLED NANOSTRUCTURES OF A BOLAAMPHIPHILIC DIACID IN THE SPREAD LANGMUIR FILM ON THE AQUEOUS SUBPHASE CONTAINING LANTHANUM ION

MINGHUA LIU*,†,‡,§, KEN-ICHI IIMURA†, and TEIJI KATO†,¶

*Laboratory of Colloid and Interface Science, Center for Molecular Science
Institute of Chemistry, CAS, Beijing, 100080, P. R. China
†Satellite Venture Business Laboratory, Utsunomiya University
Yoto 7-1-2, Utsunomiya 321-8585, Japan
§liumh@iccas.ac.cn
¶teiji@cc.utsunomiya-u.ac.jp

Received 27 November 2002
Revised 22 December 2002

The spreading behavior of a bolaamphiphilic diacid (1,18-octadecanedicarboxylic acid, ODA) on an aqueous subphase containing lanthanum chloride was investigated. ODA formed a multilayer film on the subphase, and flower- or ring-like nanoarchitectures were observed by an AFM measurement on the transferred one-layer film. It was found that while the above exotic nanostructures were formed in the spreading films at lower concentration of La^{3+} ion, only aggregated circular nanoparticles were observed for those on a higher concentration of La^{3+} ion.

Keywords: Nanoflower; bolaamphiphile; Langmuir film.

1. Introduction

Supramolecular nanoarchitectures have been attracting considerable interest in nanoscience and technology. Air/water interface can provide a good environment for the fabrication of two-dimensional nanostructures and many interesting nanostructures are assembled on the water surface.[1–3] For example, two-dimensional micelles have been fabricated at the air/water interface by using a partial fluorinated fluorocarbon compounds.[4] Recently it was further shown that even without the polar group, semifluorinated alkane $C_8F_{17}C_{16}H_{33}$ can also form interfacial micelles.[5] As compared with the large amount of work on the supramolecular assembly based on typical amphiphile in which one polar group and a long hydrophobic chain are contained, relatively less works have been reported on the bolaamphiphiles. Bolaamphiphile describes a class of amphiphile in which two polar head groups are

‡Permanent address: Institute of Chemistry, CAS, 100080, Beijing, P. R. China.

linked by one or more hydrophobic chains.[6] Bolaamphiphile may show different configurations at air–water interface.[7]

Recent work of Weissbuch *et al.* have confirmed the multilayer formation of some dicarboxylic acids on the subphase containing divalent metal ions using an *in situ* grazing-incidence X-ray diffraction (GIXD) method.[8,9] We have investigated the *in situ* coordination of a bolaamphiphilic 1,18-octadecanedicarboxylic acid (ODA) with mono- and trivalent metal ions. Fiber- and flower-like nanostructures were observed for the spread Langmuir films of ODA on the subphases containing Ag^+ and Eu^{3+}, respectively.[10] In this paper, we have extended our work to the effect of lanthanum ion on Langmuir film of ODA. The concentration of the metal ions in the subphase, which was neglected before, was also investigated. The nanoflower and nanoring architectures were observed for ODA Langmuir films spread on the subphase containing La^{3+}. The special role of the rare earth metal ions in forming the exotic nanostructure was discussed.

2. Experimental

1,18-Octadecanedicarboxylic acid (HOOC-$(CH_2)_{18}$-COOH, ODA, purchased from Tokyo Kasei) and $LaCl_3.7H_2O$ (Wako Pure Chemical Industries, Ltd.) were used without further purification. The subphase was prepared by dissolving the metal salt in a highly purified Millipore Q water (18 MΩ cm) at a concentration of 1×10^{-5}–1×10^{-3} M. The chloroform-formed solution ($\sim 10^{-4}$ M) was spread on the subphase containing different concentrations of $LaCl_3$. After waited for 30 min, the π–A isotherm were recorded. One-layer of Langmuir film on aqueous $LaCl_3$ solution was transferred onto a silicon wafer (pretreated with a RCA method) at 10 mN/m at 20°C using a scooping-up method. The morphologies of the transferred Langmuir films were observed using a Seiko AFM equipment with a contact mode.

3. Results and Discussion

Figure 1 shows the π–A isotherms of ODA spread on the subphase containing various concentrations of $LaCl_3$. Different from the isotherm of ODA on pure water surface, a condensed type isotherm was obtained in each case. This indicates that only a small amount of La^{3+} can affect the spreading behavior of ODA. However, the molecular areas of the spreading film are too small to be regarded as monolayers. Weissbuch *et al.* have investigated the spreading films of an α,ω-tetracosanedioic acid on the subphase containing metal ions and verified the multilayer formation. In addition, these isotherms are similar to those reported on the subphase of $AgNO_3$ or $EuCl_3$. On the other hand, with increasing concentration of the La^{3+}, there is a tendency that the molecular areas become larger. However, these isotherms cannot reflect any information on the molecular packing because it did not carry the monolayer. No further information could be obtained from the π–A isotherms.

Figure 2 shows the AFM images of one-layer scooped-up Langmuir film formed on the subphases containing different concentrations of $LaCl_3$ on silicon wafers. In

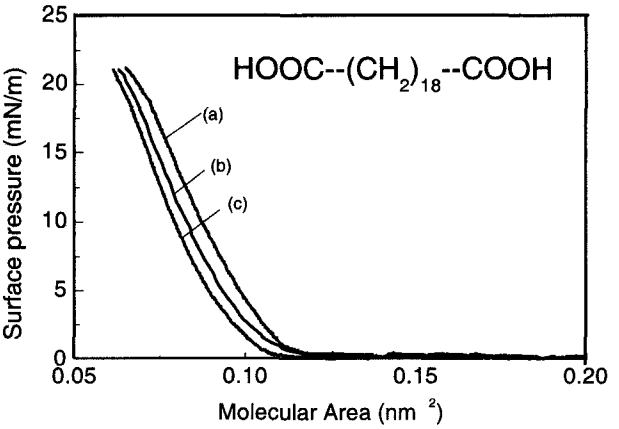

Fig. 1. π–A isotherms of ODA films spread subphases containing various concentrations of $LaCl_3$. (a) 1×10^{-5}, (b) 1×10^{-4}, and (c) 1×10^{-3} M.

the case of lower concentration of $LaCl_3$ (Figs. 2(a) and 2(b), 1×10^{-5} M), many flower-like domains are observed. The sizes of the domains are about one micrometer. It is further observed that the flowers are composed of many nanoparticles. These pictures are similar to the case of $EuCl_3$, suggesting the similarity between the La^{3+} and Eu^{3+} in interacting with the ODA.

At a middle concentration of the subphase (1×10^{-4} M, Fig. 2(c)), it formed a nanoring, i.e., the circular edges are much higher than that in the case of a lower concentration. The height differences of the ring and the center is about 14 nm. The size of the ring is about 500 nm. At a higher concentration of the La^{3+} (1×10^{-3} M, Fig. 2(d)), no ring or flower could be seen. Many aggregated nanoparticles with a size of hundred nanometers are formed. These nanoparticles showed a very rough surface. These differences might be attributed to the reaction completeness between ODA and La^{3+}. At a lower concentration of La^{3+}, the reaction between the carboxylic groups of ODA and La^{3+} was incomplete and some of the ODA were mixed in the film. These mixed ODA molecules in the film may form hydrogen bond and joined nanoparticles to form the nanoflowers. At a higher concentration, the reaction between ODA and La^{3+} undergoes completely and the resultant molecules form the circular nanoparticles. The ring structure can be regarded as an intermediate structure from the flower to nanoparticles.

On the other hand, when ODA was spread on the subphase containing divalent ions such as Cu(II) and Zn(II), only aggregated nanoparticles were found. In addition, we have also tried trivalent ions such as $AlCl_3$ and $FeCl_3$. Only irregularly aggregated nanoparticles were observed. These flower- or ring-like nanostructures are due to the higher coordination ability of the rare earth metal ions. Due to the unoccupied 4f orbital, these rare earth metal ions have higher coordination ability and can combine a large number of ligands. While a larger research interest has been devoted to the function of rare earth coordination compounds, our

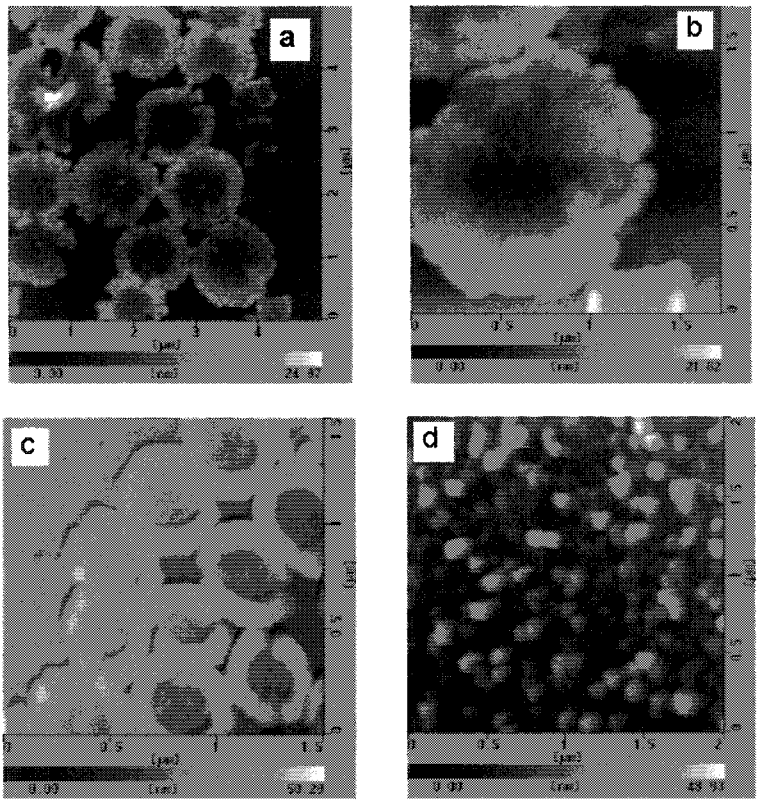

Fig. 2. The AFM images of one-layer Langmuir film formed on the subphases containing various concentrations of $LaCl_3$. (a) and (b) 1×10^{-5}, (c) 1×10^{-4}, and (d) 1×10^{-3} M.

results suggested that these rare earth metal ions may play some important roles in constructing nanostructures.

In conclusion, we have found that a bolaamphiphlic diacid can form a multilayer Langmuir film with La^{3+} on water surface. Depending on the concentration of the La^{3+}, various nanostructures could be formed. At a lower concentration, nanoflowers or nanorings were predominantly formed. While at higher concentration, the aggregated nanoparticles were formed.

Acknowledgments

This work was supported by the National Natural Science Foundation of China. The author (M. Liu) is grateful to the SVBL of Utsunomiya University.

References

1. I. Weissbuch, P. N. W. Baxter, S. Cohen, H. Cohen, K. Kjaer, P. B. Howes, J. M. Lehn, L. Leizerowitz, and M. Lahav, *J. Amer. Chem. Soc.* **120**, 4850 (1998).

2. J. A. Swift, A. M. Pivovar, A. M. Reynolds, and M. D. Ward, *J. Amer. Chem. Soc.* **120**, 5887 (1998).
3. S. Manne, J. P. Cleveland, H. E. Gaub, G. D. Stucky, and P. K. Hansma, *Langmuir* **10**, 4409 (1994).
4. T. Kato, M. Kameyama, M. Ehara, and K. Iimura, *Langmuir* **14**, 1786 (1998).
5. M. Maaloum, P. Muller, and M. P. Krafft, *Angew. Chem. Int. Ed. Engl.* **41**, 4331 (2002).
6. J. H. Fuhrhop and J. Mathieu, *Angew. Chem. Int. Ed. Engl.* **23**, 100 (1984).
7. A. Gliozzi and A. Relini, *Handbook of Nonmedical Application of Liposome*, Vol. II, eds. Y. Barenholz and D. D. Lasic (CRC Press, New York, 1995), 329 pp.
8. I. Weissbuch, S. Guo, R. Edgar, S. Cohen, P. Howes, K. Kjaer, M. Lahav, and L. Leizerowitz, *Adv. Mater.* **10**, 117 (1998).
9. I. Weissbuch, R. Buller, K. Kjaer, J. Als-Nielsen, L. Leiserowitz, and M. Lahav, *Colloids and Surfaces A* **208**, 3 (2002).
10. Q. Lu, Y. Luo, L. Li, and M. Liu, *Langmuir* **19**, 285 (2003).

This page is intentionally left blank

International Journal of Nanoscience, Vol. 1, Nos. 5 & 6 (2002) 455–459

SYNTHESIS OF NOVEL MANGANESE-BASED SINGLE-MOLECULE NANOMAGNETS

JINKWON KIM*, HAENGKYU CHO, and AHKILESH K. GUPTA
Department of Chemistry, Kongju National University
Kongju, Chungnam 314-701, Korea
**jkim@kongju.ac.kr*

JIN MOOK LIM and YOUNGKYU DO
Department of Chemistry, School of Molecular Science-BK-21 and
Center for Molecular Design and Synthesis
Korea Advanced Institute of Science and Technology
Daejeon 305-701, Korea

Received 27 November 2002
Revised 6 January 2003

New Mn12 single-molecule nanomagnets $[Mn_{12}O_{12}(O_2CCHCl_2)(H_2O)_4]\cdot 2CH_2Cl_2\cdot H_2O$ and $[Mn_{12}O_{12}(O_2CCHCl_2)(H_2O)_4]\cdot 2CH_3C_6H_5\cdot 4H_2O$ and novel Mn18 complexes $[M_{18}O_{14}(O_2CR)_{18}(hmp)_4(hmpH)_2(H_2O)_2]$ (R = Me, Et) have been synthesized and characterized by single crystal X-ray crystallography and dc- and ac-magnetic susceptibility measurements. Mn12 complexes show characteristic SMM properties, such as temperature-dependent out-of-phase ac-susceptibility. Mn18 does not show relaxation behaviors down to 2.0 K, but reveals magnetic anisotropy in reduced magnetization experiment.

Keywords: Single-molecule magnets; manganese; ac-susceptibility; magnetic hysteresis.

The synthesis of a magnetic molecule having unusually large spin value and large negative anisotropy value is an area of intensive current research, because it is the prerequisite for developing the emerging class of single-molecule magnets (SMMs). SMMs, as a prototype of nanomagnets, display intramolecular magnetic hysteresis loop; each independent molecule in these materials possesses the ability to function as a magnetizable magnet, owing to intrinsic intramolecular properties rather than intermolecular interactions and long-range ordering.[1] Thus, SMMs are regarded as the ultimate high-density memory devices in the future. Since the dodecanulear manganese cluster with the composition $[Mn_{12}O_{12}(O_2CMe)_{16}(H_2O)_4]$ (Mn12ac) had been discovered as a single-molecule magnet,[2–4] many research efforts have focused on exploring new Mn12 complexes having different alkyl or aryl substituents. It is especially important to control crystal symmetry of Mn12 complexes for systematic investigation on the origin of magnetic quantum tunneling of these complexes. The scarcity[5] of examples of Mn12 complexes possessing higher

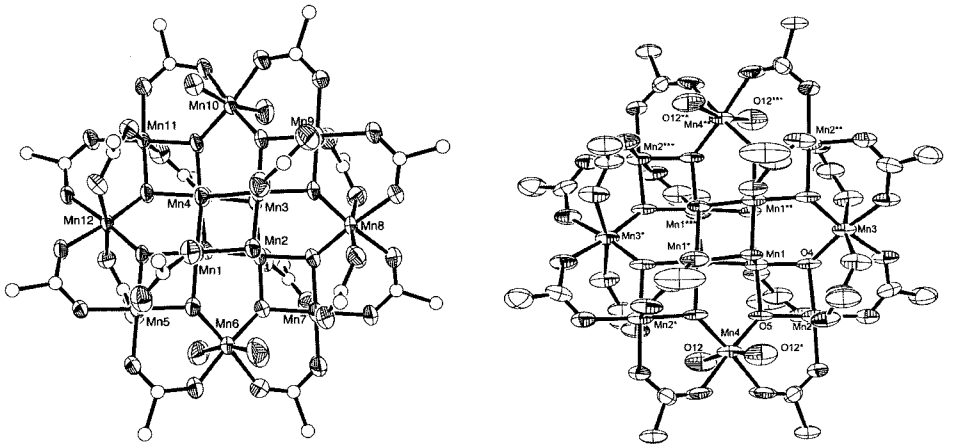

1 **2**

Fig. 1. ORTEP diagrams of $[Mn_{12}O_{12}(O_2CCHCl_2)_{16}(H_2O)_4] \cdot 2CH_2Cl_2 \cdot H_2O$ (**1**) and $[Mn_{12}O_{12}(O_2CCHCl_2)_{16}(H_2O)_4] \cdot$ toluene $\cdot 4H_2O$ (**2**) at the 50% probability level. Chlorine atoms of dichloroacetate are omitted for clarity.

symmetry than monoclinic system spurred us to find a new Mn12 having higher crystal symmetry. On the other hand, in the course of our efforts to explore a new class of SMM, we discovered novel Mn18 cluster complexes. Here, we briefly report on synthesis, structure and magnetic properties of new Mn12 and Mn18 complexes.

Mn12ac was synthesized according to the reported method.[2] An azeotropic distillation of mixture of Mn12ac with dichloroacetic acid (32 equivalents) in toluene resulted in ligand substitution. Recrystallization of dark brown solids in dichloromethane-hexane gave us analytically pure $[Mn_{12}O_{12}(O_2CCHCl_2)_{16}(H_2O)_4] \cdot 2CH_2Cl_2 \cdot H_2O$ (**1**). However, recrystallization in toluene-hexane produced $[Mn_{12}O_{12}(O_2CCHCl_2)_{16}(H_2O)_4] \cdot 2CH_3C_6H_5 \cdot 4H_2O$ (**2**). ORTEP diagrams[6] of **1** and **2** are displayed in Fig. 1. The complex **1** crystallizes in a monoclinic $P2_1/n$ space group with four molecules in a unit cell. The z-axis of each molecule is almost orthogonal relative to each other. The complex **2** crystallizes in an orthorhombic $Ccca$ space group with four molecules in a unit cell. The z-axes of molecules are almost parallel to each other. The structure features of $[Mn_{12}(\mu_3\text{-}O)_{12}]$ cores of **1** and **2** are comparable to those of the other Mn12 complexes: The inner core $[Mn_4^{IV}O_4]^{8+}$ cubane unit is held within a nonplanar ring of eight Mn^{III} atoms by eight μ_3-O^{2-} ions. The axial Mn^{III}-O bonds are tetragonally elongated due to Jahn–Teller distortion, and approximately parallel to the molecular C_2 axis. The four water molecules are located on the two Mn atoms to complete octahedral coordination.

The ac-susceptibility data were measured for both polycrystalline samples of **1** and **2** in zero dc field. As shown in Fig. 2, both complexes exhibited frequency-dependent out-of-phase susceptibility χ''_M peaks in the range of 2–10 K,

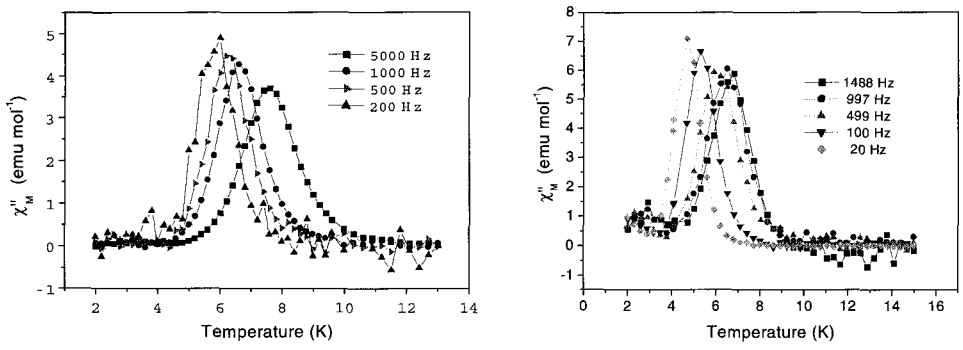

(a) (b)

Fig. 2. Temperature dependence of out-of-phase ac-susceptibility (χ''_M) for (a) **1** and (b) **2**.

demonstrating a characteristic feature of superparamagentic behaviors of single-molecule magnets. A temperature of maximum in χ''_M decreases as the frequency is decreased. In the case of complex **2**, the temperatures for a maximum in χ''_M are 4.7 K (20 Hz), 5.3 K (100 Hz), 5.9 K (499 Hz), 6.5 K (997 Hz) and 6.8 K (1488 Hz). It is not unusual to observe two peaks in χ''_M for Mn12 complexes in a temperature range of 2–7 K. Relative peak intensity of these two peaks depends on solvated molecules.[7] Jahn–Teller isomerism is proposed to explain the origin of the different relaxation behaviors based on different arrangement of coordinated water molecules.[8] However, complexes **1** and **2** have only a large single peak in this temperature range.

Octadecanuclear manganese cluster complexes with the composition of $[Mn_{18}O_{14}(O_2CR)_{18}(hmp)_4(hmpH)_2(H_2O)_2]$ (hmpH = hydroxymethyl pyridine; R = Me; **3**, Et; **4**) have been obtained by treatment of a stirred slurry of $Mn(acetate)_2 \cdot 4H_2O$, hmpH and RCOOH in methylene chloride with strong oxidizing agent $Bu^n_4NMnO_4$. X-ray crystallographic studies show that these complexes consist of mixed valent $[Mn^{II}_4Mn^{III}_{14}(\mu_3\text{-}O)_{10}(\mu_4\text{-}O)_4]$ core with peripheral chelation provided by eighteen acetate ligands, four hmp^-, two hmpH ligands, and two terminal water molecules.[9] Magnetic susceptibility data were obtained with powder samples of **3** and **4** dried under air. The magnetic susceptibility data as a function of temperature, measured with an applied field of 1 kG by using a SQUID magnetometer are displayed in Fig. 3. The manganese ions of complex **3** has Weiss constant $\theta = -75$ K in high temperature region (above 150 K) and $\theta = -14$ K in low temperature region (70 $\sim$ 150 K), indicating strong intramolecular antiferromagnetic couplings between manganese ions. Below 50 K, $\chi_M T$ drops faster down to 2.0 K (7.6 cm^3 K mol^{-1}) because of intermolecular antiferromagnetic interactions and zero-field splitting effects. Reduced magnetization data were collected in the ranges 40–50 kG and 2.0–10.0 K and the split of isofield lines shows that the zero-field splitting exists in the complex **3**.

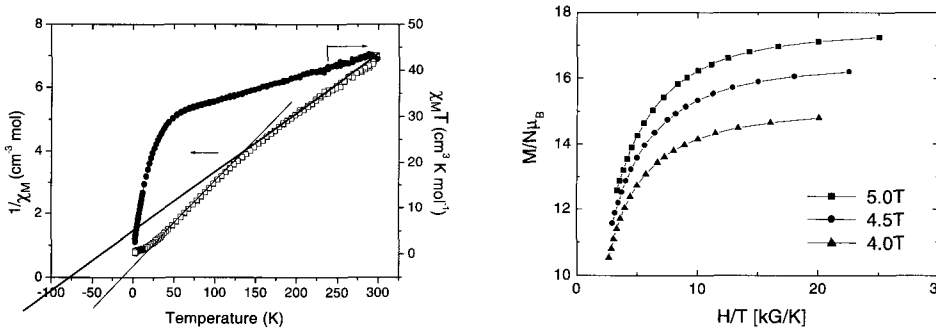

(a) (b)

Fig. 3. Temperature dependence of (a) $\chi_M T$ (•) and $1/\chi_M$ (□) and (b) plot of $M/N\mu_B$ versus H/T for **3**.

Alternating current susceptibility measurements, carried out for the powder sample **3** in the temperature range of 2.0–10 K, do not show out-of-phase (χ''_M) signals. However, Brechin *et al.* reported a new $[Mn_{18}]^{2+}$ single-molecule magnet which shows temperature dependency of ac-susceptibility in the 0.99–1.44 K region and magnetic hysteresis loop in the 0.04–1.0 K.[10] Based on these recent results, we expect our Mn_{18} cluster may exhibit single-molecule magnetic behavior below 2.0 K.

Acknowledgment

This work has been supported by the National Reseach Laboratory (NRL) program of Ministry of Science and Technology, Korea.

References

1. A. Caneschi, D. Gatteschi, C. Sangregorio, R. Sessoli, L. Sorace, A. Cornia, M. A. Novak, C. Paulsen, and W. Werndorfer, *J. Magn. Magn. Mater.* **200**, 182 (1999).
2. T. Lis, *Acta Crystallogr. B* **36**, 2042 (1980).
3. R. Sessoli, D. Gatteschi, A. Canneschi, and M. A. Novak, *Nature* **365**, 141 (1993).
4. L. Thomas, F. Lionti, R. Ballou, D. Gatteschi, R. Sessoli, and B. Barbara, *Nature* **383**, 145 (1996).
5. H.-L. Tsai, D.-M. Chen, C.-I. Yang, T.-Y. Jwo, C.-S. Wur, G.-H. Lee, and Y. Wang, *Inorg. Chem. Commun.* **4**, 511 (2001).
6. Crystal data for **1**: $C_{34}H_{30}Cl_{36}Mn_{12}O_{49}$ (including two dichloromethane and one water molecules), Fw = 3158.06, monoclinic, space group $P2_1/n$, a = 14.247(5), b = 26.006(6), c = 26.863(5) Å, β = 93.70(1)°, V = 9932(5) Å^3, Z = 4, T = 20°C, ρ = 2.112 g/cm^3, $\mu(MoK_\alpha)$ = 2.523 mm^{-1}. 17 801 reflections measured, 17 409 unique (R_{int} = 0.0217) which were used in all calculations. The final $R(F)$ and $wR(F^2)$ were 0.0820 and 0.2265, respectively. Crystal data for **2**: $C_{46}H_{48}Cl_{32}Mn_{12}O_{52}$ (including two toluene and two water molecules), Fw = 3226.52, orthorhombic, space group *Ccca*, a = 24.565(4), b = 29.612(6), c = 14.740(3) Å, V = 10 723(3) Å^3, Z = 4,

$T = -100°C$, $\rho = 1.999\ g/cm^3$, $\mu(MoK_\alpha) = 2.245\ mm^{-1}$. 27 335 reflections measured, 6399 unique ($R_{int} = 0.1378$) which were used in all calculations. The final $R(F)$ and $wR(F^2)$ were 0.1602 and 0.3025, respectively.

7. C.-D. Park, S. W. Rhee, Y. J. Kim, W. S. Jeon, D.-Y. Jung, D. Kim, Y. Do, and H.-C. Ri, *Bull. Korean Chem. Soc.* **2**, 453 (2001).
8. S. M. J. Aubin, Z. Sun, H. J. Eppley, E. M. Rumberger, I. A. Guzei, K. Folting, P. K. Gantzei, A. L. Rheingold, G. Christou, and D. N. Hendrickson, *Inorg. Chem.* **40**, 2127 (2001).
9. A. K. Gupta, S. Yoon, M. S. Lah, and J. Kim, submitted for publication.
10. E. K. Brechin, C. Boskovic, W. Wernsdorfer, J. Yoo, A. Yamaguchi, E. C. Sanudo, T. R. Concolino, A. L. Rheingold, H. Ishimoto, D. N. Hendrickson, and G. Christou, *J. Am. Chem. Soc.* **124**, 9710 (2002).

This page is intentionally left blank

International Journal of Nanoscience, Vol. 1, Nos. 5 & 6 (2002) 461–464

SIZE EFFECT OF CYANINE DYE J-AGGREGATES IN MICROMETER-SIZED POLYMER "DOMES"

OLAF KARTHAUS*, KIYOSHI OKAMOTO, and RYOTA CHIBA

Department of Photonics Material Science
Chitose Institute of Science and Technology, Bibi 65-758
Chitose, 066-8655, Japan
**PRESTO, JST, Chiyodaku, Tokyo, Japan*

KAZUAKI KAGA

Graduate School of Photonics Material Science
Chitose Institute of Science and Technology
Bibi 65-758, Chitose, 066-8655, Japan

Received 27 November 2002
Revised 11 December 2002

The fluorescence behavior of 3,3′diethyl-thiacarbocyanine iodide in micrometer-sized polystyrene droplets, or "domes" on glass substrates was investigated. The samples were prepared by casting dilute polymer/dye solutions onto the substrates. A dewetting process leads to the formation of small polymer domes with a diameter of 1–100 μm and a height of 100 nm to several μm. Fluorescence microscopy shows that the dye is incorporated into these polymer domes. It was found that the absorption and fluorescence spectra depend on the size of the polymer domes. Larger domes show red-shifted fluorescence spectra.

Keywords: Fluorescence micro-spectroscopy; size-control; dewetting.

1. Introduction

1.1. *J-aggregates*

Organic dyes are one of the important materials in nanotechnology. For photonics and molecular electronics it is essential to control the orientation and aggregation of dyes on the nanometer-size level. Once the molecular orientation and thus the intermolecular interaction can be tailored, they can be useful materials for many applications, e.g., solar cells, LEDs, sensors, etc. Cyanine dyes, for example, are used as stains for DNA and as sensitizers in photographic films. Above certain concentration cyanines may aggregate and form the so-called J-aggregates that show narrow absorption spectrum, which is red-shifted from the absorption spectrum of the isolated molecules.[1,2] J-aggregates have a small Stokes shift and thus the maximum emission in the fluorescence spectrum appears at nearly the same wavelength as the absorption. The narrow absorption spectrum of the J-aggregates makes these

compounds ideal as sensitizers in photographic films, since they absorb only photons with a narrow energy distribution. AFM and SNOM investigations have shown that J-aggregates consist of fiber-like ribbons with a diameter of several ten nanometers and a length of several ten micrometers. For most applications, the cyanine dye is mixed with a polymer solution and spin cast onto substrates, such as glass or polycarbonate, to form continuous films. The J-aggregates was formed either in solution or during the casting process. Thus it is difficult to control the size of the J-aggregates.

1.2. *Dewetting*

Here we propose a new way of controlling the size of J-aggregates by dewetting of the polymer matrix. Polystyrene, among many polymers, is known to form micrometer-sized polymer droplets, or "domes" on a substrate when it is cast from dilute solution.[3] The size of the polymer domes can be controlled by the concentration, evaporation speed, and other parameters, and is in the range of 0.2–100 μm in diameter and 5 nm–5 μm in height. Thus the volume of a single dome is in the range of 1 attoliter to a few femtoliter.

Here we describe the results of a cyanine dye, 3,3′diethyl-thiacarbocyanine iodide, mixed with a dilute polystyrene solution in chloroform. When casting, dewetting takes place, and the dye is incorporated into the polymer domes. A microscope spectrometer is used to measure the absorption and fluorescence spectra of individual domes. It was found that the spectra depend on the dome size. Thus this dewetting method can be used to tailor the photonic properties of J-aggregates and it may offer a new way to produce novel photonic devices from known materials.

2. Results and Discussions

Figure 1 shows an optical micrograph of a typical sample. The optical microscopy reveals the presence of polystyrene domes. As the dye is incorporated in the

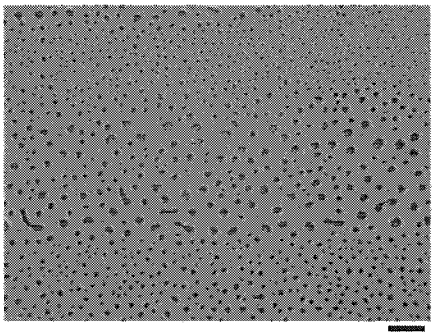

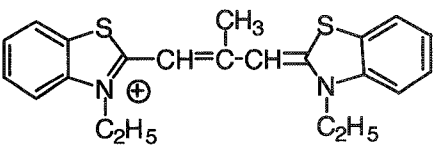

Fig. 1. Optical micrograph of a dewetted polystyrene sample with 10 wt% cyanine dye. The bar corresponds to 10 μm.

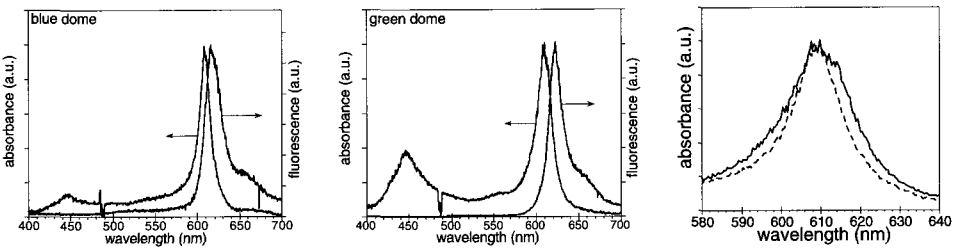

Fig. 2. (a) and (b) The absorption and fluorescence spectra of cyanine dye incorporated in polystyrene microdomes. (c) The close-up of the absorption peak of a blue dome (– – –) and a green (——).

polymer matrix, the domes show a blue or green color. Figure 2 shows the absorption and fluorescence spectra of two individual domes that show different colors, green and blue, by optical microscopy. The blue-colored dome shows a sharp absorption peak at 608 nm. This absorption is very similar to the green dome, which absorbs also at 608 nm. Thus the difference in color is not due to a different absorption maximum of the J-aggregate, but due to differences in the short wavelength absorption at 400 nm. The green dome shows a much stronger adsorption in that region. It is known that J-aggregates can have two absorption bands, which are due to the excitation of the long axis and short axis of the J-aggregate, respectively. Thus the difference in the ration of 608 nm and 450 nm absorption can be explained by a linear dichroism, which depends on the orientation or on the size of the aggregate.

The fluorescence behavior is also summarized in Fig. 2. Both domes show a sharp fluorescence peak close to the absorption, which is a proof for the presence of J-aggregates. The fluorescence maximum of the blue dome is at 616 nm, which results in a Stokes shift of 8 nm, which is in good agreement with well-ordered J-aggregates. The maximum fluorescence of the green dome is slightly red-shifted to 622 nm. Since both domes contain J-aggregates with a similar structure, this difference in Stokes shift is not expected. A careful observation of the absorption spectra shows that even though the maximum absorption is at the same wavelength, the green dome shows a long wavelength shoulder at 614 nm (see Fig. 2), which leads to a broadening of the absorption. It is known that J-aggregates have size-dependent absorption spectra. The longer the J-aggregate, the more red-shifted is the absorption spectrum.[4] Thus we may conclude that the J-aggregates in the green domes are larger than the J-aggregates in the blue dome.

The red shift in emission from the green dome can then be explained by a relaxation of the excitation energy into a lower energy level, which leads to a red shift in fluorescence. A detailed study of the fluorescence behavior of nearly 100 different domes show that there is a systematic dependence of fluorescence maximum on the dome size. It can be clearly seen that the fluorescence peak depends on the dome

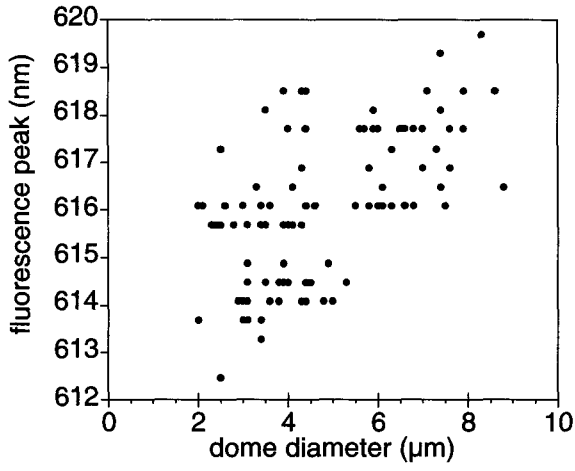

Fig. 3. Dependence of the fluorescence maximum on the dome diameter.

size in a nonlinear fashion. In larger domes, a red shift in the fluorescence peak was shown.

The J-aggregates are formed in micrometer-sized polystyrene domes on solid substrates. Each dome contains J-aggregates. As J-aggregates cannot be larger than the dome, the size of the J-aggregate can be controlled by the dome size. Smaller domes contain smaller J-aggregates, which is also apparent from the absorption spectra, where larger green domes show long wavelength shoulder in the absorption spectra. The fluorescence spectroscopy of many individual domes shows a dependence of the fluorescence maximum on the dome size. Larger domes have a red-shifted fluorescence.

Thus the present way of preparing polymer microdomes is a promising way to control the size of the dye aggregates and thus their photophysics.

Acknowledgment

O. Karthaus acknowledges the financial support of the PRESTO program "Organization and Function" of the JST.

References

1. G. Scheibe, *Angew. Chem.* **49**, 563 (1936).
2. E. E. Jelley, *Nature* **138**, 1009 (1936).
3. O. Karthaus, L. Grasjo, N. Maruyama, and M. Shimomura, *Chaos* **9**, 308 (1999).
4. K. Minoshita, M. Taiji, K. Misawa, and T. Kobayashi, *Chem. Phys. Lett.* **218**, 67 (1994).

International Journal of Nanoscience, Vol. 1, Nos. 5 & 6 (2002) 465–469

MOLECULE-UP FABRICATION AND MANIPULATION OF LIPID NANOTUBES

TOSHIMI SHIMIZU and GEORGE JOHN
CREST, Japan Science and Technology Corporation (JST)
Nanoarchitectonics Research Center (NARC)
National Institute of Advanced Industrial Science and Technology (AIST)
Tsukuba Central 5, 1-1-1 Higashi, Tsukuba, Ibaraki 305-8565, Japan

AKIHIRO FUKAGAWA and KOHZO ITO
Graduate School of Frontier Sciences, University of Tokyo
Hongo 7-3-1, Bunkyo-ku, Tokyo 113-8656, Japan

HIROSHI FRUSAWA
Department of Applied Physics, University of Tokyo
Hongo 7-3-1, Bunkyo-ku, Tokyo 113-8656, Japan

Received 27 November 2002

Self-assembling behavior of both a cardanol-appended glycolipid mixture and the fractionated four components has been examined in aqueous solutions. The cardanyl glucoside mixture differing in the degree of unsaturation in the hydrophobic chain was found to self-assemble in water to form open-ended nanotube structures with 10–15 nm inner diameters. The pure saturated homologue produced twisted helical ribbons through self-assembly, whereas the monoene derivative gave tubular structures. The rational control of helical and tubular morphologies has been achieved by a combinatorial approach through the binary self-assembly of the saturated and monoene derivatives. The flexural rigidity of a single lipid nanotube was first evaluated using optical tweezers manipulation and then compared with that of natural microtubules.

Keywords: Lipid nanotube; self-assembly; cardanyl glucoside; flexural rigidity; optical tweezers.

1. Introduction

Nanometer-sized hollow cylinder structures of graphene sheets, so-called *carbon nanotubes*, have recently been of great interest in terms of new intriguing nanostructured materials, providing many electrical and photonic applications.[1] Similar morphologies in identical size dimensions can also be obtainable from synthetic amphiphiles through self-assembly. Yager and Schoen,[2] and Nakashima *et al.*[3] are the first to find out the self-assembly of lipid nanotubes based on bilayer membranes. Although nearly two decades have passed since these first reports on the lipid nanotubes, the number of known tube-forming amphiphiles is still relatively

small.[4] The lipid nanotubes are generally produced by the transformation of vesicular assemblies with fluid bilayer membrane into tubular structures with solid chiral bilayers via a helically-wound ribbon morphologies as the intermediate. Therefore, the lipid nanotubes can be considered as the final expression of molecular chirality at supramolecular level. Here we report the efficient and facile nanotube preparation with 10–15 nm inner diameters from synthetic glycolipids **1**, easily available from renewable plant crop-derived resources.[5] Furthermore, we first describe the Young's moduli for the present single lipid nanotube in aqueous solutions.[6]

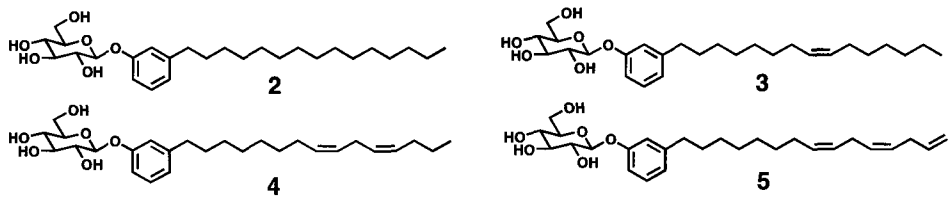

1: 2 + 3 + 4 + 5

2. Experimental

The cardanol (a mixture of long chain phenol differing in the degree of unsaturation in the hydrophobic chain) was obtained by double vacuum distillation of cashew nut shell liquid (CNSL) and was coupled with penta-O-acetyl-β-D-glucopyranose in anhydrous CH_2Cl_2 by using BF_3 OEt_2. A mixture of four components was then obtained after deprotection of acetyl group; 1-O-3′-*n*-(pentadecyl)phenyl-β-D-glucopyranoside **2** (5%), 1-O-3′-*n*-(8′(Z)-pentadecenyl)phenyl-β-D-glucopyranoside **3** (50%), 1-O-3′-*n*-(8′(Z),11′(Z)-pentadecadienyl)phenyl-β-D-glucopyranoside **4** (29%) and 1-O-3′-*n*-(8′(Z),11′(Z)-14′-pentadecatrienyl)phenyl-β-D-glucopyranoside **5** (29%). Each pure component was obtained by the fractionation of the cardanyl glucoside mixture **1** into its individual components by reverse-phase medium-pressure column chromatography. The self-assembled fibrous and tubular structures were prepared by dispersing 1–5 mg of **1–5** in 50–100 ml boiling water. The obtained clear dispersions were gradually cooled to room temperature and were incubated under ambient conditions. For the manipulation of a single lipid nanotube, we used a commercially available optical tweezers (Sigma Koki LMS-46755).

3. Results and Discussion

The cardanyl glucoside mixture **1** self-assembled into characteristic helically-coiled ribbons after 12–24 h incubation (Fig. 1(b)), whereas the saturated homologue **2** gave a helically-twisted morphology (Fig. 1(c)). Thus, we found that a different type of fibrous self-assembled morphologies were obtainable depending on the degree of unsaturation of hydrophobic long-chain phenol moieties. To the best our knowledge, the present findings can give the first example of morphological control

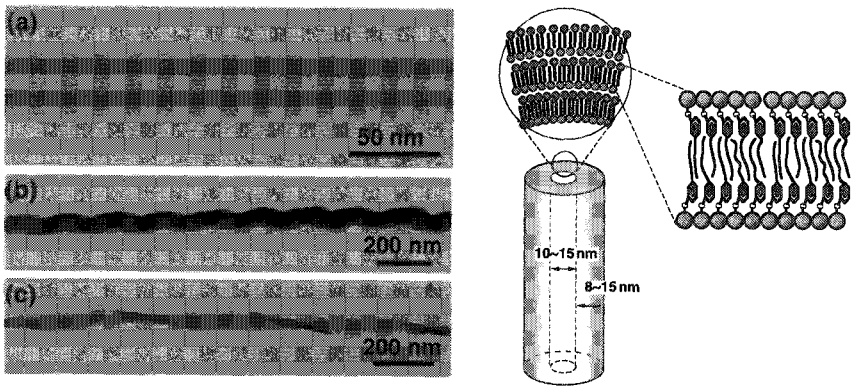

Fig. 1. (Left) TEM images of self-assembled high-axial-ratio nanostructures (HARNs) from synthetic glycolipids **1**–**5**; (a) nanotube, (b) coiled-ribbon, and (c) twisted-ribbon. (Right) Molecular packing within the lipid nanotube.

of helical nanofibers by unsaturation of the hydrophobic chains.[5,7] Interestingly, coiled ribbons formed from **1** were gradually converted into a tubular structure over a period of several days. High-resolution energy-filtering transmission electron microscopy (EF-TEM) revealed that the obtained lipid nanotubes have uniform inner diameters of 10–15 nm, outer diameters of 50–60 nm, and extended lengths of 10–1000 μm (Fig. 1(a)). It should be noted here that the present lipid nanotubes can provide hollow nanocylinders of almost the same size dimensions as multiwall carbon nanotubes. The obtained lipid nanotubes proved to be stable only at temperatures below the gel-to-liquid crystalline phase transition temperature (35–40°C) and transformed into spherical vesicles at temperatures above that. The twisted-ribbon structures formed from **2** gave no morphological change even after several months of aging, resulting into no tubular structures.

The d spacing of 3.9 nm obtained for the helically-coiled ribbons suggested the existence of interdigitated 3–4 bilayer sheets within the nanotubes (Fig. 1). In the present phenolic glycoside, π–π interaction between the aromatic rings plays a dominant role in stabilizing the nanofibers and the resulting nanotube structures. In contrast, octyl β-D-glucopyranoside without aromatic rings does not produce any fiber structures.

The differential scanning calorimetry of the fractionated diene **4** and triene **5** derivatives in the fully hydrated state displayed a gel-to-liquid crystalline phase transition at 17.0°C and −25.0°C, respectively.[8] This finding supports that the diene and triene components are in a fluid state at room temperature without participating the nanotube formation. We then employed saturated **2** and monoene **3** derivatives as lead molecules for further mixing and binary self-assembly. On self-assembly in water, the pure monoene component self-assembled into nanotube structures including tightly-coiled nanofibers. The two components were then

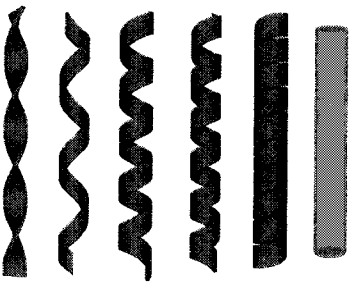

Fig. 2. Rational control of helical morphologies through binary self-assembly.

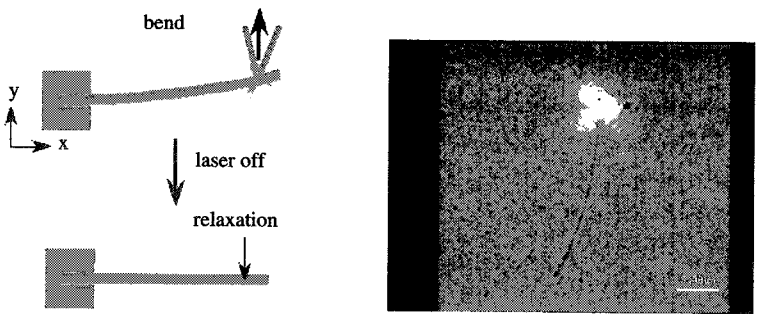

(a) (b)

Fig. 3. (a) The evaluation of flexural rigidity of a single lipid nanotube and (b) confocal laser scanning microphotograph of bow-shaped lipid nanotube in water.

mixed in many proportions ranging from 0 to 100%. On increasing the monoene content, the helical pitch decreases to give tubular morphologies. The obtained high-axial-ratio nanostructures (HARN) with various kinds of helical morphologies are schematically illustrated in Fig. 2. We thus confirmed that the binary self-assembly can generate a diversity of self-assembled HARNs, ranging from twisted-ribbons and helical-ribbons to nanotubes.

The mechanical properties of the synthetic lipid nanotubes have not been examined so far, in contrast to the extensive studies on microtubules and carbon nanotubes. We have then measured, using optical tweezers, the Young's modulus of a single lipid nanotube. The flexural rigidity K was able to be evaluated from the relaxation analysis giving the calculated relaxation time τ. Consequently, we got the flexural rigidity $K \approx 2.2 \times 10^{-22}$ [Nm^2] and the Young's modulus $E \approx 720$ [MPa] comparable to $E \approx 1000$ [MPa] for microtubules.[6]

References

1. S. Iijima and T. Ichihashi, *Nature* **363**, 603 (1993); K. Tanaka, *Carbon Nanotube* (Kagaku Doujin, Kyoto, 2001).

2. P. Yager and P. Schoen, *Mol. Cryst. Liq. Cryst.* **106**, 371 (1984).
3. N. Nakashima, S. Asakuma, and T. Kunitake, *J. Am. Chem. Soc.* **107**, 509 (1985).
4. J.-H. Fuhrhop and J. Koening, *Membranes and Molecular Assemblies: The Synkinetic Approach* (The Royal Society of Chemistry, Cambridge, 1994); T. Shimizu, M. Kogiso, and M. Masuda, *Nature* **383**, 487 (1996).
5. G. John, M. Masuda, Y. Okada, K. Yase, and T. Shimizu, *Adv. Mater.* **13**, 715 (2001).
6. H. Frusawa, A. Fukagawa, Y. Ikeda, J. Araki, K. Ito, G. John, and T. Shimizu, *Angew. Chem. Int. Ed.* **42**, 72 (2003).
7. J. H. Jung, G. John, K. Yoshida, and T. Shimizu, *J. Am. Chem. Soc.* **124**, 10674 (2002).
8. G. John, J. H. Jung, H. Minamikawa, K. Yoshida, and T. Shimizu, *Chem. Eur. J.* **8**, 5494 (2002).

This page is intentionally left blank

International Journal of Nanoscience, Vol. 1, Nos. 5 & 6 (2002) 471–476

PREPARATION AND STABILITY OF THE NANOCHAINS CONSISTING OF COPPER NANOPARTICLES AND PVA NANOFIBER

CE WANG*, ZHEN YU LI*, DONGMEI LI†,
QING BIAO YANG*, and YOULIANG HONG*

*Jilin University Alan G. MacDiarmid Institute
Changchun, P. R. China, 130012
†National Laboratory for Superhard Materials
Changchun, P. R. China, 130023

Received 27 November 2002
Revised 7 January 2003

One-dimensional nanochains consisting of Cu nanoparticles and PVA nanofiber were prepared in the presence of a deoxidant $NaHSO_3$ by electrospinning. Their morphologies and stability were characterized by TEM and UV-vis spectra. The results show that three kinds of nanochains were formed according to the ratio of diameters of the nanoparticles to the nanofiber, i.e., Cu/PVA is equal to, larger, and smaller than 1. The nanochains are stable in air.

Keywords: Nanochain; nanofiber; nanoparticle.

1. Introduction

One-dimensional (1D) nanomaterials such as nanobelt, nanowire, nanotube, nanowhisker, nanofiber, and nanochain have attracted a great deal of attention. The fabrication of 1D nanochains consisting of nanoparticles appears to be more important, since the ordering building blocks in 1D configuration is necessary to realize the assembling of nanoelectronic devices. The success of the assembling makes it possible to use and to investigate single electron tunneling effect at room temperature.

As is well known, electrospinning technology can be used to make nanofibers, whereas sol–gel process to make metal, oxide and semiconductor nanoparticles. If we can homogeneously disperse the nanoparticles into the polymeric spinning solutions and use the electrospinning technology to make the corresponding nanofibers, the nanochains can be obtained. However, incorporation of the nanoparticles into the nanofibers and the stability of the nanoparticles under a high electric field and in air, are the problems we are facing. At the 224th ACS meeting, we reported that silica and titania nanoparticles were very well embedded in the polyacrylonitrile (PAN) nanofiber.[1] Recently, Ag nanoparticles were also successfully put in PAN nanofiber.[2]

In this paper, we present the assembling and stability of copper nanoparticles in polyvinylacohol (PVA) nanofiber.

2. Experimental Method

A 0.02 g of diotyl sulfosuccinate sodium salt (AOT), a certain amount of sodium bisulfite ($NaHSO_3$) and copper chloride ($CuCl_2$) were added at the weight ratios of 1:0.5, 1:1, 1:1.5, 1:2, and 1:2.5 into a cone bottle containing 20 g of distilled water separately and stirred for 24 h at room temperature. Then, 2.4 g of PVA was added and heated to 90°C, and was kept for 2 h under a magnetic stirring. After cooling down to room temperature, the solution was continuously stirred for 48 h. A 10 g of distilled water with 0.8 g of N_2H_5OH was added to the solution and rapidly stirred at room temperature for 12 h. The obtained solutions were held in a spinning nozzle with a tip diameter of 1 mm, which, as an anode, is 13.0 cm from an Al-foil cathode. A copper grid was used to collect Cu/PVA nanochains on the cathode under a voltage of 41.0 KV. The nanochains were characterized by Transmission Electron Microscope (TEM, a Hitachi S-570 T) and UV-vis absorption spectra (Cary 100, Varian Corp.).

3. Results and Discussion

Previous work has proved that the Cu particles with a size smaller than 500 nm are unstable and rapidly oxidized in air,[3] and the oxidation of the particles encapsulated in surfactants or polymers cannot be efficiently delayed.[4] Therefore, a deoxidant $NaHSO_3$ was used here to prepare Cu/PVA nanochains. As the weight ratios of $CuCl_2$:$NaHSO_3$ were changed from 1:0.5, 1:1, 1:1.5 to 1:2 ($CuCl_2$:VA repeat unite = 1:30 wt.), a fuchsia copper sol was obtained all the time, whereas at the ratio of 1:2.5 a yellow solution was obtained. UV-vis spectra (Fig. 1) indicate that an absorption band occurs at 590 nm (1(a)) and shifts to 592 nm (1(b)), 600 nm (1(c)), and 602 nm (1(d)) with an increase in the corresponding ratios of $CuCl_2$:$NaHSO_3$ (1:0.5, 1:1, 1:1.5 to 1:2). The band disappeared at 1:2.5 of $CuCl_2$:$NaHSO_3$. It illustrates that Cu nanoparticles have been formed in the range of 1:0.5 and 1:2.0 of $CuCl_2$:$NaHSO_3$. But, their sizes differ with the amount of $NaHSO_3$, as shown in the red shift. Nevertheless, the use of excessive amount (1:2.5) of the deoxidant leads to no formation of Cu particles. The result could be attributed to the acidity of $NaHSO_3$. Namely, the pH values of the system are 10, 9, 8, 7.5 and 6 based on the weight ratios of $CuCl_2$:$NaHSO_3$ mentioned above, respectively. Therefore, pH 7 is a boundary of formation for the Cu particles, i.e., the Cu nanoparticles could be formed stably in the solution at pH $>$ 7 and no Cu particles at pH $<$ 7. The conclusion is consistent with the work by Gao *et al.*[5] But, in the range of pH 6 and pH 8, Cu_2O might exist in the nanochains. Further work is in progress.

The stability of Cu nanoparticles in the aqueous PVA solution exposed to air was measured, as shown in Fig. 2. The peaks at 584 nm (2(a)) and 592 nm (2(b)) are respectively for the sample standing for 0 d and 7 d, which prove that the Cu

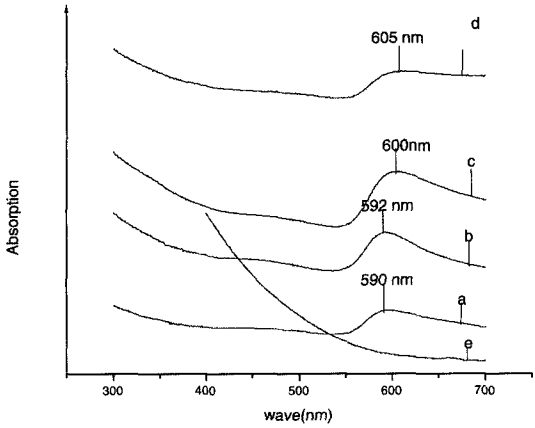

Fig. 1. UV-vis spectra ($CuCl_2$:$NaHSO_3$ = 1:0.5, 1:1, 1:1.5, 1:2, $CuCl_2$:VA repeat unit = 1:30 wt.).

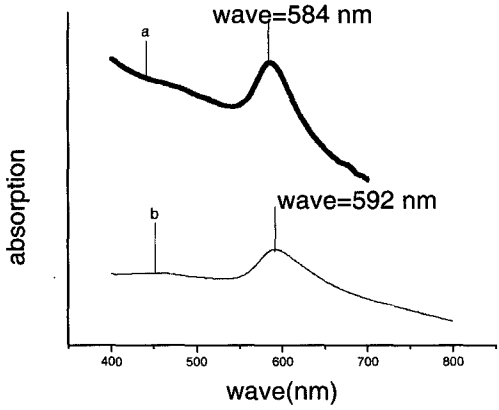

Fig. 2. UV-vis spectra of the Cu/PVA solution after standing in air for (a) 0 d and (b) 7 d.

particles were relatively stable in the solution. A red shift of the absorption band with time from 0 d to 7 d could be resulted from the agglomeration of the Cu nanoparticles.

The Cu/PVA solution system was spun based on a formulation of $CuCl_2$:$NaHSO_3$:VA:N_2H_5OH = 1:0.5:30:4 (wt.) under a high voltage of 41.0 KV. UV/vis spectra in Fig. 3 show that there is an absorption band of the Cu nanoparticles at 585 nm before and after electrospinning. It indicates that the property and structure of the Cu nanoparticles remain unchanged through the high electric field. The difference between the peak intensity should be caused by the different concentrations of the samples.

The effect of the content of Cu nanoparticles on the diameter of PVA nanofiber was shown in TEM images (Fig. 4), in which the Cu/PVA nanochains were prepared in weight ratios of 1:10 (4(b)), 1:20 (4(c)), 1:30 (4(d)) of $CuCl_2$:VA repeat unit, and

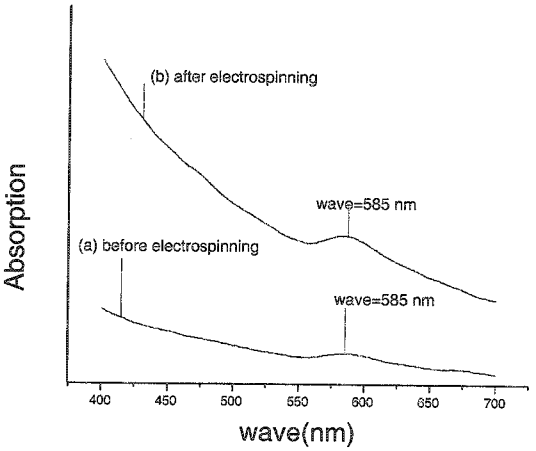

Fig. 3. UV-visible spectra of Cu/PVA solutions.

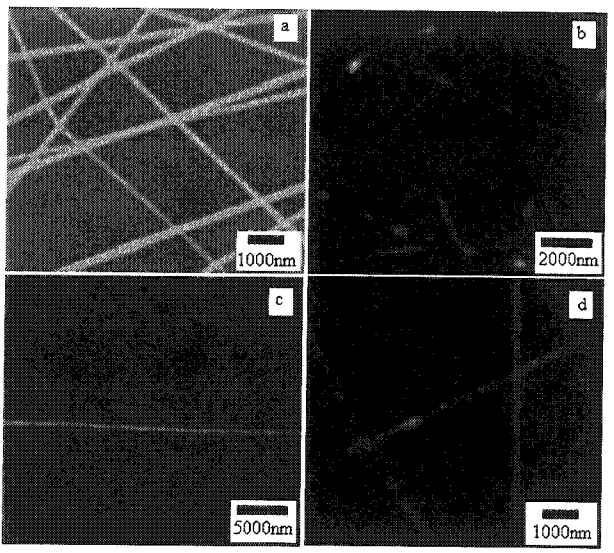

Fig. 4. TEM images of (a) pure PVA and Cu/PVA nanochains in $CuCl_2$:VA (wt.) of (b) 1:10, (c) 1:20, and (d) 1:30.

pure PVA nanofiber (4(a)) is also shown as a reference. The average diameters of the Cu nanoparticles and PVA nanofibers are shown in Table 1.

It can be seen that the average diameters of the Cu/PVA nanochains are larger than that of the pure PVA fiber. With the increasing concentration of $CuCl_2$, the average size of the Cu nanoparticles increases from 95 nm to 350 nm and to 550 nm, and the ratio of the average diameters of the Cu particles to the PVA fiber increased from 0.3, 1 to 3.1. In addition, as the ratio of $CuCl_2$:VA repeat unit is

Table 1. The relationship between the content of $CuCl_2$ and the diameters of the PVA nanofiber and Cu nanoparticles.

Sample	$CuCl_2$:VA Repeat unit	Diam. of PVA fiber (nm)			Diam. of Cu particles (nm)		
		Average	Min.	Max.	Average	Min.	Max.
0	8 wt.%	150	120	180	0	0	0
1	1:10	160	70	250	550	300	800
2	1:20	350	350	350	350	350	350
3	1:30	355	280	430	95	40	150

1:20, the diameters of the Cu particles and PVA fiber are well matched. However, it is interesting to find that the diameter of the fiber is disproportional with that of the particles. Namely, the bigger the particles in size, the thinner the fibers. This might be caused by the concentrations of the Cu ions in the free volume of PVA as well as the dispersity and electric charges intensity of the Cu particles. A low concentration of Cu^{2+} leads to the formation of the small Cu nanoparticles with a good dispersity and low charge intensity. The small particles as a physical crosslinking agent make the PVA fiber thicker. A high concentrate of Cu^{2+} ions leads to formation of the bigger Cu particles with low dispersity due to their agglomeration. The big particles possess a high charge intensity that results in strongly expulsing in the process of electrospinning under the high electric field. The expulsive force makes the fiber thinner. Consequently, three kinds of nanochains were obtained according to the ratios of diameters of the nanoparticles to the nanofibers: Cu/PVA > 1, $= 1$, and < 1.

4. Conclusion

The Cu/PVA nanochains, stable in air, have been prepared at pH > 7, in the presence of sodium bisulfite deoxidant under a high voltage of 41.0 KV. The nanochains are bigger than the pure PVA nanofiber in diameter due to the existence of the Cu nanoparticles. They can be divided into three types according to the ratio of diameter of the nanoparticles and nanofibers: Cu/PVA < 1, $= 1$, and > 1.

Acknowledgments

This work is supported by NSFC (No. 50173009) and National 973 Project (No. 2001610505).

References

1. C. Wang, Y. L. Hong, Q. B. Yang, T. Yunus, Z. Y. Li, N. Guo, Y. Y. Zhao, W. Liu, X. F. Hao, and Q. Fei, *Polym. Prep.* **43**(2), 1387 (2002).
2. Q. B. Yang, C. Wang, Y. L. Hong, Z. Y. Li, S. L. Qiu, and Y. Wei, *Synthetic Metal* **137**, 973 (2003).

3. Z. J. Liu, B. Zhao, Z. T. Zhang, and L. M. Hu, *J. East China Univ. Sci. Technol.* **22**(5), 548 (1996).
4. Z. J. Liu, B. Zhao, Z. T. Zhang, and L. M. Hu, *Chem. Bull.* **10**, 55 (1996).
5. Y. Gao, C. H. Luan, and Y. Q. Xue, *J. Taiyuan Univ. Technol.* **31**(3), 271 (2000).

International Journal of Nanoscience, Vol. 1, Nos. 5 & 6 (2002) 477–481

REMOVAL OF THE SURFACTANT SURROUNDING Ag NANOCLUSTERS SYNTHESIZED BY NEW THERMAL DECOMPOSITION METHOD

LEE DON KEUN and YOUNG SOO KANG*

Department of Chemistry, Pukyong National University, 599-1 Nam-gu Busan, 608-737, Korea

Received 27 November 2002
Revised 9 January 2003

Silver nanoclusters have been formed by thermal decomposition of Ag-oleate complex. Transmission electron microscopic (TEM) images of the particles showed two-dimensional assembly of particles with diameter of 10.5 nm. Energy-dispersive X-ray (EDX) spectrum and X-ray diffraction (XRD) peaks of the nanoclusters showed the highly crystalline nature of the silver structures. The decomposition of silver-oleate complex was analyzed by Thermo Gravimetric Analyzer (TGA) and the crystallization process was observed by XRD. The removal of the surfactant surrounding silver nanoclusters was measured by FT-IR and SEM images.

Keywords: Silver nanocluster; silver-oleate complex; nanocluster.

1. Introduction

The area of nanotechnology is witnessing an increased research activity due to its immense potential in various industrial applications such as optoelectronic devices,[1] nonlinear optics,[2] light-emitting diodes,[3] and quantum dot lasers.[4] One of the goals in nanotechnology is the organization of nanoclusters in crystalline arrays with the ability to tailor the size and separation of the nanoclusters and thereby the optical and electronic properties of the assembly.[5] The synthesis of colloidal inorganic nanocrystals especially with respect to the control of their shape, is under developed and still complicated. A new direction for synthetic methods and an understanding of the mechanisms by which the size and shape of the nanocrystals can be easily varied are the key issues in nanochemistry. For the past few years, various methods have been developed for the synthesis of one-dimensional (1D) nanomaterials including template-assisted,[6,7] vapor-liquid-solid (VLS)-assisted,[8] colloidal micellar,[9,10] and electrochemical processes.[11] Here we report a very easy, economical and nontoxic thermal decomposition method of fabricating highly crystalline and monodisperse silver nanoclusters.

*Corresponding author.

2. Experiment

$AgNO_3$ (99+%) and sodium oleate (98%) were obtained from Aldrich Chemical Co. and used without further purification. To prepare Ag-oleate complex, 1.7 g of $AgNO_3$ (10 mmol) was dissolved in deoxygenated water (300 mL, 18 MΩ, nitrogen gas bubbling for 30 min) and a 3.05 g of sodium oleate (10 mmol) was added into the resulted solution under vigorous stirring for 2 h. The precipitate was separated by filtration and washed with doubly deionized water to remove sodium and nitrate ions. After drying the Ag-oleate complex was transferred into a pyrex tube. The complex was first flushed with nitrogen, and the tube was sealed at 0.3 Torr. The sample was slowly heated from room temperature to 290°C at 2°C/min. After reaching the desired temperature, it was held at 290°C for 1 h and cooled to room temperature. The complex color was changed to black, indicating that silver nanoclusters were being formed. These silver nanoclusters can be easily redispersed in octane or toluene. In order to remove the surfactant surrounding silver nanoclusters, the black precipitate was added to 50 mL of isopropyl alcohol saturated by KOH. After standing for 2 h, the solution was filtered and washed with isopropyl alcohol saturated by KOH to be free of the surfactant.

Transmission electron microscopy (TEM) examinations of the samples were carried out on a HITACHI H-7500 (low-resolution) and a JEOL JEM2010 (high-resolution) transmission electron microscope. TEM samples were prepared on the 400 mesh copper grid coated with carbon. The size distributions of the particles were measured from enlarged photographs of the TEM images. The structural properties of synthetic nanoclusters were analyzed by XRD with a Philips X'Pert-MPD System with a Cu K_α radiation source ($\lambda = 0.154056$ nm). The decomposition of silver-oleate complex was analyzed by Thermo Gravimetric Analyzer (TGA) and the crystallization process was observed by XRD. Removal of the surfactant surrounding Ag nanoclusters was detected by FT-IR spectra and SEM.

3. Result and Discussion

The decomposition path of the silver-oleate complex was studied by TGA analysis. Figure 1 shows the weight loss for silver-oleate complex during heat treatment under air flow. A very strong endothermic peak was observed at 287°C. The peak is related to the evaporation of oleate molecules formed by the decomposition of silver-oleate complex.

Figure 2 illustrates (A) the XRD pattern of silver-oleate complex, (B) 287°C aging of silver-oleate complex. No signature of silver in the pristine silver-oleate complex has been observed in the XRD analysis (Fig. 2(A)). This indicates that the complex is amorphous. However, the signature of silver has been observed in the 287°C aged silver-oleate complex (Fig. 2(B)). The peaks are broadened due to the nanocrystalline nature of silver. The diffraction patterns of 287°C aged silver-oleate complex all match for pure silver structure (JCPDS card no. 04-0783). Figure 2(B) shows three peaks at 2θ values of 38.2°, 44.5° and 64.5° corresponding to (111),

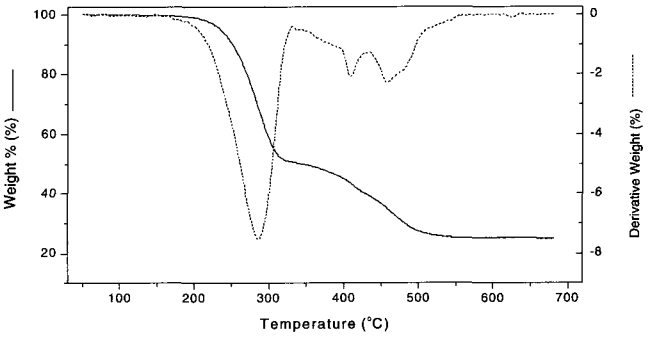

Fig. 1. The weight loss for Ag-oleate complex during heat treatment under air flow.

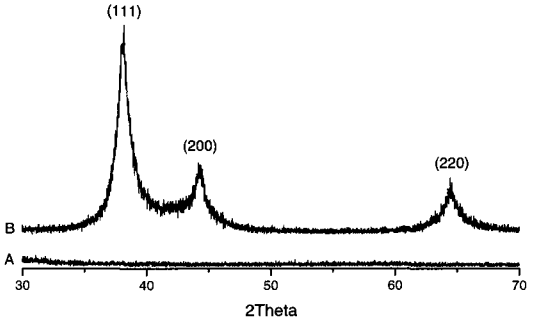

Fig. 2. (A) XRD pattern of Ag-oleate complex and (B) 300°C aging of silver-oleate complex.

(200) and (220) planes of silver, respectively. No impurity peak is observed in the X-ray diffraction pattern.

Figure 3 is the low-resolution TEM image of monodisperse nanocrystallite of silver nanoclusters. Silver nanocluster monolayer was formed by self-assembly when a drop of the nanocluster isooctane solution was carefully placed on the grid and dried in air. Most of the silver particles are spherical. Insertion in Fig. 3(B) is a histogram of the size distribution of silver nanoclusters obtained from enlarged image of Fig. 3(B). The mean size of silver nanoclusters is 10.5 nm with a standard deviation 0.7 nm. This shows that the silver nanoclusters have very narrow size distribution. A monolayer of nanoclusters was observed from the image with almost no multilayer on it. Figure 3(B) shows an example of an enlarged area where particles are packed in a highly-organized manner and monodisperse nanoclusters were arranged in a two-dimensional hexagonal closed packed way, demonstrating the uniformity of the particle size, especially when the interparticle spacing is very even. Here, as in most cases, the adjacent silver nanoclusters were separated by a region of approximately 2 nm, which did not exhibit any diffraction contrast. This distance is considerably less than twice the expected oleate length (1.75 nm); interdigitation of the alkyl chains from nearest-neighbor silver particles can be inferred.

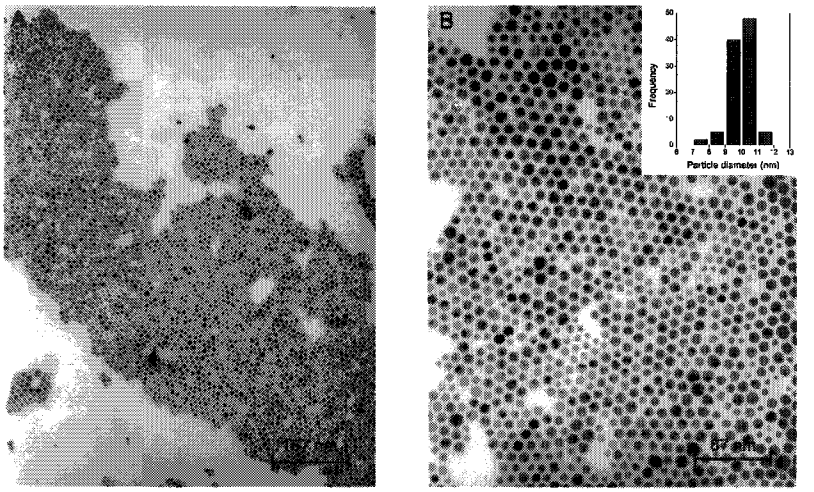

Fig. 3. (A) Low-magnification and (B) high-magnification TEM images of Ag nanoclusters. The average particle size is 10.5 ± 0.5 nm.

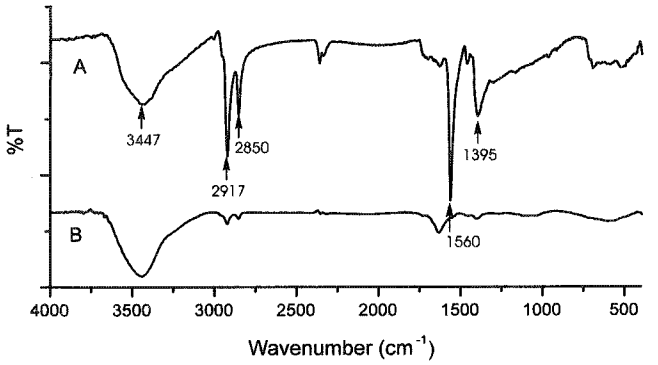

Fig. 4. (A) FT-IR spectra of Ag nanoparticles containing surfactants and (B) surfactant removed Ag nanoparticles.

Figure 4 shows (A) the FT-IR spectrum of Ag nanoclusters containing surfactants and (B) surfactants removed that of Ag nanoparticles. Figure 4(A) has two large absorption bands under 2000 cm^{-1}. These two large bands are almost coincident with those observed typically for the acetate group complexed with a metal and correspond to C=O stretching (1560 cm^{-1}) and C–O stretching (1395 cm^{-1}) in oleate molecular, respectively. In general, three bonding structures are well-known for the acetate group complexed with a metal.[12] The strong bands at 2850 cm^{-1} and 2917 cm^{-1} belong to methylene and methyl symmetric stretching vibration, respectively. This indicates that silver nanoclusters were covered with the surfactant. Figure 4(B) almost does not have the absorption bands of methylene, methyl and

acetate group complexed with a metal. This shows that the surfactant surrounding nanoclusters was successfully removed by using isopropyl alcohol saturated by KOH.

Acknowledgments

This work was supported by the Brain Busan 21 Project in 2002 and The Project of Promotion of Industry Basic Technology of Shoes from The Korean Ministry of Industry and Resources.

References

1. A. Henglein, *Top. Curr. Chem.* **143**, 113 (1998).
2. F. Ghebremichael, M. G. Kuzyk, and H. S. Lackritz, *Progress in Polymer Science* **22**, 1147 (1997).
3. V. L. Colvin, M. C. Schlamp, and A. P. Alivisatos, *Nature* **370**, 354 (1994).
4. A. P. Alivisatos and C. Semiconductor, *Science* **271**, 933 (1996).
5. C. P. Collier, R. J. Saykally, J. J. Shang, S. E. Henrichs, and J. R. Heath, *Science* **277**, 1978 (1997).
6. Y. J. Han, J. M. Kim, and G. D. Stucky, *Chem. Mater.* **12**, 2068 (2000).
7. H.-K. Kang, Y. Jun, J.-I. Park, K.-B. Lee, and J. Cheon, *Chem. Mater.* **12**, 3530 (2000).
8. L. Rivas, S. Sanchez-Cortes, J. V. Garcia-Ramos, and G. Morcillo, *Langmuir* **17**, 574 (2001).
9. J. Hu, T. W. Odom, and C. M. Lieber, *Acc. Chem. Res.* **32**, 435 (1999).
10. M. Li, H. Schnablegger, and S. Mann, *Nature* **402**, 393 (1999).
11. M. B. Mohamed, K. Z. Ismail, S. Link, and M. A. El-Sayed, *J. Phys. Chem. B* **102**, 9370 (1998).
12. S. Sakohara, M. Ishida, and M. A. Anderson, *J. Phys. Chem. B* **102**, 10169 (1998).

This page is intentionally left blank

International Journal of Nanoscience, Vol. 1, Nos. 5 & 6 (2002) 483–487

SYNTHESIS OF THICK PORPHYRIN MOLECULAR WIRES BY A PALLADIUM CATALYZED OLIGOMERIZATION

HIROAKI OZAWA* and TAKUJI OGAWA†,‡,§

Department of Chemistry, Faculty of Science, Ehime University
2-5 Bunkyocho, Matsuyama, Ehime 790-8577, Japan
†*Precursory Research for Embryonic Science and Technology*
Japan Science and Technology Corporation
1-8 Honcho, Kawaguchi, Saitama 332-0012, Japan
**ozawa@chem.sci.ehime-u.ac.jp*
‡*ogawat@dpc.ehime-u.ac.jp*

Received 27 November 2002
Revised 6 January 2003

In the aim to prepare thick porphyrin molecular wires, which is visible by atomic force microscopy (AFM), even on the rough surfaces of nanogap electrodes fabricated by electron beam lithography, dendrimer protected porphyrins whose two meso-positions are substituted with ethynyl groups. The porphyrin monomer was reacted with palladium catalyst to make oligomers. Analyses of them with time-of-flight mass spectroscopy (TOF-MS), gel-permeation-chromatography (GPC) revealed that the oligomers were distributed up to 16 mer, whose molecular weight was about 38 000 Daltons.

Keywords: Molecular wire; porphyrin wire; dendrimer; nanogap electrode.

1. Introduction

Direct measurements of electronic properties of individual molecules are still a challenging target of materials science. Several reports have already been published, however, no one has succeeded in the electronic measurement while observing the molecules between the electrodes. One reason is the roughness of the electrode surface, which was fabricated by usual electron beam lithographic methods. In order to observe individual molecules, the substrate surface should be atomically flat. However, as shown in Fig. 1 the surface of electrodes made by lithography usually has a roughness, which is not suitable for observation of individual molecules. Two approaches are possible to overcome the problem: one is making the surface of the electrodes atomically flat and another is the synthesis of thick molecular wires, which is visible even on the rough surface. This paper describes the synthesis of the dendrimer protected porphyrin molecular wires, which are possibly seen by AFM on the rough surfaces.

§Corresponding author.

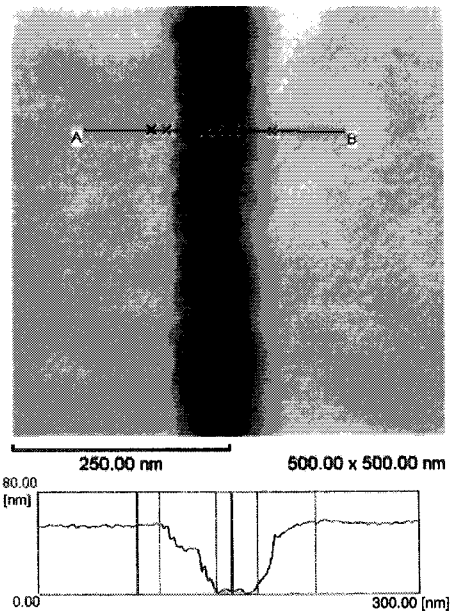

Fig. 1. The AFM image of a nanogap electrode fabricated by electron beam lithography and Ar ion beam etching.

2. Results and Discussions

2.1. *Synthesis of the dendrimer protected bis(ethynyl)porphyrin monomer 6*

We synthesized a porphyrin whose 5- and 10-position is substituted with 3,5-bis(dendrimer)phenyl group and other two meso-positions are substituted with ethynyl groups (**6**). In this paper, the second generation dendrimer was used and the exact structure is depicted in Scheme 1. The molecular mechanics estimation proved that the diameter of the molecule was about 3.8 nm.

The merits of introducing the sterically-crowded dendrimer moieties into the molecule are as follows: (1) as described in the Introduction, the AFM observation will become easier, (2) the solubility of the higher oligomers will improve because the intermolecular stacking of the π system is hindered, (3) the steric hindrance prevents the long molecules from bending, giving rigid and straight π-conjugated molecular wires. The porphyrin **6** was prepared starting from 5, 10-bis(3′, 5′-dimethoxyphenyl)porphyrin[1] as shown in Scheme 1.[2,3] In the ^{13}C NMR, the terminal ethynyl carbon appeared at 66.94 ppm, and in the ^{1}H NMR terminal ethynyl proton exhibited at 2.62 ppm, the CH-COSY spectrum was consistent with the assignment. The time-of-flight mass spectrum (TOF-MS) showed 2327 as the highest molecular weight peak that is consistent with the calculated value for $C_{136}H_{124}N_4O_{28}Zn = 2327$.

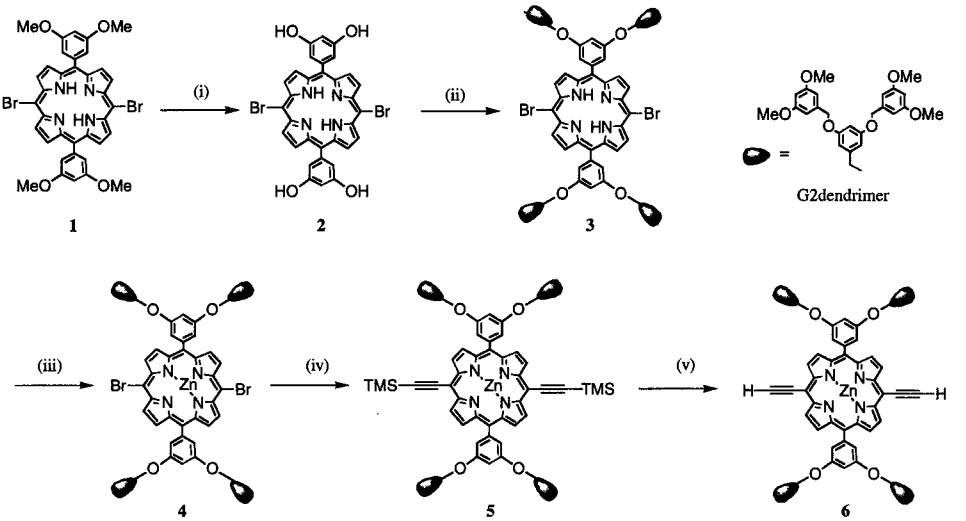

Scheme 1. Synthesis of dendrimer protected bis(ethynyl)porphyrin monomer **6**; (i) BBr_3, CH_2Cl_2, $-78°C$, (ii) G2 dendrimer bromide, K_2CO_3, 18-crown-6-ether, THF, reflux, (iii) $Zn(OCOCH_3)_2$, $CHCl_3$, reflux, (iv) TMS-acetylene, CuI, $Pd(PPh_3)_4$, Et_3N, THF, reflux, (v) n-Bu_4NF, $CHCl_3$.

2.2. *Oligomerization of the bis(ethynyl)porphyrin monomer*

At first, we tried a reported method to make the oligomers with using CuCl, tetramethylethylenediamine (TMEDA) and oxygen.[4] No identifiable product was isolated. Then the monomer **6** was reacted with $Pd(PPh_3)_4$, CuI, Et_3N in tetrahy-

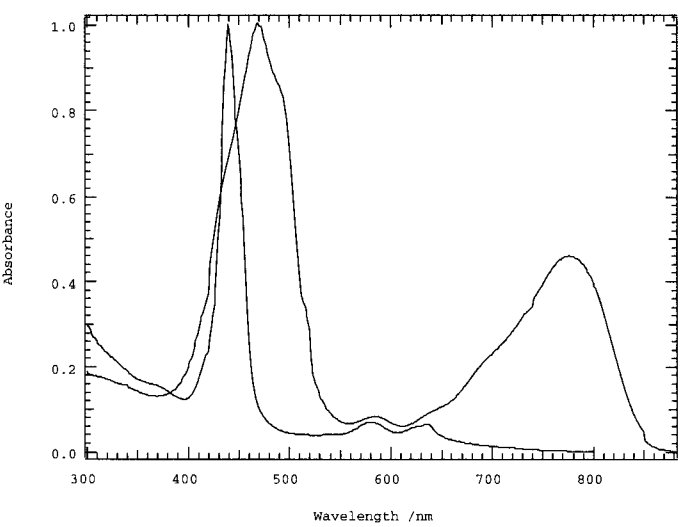

Fig. 2. The UV-vis absorption spectrum of the monomer **6** (broken line) and the oligomer (solid line).

drofuran (THF), and the product was purified by gel-permeation-chromatography (GPC) to give a yellowish black solid.

The UV-vis absorption spectrum was depicted in Fig. 2 as the solid line. The Soret peak was real-shifted about 30 nm longer as compared with the monomer **6** (broken line), and a new band appeared at around 800 nm together with Q band whose position is comparable with the monomer. The ^{13}C NMR exhibited acetylenic carbon at 67.67 and 87 ppm, which indicates that acetylenic part, was intact.

As shown in Fig. 3, the MALDI TOF-MS spectrum indicated a periodic peaks with about 2330 Daltons spacing. These data support that the oligomers were produced by the reaction as depicted in Scheme 2. The heaviest molecular peak

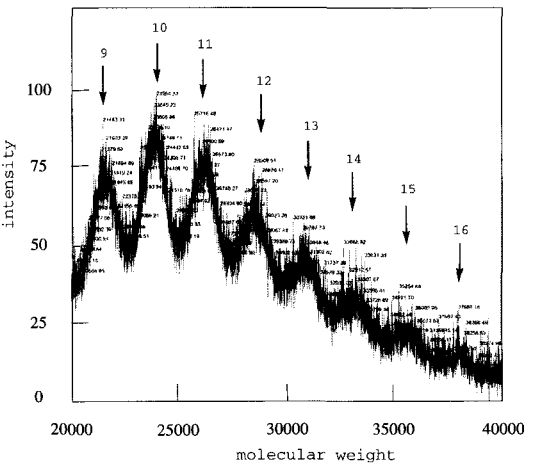

Fig. 3. The MALDI TOF-MS spectrum of the oligomers.

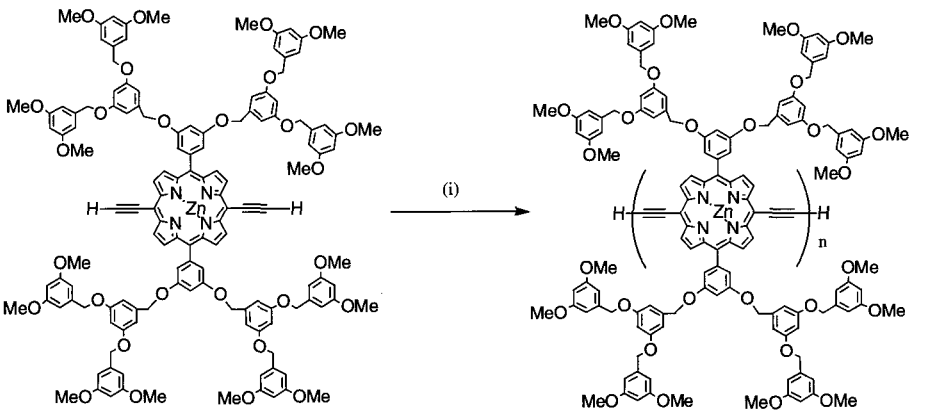

Scheme 2. Oligomerization of the bis(ethynyl)porphyrin monomer by palladium catalyst: (i) $Pd(PPh_3)_4$, CuI, Et_3N, THF.

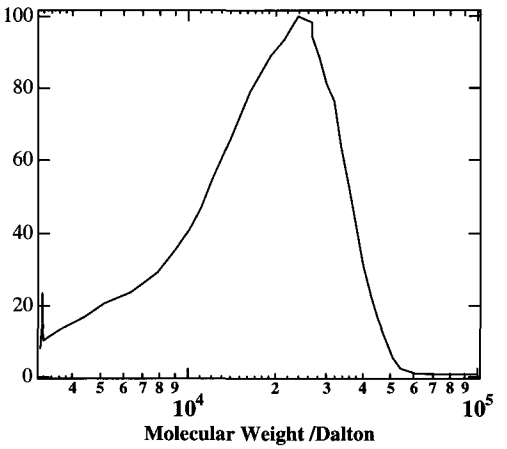

Fig. 4. The GPC analysis of the oligomers.

in the MALDI TOF-MS spectrum is calculated to be that of the 16 mer, whose molecular weight should be 37 217 Daltons. The higher homologues than 16 mer cannot be ionized in the present MALDI TOF-MS conditions although they may be produced. In order to check it, GPC analysis of the products were performed and the result is depicted in Fig. 4. The molecular weight was calibrated with standard polystyrenes. The highest peak of the product situated around 23 000–25 000 Daltons, which agrees with the result of MALDI TOF-MS were shown. In the GPC analysis, higher homologues up to 50 000 Daltons were observed. If this is the case, it corresponds to about 20 mer, i.e., about 20 nm length.

We have found that the palladium-catalyzed coupling of the acetylenic units is a better method than the previously reported conditions as it could produce a thick porphyrin molecular wires.

References

1. J. S. Manaka and D. S. Lawrence, *Tetrahedron Lett.*, 6989 (1989).
2. S. Huang and M. Tour, *Tetrahedron Lett.*, 3351 (1999).
3. D.-L. Jiang and T. Aida, *J. Am. Chem. Soc.* **120**, 10895 (1998).
4. H. L. Anderson, S. J. Martin, and D. D. C. Bradly, *Angew. Chem. Int. Ed. Engl.* **33**, 655 (1994).

This page is intentionally left blank

International Journal of Nanoscience, Vol. 1, Nos. 5 & 6 (2002) 489–494

SYNTHESIS AND PROPERTIES OF MESO-TETRAARYL RHODIUM PORPHYRIN WITH AN AXIAL LIGAND OF MOLECULAR WIRE

HIROKAZU SATO*

Graduate School of Science and Engineering, Ehime University
2-5 Bunkyocho, Matsuyama, Ehime 790-8577, Japan
sato@chem.sci.ehime-u.ac.jp

ERI SENBARA and TAKUJI OGAWA†,‡

Department of Chemistry, Faculty of Science, Ehime University
2-5 Bunkyocho, Matsuyama, Ehime 790-8577, Japan
Precursory Research for Embryonic Science and Technology
Japan Science and Technology Corporation
1-8 Honcho, Kawaguchi, Saitama 332-0012, Japan
†*ogawat@dpc.ehime-u.ac.jp*

Received 27 November 2002
Revised 12 January 2003

Tetra-*meso*-substituted rhodium(III) porphyrins with axial ligand of molecular wire were synthesized for the first time to demonstrate the preparation of self-standing molecule for measuring a single electron conductivity using scanning tunneling microscope technique. The self-standing structure of molecular wire was confirmed by X-ray crystallographic analysis. Cyclic and pulse voltammograms of each compound were measured, and these results indicated that we can freely change the energy level of self-standing molecule and estimate it by using voltammetric measurement.

Keywords: Single molecular conductivity; rhodium porphyrin; x-ray structure; cyclic voltammogram.

1. Introduction

The conductivity measurement of single organic molecule is not only a fascinating subject for basic research, but also the important field of molecular electronics.[1] Since Aviram and Ratner theoretically proposed the molecular rectification in 1974,[2] numerous experiments have been made with different approaches toward the characterization of the electronic transport property of organic molecule. Recently, one can contact an individual molecule between two electrodes and measure its conductivities,[3] with a scanning tunneling microscope (STM). Using a STM

*Permanent address: Ebara Research, Honfujisawa, Fujisawa, Kanagawa 251-8502, Japan.
‡Corresponding author.

method with self-assembled monolayers (SAMs), the observed data were claimed to contain the lateral conductance.

In this regard, we need isolated molecules on the surface of a substrate to measure the conductance of single molecules. In our previous work,[4] we prepared Sn(IV) porphyrin with 3,5-bis(methilthio)phenyl at four *meso*-positions having axial ligands, and investigated its properties on Cu(111) surface using STM techniques. Comparing the experimental results with semi-empirical molecular orbital calculations, the conductance via the molecular orbital energy level was confirmed. However, the experimental data indicated also that synthesized porphyrin leaned to one side of Cu surface because Sn(IV) porphyrin could have two axial ligands, one of which may prevent self-standing vertically.

In the present work, we report the synthesis, for the first time, of 5, 10, 15, 20-tetrakis(3,5-bis(substituted)phenyl) rhodium(III) porphyrins with an axial ligand of molecular wire. The X-ray structural analysis and characterization of these compounds are studied.

2. Results and Discussions

2.1. *Synthesis of self-standing molecules with molecular wire*

Synthetic routes to self-standing molecules are shown in Scheme 1. Reaction of 3,5-bis(substituted)benzaldehyde with pyrrole was carried out with a two-step one-pod reaction following a literature procedure.[5] Metalation was performed similar to a procedure in Ref. 6, using $[Rh(CO)_2Cl]_2$. Formation of axial ligand was performed by general lithiation method, mixing a Rh(III) porphyrin iodide in dry-toluene with 10 equivalent of lithium phenyl acetylide in dry-tetrahydrofuran (THF) at

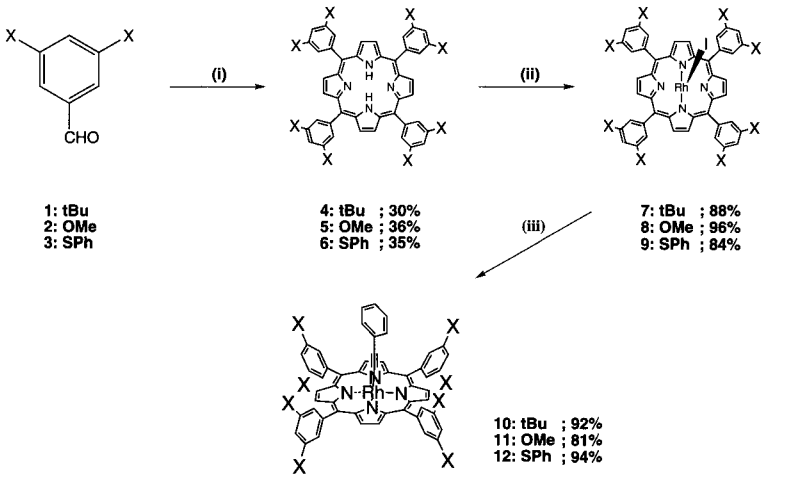

Scheme 1. Synthesis of self-standing molecules. (i) Synthesis of porphyrin, (ii) metalation, and (iii) formation of axial ligand.

−78°C, then the mixture was stirred further for 8 h at room temperature. Lithium phenyl acetylide was prepared by adding an *n*-butyl lithium to phenyl acetylene in dry-THF at −78°C. 5, 10, 15, 20-Tetrakis(3,5-bis(phenylthio)phenyl) rhodium(III) porphyrin with axial rigand of 3′, 4′-dibutyl-2, 2′; 5′, 2″-terthiophene (**13**) was also synthesized. In Scheme 1, tBu, OMe and SPh mean *t*-butyl, OCH_3 and phenylthio substituent, respectively.

2.2. *X-ray crystallographic structure*

Single-crystal X-ray analysis of **10** was measured by a Rigaku AFC5R diffractometer at room temperature. From this result, direct evidence that these compounds are able to stand on metal surface by using four substituted groups as legs, was obtained (Fig. 1). It is also confirmed that the phenyl acetylene ligand is almost perpendicular to the porphyrin plane as we expected. This indicates that these compounds are good candidates for the single molecular conductance measurement using STM method. In Fig. 1, small molecule located at the opposite site of phenyl acetylene ligand would be a solvent molecule (CH_3OH).

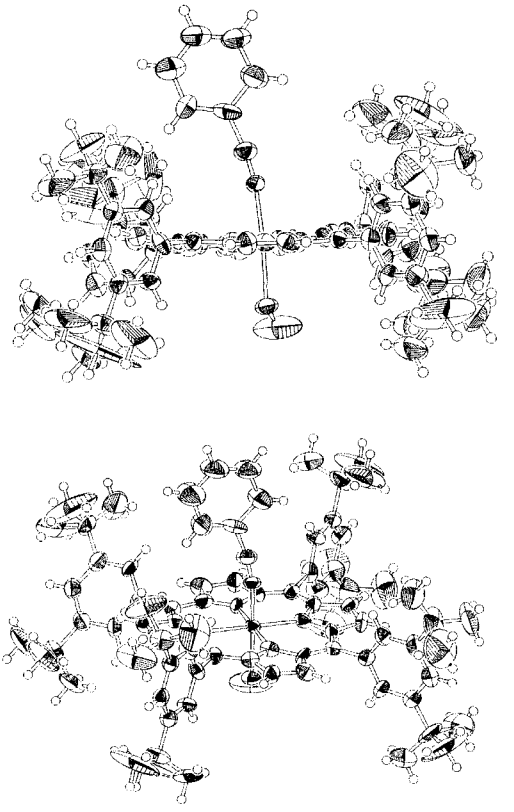

Fig. 1. X-ray structure of **10**.

2.3. *Voltammetric measurements*

Cyclic and pulse voltammetric measurements were performed at room temperature on a BAS CV 50-W voltammetric analyzer using working electrode of Pt disk, counter electrode of Pt wire, reference electrode of $Ag/AgNO_3$ in CH_3CN, and using a solution of 0.05 M tetrabutylammonium perchlorate (TBAP) in CH_2Cl_2 (freshly distilled). The cyclic voltammograms (CV) were measured with a scan rate of 100 mV/s, and the differential pulse voltammograms (DPV) were obtained with the following conditions: scan rate, 20 mV/s; pulse amplitude, 50 mV; sample width, 17 ms; pulse width, 50 mV; pulse period, 200 ms; quiet time, 2 s.

2.3.1. *5, 10, 15, 20-tetrakis(3,5-di(t-butyl)phenyl) porphyrin derivatives (4, 7, 10)*

CV and DPV of **10** and the comparison of DPV of **4**, **7**, and **10**, are shown in Fig. 2. It is obvious from Fig. 2(b) that oxidation potentials of rhodium porphyrin iodide **7** and rhodium porphyrin with an axial rigand **10** are almost the same as free-base porphyrin **4**. In contrast, the reduction potential is quite different. Two reduction potentials (−1456 mV, −1868 mV) were observed on DPV of **4**. While the reduction potential of **10** was shifted to more cathodic level (−1996 mV). This may be attributed to electron donation from the phenyl acetylene ligand.

2.3.2. *5, 10, 15, 20-tetrakis(3,5-bis(substituted)phenyle) porphyrin derivatives (10, 11, 12)*

The DPV of **10**, **11**, **12** and **13** are depicted in Fig. 3. Comparing the DPV of **10** and **11** with **12**, both the first oxidation potential (E^1_{ox}) and the first reduction potential (E^1_{red}) are shifted to a positive direction in this sequence. The energy

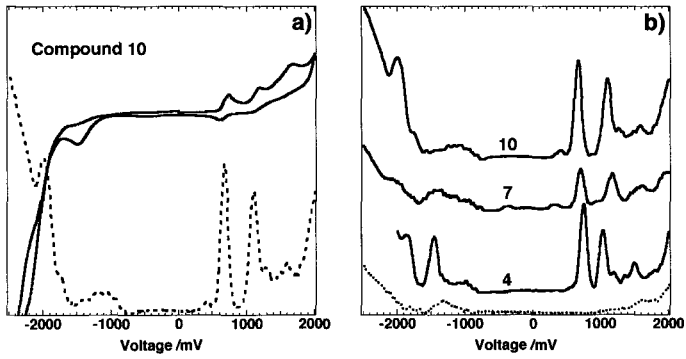

Fig. 2. (a) Voltammograms of compound **10**. The solid and broken line show the cyclic voltammogram and the differential pulse voltammogram, respectively. (b) The comparison of differential pulse voltammograms of **4**, **7** and **10**. The dotted line indicates a differential pulse voltammogram of 0.05 M TBAP in dry-CH_2Cl_2 as a background. $E_{1/2}(Fe/Fe^+) = +344$ mV.

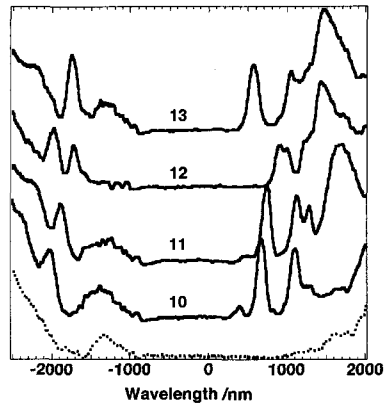

Fig. 3. The comparison of the differential pulse voltammogram of **10**, **11**, **12** and **13**. The dotted line indicates a differential pulse voltammogram of 0.05 M TBAP in dry-CH_2Cl_2 measured as a background. $E_{1/2}(Fe/Fe^+) = +344$ mV.

gaps between E^1_{ox} and E^1_{red} (the band gap energy) were not changed depending on the substituents (in this case the band gaps were about 2600 mV). This result can be supported in terms of the electron donation property of the substituents. The detail mechanism is now under consideration. By comparison of the DPV of **12** with **13**, it is clear that a molecular wire ligand was effective to arrange the band gap energy. The band gap energy of **13** was reduced to about 2300 mV. Considering that the axial rigand of **13** has terthiophene, which has more expanded π system than that of phenylacetylene of **12**, this energy reduction arises from the expansion of the π system of porphyrin induced by an axial ligand due to lowering the lowest unoccupied molecular orbital (LUMO) energy level.

These results suggest that we can tune the energy levels of self-standing molecule as our order, and they can be estimated by using voltammetric measurement.

References

1. C. Joachim, J. K. Gimzewski, and A. Aviram, *Nature* **408**, 541 (2000); J. Chen, W. Wang, J. Klemic, M. A. Reed, B. W. Axelrod, D. M. Kaschak, A. M. Rawlett, D. W. Price, S. M. Dirk, J. M. Tour, D. S. Grubisha, and D. W. Bennett, *Ann. N. Y. Acad. Sci.* **960**, 69 (2002).
2. A. Aviram and M. Ratner, *Chem. Phys. Lett.* **29**, 277 (1974).
3. C. Joachim, J. K. Gimzewski, R. R. Schlitter, and C. Chavy, *Phys. Rev. Lett.* **74**, 2102 (1995); L. A. Bumm, J. J. Arnold, M. T. Cygan, T. D. Dunbar, T. P. Burgin, L. Jones, II, D. L. Allara, J. M. Tour, and P. S. Weiss, *Science* **271**, 1705 (1996); M. A. Reed, C. Zhou, C. J. Muller, T. P. Burgin, and J. M. Tour, *Science* **278**, 252 (1997); C. Kergueris, J. P. Bourgoin, S. Palacin, D. Esteve, C. Urbina, M. Magoga, and C. Joachim, *Phys. Rev. B* **59**, 12505 (1999); X. D. Cui, A. Primak, X. Zarate, J. Tomfohr, O. F. Sankey, A. L. Moore, T. A. Moore, D. Gust, G. Harris, and S. M. Lindsay, *Science* **294**, 571 (2001); J. Reichert *et al.*, *Phys. Rev. Lett.* **88**, 176804 (2002).

4. T. Ogawa, E. Senbara, and H. Miura, *ABS. 1st Int. Conf. on Molecular and Bioelectronics*, Japan, Hyogo, 2001.
5. R. W. Wagner, D. S. Lawrence, and J. S. Lindsey, *Tetrahedron Lett.* **28**, 3069 (1987).
6. H.-J. Kim, J. E. Redman, M. Nakash, N. Feeder, S. T. Teat, and J. K. M. Sanders, *Inorg. Chem.* **38**, 5178 (1999).

International Journal of Nanoscience, Vol. 1, Nos. 5 & 6 (2002) 495–499

SYNTHESIS OF ZnS:Mn^{2+} NANOCRYSTALS AND LUMINESCENCE PROPERTIES OF LDPE FILM CONTAINING ZnS:Mn^{2+}

HO-JU JEON and YOUNG SOO KANG

Department of Chemistry, Pukyong National University
Daeyeon-3-dong Nam-gu, Pusan, 608-737, Korea

Received 27 November 2002
Revised 8 January 2003

The manganese-doped ZnS (ZnS:Mn^{2+}) nanocrystals were prepared by addition of Na_2S to an Zinc Oleate and $Mn(NO_3)_2$ solution. It was done using auto-clave method. The aging in auto-clave resulted in Mn^{2+}-doped ZnS particle. The emitting band ZnS:Mn^{2+} showed red-shift from that of ZnS and results in the emission band at 500 nm $\sim$ 650 nm (λ_{max} = 575 nm). ZnS:Mn^{2+} particles dispersed in polymer for production of the green house films. So this film will be used as light wavelength modification materials for the utilization of plant growth acceleration. Luminescence properties of the film were measured by luminescence spectrometer.

Keywords: Luminescence; ZnS:Mn^{2+}; film.

1. Introduction

Optical properties of semiconductor nanocrystallites have been investigated, since these materials have a potential application to nonlinear optical devices. The luminescence properties of nanosized luminescent semiconducting particles are substantially different from those of bulk crystalline materials. The band gap energy increases as particles become smaller, such small particles emit visible luminescence intensity much stronger than bulk crystals. Bhagrava *et al.* have reported that the luminescence enhancement of manganese-doped ZnS results from an efficient energy transfer from the ZnS host to Mn^{2+} ions was facilitated by mixed electronic states.[1] The hybridization of atomic orbital of ZnS and *d* orbital of Mn^{2+} was also suggested to be responsible for the relaxation of selection rules for the spin-forbidden $^4T_1$-$^6A_1$ transition of Mn^{2+}.[1] In this paper, we report the preparation and optical properties of Mn^{2+}-doped ZnS semiconductor nanoparticles and the film blended low density polyethylene (LDPE) with ZnS:Mn^{2+} nanoparticles. The synthesis of ZnS:Mn^{2+} was done by thermal treatment oleate complexes using auto-clave. The aging of zinc oleate and manganese-doped zinc oleate in auto-clave resulted in ZnS:Mn^{2+} nanoparticles.

2. Experiment

2.1. *Material*

Manganese (II) nitrate hydrate ($Mn(NO_3)_2$, 98%) and sodium sulfide (Na_2S, absolute) were obtained from Aldrich Chemical, Inc. Zinc chloride ($ZnCl_2$, extra pure), sodium oleate ($C_{17}H_{33}COONa$, extra pure) and low density polyethylene (LDPE) were obtained from Junsei Chemical Co., Ltd.

2.2. *Synthesis of ZnS:Mn^{2+} nanoparticle*

ZnS:Mn^{2+} was prepared by thermal decomposition of zinc oleate and manganese-doped zinc oleate complex by thermal treatment using auto-clave. A 3.783 g (12.48 mmol) of sodium oleate, 0.5 g (3.67 mmol) of zinc chloride and 0.46 g (2.57 mmol) of $Mn(NO_3)_2$ were dissolved in 100 ml of water. After 10 min, 0.487 g (6.24 mmol) of Na_2S was added into the sodium oleate aqueous solution under the constant stirring for 2 h. The mixture was slowly heated from room temperature to 300°C at 60°C/30 min using auto-clave. After reaching the desired temperature, it was held at 300°C for 2.5 h and was cooled to room temperature. The reaction product was diluted with methanol and was filtered through membrane filter (0.45 μm).

2.3. *Preparation of LDPE (low density polyethylene) film containing ZnS:Mn^{2+} nanoparticle*

The various concentration of ZnS:Mn^{2+} nanoparticles was added into the 1 g of LDPE dissolved in boiled toluene. Then, the toluene in LDPE solution was evaporated slowly at 60°C to making of the LDPE film. The quantity of added ZnS:Mn^{2+} nanoparticle was 0.001 g, 0.003 g and 0.005 g. These films containing 0.1%, 0.3% and 0.5% of ZnS:Mn^{2+} nanoparticle against quantity of LDPE.

2.4. *Apparatus*

The structure of ZnS:Mn^{2+} nanoparticle was studied with X-ray diffraction (XRD) (Philips, X'Pert-MPD system) and the analysis of element was confirmed by TEM-Energy dispersive X-ray (TEM-EDX). ZnS:Mn^{2+} nanoparticle was determined with Transmission Electron Microscope (TEM) (JEOL, JEM-2010). The emission spectra were recorded on a Luminescence Spectrometer (Perkin-Elmer, LS50B).

3. Results and Discussion

ZnS:Mn^{2+} were synthesized successfully by thermal decomposition of zinc oleate and manganese-doped zinc oleate complex with auto-clave and their crystal structures are confirmed by XRD patterns as in Fig. 1. The discernible peak in Fig. 1 can be indexed to (100), (002), (101), (102), (110), (103) and (112) planes, which

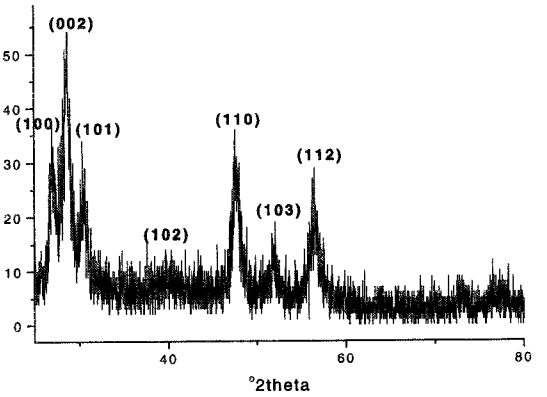

Fig. 1. X-ray diffraction patterns of ZnS:Mn^{2+} nanoparticles.

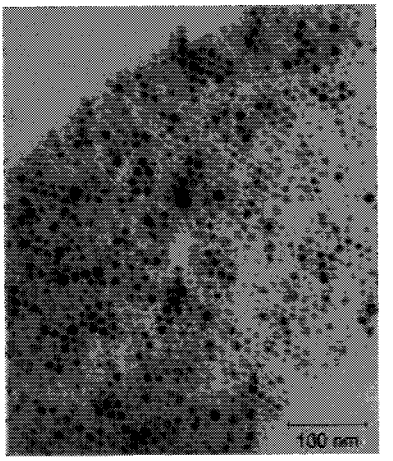

Fig. 2. TEM image of ZnS:Mn^{2+}.

corresponds to that of wurtzite structure of ZnS (JCPDS card no. 75-1534). The nanoparticles of ZnS:Mn^{2+} were depicted in the TEM image of Fig. 2. Since we synthesized violently ZnS:Mn^{2+} by auto-clave method, the particle size was not regular. The diameter was determined as 8 nm $\sim$ 13 nm from the TEM image. The amount of Zn, S, Mn in the ZnS:Mn^{2+} was confirmed by TEM-EDX and the element and atomic percentages were shown in Table 1. The element and atomic percentages mean weight ratio and molar ratio, respectively. The emission spectra of ZnS:Mn^{2+} and LDPE film containing ZnS:Mn^{2+} nanoparticle are shown in Figs. 3 and 4. ZnS:Mn^{2+} nanoparticle and the LDPE films showed an emission band at 575 nm (λ_{exc} = 312 nm). This wavelength belong to the wavelength range of plant's photosynthesis (400 nm $\sim$ 700 nm). When the amount of ZnS:Mn^{2+} nonoparticle was 0.003 g, the emission intensity was the largest.

Table 1. Energy dispersive X-ray data of ZnS:Mn^{2+}.

Element	Element %	Atomic %
S	29.60	46.36
Mn	2.72	1.63
Zn	67.69	52.00
Total	100.00	100.00

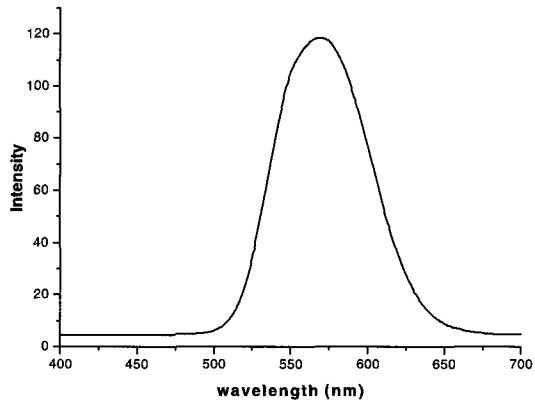

Fig. 3. Photoluminescence emission spectra of ZnS:Mn^{2+} ($\lambda_{ex} = 312$).

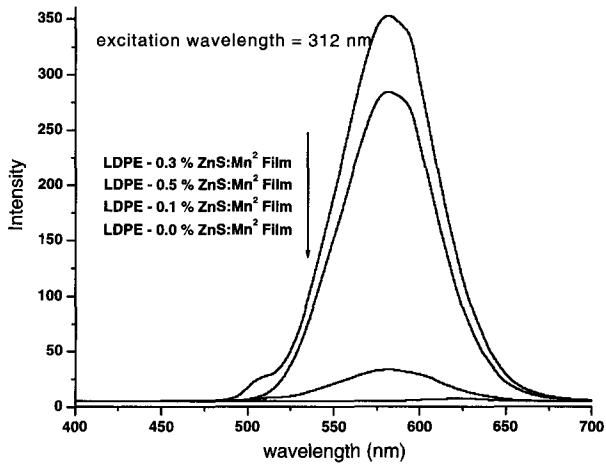

Fig. 4. Photoluminescence emission spectra of LDPE film containing various concentrations of ZnS:Mn^{2+}.

4. Conclusion

ZnS:Mn^{2+} nanoparticles were prepared by thermal annealing using auto-clave. But the size and shape were irregular, since the particles were synthesized rapidly at

high temperature and pressure with auto-clave. ZnS:Mn^{2+} results in the emission band at 500 nm $\sim$ 650 nm. Also LDPE film was emitted at same wavelength range. Because of these luminescence properties, the film will be used as light wavelength modification materials for the utilization of plant growth acceleration.

Acknowledgment

This work was financially supported by The Specific Research and Development Program of The Korean Ministry of Agriculture and Forestry, 2001.

References

1. R. N. Bhargava, D. Gallagher, X. Hong, and A. Nurmikko, *Phys. Rev. Lett.* **72**, 416 (1994).
2. A. A. Bol and A. Meijerink, *J. Phys. Chem. B* **105**, 10197 (2001).
3. C. Jin, J. Yu, L. Sun, K. Dou, S. Hou, J. Zhao, Y. Chen, and S. Huang, *J. Luminescence* **67**, 315 (1996).
4. W. Chen, R. Sammynaiken, and Y. Huang, *J. Appl. Phys.* **88**, 5188 (2000).
5. M. Nyman, K. Jenkins, M. J. Hampden-Smith, T. T. Kodas, and E. N. Duesler, *Chem. Mater.* **10**, 914 (1998).
6. A. A. Koshravi, M. Kundu, B. A. Kuruvilla, G. S. Shekhawat, R. P. Gupta, A. K. Sharma, P. D. Vyas, and S. K. Kulkarni, *Appl. Phys. Lett.* **67**, 2506 (1995).

This page is intentionally left blank

International Journal of Nanoscience, Vol. 1, Nos. 5 & 6 (2002) 501–505

A STUDY ON A NEW SYNTHETIC METHOD OF CdS AND CdSe NANOPARTICLES AND THEIR ORGANIC/INORGANIC NANOCOMPOSITE

JU YOUNG LEE and YOUNG SOO KANG

Department of Chemistry, Pukyong National University
599-1 Nam-gu, Busan, 608-737, Korea

YONG JOO KIM

Department of Applied Chemistry, Hanbat National University
16-1 Yusung-gu, Daejeon, 305-719, Korea

Received 27 November 2002
Revised 24 December 2002

Materials such as CdS and CdSe inorganic nanoparticles have photoluminescence. Sodium oleate has been used as effective stabilizers for the synthesis of CdS and CdSe nanoparticles in water by autoclave method. Photoluminescence of CdS and CdSe with particle size of 5–14 nm showed λ_{max} at 520 nm and 600 nm, respectively, when were excited at 365 nm. These nanoparticles doped into the PVA resulted in the organic/inorganic films (PVA/CdS, CdSe). Photoluminescence, X-ray diffraction and transmission electron microscopy were employed for their characterization.

Keywords: CdS; CdSe nanoparticle; PVA film; photoluminescence.

1. Introduction

The control of particle size and surface structure continue to be of interest in the investigation of semiconductor nanoparticles due to the high surface-to-volume ratio of the nanoparticles, their peculiar structure and optical properties.[1–4] Many synthetic methods, which include arrested precipitation in homogeneous solution and synthesis in confined reaction vessels such as reverse micelles[5] and vesicles,[6] have been developed for the chemical preparation of relatively monodisperse nanoparticles of various semiconductor materials. The synthesis of colloidal inorganic nanocrystals especially the control of their shape, however, is developing and still complicated. A new direction for the synthetic methods and the understanding of the mechanisms on how the size and shape of the nanocrystals are varied, are the key issues in nanochemistry. In this paper, we demonstrate a new method for CdS and CdSe nanoparticles using sodium oleate by thermal treatment using autoclave and the preparation of PVA (polyvinylacetate) films containing these nanoparticles. Sodium oleate has been used as specific stabilizers for the synthesis of CdS and CdSe nanoparticles.

2. Experiment

2.1. *Materials and analytical methods*

Cadmium chloride hemipentahydrate ($CdCl_2 \cdot 5/2H_2O$, Aldrich), sodium oleate ($C_{17}H_{33}COONa$, Junsei), sodium sulfide nonahydrate ($Na_2S \cdot 9H_2O$, $98^+\%$, Aldrich) and PVA pellets were used in their commercial form. NaHSe powders were prepared from the reaction between selenium and sodium borohydride in water. Acetone and iso-octane were all of the highest quality commercially available. Distilled water was passed through a six-cartridge Barnstead Nanopure II purification train consisting of Macropure treatment. Photoluminescence spectra were recorded on a Perkin-Elmer, LS50B. Transmission electron microscopy (TEM) images were obtained by using a Jeol, JEM-2010. X-ray powder diffraction (XRD) spectra were obtained with a Philps, X'Pert-MPD system.

2.2. *Synthesis of CdS and CdSe nanoparticle and PVA/CdS, CdSe composite films*

The synthesis of CdS and CdSe nanoparticles was achieved by reacting Na_2S and NaHSe in an aqueous solution. All materials were of the highest quality commercially available. In a typical procedure, 80 mL of mixed solution containing 0.125 M sodium oleate and water was prepared and stirred for 20 min. Then, a 5.0 mL of 6.25×10^{-2} M $CdCl_2$ was added. The resulting solution was stirred for 30 min and 6.25×10^{-2} M $Na_2S \cdot H_2O$ was added and followed by stirring for 2 h to form yellow organic solution. This solution was put into a autoclave of 100 mL capacity and was maintained at 300°C for 2 h and air-cooled to room temperature. Precipitation occurs to form nanoparticles of CdS. Then, the precipitates were washed with acetone and were filtered to remove the residues of impurities. The bright yellow product was dried in room temperature. CdSe nanoparticles were synthesized with the same method.

A 16 g of PVA pellet was dissolved in 50 ml of acetone to make PVA solution. As a same method, a 1×10^{-3} g of CdS nanoparticle was added to 1 ml of acetone. A 4.0 ml of PVA solution was mixed with 0.09 wt% of resulting CdS dissolved in acetone and loaded into a round container. In accordance with the concentration, a 0.87 and 2.62 wt% of CdS dissolved in acetone was added in PVA solution. The mixture was left for 24 h at room temperature. Finally, the transparent PVA film was obtained.

3. Result and Discussions

Figure 1 presents the absorption and photoluminescence (PL) spectra of CdS and CdSe nanoparticles prepared in aqueous solutions. Sodium oleate has been used as effective stabilizer for the synthesis of CdS and CdSe nanoparticles. The absorption spectra in Fig. 1 display an absorption range from 300 to 520 nm for CdS nanoparticles. CdSe nanoparticles had no peculiar characteristics, but it showed

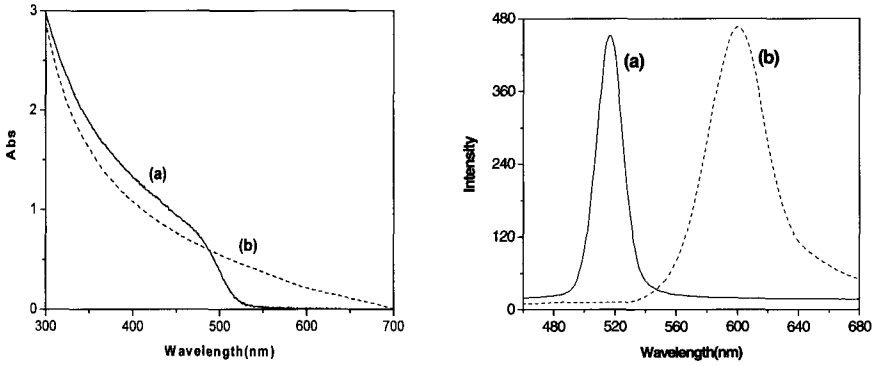

Fig. 1. (Left) Absorption and (right) photoluminescence spectra for the synthesized (a) CdS and (b) CdSe nanoparticles.

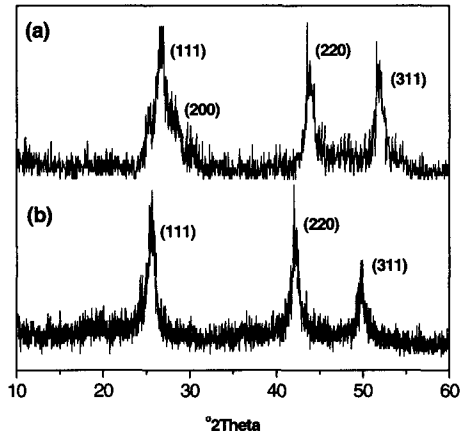

Fig. 2. X-ray powder diffraction (XRD) patterns of (a) CdS and (b) CdSe nanoparticles. These nanoparticles were capped with sodium oleate.

an absorption of general range. The photoluminescence spectrum (PL) was measured at room temperature using a 365 nm excitation. The PL spectrum in Fig. 1 shows a narrow emission band at 520 and 600 nm. The CdS nanoparticles stabilized with sodium oleate showed PL emission at shorter wavelengths corresponding to somewhat smaller size of particles. Thus, the use of sodium oleate as stabilizing agent allows the synthesis of highly crystalline CdS nanoparticles showing strong band-edge of PL. Figure 2 shows the X-ray powder diffraction (XRD) pattern of CdS and CdSe nanoparticles. All the peaks in Fig. 2 were indexed as the cubic structure of CdS, which are close to the reported data for CdS (JCPDS Card File No. 80-0019). The CdSe diffraction patterns exhibit peak positions correspond to their cubic structures (JCPDS Card File No. 19-0191).

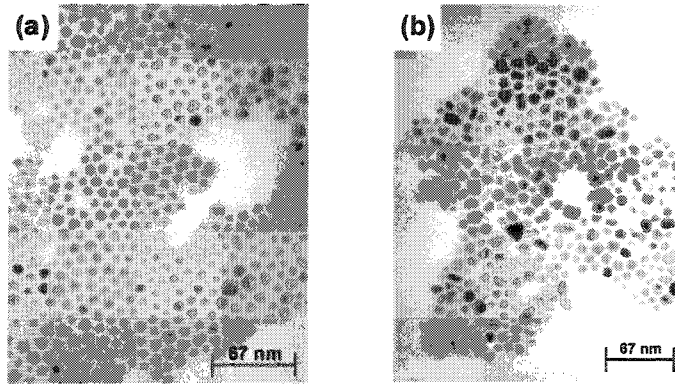

Fig. 3. Transmission electron microscopy (TEM) images of (a) CdS and (b) CdSe nanoparticles.

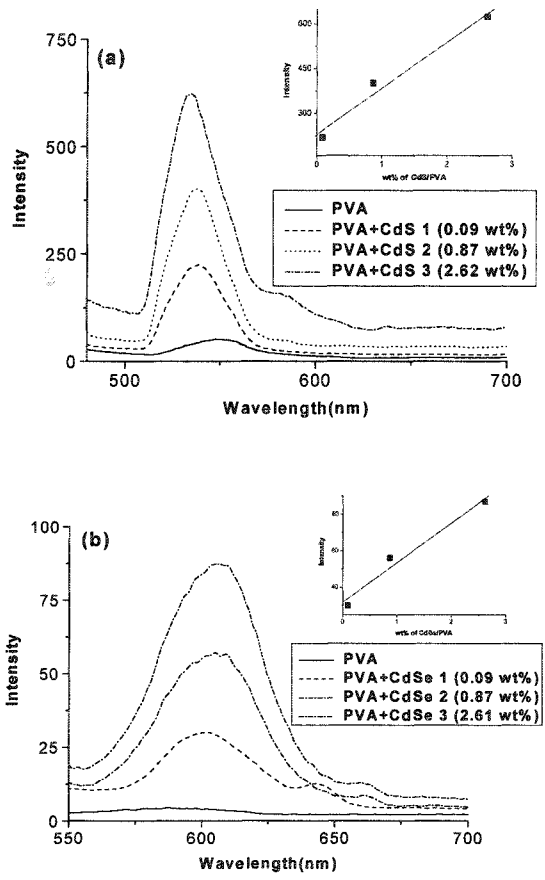

Fig. 4. PL spectra of PVA films containing (a) CdS and (b) CdSe nanoparticles. The inset shows the PL intensity according to the different concentration on the added nanoparticles.

TEM was employed to obtain direct information on the size and structure of the produced nanoparticles. The TEM images in Fig. 3 shows the CdS and CdSe nanoparticles with diameters of 5–12 nm and 7–14 nm, respectively. The particle shape is spherical and triangle. The triangle shape is made by synthetic conditions of high temperature and pressure. Figure 4 shows the PL spectra of PVA films containing CdS and CdSe nanoparticles according to different concentrations. The PL spectra are consistent with that of the synthesized CdS and CdSe nanoparticles. The PL intensity was increased with concentration on the added nanoparticles. This is shown in inset of Fig. 4. But the PL intensity was not proportional to the exact amount of added CdS and CdSe. This is due to the sintering effect of emitted light by the neighboring nanoparticles in the polymer matrices. This is also partly because the added CdS or CdSe nanoparticles were not evenly dispersed in PVA films. These PVA films absorb the ultraviolet region wavelength light (<400 nm) and emit the visible wavelength light.

Acknowledgments

This work was financially supported by The Specific Research and Development Program of The Korean Ministry of Agriculture and Forestry, 2001. Yong Joo Kim acknowledge the financial support from Korea Science and Engineering Foundation through the Advanced Materials Research Center for Better Environment at Hanbat National University.

References

1. H. Weller, *Adv. Mater.* **5**, 88 (1993).
2. L. L. Beecroft and C. K. Ober, *Chem. Mater.* **9**, 1302 (1997).
3. E. Hao, H. Sun, Z. Zou, J. Liu, B. Yang, and J. Shen, *Chem. Mater.* **11**, 3096 (1999).
4. Y. Wang and N. Herron, *J. Phys. Chem.* **95**, 526 (1991).
5. M. P. Pileni, *J. Phys. Chem.* **97**, 6961 (1993); M. P. Pileni, *Langmuir* **13**, 3266 (1997).
6. B. A. Korgel and H. G. Monbouquette, *J. Phys. Chem.* **100**, 346 (1996).
7. T. Arai, T. Orii, H. Ichikawa, S. Onari, and K. Matsuishi, *Mater. Sci. Eng. A* **217**, 159 (1996).
8. R. Garuthara and G. Levine, *J. Appl. Phys.* **80**, 401 (1996).

This page is intentionally left blank

International Journal of Nanoscience, Vol. 1, Nos. 5 & 6 (2002) 507–513

SYNTHESIS OF METAL AND METAL OXIDE NANOPARTICLES IN THE NANOSPACE OF ULTRATHIN TiO_2-GEL FILMS: ROLE OF THE ION-EXCHANGE SITE

JUNHUI HE, IZUMI ICHINOSE, SHIGENORI FUJIKAWA, and TOYOKI KUNITAKE*

Frontier Research System, The Institute of Physical and Chemical Research (RIKEN)
2-1 Hirosawa, Wako, Saitama 351-0198, Japan
**kunitake@ruby.ocn.ne.jp*

Received 6 January 2003
Revised 8 January 2003

In this work, we showed that metal salts were easily deposited as aggregates (e.g., ultrathin planar microcrystals) on the surface of TiO_2-gel films in the absence of ion-exchange sites. In contrast, metal ions were efficiently incorporated into ultrathin TiO_2-gel films, when ion-exchange sites were created using $Mg(O\text{-}Et)_2$ as template. A variety of metal ions, including those of main group, transition, and lanthanide elements were successfully doped into TiO_2 thin films by the current approach. Probable distribution of the ion-exchange site in the film interior was discussed.

Keywords: Nanoparticles; ion-exchange; template synthesis; thin film; metal–ion doping.

1. Introduction

Preparation of thin films that contain nanoparticles of semiconductors and metals is currently attracting much attention due to their promises in photonic, electronic, magnetic and chemical applications.[1–4] Recently we developed a new ion-exchange method for the incorporation of metal ions into metal oxide thin films.[5] Such ion-exchangeable ultrathin films can be fabricated on flat surfaces as well as on curved substrates. Their thicknesses can be easily controlled with the molecular precision. By combining this technique with the physical and chemical reductions, we succeeded in the preparation of noble metal nanoparticles in TiO_2 thin films.[6] It was also found that metal oxide nanoparticles were formed in TiO_2 thin films by oxygen plasma treatment of the corresponding metal nanoparticles. Repeated transformation in the nanospace of thin film by alternate H_2 and O_2 plasma treatments resulted in monodisperse metal and metal oxide nanoparticles.[7] The ion-exchange site is indispensable for the introduction of metal ions. However, its nature is still not clear. In this paper, we discuss the role and nature of the ion-exchange site created in the thin film.

*Corresponding author.

2. Results and Discussion

2.1. *Direct adsorption of metal salts on TiO_2-gel films without ion-exchange sites*

Efficient incorporation of metal ions cannot be achieved without formation of the ion-exchange site upon removal of Mg ions. The ultrathin film of metal oxides is amorphous and may contain cavities that can incorporate metal ions. Thus, it is essential to confirm that metal ions are not introduced in the interior of the thin film without the ion-exchange site.

Ultrathin TiO_2-gel films without ion-exchange sites were fabricated by the surface sol–gel process. Quartz crystal microbalance (QCM, 9 MHz, USI System, Fukuoka, Japan) was used to monitor the film assembly. In a typical procedure, a gold coated QCM electrode modified with mercaptoethanol was immersed in a titanium tetra-*n*-butoxide (Ti(O-*n*Bu)$_4$) solution (100 mM) in toluene for 10 min. After rinsed in toluene, the film was dried by flushing with N_2 gas. The electrode was then attached to a QCM frequency counter. The frequency was recorded when it reached a steady value. As shown in Fig. 1, a linear frequency shift was achieved for the fabrication of TiO_2-gel film. The film thickness (d) adsorbed on one side of the electrode was estimated to be 8.5 nm. Such ultrathin films have smooth surfaces as confirmed by scanning electron microscope (SEM).[8]

The as-assembled thin film was treated with aqueous HCl (pH 4) and aqueous NaOH (pH 10). ATR IR results showed a very small, broad absorption around 3400 cm^{-1}, indicating that there were not many hydroxyl groups left in the as-assembled TiO_2 film. Significant changes were not recorded for the above absorption after acid (pH 4)/alkali (pH 10) treatments. In the same vein, these treatments did not result in significant QCM frequency changes (totally 14 Hz). These results

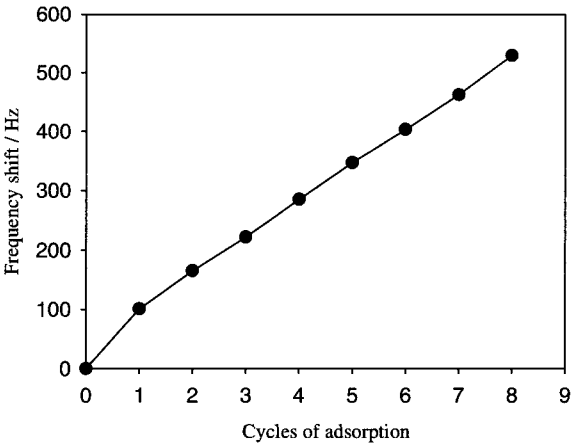

Fig. 1. Assembly of TiO_2-gel film (Ti(O-*n*Bu)$_4$/100 mM, solvent/2-ethoxyethanol, r.t., rinsing solvent/toluene).

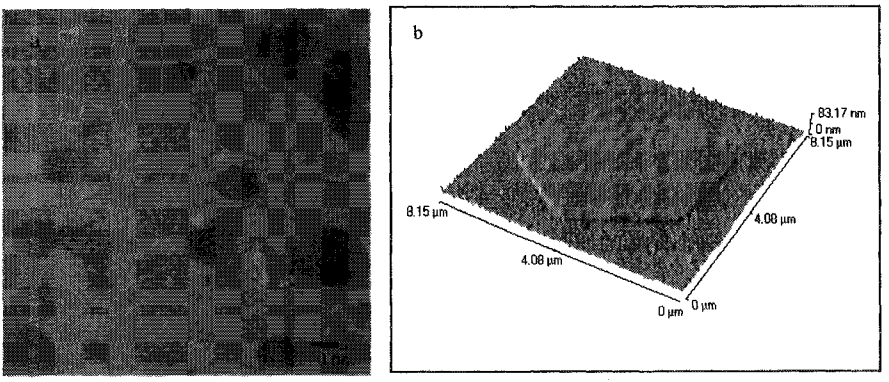

Fig. 2. (a) SEM and (b) AFM images of $LiNO_3$ deposited on TiO_2 thin film without ion-exchange sites. $LiNO_3$/10 mM, immersion time/4 h. SEM images were obtained on a Hitachi S-900 scanning electron microscope after coating the sample with 2 nm Pt by a Hitachi E-1030 ion-coater. AFM was carried out by contact mode on Explorer (TopoMetrix Corporation, USA).

suggest that the acid/alkali treatments did not significantly affect the structure of the thin film.

We then conducted direct adsorption (i.e., impregnation) of metal salts in this TiO_2 thin film. Immersion (20 min, room temperature) of this TiO_2 film in aqueous $LiNO_3$, KNO_3, $Ca(NO_3)_2$, $Ba(NO_3)_2$, $La(NO_3)_3$ and $Gd(NO_3)_3$ (10 mM each) gave rise to QCM frequency decreases of 88, 187, 144, 389, 1452 and 1301 Hz, respectively, indicating that substantial amounts of metal salts were adsorbed onto the TiO_2 film. In addition, deposition of metal salts was observed in these cases on the micrometer scale or even by naked eye, e.g., SEM observations (Fig. 2(a)) show in the case of $LiNO_3$, planar hexagonal structures were formed on film surface. The size of these structures ranges from several hundred nanometers to several microns. Atomic force microscopy (AFM) further reveals that they are actually ultrathin planar hexagonal layers with thickness of less than 30 nm (Fig. 2(b)). Lithium nitrate is known to be colorless and have a hexagonal crystalline form.[9] The nature of smooth surface of the TiO_2-gel film might allow for two-dimensional growth of $LiNO_3$ crystals on its surface, resulting in the observed ultrathin planar hexagonal crystalline layer. Similar surface crystallization is conceivable for other metal nitrates, since the observed frequency changes of individual salts are roughly proportional to their molecular weights. Apparently, the major portions of the adsorbed metal salts remain on the film surface without incorporation into the film interior. It is difficult to avoid aggregation of metal salts during the conventional impregnation.[10] The same phenomenon was observed in our experiments.

2.2. *Incorporation of metal ions in TiO_2-gel films with ion-exchange sites*

Ion-exchange sites are produced in TiO_2-gel films by the template approach as shown in Scheme 1.[5] Magnesium diethoxide ($Mg(O\text{-}Et)_2$) is used as the template.

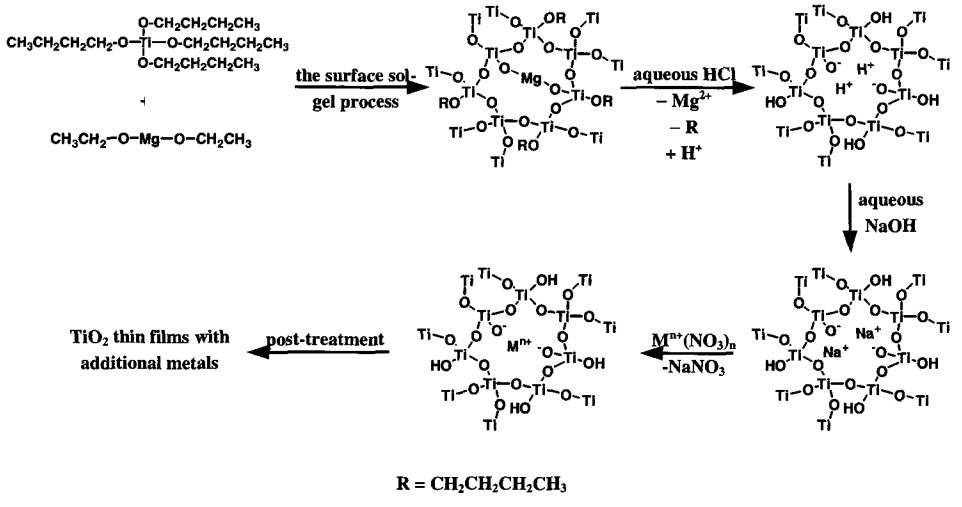

Scheme 1.

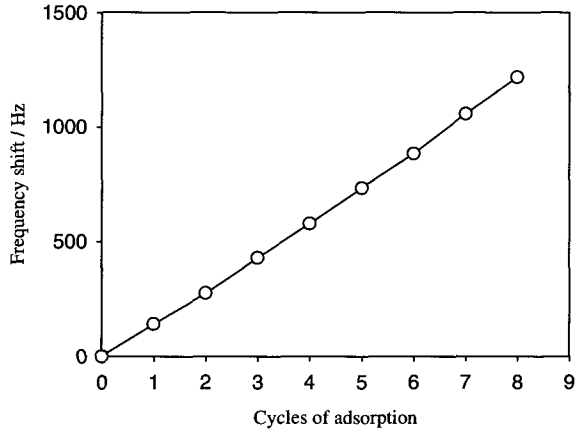

Fig. 3. Assembly of TiO_2-gel film with $Mg(O\text{-}Et)_2$ as template, $Ti(O\text{-}n Bu)_4$/100 mM, $Mg(O\text{-}Et)_2$/10 mM, solvent/2-ethoxyethanol, r.t., rinsing solvent/toluene.

Thus, ion-exchangeable thin films were assembled on substrate (QCM electrode or quartz plate) by the surface sol–gel process by dipping in a precursor solution of $Ti(O\text{-}n Bu)_4$ (100 mM) and $Mg(O\text{-}Et)_2$ (10 mM). Other conditions for the film assembly were identical to those used for the fabrication of TiO_2-gel films without ion-exchange sites (Fig. 1). Figure 3 shows QCM frequency shifts during the film assembly. Similar to the results in Fig. 1, frequency shifts also increase linearly with adsorption cycles in the presence of $Mg(O\text{-}Et)_2$. Each adsorption, however, is enhanced, as a result of the higher reactivity of $Mg(O\text{-}Et)_2$, resulting in a larger film thickness (20 nm).

After this film was treated with aqueous HCl (pH 4) and aqueous NaOH (pH 10), the template Mg^{2+} ions were replaced by Na^+ ions (Scheme 1), as confirmed by QCM frequency shifts and X-ray photoelectron spectroscopy (XPS).[5] The Na^+ ion was readily replaced by other ions, indicating that ion-exchange sites were created in the TiO_2-gel film. The effectiveness of the ion-exchange site was supported by SEM observation, and ATR IR and XPS measurements. For example, doping of Ba^{2+} for 4, 10, 25 and 50 h did not result in any crystal growth of the metal salt on the film surface (SEM observation), unlike the bare TiO_2 film (without ion-exchange sites), where metal salts tended to crystallize on its smooth surface. After removing the template Mg^{2+} ions, nanopores (less than 2 nm, TEM observation) were formed in the film, where the deposition of metal salts by crystallization is not possible. IR peaks (1390 cm^{-1}, 830 cm^{-1}, 720 cm^{-1}) and XPS peak (407 eV) characteristic of NO_3^- were not found in the doped TiO_2 thin films, indicating that metal ions alone were incorporated into the interior of the thin film without adsorption of metal nitrates themselves. All these results support the existence of ion-exchange site in the interior of metal oxide films.

A variety of metal ions were tested for ion exchange in TiO_2-gel film. The XPS results (on quartz substrate) were shown in Table 1. In the as-prepared film, the Mg/Ti ratio was estimated to be 1.2 from their XPS peak areas. All the tested metal ions that represented main group, transition, and lanthanide metal ions, were successfully incorporated homogeneously into the TiO_2 matrix. Amounts of metal ions introduced (M/Ti ratios) are varied under identical conditions. From

Table 1. Atomic ratios of doped metal ions to Ti as determined by XPS peak intensities.[a,b,c]

M	Binding energy (eV)	Assignment	M/Ti	M/Mg
Gd	143	4d	0.3–0.7	0.3–0.7
Pd	337	$3d_{5/2}$	0.14	0.12
Cr	578	$2p_{3/2}$	0.20	0.17
Mn	642	$2p_{3/2}$	0.26	0.22
Cd	406	$3d_{5/2}$	0.33	0.28
Co	781	$2p_{3/2}$	1.2	1.0
Ba	781	$3d_{5/2}$	1.4	1.2
Fe	711	$2p_{3/2}$	2.2	1.9
Ag	369	$3d_{5/2}$	3.6	3.1

[a]The concentration of aqueous metal–ion nitrate was 10 mM and the immersion time was 4 h.
[b]The Mg/Ti ratio in the as-prepared thin film was 1.2.
[c]XPS measurements were carried out on ESCALAB 250 (VG) using Al Ka (1486.6 eV) radiation.

the M/Ti and Mg/Ti values, the metal ion incorporated per ion-exchange site was estimated and expressed as M/Mg in Table 1. The Gd^{3+} peak overlaps partially with the Si peak, making it difficult to obtain accurate data. Its M/Ti and M/Mg ratios were estimated to be in the range of $0.3 \sim 0.7$. Pd^{2+}, Cr^{3+}, Mn^{2+}, and Cd^{2+} fall in the M/Ti ranges of $0.1 \sim 0.4$ and M/Mg of $0.1 \sim 0.3$, indicating that the ion-exchange sites are not fully occupied by these metal ions. Co^{2+} and Ba^{2+} have M/Ti values of 1–1.5 and M/Mg values of ca. 1, showing essentially stoichiometric ion-exchange. In the case of Fe^{3+}, the M/Ti and M/Mg ratios reach 2.2 and 1.9, respectively, three times as large as the charge-based exchange. It is known that Fe^{3+} can form ol-complexes in aqueous solutions. The high ratios might originate from the olation effect. Ag^{+} also gives a much larger doping efficiency (M/Ti = 3.6, M/Mg = 3.1) than other mono-valent metal ions (Li^{+}, K^{+}). This may be caused by the photoreduction of Ag^{+} ions.

It was noted above that the amount of Mg ion is 1.2 times larger than the matrix Ti atom. If the Mg site is uniformly distributed in the matrix, Mg and Ti atoms virtually alternate in the metal oxide network. Removal of Mg ion from such network would destroy the matrix network completely by fragmentation. As the TiO_2 film retains its integrity during this process, Mg ion must not distribute evenly in the matrix. Instead, Mg sites would form clusters in the continuous matrix of titania, and create segregated ion-exchange sites.

3. Concluding Remarks

It is clear from the above discussion that the presence of ion-exchange site in the interior of the ultrathin film is essential for efficient incorporation of a number of metal ions. Without the ion-exchange site, metal salts readily crystallize on the smooth surface of TiO_2-gel films. Unfortunately, the nature of the ion-exchange site remains to be elucidated. The Mg/Ti atomic ratio in the precursor film suggests that the ion-exchange site cannot be distributed evenly in the matrix. We separately reported that the noble metal ions introduced were easily reduced to metallic nanoparticles under mild conditions by H_2 plasma and chemical reducing agents.[6] The metallic nanoparticle is formed by agglomeration of the reduced metal atom, and the agglomeration process should be strongly affected by the nature of the ion-exchange site. If the ion-exchange site is clustered, the nanoparticle core would be created efficiently to determine the size and its distribution of the resulting metallic nanoparticle. Assuming that the metal atom travels in the metal oxide medium to form metal nanoparticles, we can estimate the traveling distance from the content of the ion-exchanged metal ion and the size of the nanoparticle formed. In the case of Ag/Ti = 0.45 and $d = 4.5$ nm (the mean diameter of silver particles obtained by H_2 plasma reduction[6]), the largest traveling distance of silver atoms is estimated to be ca. 9 nm, without assuming extensive clustering of the ion-exchange site. Similarly, when Ag/Ti = 0.81 and $d = 8.6$ nm, this distance is ca. 13 nm. Naturally, the size of the nanoparticle depends on the density of the silver atoms formed,

i.e., on the density of ion-exchange sites in the thin film. This is consistent with our previous electron microscopic observation in the *in-situ* synthesis of nanoparticles in thin films.[6]

Acknowledgment

J. He is grateful to the Japan Science and Technology Corporation (JST) for a STA fellowship.

References

1. G. Schmid, *Chem. Rev.* **92**, 1709 (1992).
2. G. Schmid and G. L. Hornyak, *Curr. Opinion Solid State Mater. Sci.* **2**, 204 (1997).
3. M. P. Pileni, *Metal Nanoparticles: Synthesis, Characterization, and Applications*, eds. D. L. Feldheim and C. A. Foss, Jr. (Marcel Dekker, New York, 2001), p. 207.
4. M. P. Pileni, *Adv. Funct. Mater.* **11**, 323 (2001).
5. J. He, I. Ichinose, S. Fujikawa, T. Kunitake, and A. Nakao, *Chem. Mater.* **14**, 3493 (2002).
6. J. He, I. Ichinose, T. Kunitake, and A. Nakao, *Langmuir* **18**, 10005 (2002).
7. J. He, I. Ichinose, S. Fujikawa, T. Kunitake, and A. Nakao, *Chem. Comm.*, 1910 (2002).
8. I. Ichinose, H. Senzu, and T. Kunitake, *Chemistry Mater.* **9**, 1296 (1997).
9. D. R. Lide (ed.), *CRC Handbook of Chemistry and Physics*, 81st edition (CRC Press LLC, Boca Raton, 2000), p. 4–69.
10. K. Nagashima, H. Kokusen, N. Ueno, A. Matsuyoshi, T. Kosaka, M. Hasegawa, T. Hoshi, K. Ebitani, K. Kaneda, H. Aritani, and S. Hasegawa, *Chem. Lett.*, 264 (2000).

This page is intentionally left blank

International Journal of Nanoscience, Vol. 1, Nos. 5 & 6 (2002) 515–519

PROPERTIES OF ZnO NANOTETRAPODS

JUNYONG KANG* and FUCHUN XU
Pen-Tung Sah MEMS Research Center and Department of Physics
Xiamen University, Xiamen 361005, China
**jykang@xmu.edu.cn*

XIANHUA ZHANG and LANSUN ZHENG
Department of Chemistry, Xiamen University, Xiamen 361005, China

TAKASHI SEKIGUCHI
National Institute for Materials Science, Tsukuba 305-0047, Japan

SHIN TSUNEKAWA, SHUN ITOH, and ATSUO KASUYA
Tohoku University, Sendai 980-8577, Japan

Received 27 November 2002
Revised 20 December 2002

ZnO nanotetrapods were synthesized by microwave plasma. The nanotetrapod structures were imaged to be straight with diameters in the range of 10 to 25 nm and lengths up to 160 nm by transmission electron microscopes (TEM). The dark field images and lattice fringes of high resolution TEM show that the crystal orientation or structure of the core is different from that of the legs. The Auger electron peak of Zn shifts more distinctly to lower energy in the legs, which indicates the degree difference of bond ionicity between the core and leg. Cathodoluminescence spectrum of a single ZnO nanotetrapod is characterized by a stronger ultraviolet emission without broad emission bands in its lower energy side. This result further suggests that ZnO nanotetrapods are free from defects.

Keywords: ZnO; property; nanotetrapods.

1. Introduction

Nanoscale science and technology have attracted great attention since the novel properties become dominant for well-known materials as their sizes reduced to some critical dimension. These properties frequently originate in lattice distortions, structure transformations, etc.[1] The variations of size and structure of nanocrystals lead to the change in their electronic structures. Very recently, nanoscale materials with different electronic structures were utilized in fabricating nanoscale junctions.[2]

*Corresponding author.

A large part of these works has been focused on one-dimensional nanoscale p–n junction and/or heterojunction for applications in nanoscale electronic and/or optoelectronic devices. ZnO is one of the potential materials for optoelectronic devices. The lazing action of ZnO has been demonstrated in disordered particles and thin films. The exciton binding energy of ZnO is about 60 meV, which is significantly larger than the thermal energy of 26 meV at room temperature.[3] Although the crystal structure of ZnO is known to be the wurtzite type only, the smoky ZnO particles produced by heating of zinc in an oxygen atmosphere have a tetrapod shape with four legs. The orientation relationship of the legs touches off a debate whether the zinc-blende type structure exists in ZnO or not.[4]

2. Experimental Details

ZnO nanotetrapods were synthesized by microwave plasma. Zinc powder in a quartz boat was set at the center of a horizontal quartz tube. Pure Ar and O_2 gases flow into the tube and an 800 W 2.45 kMHz microwave source was coupled along square rectangle wave-conduct pipe to the tube center for generating stable plasma. A tube furnace was used to obtain necessary temperature zone. The as-prepared particles were collected on the inner-wall at the downstream end of the tube after 30 min reaction. The percentage of tetrapods depends on growth temperature and gas flows. High yields were obtained with a temperature of 450°C inside the quartz tube and Ar and O_2 flows of 30 and 20 sccm, respectively. The nanotetrapod structures were imaged by transmission electron microscopes (TEM, JEM-2000EX and -2010F, JEOL). The structure information were also studied by analyzing Auger electron spectra (AES) of Zn in the nanotetrapods by a field emission AES (PHI 670). A thermal field emission scanning electron microscope (TFE-SEM, S4200, Hitachi) with low energy cathodoluminescence (CL) system was employed to detect the selective area luminescence spectrum.[5]

3. Results and Discussion

The nanotetrapod structures were imaged by TEM, as shown in Fig. 1. The as-prepared nanotetrapods consist of four straight legs with nearly uniform diameters

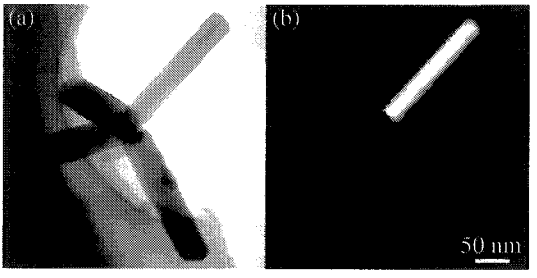

Fig. 1. Typical (a) bright and (b) dark field TEM images.

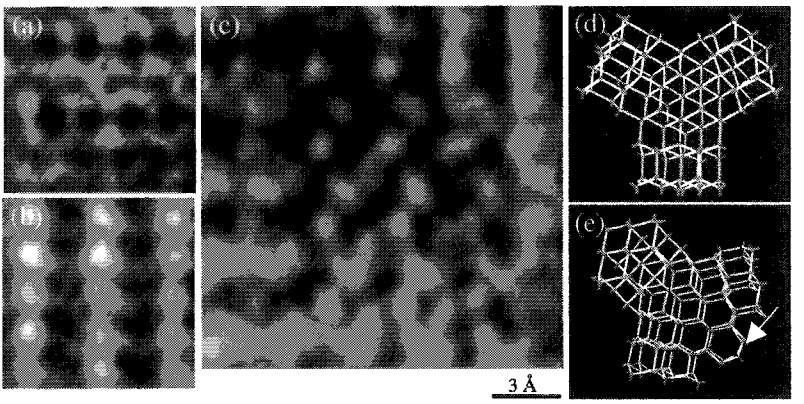

Fig. 2. Typical lattice fringes of (a) core, (b) legs and (c) coalescence between legs observed by HRTEM and their lattice model of (d) between core and legs and (e) between legs.

in range from 10 to 25 nm and lengths up to 160 nm. The dark field images show that both the legs and core were impossible to satisfy a same diffraction condition. This indicates the differences of the crystal structure or orientation between the core and legs.

The lattice structures of the ZnO nanotetrapod were further investigated by the high-resolution TEM (HRTEM). Since the four legs are not in identical orientation, appropriate orientations were selected to obtain better lattice fringes of the core, legs and their boundary in a image, as shown in Fig. 2. The lattice fringes of the core consist of a number of six-fold bright diffraction rings. The lattice fringes of the legs appear to be of parallel bright diffraction lines. The interval of the lines is measured to be 0.512 nm close to the lattice constant c of hexagonal ZnO. The lattice difference between the core and legs leads to the core region appearing as a small triangle at the joint center of three legs. These results also indicate that the crystalline of the core differs from that of the legs. The bright diffraction lines between different legs are mitered by shorter parallel rows of bright dots. The miter joints appear to be discontinuous at some regions. This suggests that the legs be first grow faster in certain crystal directions and then coalescent as laterally grow. On the basis of the above results, we believe that the ZnO nanotetrapod nucleates, grows faster in four crystal directions to form the legs under mentioned conditions and finally coalescent between the legs.

Although the crystal structure of ZnO is wurtzite type, it is impossible to construct only ZnO tetrapod with wurtzite structure. However, the tetrapod is easy to be constructed with the zinc-blende type core connecting to wurtzite type legs, as shown in Fig. 2(d). Since the four wurtzite type legs have different orientations, the bonds for an atom between the legs are on a plane instead of tetrahedral bonds, as marked in Fig. 2(e). The information from primary structure also investigated by selective area AES. The mean kinetic energy of Zn LMM Auger peaks shift from

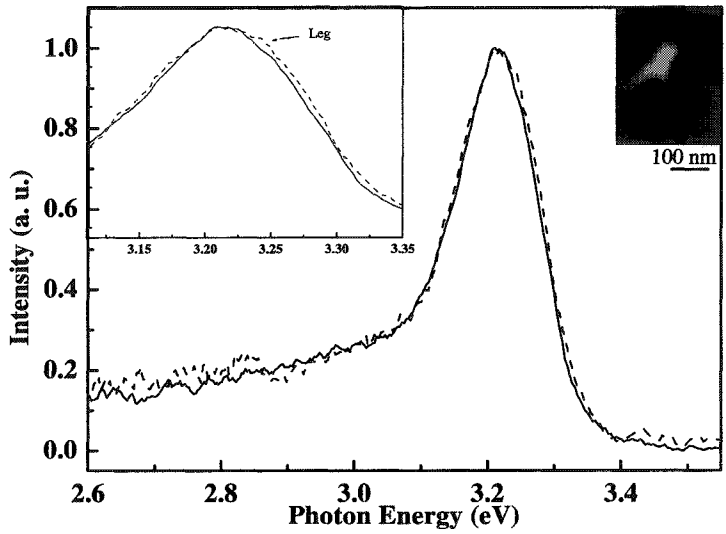

Fig. 3. CL spectra of a nanotetrapod (inset image). The several meV shift is visible in the inset spectra.

997 eV to 994.2 and 992.8 eV in the cores and legs, respectively, which indicates that the many electrons of Zn are held by O due to formation of ionic bond in ZnO and the degree of ionicity in the core is smaller than that in the legs. Generally, the tetrahedral bonds are favorable to form zinc-blende and wurtzite structures with low and high degree of ionicity, respectively. In this point of view, the lattice structure of the core is also believed to be zinc-blende type that enables the wurtzite type ZnO to grow in four equivalence directions.

The selective area CL spectrum of a single ZnO nanotetrapod is characterized by a stronger ultraviolet (UV) emission without broad defect-related emission band in its lower energy side, as shown in Fig. 3. Detailed examination showed that the emission energy in the core is several meV lower than that in the legs. This result can be attributable to the larger exciton binding energy due to the stronger Coulomb interaction in the smaller size of the core.

In conclusions, the ZnO nanotetrapod properties between the core and leg are different. This suggests that the nanotetrapod may be formed by the wurtzite structure legs and zinc-blende type core.

Acknowledgments

This work was partly supported by the Special Funds for Major State Basic Research Projects (No. 001CB610505), National Natural Science Foundation (No. 90206030, 10134030, 69976023), grants from the Ministry of Education, and the Natural Science Foundation of Fujian Province of China (No. A0020001).

References

1. J. Kang, S. Tsunekawa, and A. Kasuya, *Appl. Sur. Sci.* **174**, 306 (2001); S. Tsunekawa, K. Ishikawa, Z.-Q. Li, Y. Kawazoe, and A. Kasuya, *Phys. Rev. Lett.* **85**, 3440 (2000).
2. V. Derycke, R. Martel, J. Appenzeller, and Ph. Avouris, *Nano Lett.* **1**, 453 (2001); M. S. Gudiksen, L. J. Lauhon, J. Wang, D. C. Smith, and C. M. Lieber, *Nature* **415**, 617 (2002).
3. Z. K. Tang, G. K. L. Wong, P. Yu, M. Kawasaki, A. Ohtomo, H. Koinuma, and Y. Segawa, *Appl. Phys. Lett.* **72**, 3270 (1998).
4. M. Shiojiri and C. Kaito, *J. Crystal Growth* **52**, 173 (1981); M. Fujii, H. Iwanaga, M. Ichihara, and S. Takeuchi, *J. Crystal Growth* **128**, 1095 (1993).
5. T. Sekiguchi, *Nanoscale Spectroscopy and Its Application to Semiconductor Research*, ed. Y. Watanabe (Springer, 2002), p. 43.

This page is intentionally left blank

International Journal of Nanoscience, Vol. 1, Nos. 5 & 6 (2002) 521–525

"PROTEOSILICA" A NOVEL NANOCOMPOSITE WITH PEPTIDE ASSEMBLIES IN SILICA NANOSPACE: PHOTOISOMERIZATION OF SPIROPYRAN DOPED IN CHIRAL ENVIRONMENT

KATSUHIKO ARIGA*, TAKUJI AIMIYA†, QINGMIN ZHANG*, AKIHIRO OKABE*, MAKIKO NIKI*, and TAKUZO AIDA*,†

*ERATO Nanospace Project, JST, 2-41 Aomi, Koto-ku, Tokyo 135-0064, Japan
†Department of Chemistry and Biotechnology, Graduate School of Engineering University of Tokyo, 7-3-1 Hongo, Bunkyo-ku, Tokyo 113-8656, Japan

Received 27 November 2002
Revised 7 December 2002

Mesoporous silica composites filling densely peptide assemblies (Proteosilica) were newly synthesized as transparent films. Spiropyran guest was co-doped in the films and photoisomerization between spiropyran form and merocyanine form was repeated by alternate irradiation of visible and UV lights. Circular dichroism (CD) active spectra were observed only for the spiropyran form in the Proteosilica with hexagonal geometry. However, the CD active behavior was absent for the spiropyran in lamellar Proteosilica. Difference in peptide assembling structures would affect chiral sensitivity of the doped spiropyran guest.

Keywords: Mesoporous silica; peptides; photoisomerization.

1. Introduction

Protein architecture can be regarded as the ultimate specimen of nanosized engineering and technology because highly sophisticated functions are performed in their precisely controlled structures. If protein mimics are confined in strong and well-defined nanospaces, both structural strength and functional ability are satisfied. Mesoporous silica having regular pore arrays of molecule-comparable size[1–4] would be the most suitable medium for the protein-mimic immobilization. We have developed recently mesoporous silica filling densely peptide assemblies in its pores. This nanocomposite was named Proteosilica and provides chirally controlled environment like protein interior. In this paper, we describe preparation examples of the Proteosilica films and preliminary results on photoisomerization of spiropyran doped in the films.

2. Experimental

FT-IR spectra, XRD patterns, electronic absorption spectra, and CD spectra were recorded on JASCO FT/IR-660 plus spectrophotometer, Rigaku model

RINT2500PC small and wide-angle X-ray diffractometer, JASCO model V-570 spectrophotometer, and JASCO model J-820 spectrophotometer, respectively.

3. Results and Discussion

3.1. *Design and preparation of Proteosilica*

As shown in Fig. 1, we have developed two types of Proteosilica. Type I Proteosilica was obtained by conventional sol–gel process using peptide-carrying surfactants as templates. Structural limitations in nanosized pores forced the peptides to align in a parallel β-sheet type motif. Type II Proteosilica has pore structures with peptide segments. Sol–gel synthesis using surfactants carrying both alkoxysilane and peptide groups provided mesoporous silica with the covalently attached surfactants. Alkyl chains in the surfactants were removed selectively by acid catalyzed hydrolysis, resulting in porous mesostructured material. In this paper, we concentrate on Type I Proteosilica, and the chiral environment of the pore interior was evaluated by photoisomerization of spiropyran guest **1** (Fig. 2).

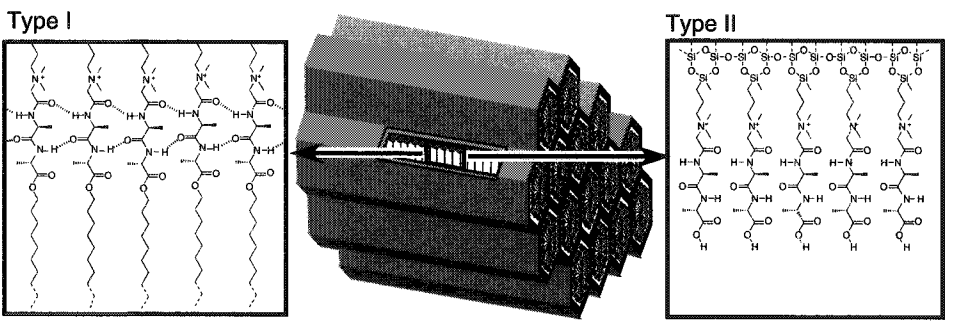

Fig. 1. Two types of Proteosilica.

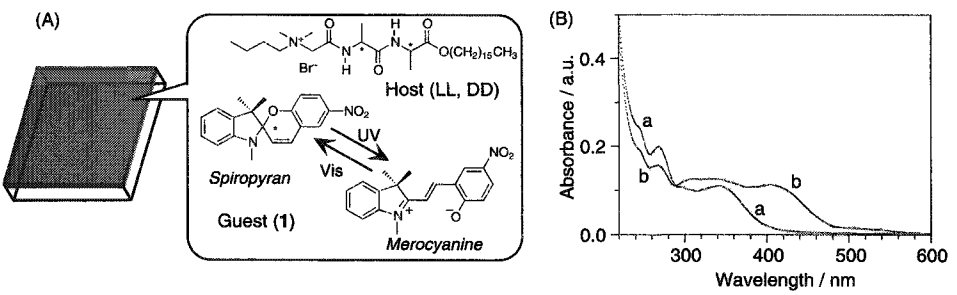

Fig. 2. (A) Formulae of peptide surfactant (LL, DD) and spiropyran guest **1**. (B) Electronic absorption spectra of hexagonal LL film containing 5 mol% of **1**: (a) in spiropyran form and (b) merocyanine form.

Alanylalanine-type surfactants, named LL and DD referred to chirality of the peptide moiety, were used as the host peptides. A mixed solution containing 0.0053 g of *conc*-HCl, 0.204 g of H_2O, 1.684 g of MeOH, and 1.00 g of tetramethyl orthosilicate (TMOS) was stirred for 10 min at room temperature. To this sol–gel solution (0.434 g), 0.1 mmol of surfactant was added and the mixture was stirred for 20 min. The spin-coated films can be obtained from this solution (final mixing molar ratio: surfactant/H_2O/HCl/TMOS/MeOH = 0.1/1.7/0.0076/1/8). Guest **1** was co-doped with the surfactant at various mixing ratios.

XRD evaluation of the prepared films revealed that the peptide-surfactants (LL and DD) provided hexagonal mesoporous structure even with 5 mol% content of **1**, while a conventional cetyltrimethylammonium bromide (CTAB) template did not induce any regular structures under the same condition. The d_{100} peak of LL-silica shifted from 4.20 to 4.50 nm upon co-doping of 5 mol% **1** but the peak sharpness remained unchanged. The corresponding peak was observed even after calcination treatment at 450°C, implying mesoporous silica with hexagonal geometry was formed.

The silica source was changed to tetraethyl orthosilicate (TEOS) and allowed us to prepare lamellar-structured composites with repeating distance of 4.55 nm (final mixing molar ratio: surfactant/H_2O/HCl/TEOS/EtOH = 0.2/4.1/0.04/1/34.8). XRD peaks corresponding to the regular structure disappeared after the calcination treatment. This fact confirms the formation of the lamellar phase.

3.2. *Photoisomerization of spiropyran in Proteosilica*

Next, photoisomerization behaviors of **1** doped in the transparent Proteosilica films were investigated spectroscopically. The acidic condition of sol–gel reaction induced isomerization of **1** into a merocyanine form just after the spin-coating process. Irradiation of a visible light (420 nm) closed the structure to result in a spiropyran form. Isomerization of **1** into the spiropyran form and the merocyanine form can be repeated upon alternate irradiation of the visible light and UV light (280 nm) to the films, respectively (Fig. 2(B)).

Circular dichroism (CD) spectra of the hexagonal LL films containing 5 mol% of **1** were measured (Fig. 3(A)). Only negligible CD signals originated from guest **1** were observed for the film containing the merocyanine form, implying that induced CD of the nonchiral merocyanine was not significant even in the chiral peptide environment. In contrast, the film with **1** in spiropyran form showed clear CD activity in the region from 250 nm to 400 nm, where the host surfactant does not have any absorbance. Alternate irradiation with the UV light and the visible light induced repeated changes in the CD spectra with a small degradation in the intensity. In addition, a complete mirror image of the CD spectra was obtained when the DD was used as the host surfactant. The latter fact confirmed that the CD signals from the guest were driven by the chiral environment of the surrounding host. The probable origins of the observed results would be from chiral-selective isomerization and/or

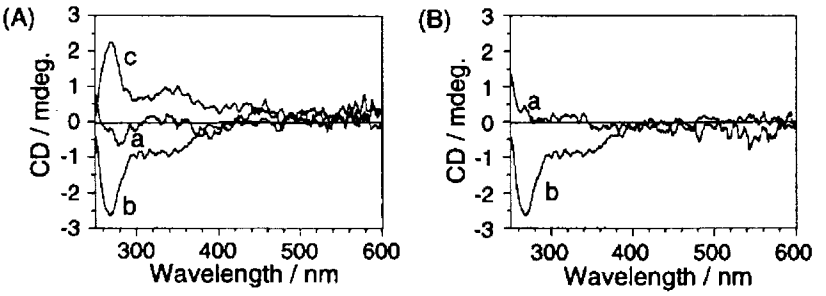

Fig. 3. CD spectra of Proteosilica film containing 5 mol% of **1**. (A) Effect of film chirality: (a) merocyanine **1** in hexagonal LL-film; (b) spiropyran **1** in hexagonal LL-film; and (c) spiropyran **1** in hexagonal DD-film. (B) Effect of film structure: (a) spiropyran **1** in lamellar LL-film and (b) spiropyran **1** in hexagonal LL-film.

induced CD signal. The detailed analyses are now under investigation. Another important factor, peptide sequence effect, is also examined currently.

Interestingly, the above-mentioned CD activity was completely absent when the film was in lamellar phase (Fig. 3(B)). This means that the chiral influence of the host on the guest depends significantly on the type of the mesostructure. The peptide assembling structures were investigated by FT-IR. Proteosilica with hexagonal structure (LL and 5 mol% of **1**) showed broad peak of amide I band [ν(C=O)] at 1667 cm^{-1} with a tiny contribution of a peak at 1645 cm^{-1}, indicating that most of the carbonyl groups are weakly bonded. The guest might be incorporated into the weak bonded peptide region and can sense chiral environment provided by the peptide-surfactant. In contrast, a quite strong peak at 1644 cm^{-1} was observed for the lamellar silica composite for the corresponding composition. The latter fact suggests that the alanylalanine segments self-assembled through hydrogen bonding and the guest **1** might be excluded from the chiral peptide region. The lack of curvature of polar region in the lamellar phase would promote self-hydrogen bonding between the peptide molecules.

4. Conclusion

Proteosilica films have macroscopically transparent appearance and microscopically protein-like environment. As demonstrated above, the films work as a nice medium for controlled molecular conversion. Therefore, they would have high potentials for applications as photonic nanodevices.

Acknowledgments

We thank Drs. Takanori Fukushima and Tetsuro Yuzawa for helpful discussions on photoisomerization, and Dr. Neale McAlpine for helpful English correction.

References

1. T. Yanagisawa, T. Shimizu, K. Kuroda, and C. Kato, *Bull. Chem. Soc. Jpn.* **63**, 988 (1990).
2. C. T. Kresge, M. E. Leonowicz, W. J. Roth, J. C. Vartuli, and J. S. Beck, *Nature* **359**, 710 (1992).
3. M. E. Davis, *Nature* **417**, 813 (2002).
4. A. Okabe, T. Fukushima, K. Ariga, and T. Aida, *Angew. Chem. Int. Ed.* **41**, 3414 (2002).

This page is intentionally left blank

International Journal of Nanoscience, Vol. 1, Nos. 5 & 6 (2002) 527–531

PREPARATION AND PROPERTIES OF AlPdRe ICOSAHEDRAL QUASICRYSTALLINE THIN FILMS BY MOLECULAR BEAM EPITAXY

KAZUHIRO KIRIHARA*, KENJI KAWAGUCHI, and NAOTO KOSHIZAKI

Nanoarchitechtonics Research Center
National Institute of Advanced Industrial Science and Technology
Central 5, 1-1-1, Higashi, Tsukuba, Ibaraki, 305-8565, Japan
**kz-kirihara@aist.go.jp*

KAORU KIMURA

Department of Advanced Materials Science, University of Tokyo
7-3-1 Hongo, Bunkyo-ku, Tokyo, 113-8656, Japan

Received 27 November 2002
Revised 17 December 2002

We obtained thin films of the AlPdRe icosahedral quasicrystals by molecular beam epitaxy and post-annealing. The thickness of the films was estimated to be smaller than 100 nm. Any preferred orientation in the X-ray diffraction peaks was not observed in the films.

Keywords: Quasicrystal; thin film; molecular beam epitaxy.

1. Introduction

Icosahedral quasicrystal (IQC) has a unique atomic structure, which can be distinguished from crystal or amorphous solid. The structure is characterized by the sharp diffraction peaks with an icosahedral rotational symmetry in reciprocal space, and the quasi-periodic packing of icosahedral atom clusters with a diameter of approximately 1 nm in real space. Unlike conventional metallic alloys, many IQCs possess a semiconductor-like electron transport behavior and a glass-like low thermal conductivity. These properties can be explained by the combination of a Hume–Rothery type pseudogap in the electron density of states at Fermi energy and a localization tendency of electrons and phonons. We reported that AlPdRe IQC possesses higher thermoelectric power and lower thermal conductivity than other IQCs and thus might be the candidate for a thermoelectric material.[1] In addition, the thermoelectric power of AlPdRe IQC exhibits stronger dependence on the sample composition

*Corresponding author.

and the amount of Ru doping than the electrical conductivity and the thermal conductivity.[2] The slight change in the concentration of Pd, Re, and additional Ru should cause significant variation in the electronic structure and the bonding nature of the IQC. Hence, further precise tuning of the sample composition and flexible control of the fourth element doping are necessary for the improvement of the thermoelectric performance. However, the previous study based on bulk samples showed some difficulties for the control of the sample composition and the porosity.[1] The thin film preparation is less porosity and more reliable researches of the thermoelectric property in comparison with the bulk samples should be carried out. In addition, the thin IQC films may provide structural modifications of a quasi-lattice or icosahedral atom clusters. Thus new physical properties other than the thermoelectric properties will appear. Consequently, a new electric device in nanometer scale can be expected. In this paper, we report the results of thin film preparations of the single phase AlPdRe IQC for various processes.

2. Experimental

The thin films of AlPdRe IQC were prepared using a molecular beam epitaxy (MBE) apparatus. The evaporation sources were a Knudsen cell for Al and electron beam guns for Pd and Re. The pressure during deposition and *in situ* annealing was $10^{-6} \sim 10^{-5}$ Pa and $5 \times 10^{-7} \sim 5 \times 10^{-6}$ Pa, respectively. The deposition rates were $0.6 \sim 1.2$ nm/min, $0.12 \sim 0.30$ nm/min, and $0.06 \sim 0.18$ nm/min for Al, Pd, and Re, respectively. These deposition rates are lower than those reported earlier.[3,4] The desired composition was $Al_{70}Pd_{20}Re_{10}$ for all the films. Sapphire R-plane, quartz, and Si (100) plane were employed as substrates. In order to check the sample composition and the oxidation, we used *in situ* X-ray photoelectron spectroscopy (XPS). *In situ* annealing of the as-deposited film was performed at 700°C up to 2 h. *Ex situ* annealing was also performed under Ar atmosphere (6N purity, flow rate of more than 500 cm^3/min) at $700 \sim 750$°C up to 2 h. The cap-layer of Al_2O_3 ($100 \sim 150$ nm) was deposited on some of the films before *ex situ* annealing. X-ray diffraction (XRD) patterns were measured to identify the alloy phase. A rotating anode type X-ray source was employed to generate Cu Kα radiation. Total thickness of the as-deposited films, which was measured by a stylus-type thickness meter, was approximately 100 nm. The surface morphology of the films was examined by a scanning electron microscope (SEM).

3. Result and Discussion

We focus on the results of simultaneous deposition of the three elements on the sapphire R-plane substrate. The simultaneous depositions were performed at substrate temperature of $30 \sim 90$°C (film A), 500°C (film B), and 700°C (film C). The XRD patterns of films A, B, and C are shown in Fig. 1. From amorphous state of the as-deposited film A (Fig. 1(a)), single phase of IQC was obtained by *ex situ* annealing (Fig. 1(b)). All of the sharp diffraction peaks can be indexed

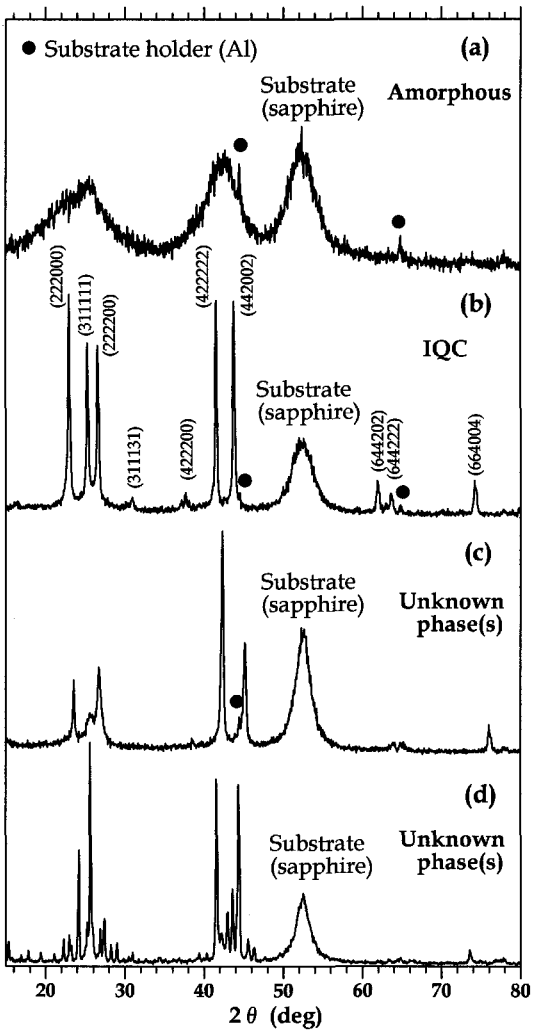

Fig. 1. XRD patterns of films A, B, and C. (a) film A (as-dep, $T_s = 30 \sim 90°C$), (b) film A (after *ex situ* annealing), (c) film B (as-dep, $T_s = 500°C$), (d) film C (as-dep, $T_s = 700°C$), and T_s is substrate temperature.

by six-dimensional indices. The XRD pattern of film A is similar to that of the powder sample (for instance, data from JCPDS No. 45-1317). Any preferred orientation in the X-ray diffraction peaks was not observed in the films. According to the SEM micrographs shown in Figs. 2(a) and 2(b), the smooth surface of the as-deposited film A has not been lost by *ex situ* annealing. The XPS spectrum of film A apparently indicated the oxidation at the surface. Considering the oxidized layer, the thickness of the IQC film is less than 100 nm. It should be noted that we have obtained thinner and flatter IQC film than the previous studies.[3–5] After Ar^+

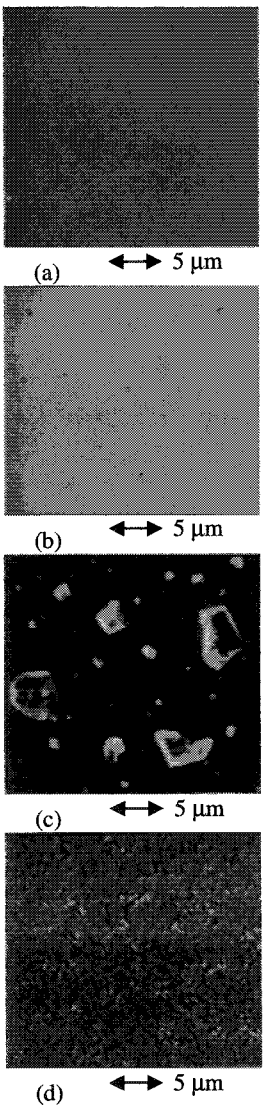

Fig. 2. SEM micrographs of films A, B, and C. (a) film A (as-dep, $T_s = 30 \sim 90°C$), (b) film A (after *ex situ* annealing), (c) film B (as-dep, $T_s = 500°C$), (d) film C (as-dep, $T_s = 700°C$), and T_s is substrate temperature.

sputtering of the oxidized layer, the surface morphology itself was not significantly changed. The XPS spectrum of the sputtered film A revealed that the oxidized layer consists mainly of aluminum and oxygen. Therefore, the composition of film A shifts from that of the as-deposited film to some extent. The measurements of the thermoelectric power and the electrical conductivity for film A are in progress. On the other hand, the simultaneous deposition at high temperature (films B and

C) exhibited no sign of IQC phase (unknown phases, Figs. 1(c) and 1(d)). The SEM micrographs show island formation and relatively rough surface for films B (Fig. 2(c)) and C (Fig. 2(d)), respectively. However, we obtained a single phase IQC with sharp XRD peaks for films B and C after the cap-layer deposition of Al_2O_3 and *ex situ* annealing. This means that the deviation of the sample composition at high temperature substrates is small and oxidation of the film during deposition is negligible. These results suggest that direct formation of IQC film needs higher substrate temperature than 700°C of instrumented limit.

According to the XRD patterns, the films deposited on the quartz substrate exhibited the entirely similar chemical reaction to the case of the sapphire substrate. However, the IQC phase was not obtained for the films deposited on the Si (100) substrate. The *in situ* XPS spectrum indicated apparently the existence of Si $2s$ and $2p$ states on the film surface, which means the atomic diffusion of Si from the substrate.

We have also performed the successive deposition with a layer sequence of Al/Pd/Re/Pd/Al at substrate temperature of 30 $\sim$ 90°C. The annealing of the multilayer enabled us to prepare the IQC film on the sapphire substrate as reported by Grenet *et al.*[3] The XRD pattern of the film by *in situ* annealing revealed relatively broad diffraction peaks and existence of a slight amount of secondary phase. In addition, large amount of porosity (diameter of 50 $\sim$ 100 μm) was distributed in the film with a cap-layer of Al_2O_3 after *ex situ* annealing. In the case of multilayer, the surface becomes rough through the inter-layer atomic diffusion during annealing.

4. Conclusions

We obtained thin films of the AlPdRe icosahedral quasicrystals by molecular beam epitaxy and post-annealing. The smooth surface of the as-deposited film has been kept through annealing without cap-layer deposition of Al_2O_3. Simultaneous deposition of the three elements is necessary in order to obtain the smooth surface. The deposition rate (maximum of approximately 2.0 nm/min) was lower than the earlier studies. The thickness of the films was estimated to be less than 100 nm. Any preferred orientation in the X-ray diffraction peaks was not observed in the films.

References

1. K. Kirihara and K. Kimura, *J. Appl. Phys.* **92**, 979 (2002).
2. K. Kirihara, T. Nagata, and K. Kimura, *J. Alloys Comp.* **342**, 469 (2002).
3. T. Grenet *et al.*, *J. Alloys Comp.* **342**, 2 (2002).
4. N. Bonasso *et al.*, *Thin Solid Film* **409**, 165 (2002).
5. R. Haberkern *et al.*, *MRS Symp. Proc.* **643**, K8.3.1 (2001); *Mat. Sci. Eng. A* **294–296**, 475 (2000).

This page is intentionally left blank

International Journal of Nanoscience, Vol. 1, Nos. 5 & 6 (2002) 533–537

FABRICATIONS OF LUMINESCENT POLYMERIC NANOPARTICLES CONTAINING LANTHANIDE (III) ION COMPLEXES

KOICHI TAMAKI and MASATSUGU SHIMOMURA*

Spatio-Temporal Function Materials Research Group
Frontier Research System, RIKEN 2-1 Hirosawa
Wako 351-0198, Japan
**Nanotechnology Research Center*
Research Institute for Electronic Science
Hokkaido University, Kita 12 Nishi 6
Kita-ku, Sapporo 060-0812, Japan

Received 27 November 2002
Revised 24 December 2002

Luminescent poly(ethylene glycol)-coated polystyrene (PSt) nanometer-sized particles (nanoparticles) containing trivalent europium or terbium ion were prepared by free-radical dispersion copolymerization of styrene, poly(ethylene glycol) (PEG) macromonomer, and the lanthanide complex which was coordinated with 1,10-phenanthroline possessing acryl group. Red and green luminescences with narrow band width were observed from each nanoparticle containing europium and terbium complexes, respectively.

Keywords: Nanometer-sized particles; lanthanide complexes; free-radical dispersion polymerization.

1. Introduction

We have reported that thin films possessing a hexagonal array of micropores ("*honeycomb films*") are formed by casting solutions of various types of polymers.[1–3] The film fabrication method is of "bottom–up" strategy and is based on self-organization process of soft materials. Using the patterned structure, composite thin films containing nanoparticles into the honeycomb micropores was fabricated.[4] The composite films will be applicable for flat, thin, and flexible luminous panels and display devices such as "*e-paper*". For the construction of the light-emitting devices, it is necessary to prepare highly luminescent nanoparticles. Because of strong luminosity with narrow band-width, lanthanide (III) ions are chosen as lumophore of the nanoparticles.

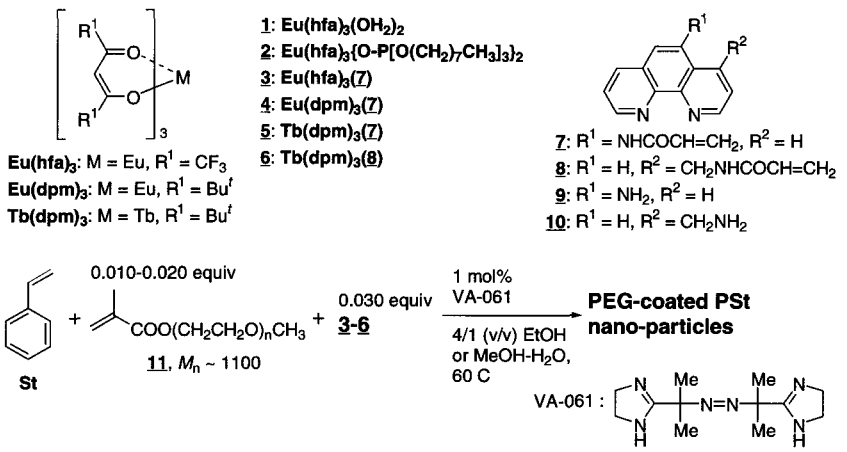

Fig. 1. Chemical structures of lanthanide complexes **1-6**, 1,10-phenanthroline derivatives **7-10**, and initiator VA-061 and reaction scheme of preparation of PEG-coated PSt nanoparticles.

Table 1. Comparison of properties of the lanthanide-containing PEG-coated PSt nanoparticles.

	Molar ratio to **St**, % (**11**, **ML**$_3$, and **7** or **8**)	D_w nm	D_n nm	Monodispersity (D_w/D_n)	λ_{max} nm	HMFW nm	I_{em}(Eu)	I_{em}(Tb)
3	0.35, 1.4, 2.5	241	211	1.14	614	9	1	—
4	0.50, 1.8, 1.6	307	287	1.07	612	5	0.89	—
5	0.80, 1.8, 1.8	265	256	1.04	545	10	—	0.11
6	0.50, 1.9, 1.6	275	256	1.07	546	11	—	1

ML$_3$: **M** = Eu or Tb and **L** = hfa or dpm; D_w and D_n: weight- and number-averaged diameter, respectively; λ_{max}, HMFW and I_{em}: Peak-top wavelength, half maximum full-width value, and relative emission intensity of the most intense emission band, respectively, excited at 360 (Eu) or 340 (Tb) nm. Molar ratios were estimated from elemental analyses.[a] D_w and D_n were estimated from the SEM images.

2. Preparations and Characterizations of Luminescent PEG-Coated PSt Nanoparticles Containing Lanthanide (III) Ion Complexes

Recently, useful preparation method of monodisperse polymeric nanoparticles *via* free-radical dispersion copolymerization of hydrophobic monomers (e.g., styrene) and hydrophilic macromonomers (e.g., **11**) in polar solvent has been reported.[5] In order to introduce illuminant lanthanide ions toward each particle core uniformly, hydrophobic lanthanide complexes were needed. But introduction of complex **1** and **2** to the PSt nanoparticles has failed because of low solubility to the hydrophobic

[a]Found in the particles containing **3**: C 83.88, H 7.21, N 0.90%; Containing **4**: C 86.53, H 7.76, N 0.52%; Containing **5**: C 85.45, H 7.60, N 0.57%; Containing **6**: C 86.23, H 7.68, N 0.50%. Calcd for $\mathbf{St}_{100}\mathbf{11}_{0.35}[\mathbf{Eu(hfa)_3}]_{1.5}\mathbf{7}_{1.3}$: C 84.01, H 6.99, N 0.84%; $\mathbf{St}_{100}\mathbf{11}_{0.50}[\mathbf{Eu(dpm)_3}]_{1.8}\mathbf{7}_{1.6}$: C 86.48, H 7.74, N 0.53%; $\mathbf{St}_{100}\mathbf{11}_{0.80}[\mathbf{Tb(dpm)_3}]_{1.8}\mathbf{7}_{1.8}$: C 85.58, H 7.75, N 0.58%; $\mathbf{St}_{100}\mathbf{11}_{0.50}[\mathbf{Tb(dpm)_3}]_{1.9}\mathbf{8}_{1.6}$: C 86.22, H 7.74, N 0.53%.

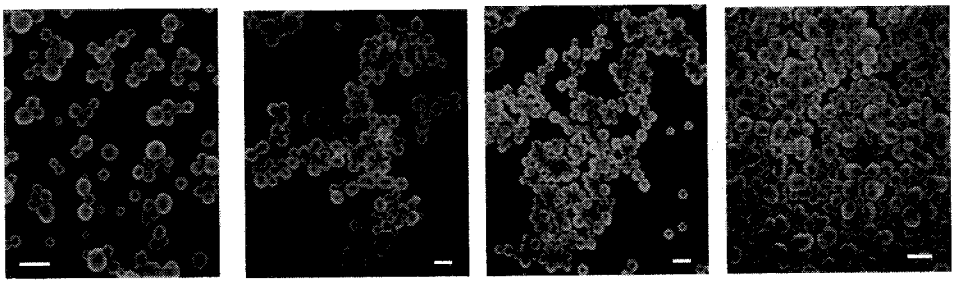

(a) (b) (c) (d)

Fig. 2. SEM images of PEG-coated PSt nanoparticles connecting (a) **3**, (b) **4**, (c) **5**, and (d) **6**. Scale bar indicates 500 nm.

particle core and to the polar polymerization media, respectively. An effective strategy of the introduction of the lanthanide complexes was the synthesis of complex monomers **3-6** and copolymerization of a mixture of the lanthanide complex **3-6**, styrene (**St**), and **11** (Fig. 1) according to Ref. 5. As a key ligand of the lanthanide monomers, two kinds of 1,10-phenanthloline **7**[6] and **8** were prepared by amidation of amino derivatives **9** and **10**[7] and acryloyl chloride, respectively. Four lanthanide complex monomers were synthesized according to general method.[8]

All nanoparticles were characterized by means of elemental analyses and SEM observations. Table 1 indicates that **11** and the lanthanide monomers **3-6** were copolymerized with **St**. It was suggested that hydrophilic PEG moiety covered hydrophobic PSt core of the nanoparticles as well as the no-doping PSt core-PEG corona nanospheres.[9] The nanoparticles with narrow size distribution were obtained in the case of the complex **4-6** (Fig. 2). From elemental analyses, dissociation of ligand **7** or **8** in some amount of complex **3-6**, typically **3**, was occurred in the copolymerization mixture.

3. Luminescence Properties of the Lanthanide Complexes and the Nanoparticles Containing the Complexes

When the nanoparticles containing lanthanide complex **3**, **4**, and **6** were excited by UV light, red (containing **3** or **4**) or green (containing **6**) luminescence from each nanoparticle were observed (Figs. 3 and 4).[b] Luminescent properties of the nanoparticles are also summarized in Table 1.

Difference of luminescence intensities between the nanoparticles was derived from that of complex monomers. Luminescence of **5** was strongly quenched than that of **6** (29% intensity of **5**, Fig. 4(a)). Excited coordinating **7** of **5** was emitted fluorescence (λ_{max} = 410 nm). Excited at 360 nm, luminescence of **4** was reduced to 8.4% intensity of **3**.

[b]Emission from the nanoparticles containing **5** was too weak to detect by fluorescent microscopes.

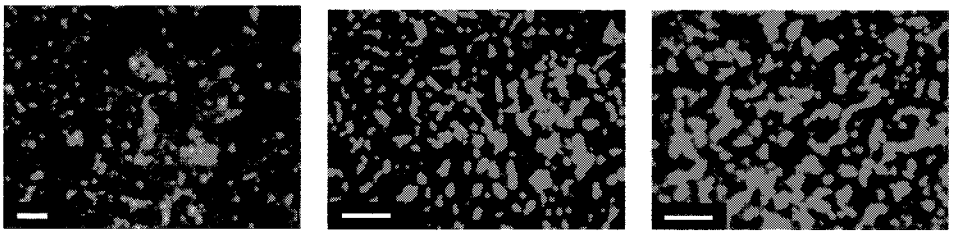

(a) (b) (c)

Fig. 3. Fluorescent microscopic images of the nanoparticles containing (a) **3**, (b) **4**, and (c) **6**, on glass substrate under irradiation of 330–385 nm UV light from mercury lamp (WU excitation method). Scale bar indicates 5.0 μm.

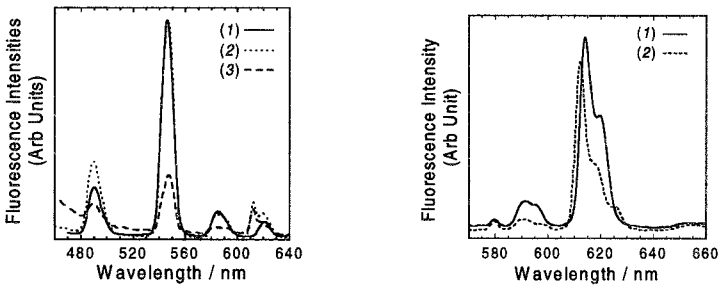

(a) (b)

Fig. 4. (a) Fluorescence spectra excited at 340 nm. (1) normalized spectrum of nanoparticles polymerizing **6** on glass substrate, (2) 2.0×10^{-5} M **6** in benzene, and (3) 2.0×10^{-5} M **5** in benzene. (b) Fluorescence spectra of the nanoparticles containing (1) **3** and (2) **4** on glass substrate excited at 360 nm.

4. Conclusions

Four kinds of PEG-coated PSt nanoparticles containing europium or terbium complex were prepared. These are typical nano- or submicron-scaled organic materials wrapping luminescent lanthanide trivalent ions. The nanoparticles connecting *tert*-butylated complex (**4-6**) had narrow size distribution and monodispersity compared to connecting fluorinated one (**3**). Luminescence intensity of the nanoparticles containing higher-luminescent complex (**3** and **6**) was stronger than that of particles containing complex (**4** and **5**). In other words, these particle properties, sizes and luminosity, were influenced by properties of lanthanide complexes.

References

1. T. Nishikawa, R. Ookura, J. Nishida, K. Arai, J. Hayashi, N. Kurono, T. Sawadaishi, M. Hara, and M. Shimomura, *Langmuir* **18**, 5734 (2002).
2. N. Maruyama, T. Koito, J. Nishida, T. Sawadaishi, X. Cieren, K. Ijiro, O. Karthaus, and M. Shimomura, *Thin Solid Films* **327–329**, 854 (1998).

3. O. Karthaus, N. Maruyama, X. Cieren, M. Shimomura, H. Hasegawa, and T. Hashimoto, *Langmuir* **16**, 6071 (2000).
4. M. Shimomura and T. Sawadaishi, *Curr. Opin. Colloid Interface Sci.* **6**, 11 (2001).
5. M.-Q. Chen, T. Serizawa, A. Kishida, and M. Akashi, *J. Polym. Sci. A: Polym. Chem.* **37**, 2155 (1999).
6. H. Shu, H. Li, P. Wang, and Z. Tang, *Sichuan Daxue Xuebao, Ziran Kexueban* **37**, 470 (2000).
7. R. H. Terbrueggen, T. W. Johann, and J. K. Barton, *Inorg. Chem.* **37**, 6874 (1998).
8. J. F. Desruex, *Lanthanide Probes in Life, Chemical and Earth Sciences, Theory and Practice*, eds. J.-C. G. Bünzli and G. R. Choppin (Elsevier, Amsterdam, 1989), p. 43.
9. T. Serizawa, S. Takehara, and M. Akashi, *Macromolecules* **33**, 1759 (2000).

This page is intentionally left blank

International Journal of Nanoscience, Vol. 1, Nos. 5 & 6 (2002) 539–543

PREPARATION AND CHARACTERIZATION OF SiO_2 NANOPARTICLE AND MESOPOROUS SILICATE MOLECULAR SIEVE MCM-48

KYUNG WON SEO, SUNG DU MOON, and YOUNG SOO KANG

Department of Chemistry, Pukyong National University
599-1 Nam-gu, Busan, 608-737, Korea

YONG JOO KIM

Department of Applied Chemistry, Hanbat National University
599-1 Yusung-gu, Daejeon, 305-719, Korea

Received 27 November 2002
Revised 24 December 2002

Nanosize SiO_2 particles with narrow size distribution were produced by modified Stober–Fink–Bohn method. Average particle size was determined as 170 nm by SEM image. Organosilica mesoporous molecular sieve (MCM-48) was synthesized. The calcined MCM-48 has pore diameter of 26.8 Å and a surface area of 1024 m^2g^{-1} by BET (Brunauer–Emmet–Teller) measurement.

Keywords: Nanoparticle; mesoporous molecular sieve; SiO_2.

1. Introduction

The discovery of the M41S family of mesoporous molecular sieves[1,2] has expanded the range of uniform pore sizes from the microporous (<13 Å, as found in zeolites) into the mesopore range (>20 Å) and generated considerable interest in open structured inorganic materials. Three subgroups of the family have been reported: a hexagonal phase referred to as MCM(Mobile Company Material)-41, a cubic phase (space group Ia3d) known as MCM-48, and MCM-50, an unstable lamellar phase.[3] The procedures used for the preparation of mesoporous silica materials are similar to those in the synthesis of zeolites, except that a surfactant instead of an inorganic base or an amine is used as the template. Mesoporous silica is made under mild hydrothermal conditions (typically below 120°C) in the presence of anionic, cationic, or neutral surfactants, under either basic or acidic conditions.[4,5] Since the atomic arrangement in these materials is not crystalline, we shall refer to "crystallinity" in the sense of the regular arrangement of uniform channels, the only element of order. All references to a unit cell, etc. should be interpreted accordingly. Surfactant

chemistry is the key to the formation of mesoporous silica. The silicate species in solution play an important role in the organization of the surfactant molecules, and the electrostatic interaction between the inorganic and surfactant ions determines the morphology of the mesophase. Interest in the mesoporous silica sieves has been concentrated almost exclusively on MCM-41 and very little information is available on MCM-48.

2. Experiment

2.1. *Material*

All solvents and chemicals are of reagent quality and are used without further purification except tetraethylorthosilicate (TEOS, Aldrich 99.5%) which is freshly vacuum distilled before use. Ethanol and cetyltrimethylammonium bromide (CTBr, 99%) are obtained from Aldrich Chemical Co. Ammonium hydroxide (29.6%) are obtained from Fisher Chemical Co.

2.2. *Synthesis of SiO_2 nanoparticle*

Spherical hydrous SiO_2 nanoparticles with narrow size distribution were produced by modified Stober–Fink–Bohn method.[6] Under the conditions of constant stirring at room temperature, TEOS (0.5 mol) was added to a solution of 30 ml reagent-grade ethanol and concentrated ammonium hydroxide (2.2 mol). TEOS underwent hydrolysis/condensation reaction, forming poly-silicylic acid. Within minutes, precipitation of uniform spherical SiO_2 nanoparticles was occurred. By controlling the reactant concentrations, average diameter of particle in the range of 0.05 to 0.6 μm could be produced. 1.5 g SiO_2 nanoparticles are washed six times with 30 ml of 200 proof ethanol by repeated centrifugation and ultrasonic dispersion cycle in order to remove impurities, such as ammonia, water, and unreacted tetraethylorthosilicate. SiO_2 nanoparticles were then dried at 100°C in an oven.

2.3. *Synthesis of organosilica mesoporous material*

Purely siliceous MCM-48 was synthesized following literature prodedure.[7] The sodium silicate solution was prepared using colloidal silica (39.5 wt% SiO_2, 0.4 wt% Na2O, and 60.1 wt% H_2O) added to the heated 0.1 M NaOH solution, whose molar composition is 0.25 Na_2O: 1.0 SiO_2: 12.5 H_2O. This solution was placed into the autoclave containing the surfactant solution of a mixture of CTABr, ethanol, and H_2O. The molar composition of resultant gel mixture is 1.4 SiO_2: 1.0 CTABr: 0.35 Na_2O: 5.0 EtOH: 140 H_2O. The mixture was heated for 16 h at 140°C. The product was then slurried in an ethanol–HCl mixture (0.1 mol of HCl per L of ethanol), filtered, washed with ethanol, dried in an oven, and calcined in air at 550°C for 8 h.

2.4. *Characterization of SiO_2 nanoparticle and organosilica mesoporous material by XRD, SEM, BET*

The structure of SiO_2 nanoparticle and MCM-48 was studied with X-ray diffraction (XRD) (Philips, X'Pert-MPD system). Before the experiments, MCM-48 was dehydrated at 350°C for 12 h. Scanning electron microscopy (SEM) examinations of the samples were carried out on a HITACHI S-2400. The samples were coated with gold using a prior to imaging. The cumulative surface area of mesopores was obtained from BET (Quntachrome Co.) measurement.

3. Result and Discussion

The X-ray diffraction patterns show that the precursor changed to the calcined SiO_2 nanoparticle as increasing calcinations temperature. Figure 1 shows that diffraction patterns of SiO_2 nanoparticle corresoponding to cristobalite SiO_2 have been found for the samples calcined at 1200°C. No significant change in the structure has been found after heat-treatment temperature up to 1000°C. A small amount of SiO_2 has been detected after calcining below 1000°C, but most of them are assigned as an amorphous structure. The single-phase cristobalite SiO_2 has been observed in the sample calcined at 1200°C for 24 h. Figure 2 is the scanning electron microscopy (SEM) image of SiO_2 nanoparticles. All powders were dried under vacuum for 3 h at 100°C before characterization. Most of the SiO_2 nanoparticles are spherical. Average particle size was determined as 170 nm. The quality of MCM-48 was confirmed by XRD measurement. The powder X-ray diffraction patterns of the products of MCM-48 feature distinct Bragg peaks in the range $2\theta = 2 \sim 8°$, which can be indexed to different *hkl* reflections in good agreement with the patterns from a purely siliceous MCM-48. The XRD pattern of MCM-48 (Fig. 3) shows typical peaks of the cubic crystallographic space group Ia3d, which indicates that the crystallites are particularly well developed. The (211) peak is sharp and intensive. The (220),

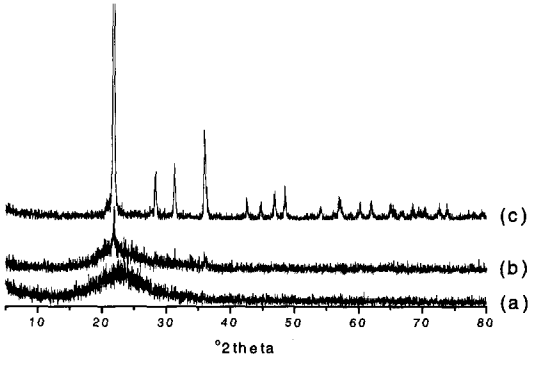

Fig. 1. X-ray diffractograms of the calcined powders of heat treated at (a) 800°C, (b) 1000°C, and (c) 1200°C.

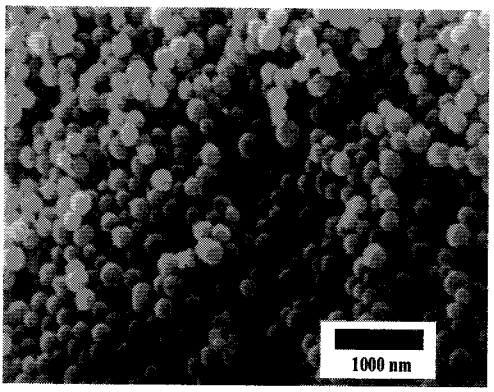

Fig. 2. Scanning electron microscopic images of SiO_2 nanoparticles.

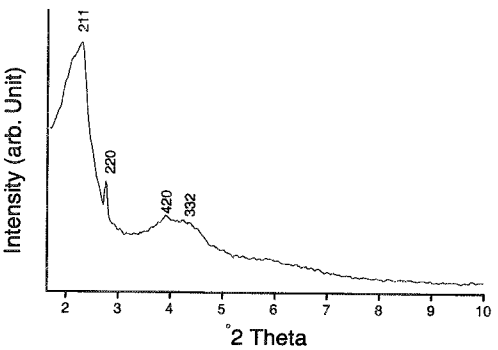

Fig. 3. XRD patterns of calcined MCM-48.

(420) and (332) peaks are well resolved. The calcined MCM-48 has pore diameter of 26.8 Å and a surface area of 1024 m^2g^{-1} by BET.

Acknowledgments

This work was financially supported by The Specific Research and Development Program of The Korean Ministry of Agriculture and Forestry, 2001. Yong Joo Kim acknowledge the financial support from Korea Science and Engineering Foundation through the Advanced Materials Research Center for Better Environment at Hanbat National University.

References

1. J. S. Beck, J. C. Vartuli, W. J. Roth, M. E. Leonowicz, C. T. Kresge, K. D. Schmitt, C. T. W. Chu, D. H. Olson, E. W. Sheppard, S. B. McCullen, J. B. Higgins, and J. L. Schlenker, *J. Am. Chem. Soc.* **114**, 10834 (1992).
2. C. T. Kresge, M. E. Leonowicz, W. J. Roth, J. C. Vartuli, and J. S. Beck, *Nature* **359**, 710 (1992).

3. X. S. Zhao, C. Q. Lu, and G. J. Millar, *Ind. Eng. Chem. Res.* **35**, 2075 (1996).
4. Q. Huo, D. I. Margolese, U. Ciesla, P. Feng, T. E. Gier, P. Sieger, R. Leon, P. M. Petroff, F. Schüth, and G. D. Stucky, *Nature* **368**, 317 (1994).
5. J. C. Vartuli, K. D. Schmitt, C. T. Kresge, W. J. Roth, M. E. Leonowicz, S. B. McCullen, S. D. Hellring, J. S. Beck, J. L. Schlenker, D. H. Olson, and E. W. Sheppard, *Stud. Surf. Sci. Catal.* **84**, 53 (1994).
6. W. Stober, A. Fink, and E. Born, *J. Coll. Interf. Sci.* **26**, 62 (1968).
7. J. M. Kim, S. K. Kim, and R. Ryoo, *Chem. Commun.* **259** (1998).

This page is intentionally left blank

International Journal of Nanoscience, Vol. 1, Nos. 5 & 6 (2002) 545–549

SECOND HYPERPOLARIZABILITIES OF MOLECULAR AGGREGATES: INTERMOLECULAR ORBITAL-INTERACTION AND SPIN-CONFIGURATION EFFECTS

MASAYOSHI NAKANO*, SATORU YAMADA,
MASAHIRO TAKAHATA, and KIZASHI YAMAGUCHI

Department of Chemistry, Graduate School of Science, Osaka University
Toyonaka, Osaka 560-0043, Japan
**mnaka@cheng.es.osaka-u.ac.jp*

Received 27 November 2002
Revised 6 December 2002

Toward an understanding of intermolecular-interaction effects on the third-order nonlinear optical properties of nanostructured molecular aggregates, we investigate the longitudinal second hyperpolarizabilities (γ) of model dimers composed of neutral (C_5H_7) and charged ($C_5H_7^+$) monomers using *ab initio* molecular orbital methods. It is found that π–π orbital interaction in the stacking direction remarkably affects the γ values of dimers, while the difference in spin configuration hardly causes significant changes in γ for the present models due to weak exchange interactions between monomers.

Keywords: Nonlinear optics; second hyperpolarizability; π–π orbital interaction; spin configuration.

1. Introduction

A large number of π-conjugated organic and inorganic molecular systems have been investigated due to their large nonlinear optical (NLO) properties. Most of these systems are closed-shell neutral molecules, which are chemically stable. In previous studies,[1–4] we have found that the molecules with symmetric resonance structure with invertible polarization (SRIP) tend to exhibit negative off-resonant second hyperpolarizabilities (γ), which are the origin of the self-defocusing effects of the incident laser beam. It is also found that such systems exhibit a large enhancement of two-photon absorption (TPA) cross section. A simple method of obtaining a large contribution of SRIP was found to be an introduction of charged defects.[4]

From the viewpoint of the molecular design of nanostructured NLO molecular aggregates, the elucidation of intermolecular-interaction effects on γ is important.[5,6]

*Corresponding author. Present address: Division of Chemical Engineering, Department of Materials Engineering Science, Graduate School of Engineering Science, Osaka University, Toyonaka, Osaka 560-8531, Japan.

In this study, therefore, we investigate the intermolecular-interaction effects on γ values for two types of model dimers composed of neutral (C_5H_7) and cationic ($C_5H_7^+$) monomers, respectively. The γ values for monomers and dimers are calculated using *ab initio* molecular orbital (MO) and density functional (DF) methods. Further, since open-shell molecules are expected to be novel candidates for NLO systems,[2] the spin-configuration effect on the γ is also examined using the neutral dimers with singlet and triplet states. On the basis of the present results, a novel structure-property relation in γ of molecular aggregates is discussed in view of the intermolecular orbital-interaction effect.

2. Calculated Systems and Calculation Methods

Figure 1 shows the structures of monomers (cation $C_5H_7^+$ (M-c) and neutral doublet C_5H_7 (M-n)) and their dimers (dication (D-dc), neutral singlet (D-s) and neutral triplet (D-t)), in which the monomers lie on two z–x planes in a cofacial arrangement. These dimers have the same distance (van der Waals radius, 3.0 Å) between cofacial monomer planes and have complete overlaps (in the stacking direction) between upper and lower molecules (**1-1′**, **2-2′**, **3-3′** and **4-4′**). The geometries of monomers are optimized under the C_{2v} symmetry using a hybrid DF, i.e., B3LYP, method with a standard basis set (6-31G**). All calculations are performed by using GAUSSIAN 98 program package.[7]

In general, electron-correlation effects on γ for charged and/or open-shell molecules are known to be remarkable,[9] so that we apply several *ab initio* MO methods, i.e., the Hartree–Fock (HF), the Møller–Plesset perturbation (MP2 and MP4) and the coupled-cluster (CCSD(T)) methods, as well as a hybrid DF (BHandHLYP) method to the calculation of longitudinal γ (γ_{zzzz}) for monomers. The γ values are calculated by the finite-field (FF) approach using the fourth-order numerical differentiation of the total energy E with respect to the applied field.

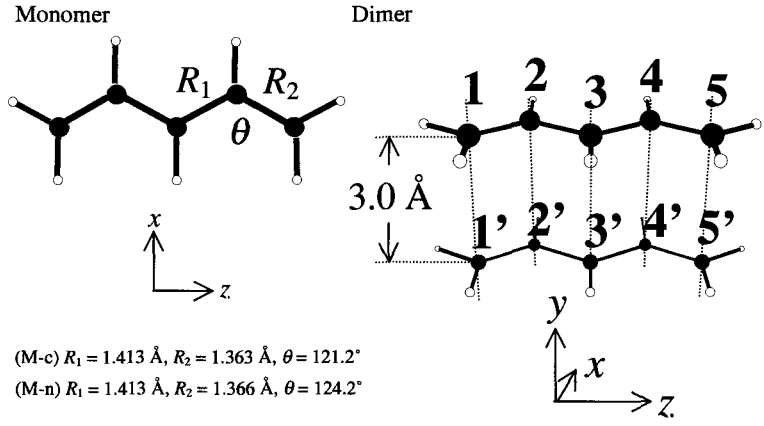

Fig. 1. Structures of cationic (M-c), neutral (M-n) monomers and three types of dimers: dication (D-dc), neutral singlet (D-s) and neutral triplet (D-t) states.

3. Results and Discussion

Table 1 gives the electron-correlated *ab initio* MO and BHandHLYP calculation results for monomers. Similarly to the previous studies,[1–4] cationic (M-c) and neutral (M-n) monomers are found to provide negative and positive γ values, respectively. Judging from the fact that the CCSD(T) is the highest electron-correlation method in this study, the electron-correlation effect at the MP2 level is sufficient for cationic monomer (M-c), while the MP2 and MP4 methods, instead of improving, overshoot the γ for neutral monomer (M-n) calculated by the CCSD(T) method, which gives a similar γ value to that at the HF level. These results suggest that low-order electron-correlation effects fail in the sufficient (converged) description of γ for open-shell molecules. It is also shown that the BHandHLYP method cannot reproduce well the γ value of cationic monomer (M-c) at the CCSD(T) level, while that can provide a similar γ value to the CCSD(T) value for (M-n). As a result, we can use the MP2 and HF methods to obtain reliable γ values for dicationic dimer (D-dc) and neutral (D-s and D-t) monomers, respectively.

The longitudinal γ values per monomer for these dimers and γ for cationic (at the MP2 level) and neutral (at the HF level) monomers are given in Table 2. These results indicate that the intermolecular interactions between cationic (neutral) monomers significantly reduce the magnitude of γ per monomer as compared with that for an isolated monomer (about 50% decrease). From the configurations of the present dimers, the π–π orbital interactions between upper and lower monomers are predicted to significantly affect the longitudinal γ. The HOMOs of monomers are near-degenerate in dimers and one of their orbitals in dimer exhibits a bonding-like (in-phase) interaction between upper and lower monomers. We predict that this

Table 1. Longitudinal $\gamma(\gamma_{zzzz})$ values [a.u.] of charged (M-c) and neutral (M-n) monomers, C_5H_7.

Method	(M-c)	(M-n)
HF	−2965	9493
MP2	−11270	16810
MP4	−12330	14480
CCSD(T)	−13300	9653
BhandHLYP	−3229	10340

Table 2. Longitudinal $\gamma(\gamma_{zzzz})$ [a.u.] per monomer of dimers (D-dc), (D-s) and (D-t).

	(D-dc)[a]	(D-s)[b]	(D-t)[b]
γ(dimer)/monomer	−5362	5278	5474
γ of isolated monomer	−11270	9493	9493

[a]Restricted MP2/6-31G** method is used.
[b]Unrestricted HF/6-31G** method is used.

bonding interaction tend to prevent the π-electrons from virtually transferring in the longitudinal direction (z) in each monomer, which originate in the longitudinal γ. It is also noted that the difference in the spin configuration hardly causes the difference between the γ value of (D-s) and that of (D-t), which are considerably smaller than that of an isolated monomer (M-n).

4. Summary

We investigated the longitudinal γ values of monomer and dimer models of charged and neutral symmetric π-conjugated molecules. It was found that the γ values are remarkably affected by the π–π orbital interactions between upper and lower monomers: bonding-like interaction is predicted to significantly reduce the magnitude of longitudinal γ. Since in general there exist positive and negative contributions to γ in different spatial regions,[9] such orbital-interaction effects at relevant regions are expected to control the magnitudes and sign of total γ for large-size molecules and molecular aggregates. In contrast, the difference in spin configuration does not cause a significant change in the longitudinal γ of the present models due to weak exchange interactions between monomers. However, in the case of strong inter- and intra-molecular interactions, e.g., transition-metal clusters, such spin-configuration effects will be important. In conclusion, the present study suggests a novel structure-property relation of γ based on intermolecular orbital interaction, which is utilized to construct a guideline of controlling NLO properties of nano-structured molecular systems by chemical perturbation, i.e., orbital–orbital interaction. We are now in progress of further investigations on the hyperpolarizabilities of large-size molecular aggregates along this line using hyperpolarizability density,[8–11] which can elucidate the spatial contribution of electrons to hyperpolarizabilities.

Acknowledgment

This work was supported by Grant-in-Aid for Scientific Research (No. 14340184) from Japan Society for the Promotion of Science (JSPS).

References

1. M. Nakano and K. Yamaguchi, *Chem. Phys. Lett.* **206**, 285 (1993).
2. M. Nakano, S. Kiribayashi, S. Yamada, I. Shigemoto, and K. Yamaguchi, *Chem. Phys. Lett.* **262**, 66 (1996).
3. M. Nakano, S. Yamada, and K. Yamaguchi, *Chem. Phys. Lett.* **311**, 221 (1999).
4. H. Fujita, M. Nakano, M. Takahata, and K. Yamaguchi, *Chem. Phys. Lett.* **358**, 435 (2002).
5. M. Ottonelli, G. F. Musso, D. Comoretto, and G. Dellepiane, *Phys. Chem. Chem. Phys.* **4**, 2754 (2002).
6. H. Kishida, H. Matsuzaki, H. Okamoto, T. Manabe, M. Yamashita, Y. Taguchi, and Y. Tokura, *Nature* **405**, 929 (2002).
7. M. J. Frisch *et al.*, *Gaussian 98* (Gaussian, Inc., Pittsburgh, PA, 1998).
8. M. Nakano, K. Yamaguchi, and T. Fueno, *Chem. Phys. Lett.* **185**, 550 (1991).

9. M. Nakano, I. Shigemoto, S. Yamada, and K. Yamaguchi, *J. Chem. Phys.* **103**, 4175 (1995).
10. M. Nakano, S. Yamada, I. Shigemoto, and K. Yamaguchi, *Chem. Phys. Lett.* **250**, 247 (1996).
11. M. Nakano, H. Fujita, M. Takahata, and K. Yamaguchi, *Chem. Phys. Lett.* **356**, 462 (2002).

This page is intentionally left blank

International Journal of Nanoscience, Vol. 1, Nos. 5 & 6 (2002) 551–555

FABRICATION OF CdS DOT ARRAY USING POLYMER HONEYCOMB TEMPLATE

NOBUKO FUKUDA and MASATSUGU SHIMOMURA*

Dissipative-Hierarchy Structures Laboratory
Spatio-Temporal Function Materials Research Group
Frontier Research System, RIKEN, 2-1 Hirosawa
Wako, Saitama 351-0198, Japan

Received 27 November 2002

We fabricated periodic structures of CdS using honeycomb films consisting of an amphiphilic copolymer as a template. The honeycomb film using an amphiphilic copolymer was fabricated on the water surface under highly humid condition and was then transferred onto a solid substrate. The pore size in the honeycomb film was ca. 5 μm. The CdS nanoparticles were synthesized using a gelatin as an inhibitor of rapid nuclear growth and then the gelatin was removed by decomposition using an enzyme. The CdS particles were introduced into pores of the honeycomb film by casting, dipping, and electrochemical deposition. Dipping the honeycomb film into CdS suspension under ultrasonication, periodic deposition of CdS particles in the honeycomb holes was achieved. The CdS-honeycomb film composite was calcinated at 450°C for 30 min in order to remove organic moiety. After calcination, periodic arrangement of porous CdS dots with diameter of 3–5 μm was partially formed. The CdS dots are applicable to photoelectrochemical and optical devices such as a photodiode.

Keywords: CdS nanoparticles; honeycomb film; CdS dots.

1. Introduction

Recently self-organization and self-assembly of function materials have been widely focused with the view of bottom–up process for formation of functional interface. We have already reported an elegant fabrication process of a polymer thin film with a hexagonal array of micropores like a honeycomb.[1,2] The honeycomb film was fabricated using amphiphilic copolymers on water surface or solid substrates under highly humid atmosphere. The porous structure bases on hexagonal packing of water microspheres formed by the condensation of gaseous water at the air–polymer solution interface as evaporation of the solvent.[3,4] On the other hand, the honeycomb film can be used as a template[5] for the fabrication of periodic

*Nanotechnology Research Center, Research Institute for Electronic Science, Hokkaido University, N12W6, Sapporo 060-0812, Japan.

metal and semiconductor dots, which are attractive materials as a photonic crystal and a microphotoelectric conversion interface. In this paper, we report the elegant fabrication process of CdS dots on an indium tin oxide (ITO) electrode using the polymer honeycomb film as a template.

2. Fabrication of Polymer Honeycomb Films

Poly[*N*-dodecylacrylamide-*co*-*N*-(ω-carboxyhexylacrylamide)] (CAP) (Scheme 1) was synthesized as described previously.[1,2] A Petri-dish was filled with Milli-Q grade water. A benzene solution of 1.0 g L^{-1} CAP was cast onto the water surface and then a droplet of the CAP solution was formed. Humid air was blown to the droplet from a glass tube until the solvent was completely evaporated. The resulting opaque film was transferred onto an ITO electrode by horizontal deposition from the atmosphere side or scooping from the water-subphase side (Scheme 2) and then annealed at 55°C for 5 min in a temperature-controlled box in order to immobilize the film onto the substrate. The honeycomb pattern was observed by a scanning electron microscope (SEM) (S-5200, HITACHI) and the diameter of the pores was estimated to be ca. 5 μm (Fig. 1).

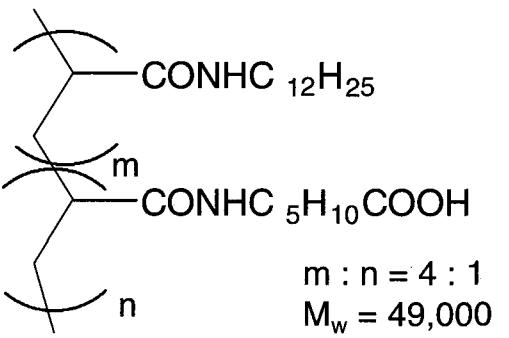

Scheme 1. Chemical structure of CAP.

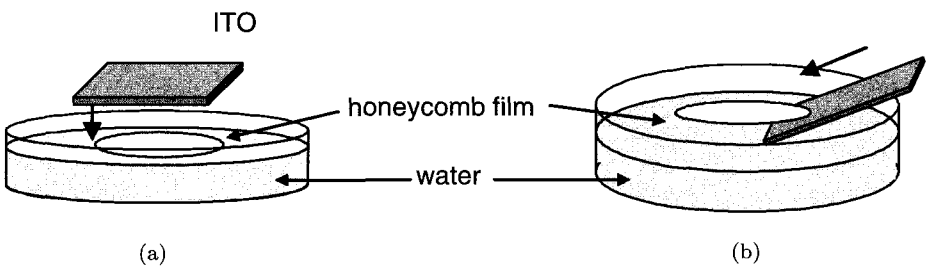

Scheme 2. The transfer scheme of the honeycomb film from the water surface to an ITO substrate by (a) horizontal deposition from the atmosphere side and (b) scooping from the water-subphase side.

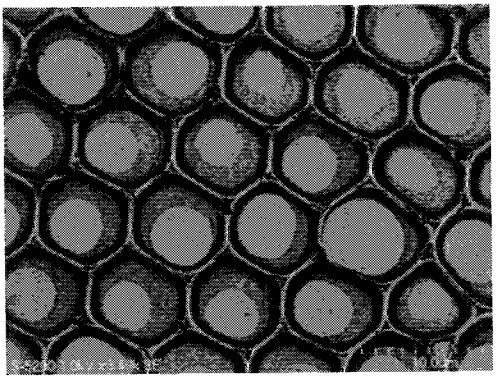

Fig. 1. The SEM image of the honeycomb film transferred by horizontal deposition from the atmosphere side onto an ITO substrate.

3. Introduction of CdS Nanoparticles into Polymer Honeycomb Films

The CdS nanoparticles were synthesized in a gelatin solution (pH = 8.5) and then the gelatin was removed by decomposition using an enzyme.[6,7] The diameter of the CdS particles was estimated to be 2–3 nm by transmission electron microscopy. The CdS nanoparticles were introduced by dipping of the polymer honeycomb film into the CdS suspension (pH = 2.0) for 30 min under ultrasonication. The honeycomb film was rinsed by distilled water and dried under vacuum at room temperature after withdrawing from the suspension. The introduction of CdS nanoparticles into the pore depends on the rim width exposed to the CdS suspension. The rim width changes by the transfer process of the honeycomb film from the water surface onto

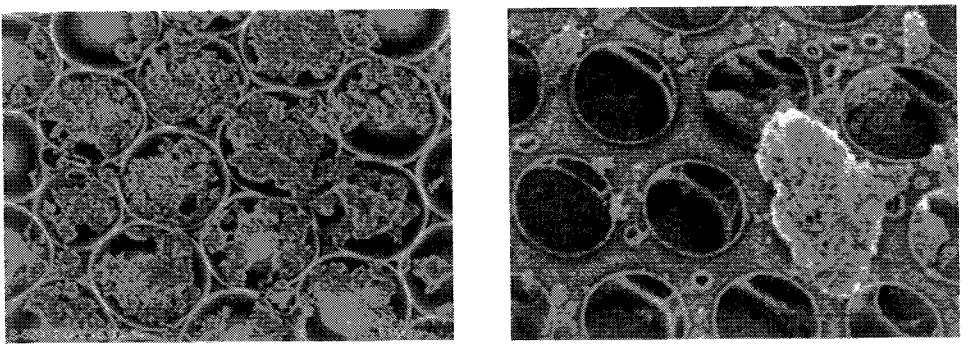

(a) (b)

Fig. 2. The SEM images of honeycomb films transferred from the water surface onto ITOs by (a) horizontal deposition from the atmosphere side and (b) scooping from the water-subphase side after dipping into CdS suspension under ultrasonication for 30 min.

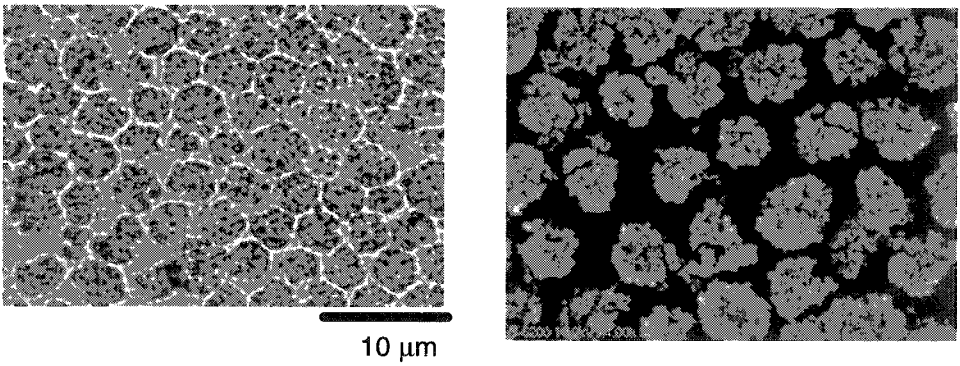

(a) (b)

Fig. 3. (a) The optical micrograph and (b) the SEM image of CdS dots on an ITO.

an ITO substrate. When the honeycomb film was transferred onto the ITO surface by horizontal deposition from the atmosphere side, aggregated CdS nanoparticles were filled in pores of the honeycomb film (Fig. 2(a)). While the honeycomb film was scooped from the water-subphase side onto the ITO substrate, however, the aggregated CdS particles were not embedded into the holes but adhered onto the honeycomb rim (Fig. 2(b)).

4. Fabrication of CdS Dots

The CdS-introduced honeycomb film was calcinated in an oven at 450°C for 30 min and then rinsed by benzene to remove the organic part. The CdS dots with diameter of 3–5 μm were fixed on ITO substrate and some dots were partially arrayed periodically (Fig. 3). These CdS dots are porous so that each dot has large surface area, that is useful for chemical and electrochemical reactions between the CdS surface and other molecules. Thus the CdS dots are applicable to a micro-photoelectric conversion interface. In addition, we need to control the dot size and improve the regularity of the dot shape and the dot array, leading to a photonic band effect.

5. Conclusion

We fabricated CdS dots using a honeycomb film consisting of an amphiphilic copolymer as a template. The introduction of CdS nanoparticles into the micropores of the honeycomb film was carried out by dipping into the corresponding suspension under ultrasonication. When the side with the narrow rim of the honeycomb film was exposed to the CdS suspension, CdS nanoparticles were introduced into the micropores. The porous CdS dots with diameter of 3–5 μm were fabricated by calcination of the CdS-introduced honeycomb film. Currently we are improving the

regularity of the dot shape and the dot array to the application as a photoelectric conversion interface and a photonic crystal.

References

1. N. Maruyama, T. Koito, J. Nishida, T. Sawadaishi, X. Cieren, K. Ijiro, O. Karthaus, and M. Shimomura, *Thin Solid Films* **327–329**, 854 (1998).
2. T. Nishikawa, R. Ookura, J. Nishida, K. Arai, J. Hayashi, N. Kurono, T. Sawadaishi, M. Hara, and M. Shimomura, *Langmuir* **18**, 5734 (2002).
3. T. Nishikawa, J. Nishida, R. Ookura, S.-I. Nishimura, S. Wada, T. Karino, and M. Shimomura, *Mater. Sci. Eng. C* **10**, 141 (1999).
4. O. Karthaus, N. Maruyama, X. Cieren, M. Shimomura, H. Hasegawa, and T. Hashimoto, *Langmuir* **16**, 6071 (2001).
5. M. Shimomura, T. Koito, N. Maruyama, K. Arai, J. Nishida, L. Gråsjö, O. Karthaus, and K. Ijiro, *Mol. Cryst. Liq. Cryst.* **322**, 305 (1998).
6. T. Sugimoto, G. E. Dirige, and A. Muramatsu, *J. Colloid Interface Sci.* **173**, 257 (1995).
7. T. Sugimoto, G. E. Dirige, and A. Muramatsu, *J. Colloid Interface Sci.* **176**, 442 (1995).

This page is intentionally left blank

International Journal of Nanoscience, Vol. 1, Nos. 5 & 6 (2002) 557–562

FORMATION OF GOLD NANOPARTICLES/OLIGOTHIOPHENE DITHIOLS COMPOSITE THIN FILMS BETWEEN MICROGAPPED GOLD ELECTRODES AND THEIR ELECTRONIC PROPERTIES

SEISUKE MAEDA* and TAKUJI OGAWA†

Department of Chemistry, Faculty of Science, Ehime University
2-5 Bunkyocho, Matsuyama, Ehime 790-8577, Japan
†*Precursory Research for Embryonic Science and Technology*
Japan Science and Technology Corporation
1-8 Honcho, Kawaguchi, Saitama 332-0012, Japan
**maeda@chem.sci.ehime-u.ac.jp*
†*ogawat@dpc.ehime-u.ac.jp*

Received 27 November 2002

We have studied the construction and electronic characteristics of a series of devices made from gold microgap electrodes, gold nanoparticles and conjugated oligothiophene dithiols. The formations of gold nanoparticle/oligothiophene dithiol composites on gold surface were monitored by quartz crystal microbalance (QCM) using gold electrode coated crystal oscillator. The formation speed was the fastest for terthiophene dithiol followed by hexathiophene and nanothiophene dithiols, the latter two showed almost the same formation speed. The current–voltage (I/V) curves of these devices were measured at various temperatures to show that at high temperature (>200 K) they were almost straight line; at lower temperature they became parabolic, and at 4 K a completely blocked region appeared between −12 to +12 V. We attributed the parabolic I/V curve to a tunneling mechanism and the blocked region to the Coulomb blockade phenomena.

Keywords: Microgap electrode; oligothiophene; gold nanoparticle; the Coulomb blockade.

1. Introduction

Self-assemblies of nanometer scale constitutes such as molecules or nanoparticles in micro- or nanoscale fabricated solid structures are essential for bottom–up nanoscience and nanotechnology. We are interested in using chemical adsorption of organic functionality to metal surface for such self-assembly, because the chemical bondings are the strongest between them, that can affect the electronic states of them to exhibit possibly new phenomena.

It has been reported that the mixing of organic dithiols with protected gold nanoparticles in solution make a three-dimensional composite.[1] In a previous paper

†Corresponding author.

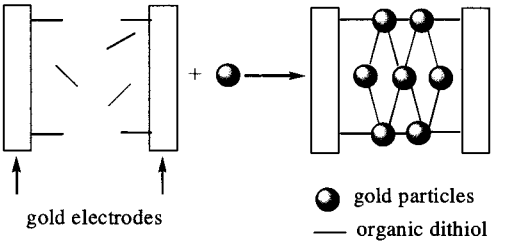

Fig. 1. Conceptual picture of our experiment.

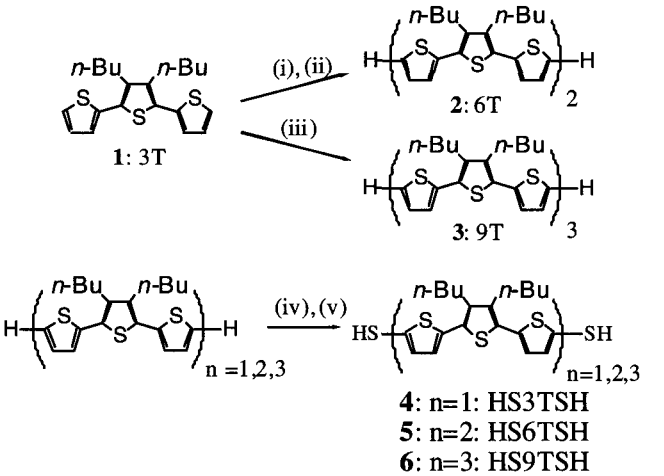

Reagents: (i) N-bromosuccinimide (NBS)/dimethylformamide (DMF); (ii) Zn, $NiBr_2$, triphenylphosphine/DMF; (iii) NBS, Mg, $NiCl_2$(diphenylphosphinopropane)/tetrahydrofuran (THF); (iv) KSCN, Br_2/CH_3OH, $CHCl_3$; and (v) $LiAlH_4$/THF.

Scheme 1. Synthetic scheme of the oligothiophene dithiol.

we found that by mixing them in the presence of gold microgap electrodes, a thin film of the three-dimensional composites were formed on and between the electrodes (Fig. 1), and sigmoidal current/voltage (I/V) curves were obtained for the devices made from 1–3 nm diameter gold nanoparticles and 1,10-decanedithiol.[2] This time, we have synthesized a series of oligothiophenes dithiols (Scheme 1, **1**–**3**), fabricated the devices, and measured their electronic properties in temperature range of 4–200 K.

2. Results and Discussion

2.1. *Synthesis of oligothiophene dithiols*

In order to see the structure–properties relationships, we synthesized terthiophene dithiol (**4**), hexathiophene dithiol (**5**) and nonathiophene dithiol (**6**) for the above-

described devices, by the method shown in Scheme 1. The butyl groups were introduced at β-position to improve the solubility of these oligomers.

A 3′,4′-Dibutyl-2,2′;5′,2″-terthiophene (**1**; 3T) was prepared by modulation of a reported method. The hexathiophene (**2**; 6T) and nonathiophene (**3**; 9T) were synthesized from the terthiophene **1** as the building unit. A 5-Bromo-terthiophene (3T-Br) was prepared by bromination of **1** with N-bromosuccinimide, which was homo-coupled by a nickel catalyst to form hexathiophene **2**. A Nonathiophene **3** was obtained by the nickel catalyzed coupling of 5,5″-dibromoterthiophene (Br-3T-Br), which was prepared by a double bromination of **1**, with the Grignard reagent prepared from 5-bromoterthiophen. The thiol groups at both ends of the oligothiphenes were introduced as a connecting functionality to the gold surface. The cyanothio groups were substituted at both ends of the oligothiophenes by using bromine and potassium thiocyanate, and the bis(cyanothio)oligothiophenes were reduced by $LiAlH_4$ to give the oligothiophene dithiols (**4**, **5** and **6**).[3]

2.2. *Preparation of the gold nanoparticles*

The gold nanoparticles of 1–3 nm diameter were prepared by modulation of the reported method.[1] In the report, 1-dodecanethiol was used as the surface coating reagent, however the thiol is so strongly bonded to the gold nanoparticles that no substitution was possible with other thiols afterward. We prepared gold nanoparticles protected by 2-methylundecan-2-thiol (*tert*-dodecanethiol). The latter gold nanoparticles were stable enough for column purification using silica-gel and toluene as the eluent, and enough reactive toward the oligothiophene dithiols to make the three-dimensional network as shown in Fig. 1. By the column purification, the ammonium salt which was used in the preparation procedure was completely removed as was checked by the ^1H NMR spectral investigation.

2.3. *Thickness measurement of the three-dimensional composite films by quartz crystal microbalance (QCM)*

By mixing the gold nanoparticles protected by the *tert*-dodecanethiol with oligothiophene dithiols in toluene in the presence of microgapped gold electrodes tips, the three-dimensional composite was formed on the surface of the tips. In the discussions about the electronic conductivity of the devices, the thicknesses of the films are indispensable. We tried atomic force microscopy (AFM) to measure the thickness of them to find the difficulty of defining the common reference planes. The QCM measures the weight of the film deposited on the surface of the quartz crystals, thus if the density of the materials is known the thickness will be calculated. By simultaneously dipping the quartz crystal into the solution with the microgapped gold electrodes tips, a rough estimations of the film thickness made on the tips are possible.

We prepared the following solutions: (A) 10 mmol/dm^3 protected gold nanoparticle solution in toluene; (B) 1 mmol/dm^3 oligothiophene dithiol solutions in

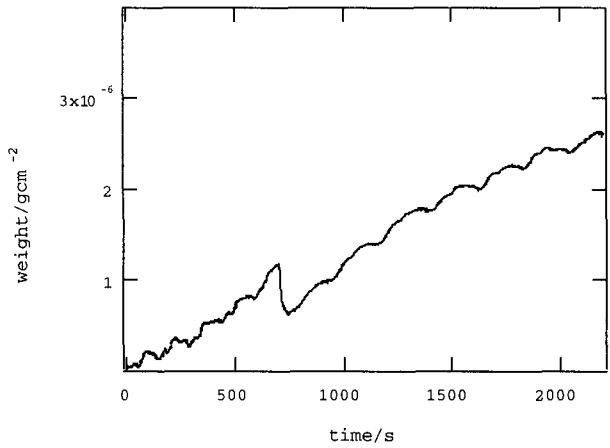

(a)

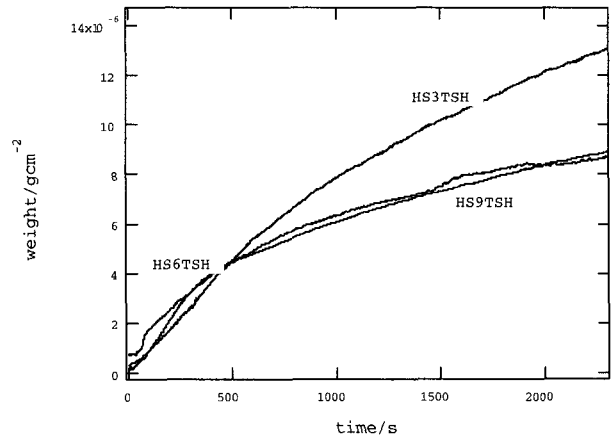

(b)

Fig. 2. The weight change of the deposited film as measured by QCM. (a) 1 mmol/dm^3 hexathiophene dithiol **5** and 10 mmol/dm^3 protected gold nanoparticle in toluene. (b) 10 mmol/dm^3 oligothiophene dithiols **4**, **5**, **6** and 10 mmol/dm^3 protected gold nanoparticle in toluene.

toluene; (C) 10 mmol/dm^3 oligothiophene dithiol solutions in toluene. In the first experiment, a quartz crystal was dipped into ca. 8 cm^3 toluene to which 1 cm^3 of solution B was added followed by the addition of 1 cm^3 of solution A. The zero time was defined as the time when solution A was added, and the change of weight was plotted against time. Figure 2(a) shows a typical case for oligothiophene dithiol **5**. As shown, a relatively long term oscillation was observed with ca. 200 s. This could be a spatiotemporal chaotic phenomena and detailed mechanism will be discussed in future reports.

When more concentrated solution of oligothiophene dithiols were used (solution C) such chaotic phenomena was not observed and monotone increasing curve was exhibited as shown in Fig. 2(b). If we assume the average density of the composite to be 10 g/cm^3, 10×10^{-6} g/cm^2 corresponds to 10 nm. Consequently, for the dithiol **4** ca. 1500 s after the addition of the gold nanoparticles, about 10 nm average thickness of the film was formed on the surface of gold.

2.4. *Measurements of the electronic properties of the devices*

We measured the electronic characteristics of these devices at various temperatures from 298 K to 4 K. The results of a device made from the gold nanoparticles and nonathiophene dithiol **6** measured at 200 K was shown in Fig. 3(a). The

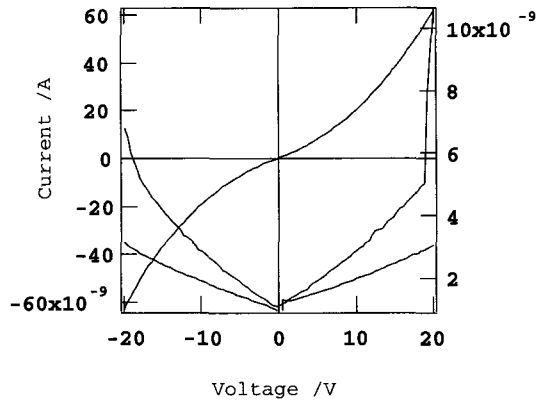

(a)

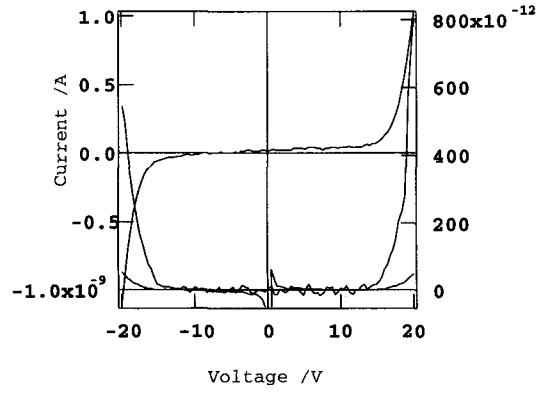

(b)

Fig. 3. Current (—), differential conductance (- - -), and conductance (. . .) of the device made from the Au nanoparticles and **6**, measured at (a) 200 K and (b) 4 K.

current–voltage curve was sigmoidal and the conductance–voltage curve was almost straight line. Such $I = kV^2$ relationship can be attributed to a tunneling mechanism. Figure 3(b) is a result of the same device measured at 4 K, showing a clear blockade region at around −12 to +12 V.

This blockade can be the Coulomb blockade phenomena; when an electron charges a gold nanoparticle, the next coming electron needs to overcome the Coulomb repulsive potential to pass through it. If we assume that the size of one unit (gold nanoparticle and oligothiophene) is about 5 nm, about 200 units are present between 1000 nm gap. On this assumption, 12 V bias voltage affords 60 mV potential for each unit. The charging energy (U_c) is defined as $U_c = e^2/8\pi\varepsilon r$, where r is the diameter of the charged metal. For r = 1–3 nm particles, U_c is calculated to be in the range of 100–200 mV, which is reasonably consistent with the estimated potential of 60 mV.

References

1. M. Brust, M. Walker, D. Bethell, D. J. Schiffrin, and R. Whyman, *J. Chem. Soc., Chem. Commun.*, 801 (1994); M. Brust, D. Bethell, D. J. Schiffrin, and C. J. Kiely, *Adv. Mater.* **7**, 795 (1995); M. Burst, J. Fink, D. Bethell, D. J. Schiffrin, and C. Kiely, *J. Chem. Soc., Chem. Commun.*, 1655 (1995); C. S. Weisbecker, M. V. Merritt, and G. M. Whitesides, *Langmuir* **12**, 3763 (1996).
2. T. Ogawa, K. Kobayashi, G. Masuda, T. Takase, and S. Maeda, *Thin Solid Films* **393**, 374 (2001).
3. K. Zong, W. Chen, M. P. Cava, and R. D. Rogers, *J. Org. Chem.* **61**, 8117 (1996).

International Journal of Nanoscience, Vol. 1, Nos. 5 & 6 (2002) 563–567

PREPARATION OF ZnO NANOPARTICLES BY PRECIPITATION/MECHANOCHEMICAL METHOD

SHICHENG ZHANG*, LEI CHI, and XINGGUO LI

State Key Laboratory of Rare Earth Materials Chemistry and Applications
Peking University, Beijing 100871, the People's Republic of China
**s.c.zhang@263.net*

Received 27 November 2002

The ZnO nanoparticles were synthesized by using a combination of precipitation and mechanical milling. Basic zinc carbonate precursor was prepared by precipitation process using zinc sulfate as the starting material. Under the mechanochemical effect, parts of the basic zinc carbonate were transformed into ZnO. In the closed system of milling, in order to produce pure ZnO nanoparticle phase, further heat processing was needed. But the ultimate ZnO particles were more uniform and the particle size distribution was narrower. The effects of mechanical milling process on properties of ultimate ZnO particles were also investigated.

Keywords: ZnO; nanoparticles; mechanochemical.

1. Introduction

The ZnO nanoparticles are important materials and have been widely used in pigments, rubber additives, gas sensors, varistors, transducers, transparent UV-protection films, UV light-emitting devices, chemical sensors, etc. In order to obtain high quality zinc oxide powders with fine particle size, narrow size distribution and special morphology, various preparation techniques have been used, including precipitation,[1] sol–gel,[2] microemulsion,[3] hydrothermal method,[4] laser vaporization–condensation,[5] etc. Some combination methods were still being used, such as precipitation/microwave,[6] precipitation/sonochemical,[7] precipitation/mechanical milling,[8] etc. Among them, the precipitation method has been used industrially. Commonly, the precipitation method needs heat processing of precipitation precursor, which consumes more energy. During the heat processing, the particles subject to agglomerate, which leads to broaden particle size distribution. In this paper, we try to use the combination of precipitation and mechanical milling to decrease the energy consumption and get uniform ZnO nanoparticles.

*P. O. Box 171, College of Chemistry and Molecular Engineering, Peking University, Beijing 100871, P. R. China.

2. Experimental Section

Part of the experimental procedure was similar to that of Deng *et al.*[8] Zinc oxide powder was prepared through three steps: (1) precipitation process, (2) mechanical milling of the precipitation precursor, and (3) further heat processing. First, basic zinc carbonate precursor was precipitated from zinc sulfate. 50 mL 1 $molL^{-1}$ Na_2CO_3 solution was added dropwise into 50 mL 1 $molL^{-1}$ $ZnSO_4$ solution under vigorous stirring. Subsequently, the precipitation was stirred for 2 h under certain temperature, washed with deionized water and ethanol, and then dried in an oven at 60°C.

In the mechanical milling process, sodium chloride was added to avoid agglomeration. The mixture of 10 g basic zinc carbonate and 40 g NaCl was milled at 300 rpm in a Fritsch-5 Planetary Mill. The 10 mm diameter agate balls were used. In order to study the influence of milling time, samples were taken at 5 h, 10 h, 15 h, 20 h, and 30 h.

For the production of pure ZnO nanoparticles phase, further heat processing was needed. The as-milled powders were heated in air in ceramic crucibles for 2 h at 300°C. Furthermore, the products were washed with deionized water and dried in oven at 60°C.

The structure and morphology of basic zinc carbonate, as-milled powders, and ultimate products were investigated using X-ray diffraction (Rigaku D/MAX-RA diffractometer with CuK_α radiation), transmission electron microscopy (JEM 200CX TEM), and scanning electron microscopy (AMRAY-1910 FE SEM). A thermogravimetric analysis (TGA) was carried out using Du Pont thermal analysis system (Dupont 1090B TGA 951 thermogravimetric Analyzer) with a heating rate 10°/min. The BET surface area was measured using a SA3100 surface area analyzer.

3. Results and Discussions

3.1. *Mechanochemical decomposition of as-precipitated powders*

Figure 1 shows the X-ray diffraction patterns of as-precipitated and as-milled powders. It can be found that all the peaks of as-precipitated powders can be identified as reflections of the $Zn_5(OH)_6(CO_3)_2$ phase.[9]

With traditional precipitation method, the ZnO was formed by decomposing carbonate or hydroxide of zinc under high temperature (over 300°C). To our knowledge, there are no reports about the preparation of ZnO by decomposing zinc compound with ball mill. Deng had reported the mechanical milling of zinc hydroxide, but had not got the ZnO phase in the as-milled power.[8] From Fig. 1, it can be seen that the ZnO phase had already appeared after milling 5 h, and with the prolonging of the heat processing time, the amount of ZnO was increased. But the pure ZnO phase could not be achieved. The reason may be interpreted from the formation mechanism of ZnO.

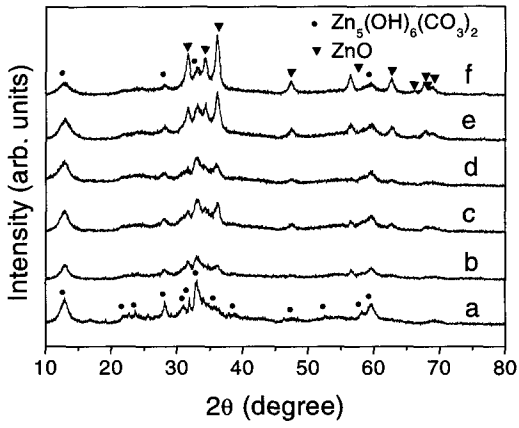

Fig. 1. X-ray diffraction patterns of (a) as-precipitated and as-milled powders with different milling time: (b) 5 h; (c) 10 h; (d) 15 h; (e) 20 h; and (f) 30 h.

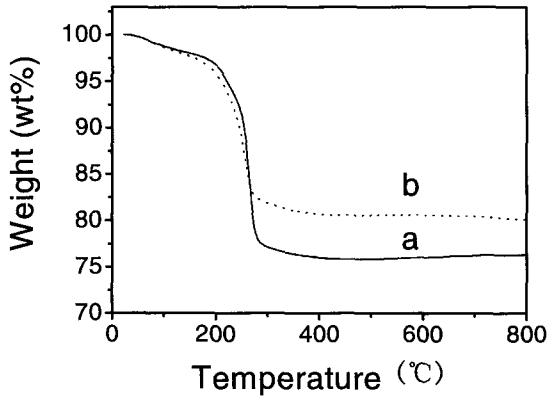

Fig. 2. Thermogravimetric analysis of (a) as-precipitated powders and (b) as-milled powders (30 h).

The decomposition reaction of basic zinc carbonate proceeds according to Eq. (1):

$$Zn_5(OH)_6(CO_3)_2 \leftrightarrow 5ZnO + 2CO_2 + 3H_2O\,. \tag{1}$$

For the mechanical milling proceeded in a closed system, with proceeding of the reaction, the partial pressure of CO_2 was becoming bigger and restrained the reaction. If in an open system, the reaction proceeds thoroughly, the pure ZnO phase can be obtained. This perhaps is easier to realize for industrial equipment.

Figure 2 shows the TGA measurements on the basic zinc carbonate and as-milled powders. It can be seen that both of them lost their weight in two steps, the first step at around 100°C, and the second step at 246°C and 228°C, respectively. The first step of the thermal decomposition is the loss of water followed by

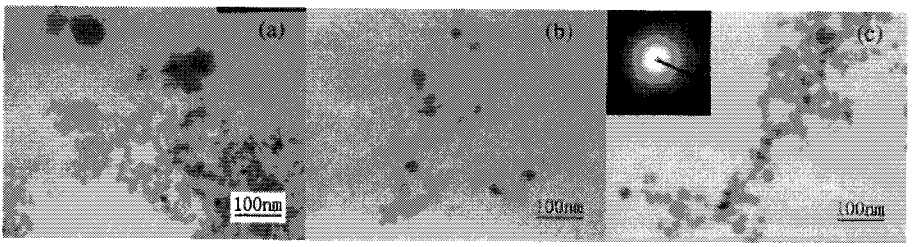

Fig. 3. Morphologies of (a) as-precipitated powder and as-milled powder with milling time (b) 5 h and (c) 15 h after heat processing.

the decomposition of the $Zn_5(OH)_6(CO_3)_2$ phase to ZnO, as seen from the weight loss. The as-milled powder is a mixture of ZnO and $Zn_5(OH)_6(CO_3)_2$. Its residue of thermal decomposition is higher than that of as-precipitated powder. The decomposition temperature of $Zn_5(OH)_6(CO_3)_2$ in as-milled state is lower than that of as-precipitated state. Maybe, there are some residual stresses in the as-milled powders, or the mechanical milling process lowers the activation energy of the decomposition of $Zn_5(OH)_6(CO_3)_2$.

From the TEM results, the as-precipitated powder was needle-like and agglomerated to large particles. After being milled, the powder was more uniform and the agglomerated particles were smaller.

3.2. *Further heat processing*

From Fig. 2, a temperature as low as 300°C is sufficient for complete decomposition of the zinc compound. For the production of pure ZnO phase, the as-milled powder was annealed at 300°C. After heat processing, all the samples were transformed to ZnO phase. From the results of TEM (Fig. 3) and BET, with the prolonging of milling time, the particle sizes of ZnO from precursors being milled were decreased from ~38 nm to approximately 18 nm. This result could also be conformed by broaden of the peaks of XRD. From Fig. 3, it could also be shown that, after being milled, the particle size distribution was narrower and the particles were more uniform.

4. Conclusions

In this paper, we used $Zn_5(OH)_6(CO_3)_2$ as the as-precipitation precursor, from which ZnO nanoparticles can easily obtain directly by mechanical milling. For the close system of milling, it was difficult to get pure ZnO nanoparticle phase, and further heat processing was needed. Mechanical milling can reduce the decomposition temperature of $Zn_5(OH)_6(CO_3)_2$ about 20°C and it also can lead to the reduction of particles size, narrow particle size distribution, and uniform particles. With the prolonging of milling time, the particle size decreased from ~38 nm to approximately 18 nm in our experiments.

Acknowledgments

This work was supported by NSFC (Nos. 20025103 and 20171002) and MOST of China (No. 2001CB610503).

References

1. J. E. Rodríguez-Paéz, A. C. Caballero, M. Villegas, C. Moure, P. Durán, and J. F. Fernández, *J. Euro. Ceram. Soc.* **21**, 925 (2001).
2. D. Mondelaers, G. Vanhoyland, H. Van den Rul, J. D'Haen, M. K. Van Bel, J. Mullens, and L. C. Van Poucke, *Mater. Res. Bull.* **37**, 901 (2002).
3. D. Kaneko, H. Shouji, T. Kawai, and K. Kon-No, *Langmuir* **16**, 636 (2000).
4. W. J. Li, E. W. Shi, M. Y. Tian, B. G. Wang, and W. Z. Zhong, *J. Mater. Res.* **14**, 1532 (1999).
5. M. S. El-Shall, D. Graiver, U. Pernisz, and M. I. Baraton, *NanoStructured Mater.* **6**, 297 (1995).
6. S. Komarneni, M. Brunoa, and E. Mariani, *Mater. Res. Bull.* **35**, 1843 (2000).
7. R. Vijaya Kumar, Y. Diamant, and A. Gedanken, *Chem. Mater.* **12**, 2301 (2000).
8. H. M. Deng, J. Ding, Y. Shi, X. Y. Liu, and J. Wang, *J. Mater. Sci.* **36**, 3273 (2001).
9. JCPDS 19-1458.

This page is intentionally left blank

International Journal of Nanoscience, Vol. 1, Nos. 5 & 6 (2002) 569–573

IMPRINT OF HONEYCOMB PATTERN ON PDMS ELASTOMER

TAKUYA OHZONO, NOBUKO FUKUDA,
TAKEHIRO NISHIKAWA, and MASATSUGU SHIMOMURA*

Dissipative-Hierarchy Structures Laboratory
Spatio-Temporal Function Materials Research Group
Frontier Research System, RIKEN
2-1 Hirosawa, Wako, Saitama 351-0198, Japan

Received 27 November 2002
Revised 17 December 2002

Recently a method that utilizes the condensation of micrometer-sized water droplets on evaporating solutions of polymers has been reported for the preparation of porous thin films with fine hexagonal periodicity, honeycomb films. Here we report a method for imprinting a honeycomb pattern on the PDMS (poly(dimethyl siloxane)) elastomer. For the preparation of the honeycomb film, a benzene solution of amphiphilic copolymer was cast at high atmospheric humidity. On the film the PDMS precursor was poured and cured. The cured PDMS with the honeycomb film was peeled from the slide glass. The PDMS was rinsed with the solvent to remove the honeycomb film. The exposed PDMS surface was observed using SEM and AFM. The pattern-imprinted PDMS surface can be used as a template for patterning of materials, which are difficult to produce a honeycomb pattern by the conventional method described above. Here, we show some examples of such honeycomb-originated structures composed of polymers or nanoparticles, which were fabricated using the pattern-imprinted PDMS. The present study shows an example of the secondary uses of the self-organized structures for the cost-saving micro/nanofabrication of various materials.

Keywords: Honeycomb pattern; soft lithography; pattern transfer.

Photolithography and other lithography, which are recognized as top–down approaches, have been the most successful techniques for the fabrication of fine micro/nanoscale textures. On the other hand nonlithographic approaches have also been extensively investigated to reduce or replace the complex process involved in those lithographic techniques. For example, it has been reported that microtextures can be fabricated using the self-organization of polymers.[1,2] Polymer films having a honeycomb structure have been produced by evaporating a solution of various materials.[3–9] The spontaneous formation of the hierarchical structures that range from nanoscale to the mesoscopic alignment is an intriguing feature of the

*Nanotechnology Research Center, Research Institute for Electronic Science, Hokkaido University, N12W6, Sapporo, 060-0812, Japan.

lithography-free fabrication process using the self-organization of the system, because the technique is more cost-saving and technologically simpler than the lithographic techniques. However, there are a lot of limitations for the materials to be fabricated only by the self-organization process, because the process is often sensitive to the materials included. Therefore, it is important to establish methods to transfer the useful self-organized structures or patterns to other various materials, which are difficult to be fabricated by the self-organized process. In other words, the secondary use of the self-organized structures or patterns is demanded for the wide variety of the nano/microfabrication of various materials.

In the present study, we show some examples of the process, the transfer of the self-organized structures or patterns. We have chosen the honeycomb structure of a polymer film produced by evaporating a volatile solution of polymers as an example of the self-organized structure to be transferred. The soft lithographic method has been employed for the pattern transfer. The poly(dimethyl siloxane), PDMS, elastomer mold that has the negative pattern of the original honeycomb structure has been fabricated and used for the patterning of other materials, such as PDMS, nanoparticles, and polymers. It has been demonstrated that we are able to imprint the honeycomb pattern on the PDMS and generate honeycomb-structure-originated patterns of those materials by simple procedures.

For preparation of the honeycomb film twenty microliters of dilute benzene solution of amphiphilic copolymer **1** (0.9 g/L)[10] were cast onto a cleaned glass slide and humidified air (20°C and 80% r.h.) was blown to the solution surface from a

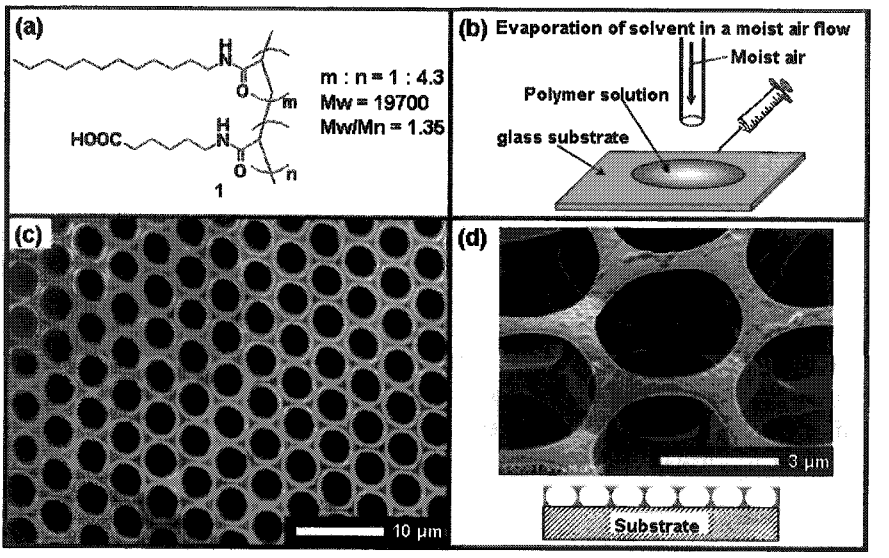

Fig. 1. (a) The chemical structure of the polymer **1**. (b) An experimental setup for the honeycomb film formation. (c) An optical microscopic image of the film. (d) An SEM image and a schematic illustration for the cross section of the film used in this study.

glass pipe nozzle ($\phi = 5$ mm) at the flow rate in the range from 100 to 300 mL/min (Fig. 1). The fabricated porous film was dried in the ambient atmosphere. The honeycomb structure was spontaneously formed through the self-assembling process.

For preparation of the poly(dimethyl siloxane), PDMS, elastomer (Sylgard184, Dow-corning) mold, the precursor was poured onto the honeycomb film on the glass slide. The PDMS was cured at 70°C for 2 h. The cured PDMS was peeled from the glass slide and was rinsed with benzene for removal of the polymer from the PDMS (Fig. 2(a)). Then, the PDMS mold was dried. The top surface profile of the mold showed the negative of the bottom-half part of the original honeycomb film (Fig. 2(b)) and the top-half part of the film was buried inside the mold (Fig. 2(c)). The microstructure of the film was successfully imprinted on the PDMS.

Four examples of the material patterning using the prepared PDMS molds are briefly shown in Fig. 3. Although the details are not described here, the results indicate that the bottom-half part of the original honeycomb structure could be transferred to various materials, such as PDMS, silica nanoparticles, and the poly(L-lactic acid). Furthermore, the secondary imprint on the PDMS enables us to do third pattern transfer that is the case of example (III). In other words, it has been demonstrated that both the negative and the positive pattern transfers of the honeycomb pattern are possible with the soft lithographic method.

In summary, the structure of the bottom-half part of the honeycomb film was imprinted on the PDMS elastomer. The PDMS mold was used as a template for the patterning of other materials. The present study represents an example of the

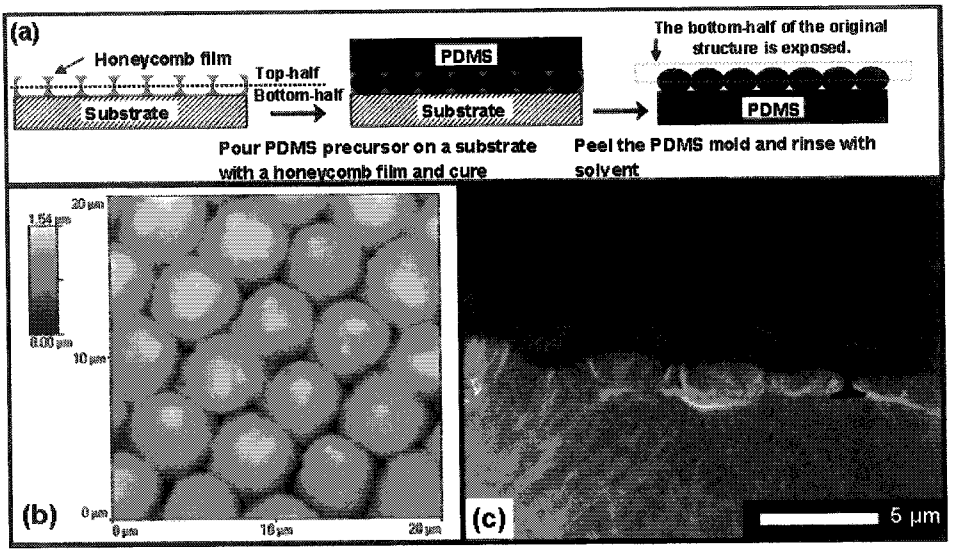

Fig. 2. (a) Schematics of the pattern imprinting process. (b) An AFM image of the pattern-imprinted PDMS mold. (c) An SEM image of a cross sectional part of the pattern-imprinted PDMS mold. The outline for a part of the profile is emphasized by the black line.

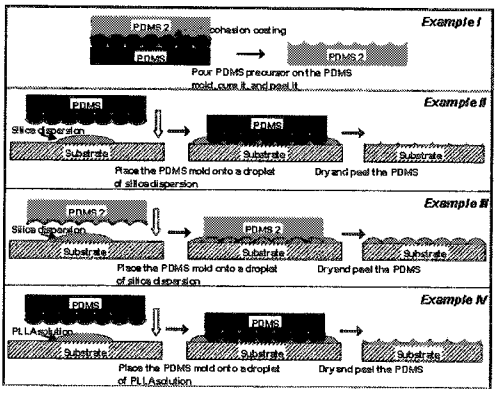

(a)

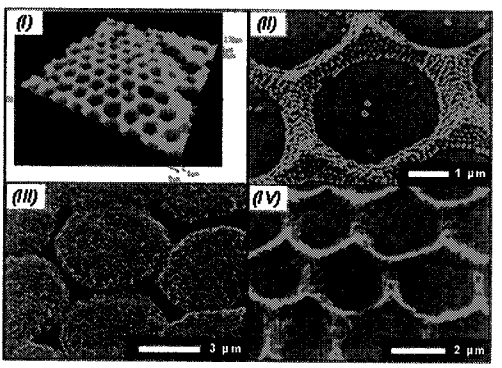

(b)

Fig. 3. (a) Schematics of each patterning process. (I) The PDMS was patterned using the PDMS mold to obtain another PDMS mold with a positive pattern of the honeycomb structure. The surface of the original PDMS mold was treated by the perfluoroalkylated silane coupling agent to form an thin anti-cohesion coating, which prevents direct contact between the original and the newly-prepared PDMS and promotes their exfoliation. The PDMS precursor was cured on the original PDMS mold with the same condition described previously, and peeled. The anti-cohesion coating was also done for the PDMS mold when it is used for patterning on other below cases. (II) Silica beads (ϕ = 100 nm, Nissan Chemical, Japan) was patterned on a cover glass using the PDMS mold. Ten microliters of the colloidal silica aqueous dispersion was placed on the cover glass and the PDMS mold was placed over the droplet. The solution was spread between the cover glass and the PDMS mold. At this time the excess solution oozed to the edge of the PDMS mold was removed with blotting paper. The cover glass with the mold was dried overnight (20°C and 20% r.h.), then, the PDMS mold was removed. (III) Silica beads (ϕ = 100 nm) was patterned using the PDMS mold with a positive pattern of the honeycomb structure, which was prepared at the example (I). The procedure was same as that for the example (II). (IV) The poly(L-lactic acid); PLLA, ($M_w = 8.5 \times 10^4$ to 1.6×10^5) was patterned using the PDMS mold as an example of the patterning of polymers from solution. Ten microliters of the chloroform solution was placed on the cover glass and the PDMS mold was quickly placed over the droplet of the solution. The solution was spread between the cover glass and the PDMS mold. The cover glass with the mold was dried overnight (20°C and 20% r.h.), then, the PDMS mold was removed. Prepared samples were observed using the atomic force microscope, AFM (Explorer SPM, ThermoMicroscopes) and scanning electron microscope, SEM (S-5200, Hitachi). (b) (I) An AFM image and (II)–(IV) SEM images of each patterned material.

secondary use of the fine structure formed through the self-assembling process. The secondary use leads to a structure and a pattern of a complexity that would be difficult to fabricate by other methods.

References

1. G. J. Liu and J. F. Ding, *Adv. Mater.* **10**, 69 (1998).
2. G. Reiter, *Phys. Rev. Lett.* **68**, 75 (1992).
3. G. Widawski *et al.*, *Nature* **387**, 369 (1994).
4. S. A. Jenekhe and X. L. Chen, *Science* **283**, 372 (1999).
5. N. Maruyama *et al.*, *Thin Solid Films* **327–329**, 854 (1998).
6. O. Karthaus *et al.*, *Langmuir* **16**, 6071 (2000).
7. U. Stalmach *et al.*, *J. Am. Chem. Soc.* **122**, 5464 (2000).
8. L. V. Gover *et al.*, *Macromol. Chem. Phys.* **201**, 2721 (2000).
9. T. Yonezawa *et al.*, *Adv. Mater.* **13**, 140 (2001).
10. T. Nishikawa *et al.*, *Langmuir* **18**, 5734 (2002).

This page is intentionally left blank

International Journal of Nanoscience, Vol. 1, Nos. 5 & 6 (2002) 575–579

MANIPULATION OF CARBON NANOTUBE BUNDLES WITH CONTACT MODE ATOMIC FORCE MICROSCOPY

ZIYONG SHEN*, SAIJIN LIU, SHIMIN HOU, and ZENGQUAN XUE
Department of Electronics, Peking University, Beijing 100871, China
**szy@ele.pku.edu.cn*

ZHENNAN GU
College of Chemistry and Molecular Engineering
Peking University, Beijing 100871, China

Received 27 November 2002
Revised 19 December 2002

The cutting and splitting of carbon nanotube bundles were realized with an atomic force microscopy (AFM) in contact mode. The results of manipulating were found depending on the tip–bundle interaction and bundle–substrate interaction. With an optimal force load of AFM tip, the lateral force applied on the nanotube bundle could overcome the adhesive interaction between nanotubes within the bundle, consequently separating individual nanotubes from the bundle. The threshold of the tip force load was found to be ~45 nN in our experiments. This technique provides new possibilities for the controllable manipulation of carbon nanotubes.

Keywords: Carbon nanotube; atomic force microscopy; manipulation.

1. Introduction

Carbon nanotubes (CNTs) have unique structures and novel mechanical and electronic properties. Single-walled carbon nanotubes (SWCNTs) are one-dimensional conductors or semiconductors depending on their radius and helicities. The transport properties of SWCNTs can be greatly modified by native defects or localized distortion of the lattice induced by artificially bending.[1] These outstanding electronic properties together with their nanometer scale size and high strength as well as flexibility, make nanotubes the ideal building block for nanotechnology and nanoelectronics.

Atomic force microscopy (AFM) is a powerful tool and has been successfully applied in the research of mechanical properties of nanotubes. In this work, we report our approach to manipulating the SWCNT bundles with an AFM. Our results show that the manipulating results depend on the tip–bundle interaction as

*Corresponding author.

well as the bundle–substrate interaction. Controllable cutting and splitting of CNT bundles were realized by carefully optimizing of the tip–bundle interaction. This technique will provide new chance for the nanotube application.

2. Experiments

The SWNTs used in this work were produced by the arc discharge method using Y-Ni catalyst. Previous study have shown that most of the produced SWNTs have a diameter of 1.3–1.4 nm and are dominated by armchair (n, n) type carbon nanotubes (n = 8, 9, 10, 11).[2] The SWNTs were purified and ultrasonically dispersed in isopropanol. A few drops of the solution were deposited on the surface of highly oriented pyrolytic graphite (HOPG) and dried in air at room temperature. A commercial AFM (Solver P47, NT-MDT) was used to image and manipulate CNT bundles. The AFM was operated in contact mode and an ultrasharp Si tip with a radius of curvature of about 10 nm was used.

3. Results and Discussions

The adsorbed nanotubes on HOPG exhibited two types of morphologic character in AFM images. One type of bundles had rough surface and usually were curved or bended (Fig. 1(a)). These bundles consisted of nanotubes which had structural defects formed during the arc discharge process, so it was easy for them to bond with metal catalyst clusters, carbon onions or amorphous carbon. We found some of the bundles were difficult to image stably, due to their weak interaction with the substrate. But when the bundles attached with big particles, they could be stabilized by pinning on the substrate through the particles. In this case, the bundles could be bent or cut with AFM tip easily. Figures 1(a) and 1(b) show the AFM images of a bundle before and after a cutting manipulation.

The manipulation procedure followed several steps. First, the surface was imaged in a standard way in contact mode; the bundle and the manipulating area were selected. Then the tip–bundle interaction was enhanced by gradually increasing the setpoint value of the tip. Afterward multiple successive lines were scanned over the selected area according to the predefined direction. In the scanning process, the

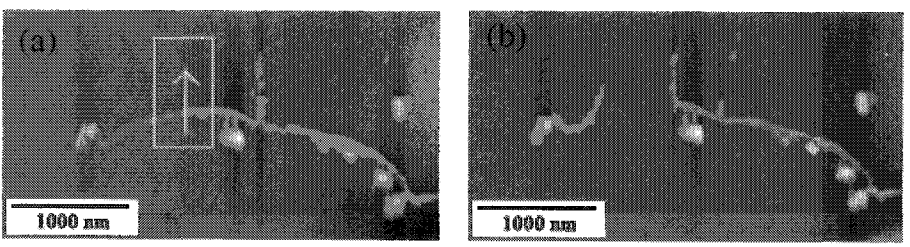

Fig. 1. AFM topographic images of a bundle (a) before and (b) after a cutting manipulation. The white rectangle frame and arrow show the manipulating area and tip scanning direction.

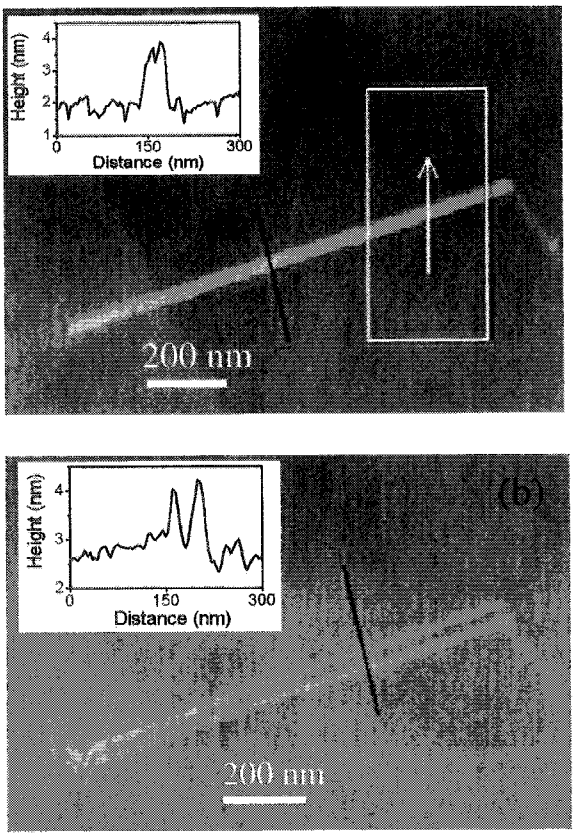

Fig. 2. AFM topographic images of a bundle (a) before and (b) after a splitting manipulation. The white rectangle frame and arrow show the manipulating area and tip scanning direction. The insets show cross section analysis of the corresponding bundle along the black lines.

feedback loop was cut off and the tip was scanned with a high speed (10 μm/s). As a result, a strong force would exert on the side of the bundle by the tip. It can be seen from Fig. 1(b) that the bundle was cut off under the force of the tip, but the position of the bundle was not changed, indicating the attached particles had strong interaction with the substrate, thus pinned the bundle on the HOPG surface and limited its moving under the force of the tip. This result also shows the bundle in Fig. 1(a) had high density of defects and could be deformed or broken easily under external forces.

Figure 2(a) shows a typical AFM image of another type of bundles adsorbed on the HOPG surface. This bundle has a length of 1.3 μm and a height of $\sim$2.0 nm. Its surface is quite smooth without any particles attached, indicating the perfect structures of the composed SWCNTs. By carefully optimizing the normal forces exerted on the bundles by the AFM tip, we realized the splitting of these bundles, and individual SWCNT were separated from bundles successfully. The manipulation

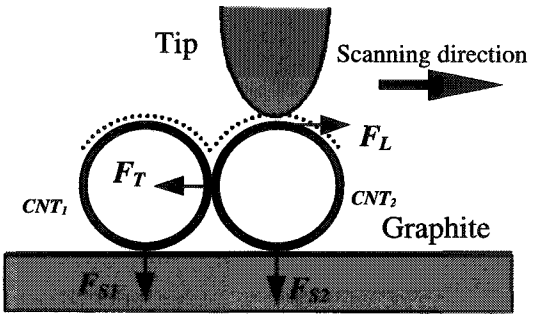

Fig. 3. Illustration of the interaction between the tip, the bundle and the surface as the tip moved above the bundle surface during the manipulating cycles.

procedure was like before, but the tip force load was increased for a small value (about 5 $\sim$ 10 nN) by directly lowering the tip toward the surface in small steps in every manipulating cycles. In the process of manipulating, the tip force load was increased gradually and new manipulating cycle was repeated until the bundle was successfully split. During manipulating cycles, the feedback loop was on and we kept its value and the scanning speed of the tip the same as those in the normal imaging condition. As a result, the tip would move over the bundle rather than push it away from side (Fig. 3). We believe this is the key fact for us to successfully split the bundle.

Figure 2(b) displays the topographic image of the bundle in Fig. 2(a) after manipulating with a tip force load of about 45 nN. It can be clearly seen from the image that the original bundle was split into two well-separated nanotubes under the force of the AFM tip. Although the topography of the original bundle in Fig. 2(a) is very uniform, the cross section analysis (inset to Fig. 2(a)) shows this bundle has a "raft" structure[3] and consists of two SWCNTs packed in parallel. The separated nanotubes have diameters of $\sim$1.5 nm and $\sim$1.8 nm, respectively, measured from their heights (inset to Fig. 2(b)). Since two nanotubes lay closely, we scanned the sample with different substrate orientations and verified that they were not artifacts caused by the "double tip" effect.

The interaction energy between nanotube and graphite surface was found having sharp potential energy minima when the nanotube is in atomic scale registry with the surface,[4] which would lead to orientational locking of nanotubes on the graphite surface. The total interaction energy scaled with the square root of the radius of nanotube. So the orientation and interaction energy of the bundle in Fig. 2(a) are dominated by the nanotube with a larger radius. When the AFM tip scanned over the bundle, a lateral force F_L was applied on the nanotube by the tip (Fig. 3). This force scales with the force load of the tip and tends to move the bundle along the tip scanning direction. At the same time, there is a binding force F_T between two SWCNTs, and normal forces F_{S1} and F_{S2} exist between the bundle and the graphite surface. The binding force F_T is weak compared with F_{S1} or F_{S2} because both

the interacting partners of F_T has curved surface. When we gradually increased the lateral force of the tip by increasing the tip force load, it is possible to satisfy the condition of $F_L > F_T$, consequently, the two nanotube will be separated by the lateral force of the tip. The separated nanotube would continue to move on the surface under the force of the tip, but whether it was sliding or rolling cannot be determined in our experiment. It would depend on the tip lateral force F_L and the friction force between the separated SWCNT and the underlying graphite surface.

4. Conclusion

In summary, we demonstrated that SWCNT bundles could be cut or split with an AFM tip. The manipulating results depended on the tip–bundle interaction as well as the bundle–substrate interaction. Bundles with perfect structures could be split by optimally controlling the normal force of the tip. Individual nanotubes thus could be separated from bundles using this technique. This technique will be helpful for the research and applications of new quantum devices based on carbon nanotubes.

Acknowledgments

This work was supported by National Natural Science Foundation of China [Nos. 69902002, 50202001, and 60211240632] and MOST of China [No. 2001CB610503].

References

1. D. Bozovic, M. Bockrath, J. H. Hafner, C. M. Lieber, H. Park, and M. Tinkham, *Appl. Phys. Lett.* **78**, 3693 (2001).
2. Z. Shi, Y. Lian, X. Zhou, Z. Gu, Y. Zhang, S. Iijima, L. Zhou, K. T. Yue, and S. Zhang, *Carbon* **37**, 1449 (1999).
3. S. S. Wong, A. T. Woolley, T. W. Odom, J. Huang, P. Kim, D. V. Vezenov, and C. M. Lieber, *Appl. Phys. Lett.* **73**, 3465 (1998).
4. A. Buldum and J. P. Lu, *Phys. Rev. Lett.* **83**, 5050 (1999).

This page is intentionally left blank

International Journal of Nanoscience, Vol. 1, Nos. 5 & 6 (2002) 581–585

SYNTHESIS OF CdTe NANOPARTICLE BY γ-IRRADIATION

SONG JA JO and YOUNG SOO KANG
Department of Chemistry, Pukyong National University, 599-1 Nam-gu Busan, 608-737, Korea

Received 27 November 2002
Revised 15 January 2003

Semiconductor CdTe nanoparticles were synthesized by the γ-irradiation of Cd ion complex at room temperature. Cd-olate complex was reacted with aqueous NaHTe solution. The products were investigated by X-ray Powder Diffraction (XRD) and Transmission Electron Microscopy (TEM). The optical properties of CdTe were investigated with UV-vis and photoluminescence (PL) spectra.

Keywords: Tellurium nanoparticles; γ-radiation.

1. Introduction

The synthesis with defined nanometer scale features is of great interest in material chemistry. Considerable progress has been made in group of II–VI semiconductor crystallines and its nanocrystallines. In the past, the methods involved solid reactions, aqueous solutions, gas reactions and the precursor ones. But such II–VI materials have been prepared at high temperature (above 500°C) or toxic gas H_2S.[4–8] It has been reported that the nanoscale products have different properties from each method. The new nanoscale materials have potential applications in both mesoscopic research and the development of nanodevices. Little research has been done on the one-dimensional nanomaterials such as nanowires, nanorod or nanotube at ambient conditions.[1] In the present study, radioactive radiation such as γ-ray was used to initiate the growth of cadmium sulfide particles by the reaction of solvated electron with the thiol (3-mercapto-1, 2-propandiol RSH) to release HS^- ions, and the resultant colloidal solutions including nanoparticle were studied. Recently γ-ray radiation has been used to produce nanocrystalline metals, alloys, metal oxide, and composites (ZnS, PbS and CuS, etc).[1–3,5] Yi Xie and co-workers reported a novel simultaneous *in situ* formation (SISF) technique for the synthesis ZnS nanowires via γ-irradiation.[1] Due to the work at atmospheric pressure and in the room temperature, this method can be used as a new method for the synthesis of inorganic nanoparticles via more simple process than the one in the past. In this paper, we synthesized CdTe nanoparticle by γ-ray radiation. The produced CdTe nanoparticles were studied on the crystal structure and on the optical properties.

2. Experiment

2.1. *Material*

Cadmium nitrate tetrrahydrate ($Cd(NO_3)_2 \cdot 4H_2O$, 99%), sodium borohydride ($NaBH_4$, 98%) and tellurium (Te, 99.8%) were obtained from Aldrich. Sodium oleate ($C_{17}H_{33}COONa$, 98%) was obtained from Junsei Chemical Co. Ltd.

2.2. *Synthesis of CdTe nanoparticle*

Sodium oleate (10.9 mmol) was dissolved in 80 ml of water to obtain aqueous solution. $Cd(NO_3)_2$ (5.5 mmol) was dissolved in 1 ml of water and mixed with the prepared sodium oleate solution. Tellurium (60.8 mmol) was dispersed in 25 mL of water to obtain aqueous solution. $NaBH_4$ (60.8 mmol) was dissolved in 25 mL of water and mixed with the prepared solution of Te in darkness. NaHTe solution (5.5 mmol) powders were added into mixed solution of sodium oleate and $Cd(NO_3)_2 \cdot 4H_2O$ and then continuously stirred for 2 h. The reactants were irradiated with γ-ray of a dose of 1.8×10^4 Gy in the field of a ^{60}Co γ-ray source. The product was washed with acetone, filtered and then dried at room temperature. The color of both products is reddish powders.

2.3. *Apparatus*

The samples were characterized by X-ray powder diffraction (XRD) patterns to investigate the crystal structure. XRD spectra were collected using a Philips, X'Pert-MPD system. Transmission Electron Microscopy (TEM) was investigated to study the morphology and particle sizes. TEM images were obtained using a Jeol, JEM-2010. The photoluminescence (PL) spectra were obtained to study the optical properties of the synthesized CdTe nanoparticles. PL spectra were recorded on a Perkin-Elmer (LS50B).

3. Result and Discussion

Figure 1 shows the XRD patterns of the CdTe nanoparticles synthesized by γ-ray radiation. The discernible peaks can be indexed to (111), (220), and (311) planes of the cubic structure of CdTe with cell constant $a = 5.641$ Å as Fig. 1. These are corresponding to the structure of CdTe (JCPDS, card no. 75-2086). A drop of CdTe nanoparticle in iso-octane was placed on the grid and dried in air. TEM image in Fig. 2 shows that CdTe nanoparticle was synthesized with the irregular spherical shape and rod shape. The size of CdTe nanocrystallines has been determined as $4 \sim 6$ nm size from the TEM image as in Fig. 2. This result indicates that the synthesis of CdTe nanoparticle by γ-ray radiation should be carried out by more carefully controlling the condition such as molar ratio among reactants, dose of γ-ray and radiation time. Further control of such conditions will be reported on the following report. The optical properties of as-prepared products including

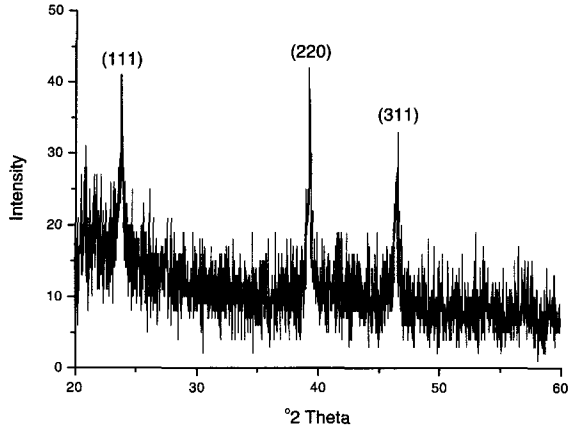

Fig. 1. XRD patterns of the synthesized CdTe nanoparticles by γ-ray radiation at room temperature.

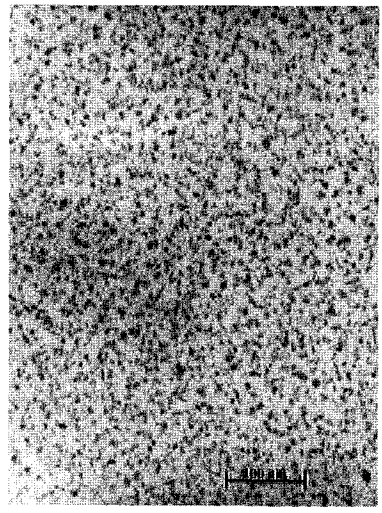

Fig. 2. TEM images of the synthesized CdTe nanoparticles by γ-ray radiation at room temperature.

the cadmium oleate and the synthesized CdTe powders were studied with photoluminescence spectra as in Fig. 3. Because the cadmium oleate was mixed with CdTe nanoparticles, the spectrum showed two major peaks at 420–500 nm and 500–540 nm. So, to get the spectrum of only the synthesized CdTe nanoparticle, the photoluminescence wavelength was cut-off at 500 nm and the spectrum shows the band at wavelength of 480–560 nm after the removal of cadmium oleate band as shown in Fig. 4. The photoluminescence spectrum of CdTe nanoparticle synthesized by γ-ray radiation shows a band at 500–540 nm as in Fig. 4. The synthesized

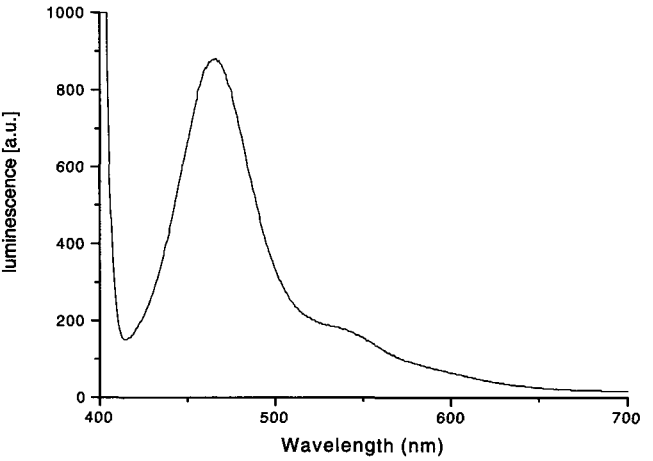

Fig. 3. Photoluminescence spectra for the cadmium oleate and the synthesized CdTe nanoparticles dispersed in iso-octane, $\lambda_{exc} = 389$ nm by γ-ray radiation at room temperature.

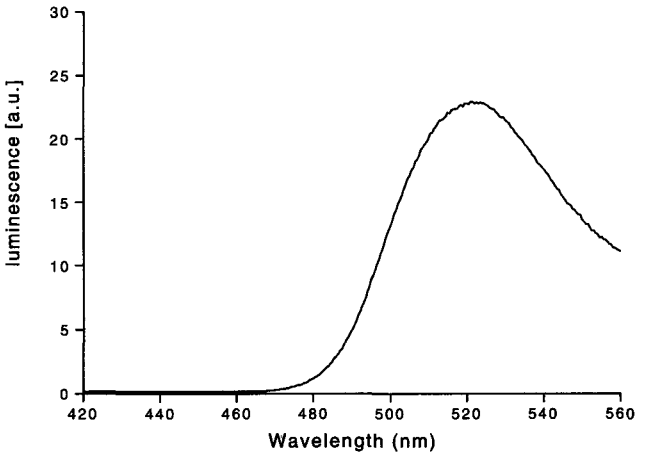

Fig. 4. Photoluminescence spectra for the synthesized CdTe nanoparticles dispersed in iso-octane after the removal of cadmium oleate, $\lambda_{exc} = 389$ nm by γ-ray radiation at room temperature.

nanoparticles were in the size quantization regime and showed a well-developed size-dependant maximum near the absorption onset, which was ascribed to the excitonic transition. This maximum shifted to higher energies with decreasing particle size indicates the increase of the nanocrystal's bandgap.

4. Conclusion

CdTe nanoparticle was synthesized by γ-ray radiation. The CdTe nanoparticle showed the size distribution range of 4 $\sim$ 6 nm and morphologies of the irregu-

lar spherical shape and rod shape. Photoluminescence spectra also showed a wide band around 520 nm. This is the first reported new method and this method will be further modified by the different concentration and radiation dose.

Acknowledgment

This study was financially supported by the Korean Ministry of Science and Technology (MOST) as Nuclear R&D Program.

References

1. X. Jiang, Y. Xie, J. Lu, L. Zhu, W. He, and Y. Qian, *Chem. Mater.* **13**, 1213 (2001).
2. Y. Liu, Y. Qian, M. Zhang, Z. Chen, and C. Wang, *Mater. Lett.* **26**, 81 (1996).
3. Z. P. Qiao, Y. Xie, J. G. Xu, Y. J. Zhu, and Y. T. Qian, *J. Colloid Interface Sci.* **214**, 459 (1999).
4. S.-H. Yu, Y.-S. Wu, J. Yang, Z.-H. Han, Y. Xie, Y.-T. Qian, and X.-M. Liu, *Chem. Mater.* **10**, 2309 (1998).
5. H. Liu, X. Ge, X. Xu, Z. Zhang, and M. Zhang, *Radiation in Phys. Chem.* **55**, 357 (1999).
6. R. J. Bandaranayake, G. W. Wen, J. Y. Lin, H. X. Jiang, and C. M. Sorensen, *Appl. Phys. Lett.* **67**, 831 (1995).
7. P. V. Braun, P. Osenar, V. Tohver, S. B. Kennedy, and S. I. Stupp, *J. Am. Chem. Soc.* **121**, 7309 (1999).
8. P. V. Braun and S. I. Stupp, *Mater. Res. Bull.* **34**, 463 (1999).
9. Y. Li, D. Xu, Q. Zhang, D. Chen, F. Huang, Y. Xu, G. Guo, and Z. Gu, *Chem. Master.* **11**, 3433 (1999).
10. A. L. Rogach, *Mater. Sci. Eng. B* **69–70**, 435 (2000).

This page is intentionally left blank

International Journal of Nanoscience, Vol. 1, Nos. 5 & 6 (2002) 587–592

FABRICATION AND CHARACTERIZATION OF QUINACRIDONES NANOCRYSTALS BY HIGH-TEMPERATURE AND HIGH-PRESSURE CRYSTALLIZATION METHOD

BO LI*, HITOSHI KASAI*, HIDETOSHI OIKAWA†, SHUJI OKADA*, KUNIO ARAI‡, and HACHIRO NAKANISHI*

CREST, Japan Science and Technology Corporation
**Institute of Multidisciplinary Research for Advanced Materials, Tohoku University Sendai 980-8577, Japan*
†National Institute for Materials Science, 1-2-1 Sengen, Tsukuba-shi, Japan
‡Department of Chemical Engineering, Tohoku University, Sendai 980-8579, Japan

Received 27 November 2002
Revised 10 January 2003

The high-temperature and high-pressure liquid (HTPL) crystallization method was proved to be effective to fabricate nanocrystals of quinacridone and its dimethyl derivative. The quinacridone nanocrystals were spherical shape and monodispersed with the average size of around 50 nm, respectively. It was found that quinacridone nanocrystal in different crystal form could be obtained by changing experimental conditions in HTPL method.

Keywords: High-temperature and high-pressure liquid; supercritical fluid; nanocrystals; reprecipitation; quinacridone.

1. Introduction

Organic particles in nanoscale always possess interesting properties and promising applications. As a result, the preparation of organic nanocrystals attracts much interests. The reprecipitation method is one of the applicable techniques to prepare organic nanocrystals.[1,2] In this process, it is indispensable to prepare the solution of the target compound. So it is difficult to apply the simple reprecipitation method in preparing nanocrystals of some hardly-soluble compounds. Generally, the solubility of compounds increases in a high-temperature and high-pressure liquid (HTPL). Therefore, the reprecipitation of nanocrystals from HTPL including supercritical fluid (SCF) is a practicable technique. Actually, we have already succeeded in preparing nanocrystals of some organic compounds with low solubility, such as phthalocyanine and fullerene C_{60} by the HTPL or SCF crystallization method.[3–5] The crystal size and forms of the resulting nanocrystals could be controlled by changing the experimental conditions.

Quinacridone and its derivatives are well-known red pigments and electroluminescent materials because of their outstanding properties.[6,7] The crystal size and

its distribution are important factors to their real applications. However, it was so difficult to fabricate small-sized and monodispersed quinacridone nanocrystals using the conventional technique, such as milling and/or acid-pasting method. In addition, the acid-pasting method using concentrated sulfuric acid is a possibility of causing some problems. Thus, it is considered that HTPL crystallization method has obvious advantage and potential application in industry.

In this paper, we report the preparation of monodispersed nanocrystals of quinacridone and its dimethyl derivative by HTPL crystallization method, and their properties are investigated.

2. Experimental

The quinacridone used in this study was purchased from Tokyo KASEI. The commercial Pigment Red 122 was selected as the derivative of quinacridone, as shown in Fig. 1.

The apparatus and the process of HTPL method were referred to the previous reports.[3,4] At certain HTPL temperature and constant system pressure, the bulk crystals inserted in the sample tube were dissolved in HTPL and flew out. After mixing with cooling solvent, the nanocrystals could be obtained in the state of liquid dispersion.

Water was used as HTPL solvent. Water, methanol, acetone or ethanol was selected as the cooling solvent. The pressure in the system was controlled to be 24 MPa. The temperature of HTPL was set to be less than 370°C. The flow rate of HTPL and cooling solvent were both 5 ml/min. The obtained nanocrystals were characterized by UV-vis absorption spectra, powder X-ray diffraction (XRD) and scanning electron microscope (SEM).

3. Result and Discussion

3.1. *Quinacridone nanocrystals*

When the temperature of water as HTPL reached 250°C, the color of the obtained liquid changed from colorless to red. It means that the quinacridone began to

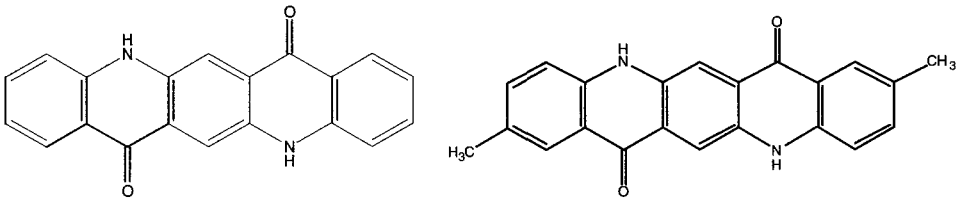

(a) (b)

Fig. 1. (a) The quinacridone and (b) the quinacridone dimethyl derivative.

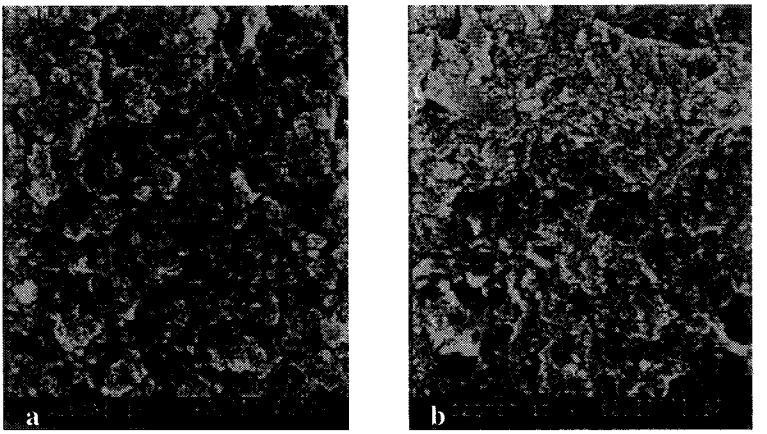

Fig. 2. The SEM images of quinacridone nanocrystals. HTPL temperature is (a) 260°C and (b) 340°C.

dissolve and the nanocrystallization occurred. The red dispersion liquid is stably-kept for a long time without aggregation and precipitation.

Figure 2 shows the SEM images of quinacridone nanocrystals prepared by the reprecipitation process from HTPL water solution to water. The shape and average size were spherical and around 60 nm (Fig. 2(a)). When the temperature of HTPL increased, it is true that the concentration of the soluble compound also increased. The SEM images of nanocrystals prepared at high HTPL temperature were shown

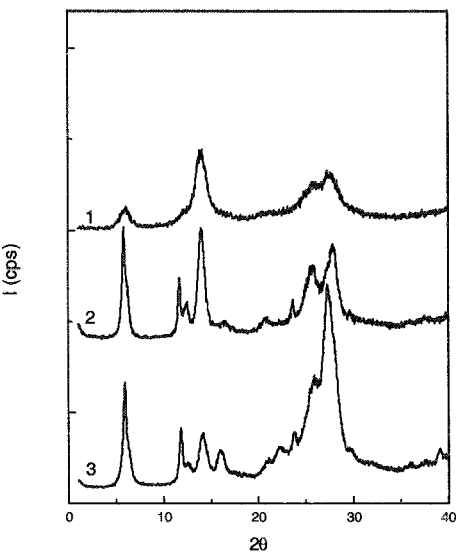

Fig. 3. The XRD patterns of quinacridone nanocrystals prepared at different HTPL temperature. 1: 260°C, 2: 290°C, and 3: 340°C.

in Fig. 2(b) indicated the appearance of large-sized particles. These large-sized particles may be formed due to the acceleration of nuclei growth in the solution of high concentration.

Figure 3 shows XRD patterns of quinacridone nanocrystals prepared at different HTPL temperature. The form of nanocrystals prepared at 260°C was pure γ form.[8–10] With increasing the temperature of HTPL solvent, the characteristic diffraction peak was appeared at about 12° (2θ), and was ascribed to β form. As a whole, the form of nanocrystals prepared at 340°C was a mixture of β form and γ form. The optical absorption spectra of nanocrystals dispersion liquid prepared at different HTPL temperature were shown in Fig. 4. The line 1 was pure γ form. It was considered that the shoulder band around 590 nm of lines 2 and 3 indicated the existence of β form. However, in the case of using water as cooling solvent, it was difficult to prepare the nanocrystals with pure β form.

In the case of HTPL water system, besides water was used as cooling solvent, other solvent, such as methanol, acetone or ethanol was applicable to cool down the HTPL solution. When the cooling solvent was changed, the cool down efficiency and the crystallization speed were obviously different because the heat capacity of cooling solvent changed. The effect of cooling solvent was summarized as follows.

The absorption spectra of quinacridone nanocrystals dispersion liquid prepared with different cooling solvent were shown in Fig. 5. The nanocrystals using methanol as cooling solvent was pure γ form, while those using ethanol as cooling solvent was pure β form. This was also recognized by XRD data. In the case of using acetone as

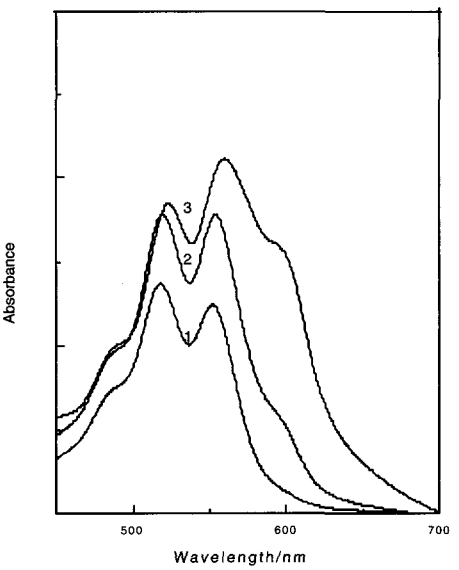

Fig. 4. The absorption spectra of quinacridone nanocrystals aqueous dispersion prepared at different HTPL temperature. 1: 260°C, 2: 290°C, and 3: 340°C.

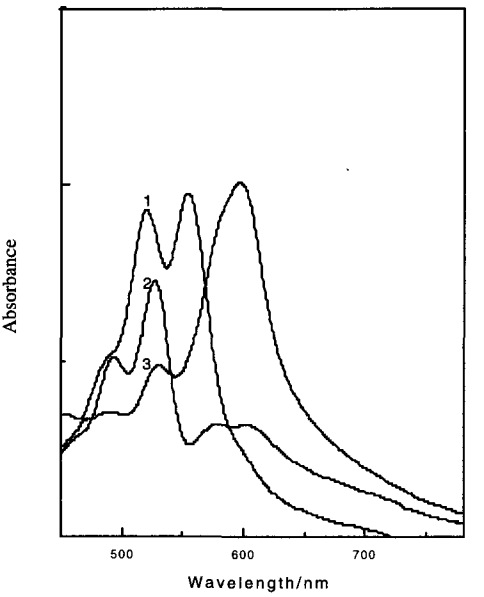

Fig. 5. The absorption spectra of quinacridone nanocrystals dispersion liquid prepared with different cooling solvent, respectively. 1: methanol, 2: acetone, and 3: ethanol.

cooling solvent, the crystal form was like a mixture of γ type and β type. The shape of nanocrystals using methanol as cooling solvent was spherical with the average size of 40 nm. The nanocrystals using acetone and ethanol as cooling solvent had spherical, flake and plate shape. In future, the size-control would be accomplished by using mixture cool solvent and changing ratio of the solvent. For example, the half-and-half of acetone and water in cooling solvent will be illustrated. Anyway, in HTPL water system, the form of quinacridone nanocrystals with about 50 nm in size could be controlled by changing the cooling solvent used.

3.2. *Nanocrystals of 2,9-dimethyl-quinacridone*

The 2,9-dimethyl-quinacridone is widely used as one of the red pigments. Therefore, fabrication of the nanocrystals was considered to be significant. When water was used as the cooling solvent, the nanocrystals obtained was spherical with average size of 30 nm by SEM observation. Figure 6 shows the absorption spectra of 2,9-dimethyl-quinacridone nanocrystals aqueous dispersion. The crystal form seemed to be γ form. The temperature of HTPL did not affect the size and shape of nanocrystals. In the next step, the form of 2,9-dimethyl-quinacridone nanocrystals would be attempted by changing the cooling solvent used.

In conclusion, the nanocrystals of quinacridone and its derivative could be fabricated by the HTPL crystallization method. The average size was around 50 nm. The control of crystal form was accomplished by changing the cooling solvent used.

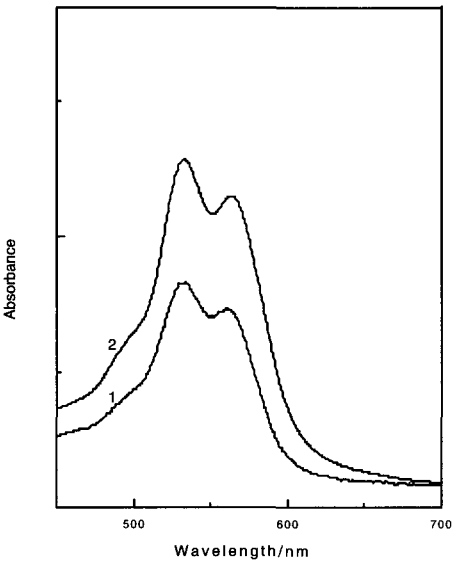

Fig. 6. The absorption spectra of 2,9-dimethyl-quinacridone nanocrystals aqueous dispersion. The HTPL temperature is 1: 290°C and 2: 340°C.

The HTPL recrystallization method is effective in preparing nanocrystals of hardly-dissolved compound.

References

1. H. Kasai, H. S. Nalwa, S. Okada, H. Oikawa, and H. Nakanishi, *Handbook of Nanostructured Materials and Nanotechnology*, Vol. 5 (Academic Press, San Diego, 1999), p. 439.
2. H. Oikawa, T. Oshikiri, H. Kasai, S. Okada, S. K. Tripathy, and H. Nakanishi, *Polym. Adv. Technol.* **11**, 783 (2000).
3. Y. Komai, H. Kasai, H. Hirakoso, Y. Hakuta, S. Okada, H. Oikawa, T. Adschiri, H. Inomata, K. Arai, and H. Nakanishi, *Mol. Cryst. Liq. Cryst.* **322**, 167 (1998).
4. Y. Komai, H. Kasai, H. Hirakoso, Y. Hakuta, H. Katagi, S. Okada, H. Oikawa, T. Adschiri, H. Inomata, K. Arai, and H. Nakanishi, *Jpn. J. Appl. Phys.* **38**, L81 (1999).
5. H. Kasai, S. Okazaki, T. Hanada, S. Okada, H. Oikawa, T. Adschiri, K. Arai, K. Yase, and H. Nakanishi, *Chem. Lett.*, 1392 (2000).
6. D. S. Filho and C. M. F. Oliveira, *J. Mater. Sci.* **27**, 5101 (1992).
7. S. E. Shaheen, G. E. Jabbour, B. Kippelen, N. Peyghambarian, J .D. Anderson, S. R. Marder, N. R. Armstrong, E. Bellmann, and R. H. Grubbs, *Appl. Phys. Lett.* **74**, 3212 (1999).
8. G. D. Potts, W. Jones, J. F. Bullock, S. J. Andrews, and S. J. Maginn, *J. Chem. Soc., Chem. Commun.*, 2565 (1994).
9. G. Lincke and H.-U. Finzel, *Cryst. Res. Technol.* **31**, 441 (1996).
10. G. Lincke, *J. Mater. Sci.* **32**, 6447 (1997).

International Journal of Nanoscience, Vol. 1, Nos. 5 & 6 (2002) 593–596

THE ELECTROCHEMICAL STUDIES ON A SELF-ASSEMBLED VIOLOGEN MONOLAYER USING QUARTZ CRYSTAL MICROBALANCE

J. Y. OCK*, H. K. SHIN, and Y. S. KWON
Department of Electrical Engineering, Dong-A University, Busan, 604-714, Korea
**ockjy@donga.ac.kr*

S. H. SONG and S. M. CHANG
Department of Chemical Engineering, Dong-A University, Busan, 604-714, Korea

D. J. QIAN and J. MIYAKE
Tissue Engineering Research Center, AIST, Tsukuba, 305-8562, Japan

Received 27 November 2002
Revised 24 December 2002

The electrochemical behavior of viologen self-assembled monolayer has been investigated with QCM, which has been known as ng order mass detector. The self-assembly process of viologen was monitored using resonant frequency (ΔF) and resonant resistance (R). The QCM measurements indicated a mass adsorption for viologen assembling on the gold surface with a frequency change of about 300, 135 Hz and its surface coverage (Γ) was calculated to be 5.02×10^{-9} and 1.64×10^{-9} mol/cm^2. A reversible redox process was also observed and analyzed with an ionic interaction at the viologen/solution interface using ΔF.

Keywords: Viologen; self-assembly; quartz crystal microbalance (QCM); cyclic voltammogram (CV).

1. Introduction

Particularly, viologens have been extensively investigated in the literature due to their well-behaved electrochemistry, and has led to their use in a variety of studies, including electron transfer mediation to various biological molecules, the surface-enhanced Raman studies of the adsorption at electrode surfaces, the behavior of supramolecular assemblies at electrode surfaces and the applications for the electrochromic display devices.

The viologens exist in three main oxidation states, namely, $V^{2+} \leftrightarrow V^{+}_{\bullet} \leftrightarrow V^{0}$. These redox reactions, especially the first one ($V^{2+} \leftrightarrow V^{+}_{\bullet}$), are highly reversible

*Corresponding author.

and can be cycled many times without significant side reactions.[1] In this study, the electrochemical behavior of the self-assembled viologen monolayer has been investigated with QCM, which has been known as a nanogram order mass detector. The self-assembly process of the viologen was monitored using a resonant frequency (ΔF) and a resonant resistance (R).

2. Experimental Analysis

Figure 1 shows the chemical structure of the viologens incorporated with a thiol group. The rest of the reagents used in this experiments were of analytical grade and were used without any purification. All solutions were prepared using Milli-Q water. The QCM measurements were carried out using AT-cut gold-coated quartz crystals with a resonant frequency of 9 MHz (5 mm diameter Seiko EG&G, Japan). The gold electrodes of the QCM was cleaned in a piranha solution (H_2SO_4/H_2O_2; 3:1), and was exposed to a solution of mixture of V_8SH and SH_8V_8SH in ethanol-acetonitrile (1:1, v/v) purged with Ar gas. The concentration was 2 mmol/l. The resonant frequency (ΔF) and the resonant resistance (R) have been measured using QCA 922 (Seiko EG&G, Japan) and the cyclic voltammetry (CV) was measured using potentiostat 263A (Seiko EG&G Instrument, Japan). The QCM electrode modified with the self-assembled viologen and Pt plate were used as the working and counter electrode, respectively. A KCl-saturated Ag/AgCl was a reference electrode. 0.1 mol/l $NaClO_4$ was used as the electrolyte solution. An initial potential of -800 mV was applied for 5 s, and subsequent cyclic scans to a final potential of -800 mV were done for 10 cycles. An estimation of the peak currents and surface coverage was based on the curve of the 10th cycle: also the CV curve shown in the present work were 10th cycle.

3. Results and Discussion

Figure 2 shows the frequency shift (ΔF) as a function of time (t) for the QCM gold resonator in the 2 mmol/l V_8SH and SH_8V_8SH ethanol/acetonitrile solution. In both cases, the resonant frequency dramatically decreased and saturated. The

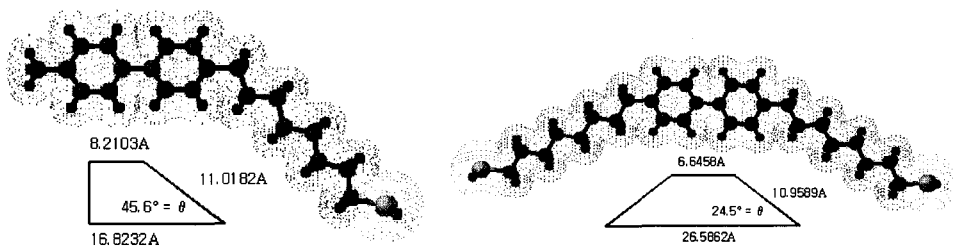

Fig. 1. The chemical structure of viologen used in this study. (a) V_8SH and (b) SH_8V_8SH.

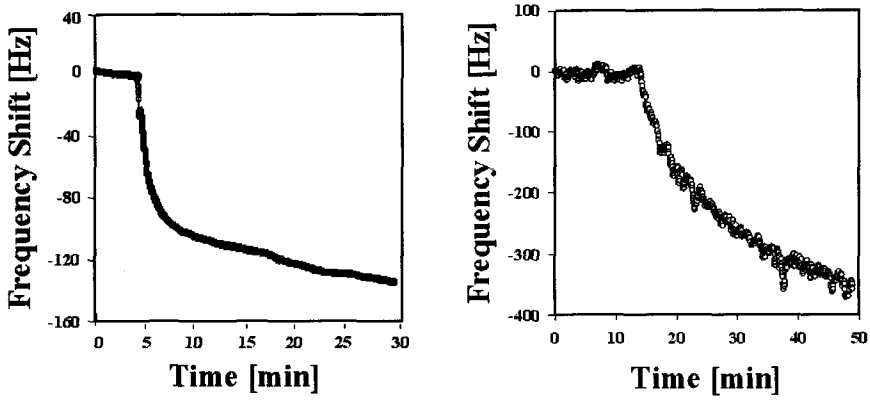

Fig. 2. The time-dependent frequency shift during self-assembly process of viologen. (a) V_8SH and (b) SH_8V_8SH.

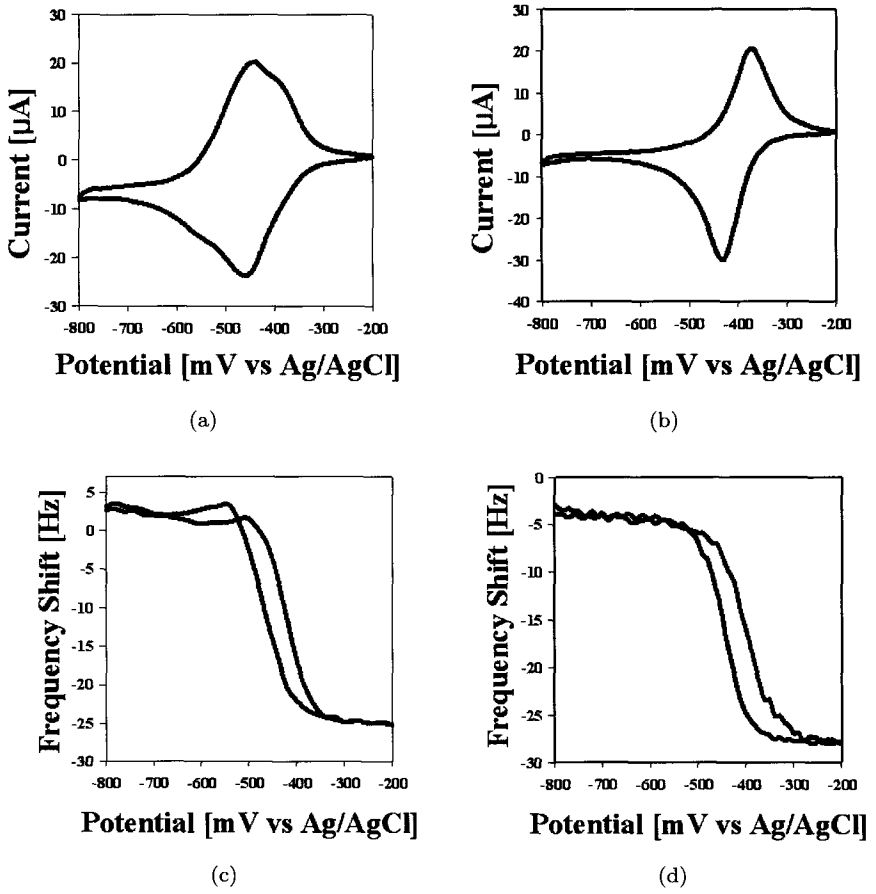

Fig. 3. The cyclic voltammogram and resonant frequency shift of QCM modified with viologen SA monolayer (a) and (c) V_8SH and (b) and (d) SH_8V_8SH.

measured ΔF for V_8SH and SH_8V_8SH was about 300 and 135 Hz, respectively. From these ΔF values, we calculated that the mass of the adsorbed V_8SH and SH_8V_8SH was about 320 and 144 ng, according to Eq. (1).[2]

$$\Delta F = \frac{-2F_0^2 \Delta m}{A \bullet \rho_q^{1/2} \bullet \mu_q^{1/2}}, \tag{1}$$

where, F_0 is the fundamental resonant frequency of 9 MHz, $\Delta m(g)$ is the mass gain, A is the electrode area (0.196 cm^2), ρ_q is the density of the quartz (2.65 g/cm^3), and μ_q is the shear module (2.95×10^{11} dyn/cm^2). By considering the mass gain and the molecular weight, we can calculate the surface coverage (Γ) to be 5.02×10^{-9} and 1.64×10^{-9} mol/cm^2. Figure 3 shows that the oxidative cyclic voltammetry of two self-assembled monolayers of viologen in 0.1 mol/l $NaClO_4$ electrolyte solution with 100 mV/s of the scan rate. The cathodic and anodic potential peaks of V_8SH are centered at -450 to -470 and -430 to -450 mV in Fig. 3(a) and SH_8V_8SH are centered at -430 to -450 and -350 to -370 mV in Fig. 3(b). In Figs. 3(c) and 3(d), the resonant frequency was dramatically changed at redox peaks, which can explain ionic behavior at a viologen/electrolyte interface. For both cases, the measured ΔF of ionic behavior was about 25 Hz. Therefore, if we consider the ΔF and redox process simultaneously, we can analyze more precisely the ionic behavior or any electrochemical phenomenon at interface. Moreover the quantitative analysis of ΔF and the oxidation peak is under consideration.

4. Conclusion

The self-assembly process of the viologen was monitored using resonant frequency (ΔF). The mass adsorption was calculated to be 320 and 144 ng. The surface coverage (Γ) was calculated to be 5.02×10^{-9} and 1.64×10^{-9} mol/cm^2. In addition to this, two pairs of reversible redox peaks were observed, and the electrochemical properties were analyzed using the behavior of resonant frequency (ΔF) simultaneously.

Acknowledgment

This work was supported by the KOSEF through the CIIPMS at Dong-A University.

References

1. N. Nakamura, H. X. Huang, D. J. Qain, and J. Miyake, *Langmuir* **18**, 5804 (2002).
2. H. Muramatsu, E. Tamuiya, and I. Karube, *Anal. Chem.* **60**, 2142 (1988).

International Journal of Nanoscience, Vol. 1, Nos. 5 & 6 (2002) 597–601

CONTROLLED AGGREGATION OF AZOBENZENE BASED ON DNA-MIMETICS AT THE AIR–WATER INTERFACE

KUNIHARU IJIRO*,† JIN MATSUMOTO†,
MITSUHIKO MORISUE*, and MASATSUGU SHIMOMURA*,‡

*Research Institute for Electronic Science, Hokkaido University
N12W6, Kita-ku, Sapporo 064-0812, Japan
†Precursory Research for Embryonic Science and Technology
Japan Science and Technology Corporation (PRESTO, JST)
‡Nanotechnology Research Center, Research Institute for Electronic Science
Hokkaido University, N12W6, Kita-ku, Sapporo 060-0812, Japan
‡shimo@poly.es.hokudai.ac.jp

Received 27 November 2002
Revised 24 December 2002

Monolayers of thymine amphiphile containing azobenzene chromophore (Azo-Thy) were prepared on various aqueous oligonucleotide (dA_{30}, $d(GA)_{15}$, $d(GGA)_{10}$) subphases. Pressure–area isotherms and reflection absorption spectra of the monolayers on dA_{30} or $d(GA)_{15}$ solution showed that the H-aggregate of the azobenzene units was formed at higher surface pressure than 25 mN/m. In contrast, the monolayer on an aqueous $d(GGA)_{10}$ solution did not form any aggregates of the azobenzene units even at high surface pressure. Base-pair formation between Azo-Thy and template $d(GGA)_{10}$ could give free volume to the azobenzene units in the monolayer to prevent the aggregation of the azobenzene units at the air–water interface.

Keywords: Monolayer; azobenzene; DNA; base pair; DNA-mimetics; molecular recognition.

1. Introduction

The organizing functional molecules, e.g., chromophore, with complete control is important for construction of molecular devices as well as biomimetics for the light harvesting system. The utilization of not only covalent bonds but also weak intermolecular interactions (e.g., hydrogen bonds, van der Waals forces, and hydrophobic interactions) enables us to assemble molecules into devices.[1,2] DNA has a double helical supramolecular structure composed of complementary base pairs between adenine–thymine and guanine–cytosine. We have already reported that the nucleobase amphiphiles formed base pairs and base trimers at the air–water interface, which were similar to the natural DNA duplex and triplex.[3–6] By utilizing the

‡Corresponding author.

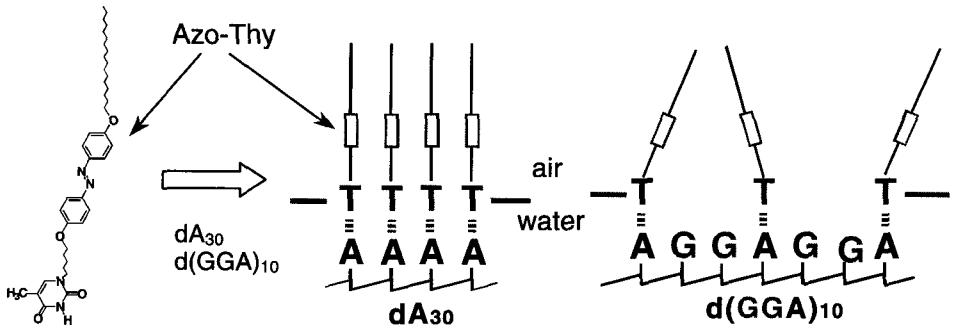

Fig. 1. Schematic illustration of the molecular organization on oligonucleotide solutions.

air–water interface as a field of molecular recognition, we attempt to organize functional molecular assemblies containing polymerizable group or chromophore along single-strand DNA as template by formation of base pairs and base trimers.[7,8] It is possible to prepare nucleobase monolayers transcribed the information of the template DNA. In this report, we prepared azobenzene-containing nucleobase monolayers at the air–water interface on aqueous oligonucleotide solutions. Azobenzene chromophore is known to form H- or J-aggregates in condensed states.[9] Monolayers of thymine amphiphile containing azobenzene chromophore (Azo-Thy) were prepared on various aqueous oligonucleotide (dA_{30}, $d(GA)_{15}$, $d(GGA)_{10}$) subphases in order to control distance between Azo-Thy molecules by complimentary base-pairing between Azo-Thy and adenine moieties of the oligonucleotides as templates (Fig. 1).

2. Experiments

Synthesis of thymine nucleobase amphiphile containing azobenzene chromophore in the hydrophobic carbon chain (Azo-Thy) was described elsewhere.[8] Oligodeoxynucleotides (ODNs), dA_{30}, $d(GA)_{15}$, and $d(GGA)_{10}$, were purchased from Invitrogen and were used without further purification. Chloroform (Spectrosol, Dojin) and ethanol (Wako), which was used as a spreading solution, was of spectroscopic grade. Buffer solution (pH 7.8), which consist of 10 mM Tris-HCl aqueous solution and 1 mM EDTA, was used as subphase solution. Pressure–area (π–A) isotherms were measured with a computer-controlled film balance system FSD-300 (USI System, Japan). Compression was started 15 min after spreading at the rate of 0.03 $nm^2 \cdot molecule^{-1} \cdot min^{-1}$. The subphase temperature was maintained at $20 \pm 0.1°C$. The surface pressure was measured by a Wilhelmy plate, which was calibrated with the transition pressure of a stearic acid monolayer.

Chloroform/ethanol (9/1 v/v) solution of 1 mM Azo-Thy was spread on the buffer solution with and without 25 nM oligonucleotide. Reflection absorption spectra of the monolayers on a water subphase were measured *in situ* with a multispectrophotometer equipped an optical fiber (LB-100, Jasco).

3. Results and Discussion

Figure 2 shows π–A isotherms of Azo-Thy monolayers on the buffer solutions with or without various ODNs. On the buffer solution without ODNs, a phase transition of the monolayer was observed at the surface pressure of 10 mN/m. A solid-state monolayer was formed at higher surface pressure than that of the phase transition. When dA_{30} was added to the subphase solution, the monolayer expanded and the surface pressure of the phase transition increased compared to that of the monolayer on the buffer solution without ODN. The Azo-Thy molecules and dA_{30} could be interacted by the adenine–thymine base-paring at the air–water interface. On the $d(GA)_{15}$ subphase, the monolayer expanded only below the surface pressure of the phase transition. By addition of $d(GGA)_{10}$ to the buffer solution, a phase transition was not observed and the expansion of the monolayer was maintained even at higher surface pressure than the phase transition. These indicate that $d(GA)_{15}$ and $d(GGA)_{10}$ were bound to the Azo-Thy monolayers and the molecular density of Azo-Thy in the monolayers could depend on the adenine sequences of the ODNs.

In order to investigate the molecular packing of the Azo-Thy molecules in the monolayers on the ODNs subphase, *in situ* reflection absorption spectra of the Azo-Thy monolayers were observed. Absorption maxima of the monolayers on the dA_{30} and $d(GA)_{15}$ subphases were 315 and 314 nm at 25 mN/m, respectively (Fig. 3). This indicates that H-aggregates of the azobenzene moieties were formed in the monolayers. On the other hand, the monolayer on the $d(GGA)_{10}$ subphase gave the absorption maximum of 358 nm at 25 mN/m. This absorption spectrum corresponded to that in a solution. Thus the azobenzene moiety in the monolayer on

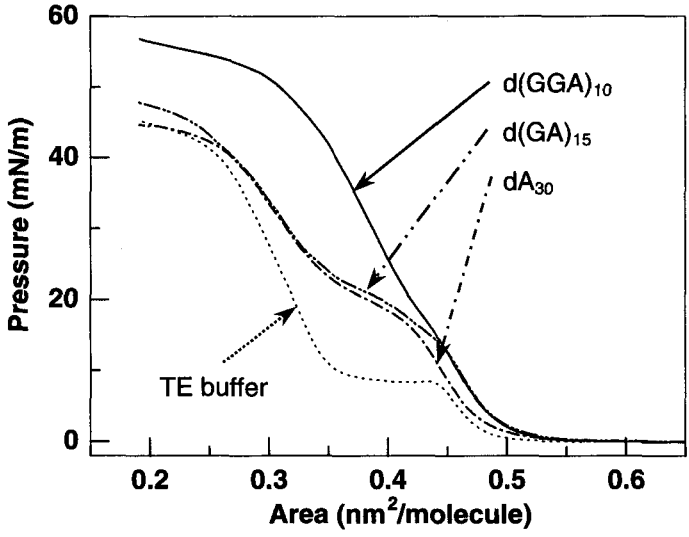

Fig. 2. Pressure–area isotherms of Azo-Thy on the buffer solutions with and without oligonucleotides.

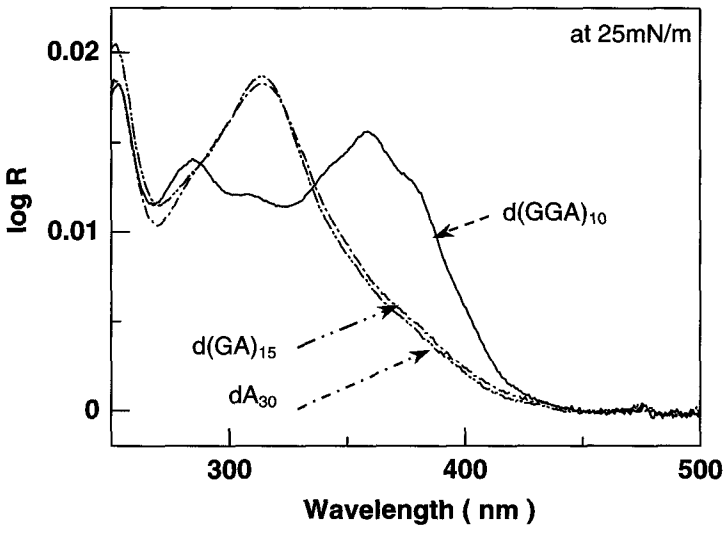

Fig. 3. Reflection absorption spectra of Azo-Thy monolayers on the oligonucleotide solutions.

the $d(GGA)_{10}$ subphase was not aggregated even at high surface pressure. Thymine moiety of Azo-Thy can bind to adenine of ODN specifically. The π–A isotherm of Azo-Thy was not changed on the polyG subphase (data not shown). Thus Azo-Thy cannot interact with guanine at the air–water interface. Only adenine of ODNs could bind to the Azo-Thy molecules at the air–water interface. Guanine moieties could keep Azo-Thy molecules away and disturb the aggregation in the monolayer even at high surface pressure.

4. Conclusion

Molecular arrangement of the thymine amphiphile containing azobenzene chromophore can be achieved by thymine–adenine base-pairing between the amphiphile and oligonucleotide at the air–water interface. Aggregation of azobenzene in the monolayers can be controlled by the adenine sequences of the oligonucleotides dissolved in the subphases.

References

1. M.-S. Choi, T. Aida, T. Yamazaki, and I. Yamazaki, *Chem. Eur. J.* **8**, 2667 (2002).
2. R. P. Sijbesma and E. W. Meijer, *Curr. Opin. Colloid Interface Sci.* **4**, 24 (1999).
3. M. Shimomura, F. Nakamura, K. Ijiro, H. Taketsuna, M. Tanaka, H. Nakamura, and K. Hasebe, *J. Am. Chem. Soc.* **119**, 2341 (1997).
4. F. Nakamura, K. Ijiro, and M. Shimomura, *Thin Solid Films* **329**, 603 (1998).
5. M. Shimomura, J. Matsumoto, F. Nakamura, T. Ikeda, T. Fukasawa, K. Hasebe, T. Sawadaishi, O. Karthaus, and K. Ijiro, *Polym. J.* **31**, 1115 (1999).
6. M. Weisser, J. Kashammer, B. Menges, J. Matsumoto, F. Nakamura, K. Ijiro, M. Shimomura, and S. Mittler, *J. Am. Chem. Soc.* **122**, 87 (2000).

7. J. Matsumoto, K. Ijiro, and M. Shimomura, *Chem. Lett.*, 1280 (2000).
8. M. Morisue, H. Nakamura, K. Ijiro, and M. Shimomura, *Mol. Cryst. Liq. Cryst.* **337**, 457 (1999).
9. M. Shimomura, S. Aiba, N. Tajima, N. Inoue, and K. Okuyama, *Langmuir* **11**, 969 (1995).

This page is intentionally left blank

International Journal of Nanoscience, Vol. 1, Nos. 5 & 6 (2002) 603–609

TWO-DIMENSIONAL PATTERNED NANOCRYSTALLINE Si ARRAY PREPARED BY LASER INTERFERENCE CRYSTALLIZATION OF ULTRA-THIN AMORPHOUS Si:H SINGLE-LAYER

XINFAN HUANG*, XIAOWEI WANG, FENG QIAO, LEYI ZHU, WEI LI, XUEFEI LI, and KUNJI CHEN

National Laboratory of Solid State Microstructures and Department of Physics
Nanjing University, Nanjing 210093, People's Republic of China

LIN KANG

Department of Electronic Science and Engineering, Nanjing University
Nanjing 210093, People's Republic of China

Received 20 November 2002
Revised 9 January 2003

We employ the method of phase-modulated KrF excimer pulsed laser interference crystallization to fabricate nanometer-sized crystalline silicon with two-dimensional patterned distribution within the ultra-thin amouphous Si:H single-layer. The local phase transition occurs in ultra-thin a-Si:H film after laser interference crystallization under proper energy density. The results of atomic force microscopy, Raman scattering spectroscopy, cross-section transmission electron microscopy and scanning electron microscopy demonstrate that Si nanocrystallites are formed within the initial a-Si:H single-layer, selectively located in the discal regions with the diameter of 250 nm and patterned with the same 2D periodicity of 2.0 μm as the phase-shifting grating. The results demonstrate that the present method can be used to fabricate patterned nc-Si films for device applications.

Keywords: Nanocrystalline Si; laser interference crystallization; microstructures.

1. Introduction

Nanometer-sized crystalline silicon (nc-Si) has long been the subject of great interest due to its potential application in the future optoelectronics and nanoelectronics.[1–7] One important need for the commercial application of silicon-based device is to find a manufacturing technique that can control the sizes and the densities of nanocrystals as well as their positions. Moreover, such technique must be compatible with standard Si microelectronics process. For the purpose of device application, in many

*Corresponding author.

cases, patterned nc-Si structures are necessary.[8] However, for the patterned generation, the standard technique of optical lithography is limited by its resolution capability and its indirect technique process. Although the focused electron beam or ion beam technique overcomes the shortcomings of optical lithography, it requires expensive equipment and its yield is low for large-scale production due to its serial scanning process. Therefore, it is also limited for a wide use.

In the last decade, the method of pulsed laser interference crystallization with two/multi-beam-interference system has been reported for preparing microcrystalline-silicon (μc-Si) films. By this method, a one/two-dimensional interference pattern is achieved.[9–11] In our previous work, by the method of phase-modulated KrF excimer pulsed laser interference crystallization (LIC), we have successfully fabricated one-dimensional (1D) self-organized Si dots in amorphous Si:H (a-Si:H) films which is 50 nm thick.[12] Further, by LIC we realized constrained crystallization of ultra-thin a-Si:H sublayers within a-Si:H/a-SiN$_X$:H multilayers and controlled the transverse and longitudinal positions of nc-Si dots to achieve three-dimensional ordered distribution of nc-Si.[13,14]

In this paper, we attempt to realize two-dimensional (2D) ordered distribution of nc-Si in the plane of the ultra-thin a-Si:H single-layer. The LIC method is again employed to crystallize ultra-thin a-Si:H film with the thickness of only 10 nm. Simply combining 2D phase-shifting grating with our pulsed laser irradiation system, periodic high intensity contrast patterned energy distribution of laser is achieved on the surface of a-Si:H film. Upon pulsed laser irradiation, a new kind of nc-Si material has been fabricated over large areas, where nc-Si dots were locally formed in ultra-thin a-Si films with the thickness of 10 nm in the form of regularly patterned 2D arrays. Under optimized conditions, the patterned arrays are composed of nc-Si dots with uniform sizes.

2. Experimental

Ultra-thin a-Si:H single-layer (10 nm) films were prepared on SiO_2/Si or SiN_x/Si substrates in the plasma-enhanced chemical vapor deposition (PECVD) with the following typical parameters: RF power 30 W, substrate temperature 250°C, reaction pressure 16 Pa, pure silane (SiH_4) serving as reactive gas, deposition rate about 0.1 nm/s. SiO_2 (500 nm)/Si substrates were prepared by means of thermal oxidization of (100) Si wafer. The SiN_x (50 nm) were deposited on (100) Si wafer by PECVD method using mixing gases of SiH_4 and NH_3 as reactive gas.

The crystallization of a-Si:H thin films was performed by laser irradiation with a 30 ns pulsed KrF (λ = 248 nm) excimer laser at room temperature. The laser beam is focused, by a fused quartz lens (f = 24 cm), to increase its energy density. During the LIC treatment, a sample was placed with contact of the phase grating mask behind it. The surface-relief 1D and 2D phase-shifting gratings, which were used in the laser patterned local crystallization experiment, are designed with 2 μm periodicity and 260 nm depth. Upon laser irradiation, a transient thermal 1D grid

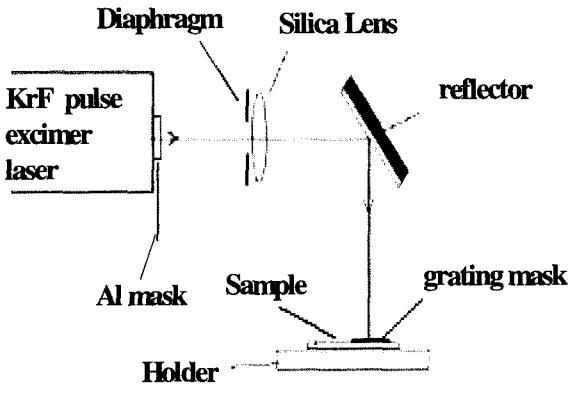

Fig. 1. The schematic experiment setup of laser interference crystallization.

and 2D matrix are directly formed on the surface of sample, leading to the local crystallization of the a-Si:H films. Figure 1 shows the schematic of the experimental setup. The periodic patterned energy distribution of laser on the surface of the sample has published elsewhere.[15]

The crystallinity, morphology and microstructures of crystallized sample are then characterized by atomic force microscopy (AFM), Raman scattering spectroscopy, cross-section transmission electron microscopy (X-TEM) and scanning electron microscopy (SEM). The Raman measurements are done on a T64000 Raman system. The TEM measurements are performed with JEM200CX microscope working at 200 kV. The AFM equipment with a Nanoscope III system (Digital Instruments, USA) is employed in contact mode. The SEM analysis is carried out on a LEO-1550 SEM system.

3. Results and Discussion

Figure 2 shows the Raman scattering spectra of the sample after laser-induced crystallization (LC) without using the phase-shifting grating mask. The energy density of the laser is 162 mJ/cm^2 with a single shot. The curve shows a sharp peak around 515.9 cm^{-1} corresponding to TO mode of nc-Si with a weak shoulder corresponding to TO mode of a-Si, which demonstrates that nc-Si has formed in the sample. The average size of nc-Si is estimated to be 4.7 nm according to the phonon confinement model.[16] Since there was some residue of a-Si species, we calculate the fractions of nc-Si in the sample, defining the crystallinity of fraction ratio $[I_c]/([I_c]+[I_a])$ where I_c and I_a are the integrated areas of the TO peaks of nc-Si and a-Si, respectively. The fraction of crystalline Si is about 85% which means that almost a-Si in as-deposited layer has been transformed to nanocrystallites after the LC under proper energy density.

The AFM results of the sample shown in Fig. 2 are shown in Fig. 3(c). It is clear that the sample is densely composed of Si grains with lateral size of about 20 nm

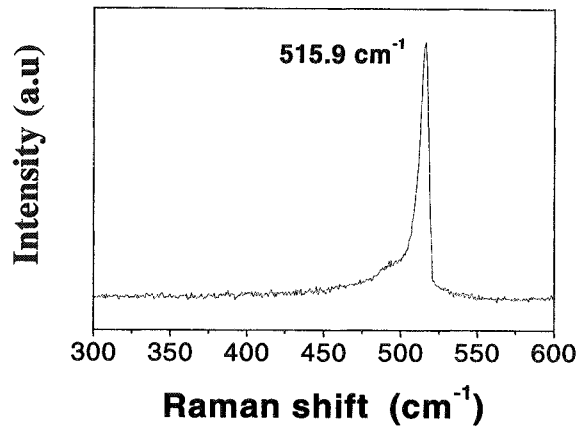

Fig. 2. The Raman scattering spectra of the sample after laser crystallization without the phase-shifting grating mask.

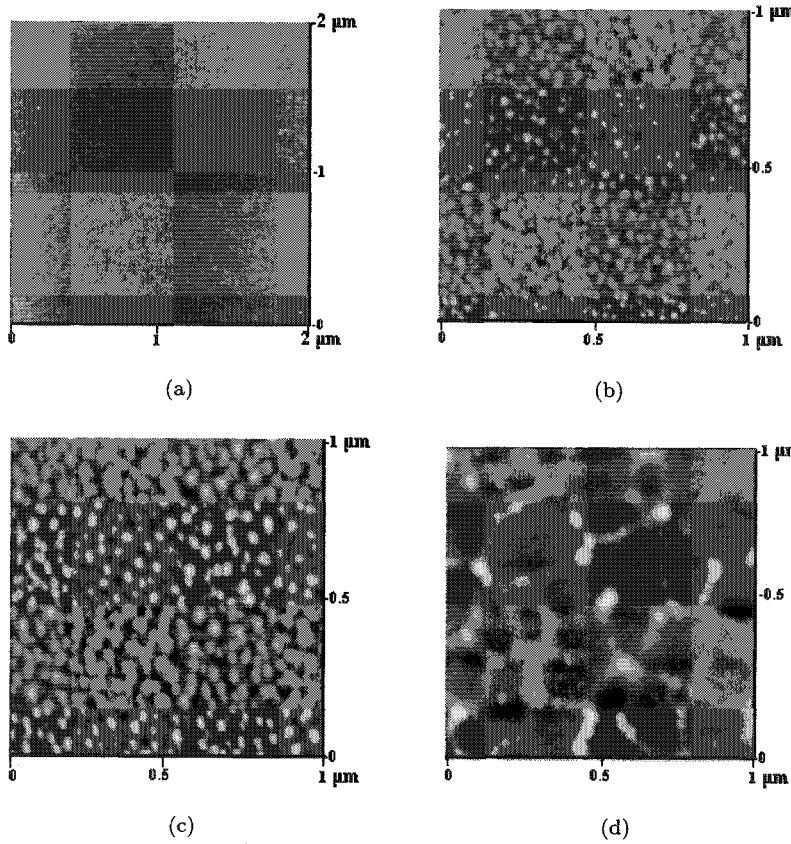

Fig. 3. The AFM photographs of the morphology of the sample after laser crystallization under different energy. (a) 125 mJ/cm^2; (b) 150 mJ/cm^2; (c) 162 mJ/cm^2; and (d) 190 mJ/cm^2.

and longitudinal size of about 10 nm. We calculate the density of nc-Si grains by counting the grains in the area of 5 μm $\times$ 5 μm. The result shows that the density is about $4 \times 10^{10}/\text{cm}^2$. Comparing with the results of Raman spectra, the size of nc-Si grains obtained from the AFM image is larger. We consider this is because every Si grain may be made up of several crystalloids with smaller sizes.

We also studied the effect of laser energy density (from 125 mJ/cm^2 to 190 mJ/cm^2) on the nc-Si formation by AFM analysis. From Fig. 3(d) we found that as-deposited a-Si layer on the SiO_2/Si substrate has been damaged due to irradiation under laser energy density of 190 mJ/cm^2. With decreasing laser energy densities (from Fig. 3(c) to Fig. 3(b)), we obtained higher quality nc-Si films. With laser energy density further decreased, no transition takes place in a-Si:H film (Fig. 3(a)).

Based on the above results, we attempt to control the positions of nc-Si in the plane of films after laser interference crystallization (LIC) by employing 2D phase-shifting grating as shown in Fig. 4, which is the photograph of SEM of the surface-relief structure of 2D phase-shifting grating mask. We can see that its periodicity is 2 μm as designed.

Figure 5 is the SEM image of the sample after LIC with 2D grating mask, whose energy density is 30 mJ/cm^2 in front of 2D grating. A 2D submicrometer pattern (formed by crystallized zones in a-Si:H films) is clearly revealed. The white disks (crystallized zones) with a diameter of 250 nm and a period of 2 μm are composed of several Si crystallites. The gray regions around the white disks correspond to remain amorphous Si because only in the white disks can a solid-phase crystallization take place where the energy density exceeds the crystallization threshold.[17] Moreover, morphology of every disk is nearly the same, which demonstrates LIC method is effective for fabricating nc-Si patterns. In addition, the crystallized zones on the surface gradually disappeared with the decrease of the laser energy density.

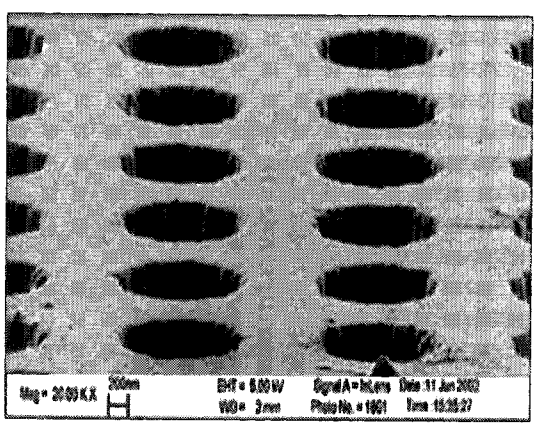

Fig. 4. The SEM photograph of the surface-relief structure of 2D phase-shifting grating.

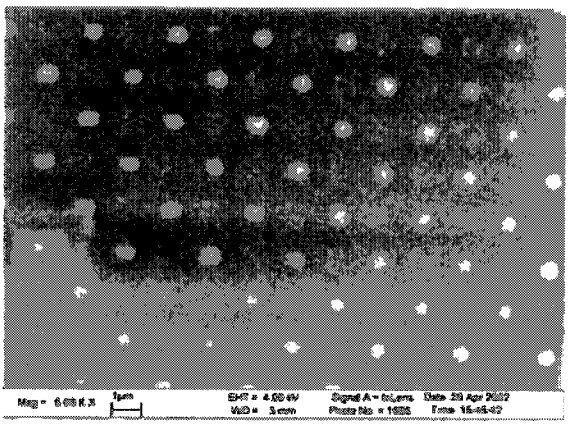

Fig. 5. The SEM photograph (top-view) of a similar-structured sample after LIC with energy density of 30 mJ/cm^2 in front of 2D grating.

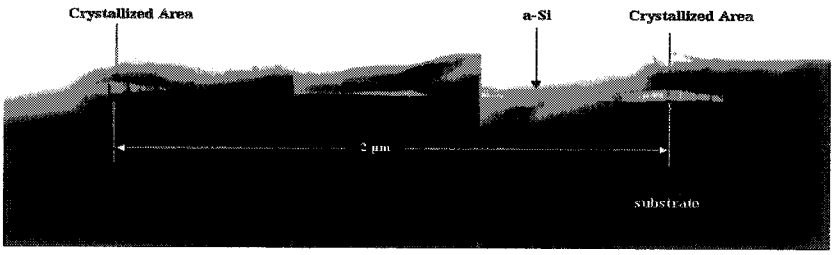

Fig. 6. The cross-section TEM photographs of two adjacent crystallization regions in ultra-thin a-Si single layer after LIC with energy density of 39 mJ/cm^2 in front of 2D grating. The substrate is SiN_x/Si.

The surface of the sample irradiated with the energy density of 25 mJ/cm^2 is almost smooth and no periodic disks on the surface of this sample were observed in the AFM analysis. By cross-section TEM technique, we successfully observed the microstructure of two adjacent crystallization regions shown in Fig. 6, which confirms the formation of Si crystallites in as-deposited ultra-thin a-Si layer (10 nm) after LIC. It clearly shows that the Si crystallites are closely arranged one by one in the crystallized area. The size of crystallites in the middle of the regions is larger than that on the border because of the rearrangement of laser energy after laser beams interfere with each other. The interface between the crystallized and the amorphous zones is also abrupt after laser irradiation.

4. Conclusion

In summary, we utilized AFM, Raman, TEM, and SEM techniques to investigate the surface morphology and the structure properties of ultra-thin a-Si:H single layer

deposited on SiO_2/Si or SiN_x/Si substrate, which is fabricated by PECVD and then crystallized by laser irradiation. The experimental results show that nc-Si is formed in certain regions with the same periodicity of 2.0 μm as that of phase-shifting grating mask. Particularly the patterned distribution of nc-Si can be varied by changing the geometry of the phase grating mask, using the 1D grating for getting 1D ordered distribution of nc-Si and 2D grating for getting 2D distribution. Changing laser energy density can control the surface morphology of the samples. So the method of pulsed laser interference crystallization (LIC) is one of the most promising methods to fabricate patterned nc-Si with low-temperature and compatible with a standard microelectronic processing.

Acknowledgments

The authors would like to acknowledge the supports of State Key Program for Basic Research of China (Grant No. 2001 CB 610503), the National Nature Science Foundation of China (Grant Nos. 90101020 and 60071019), and Nature Science Foundation of Jiangsu Province (BK2001028, BG2001002). This work was also partly supported by the NPTND of Korea MOST.

References

1. L. T. Canham, *Appl. Phys. Lett.* **57**, 1046 (1990).
2. L. Tsybeskov, K. D. Hirschman, S. P. Duttagupta, M. Zacharias, P. M. Fauchet, J. P. McCaffrey, and D. J. Lockwood, *Appl. Phys. Lett.* **72**, 43 (1998).
3. X. Gu, H. Qin, H. Lu, K. Chen, and X. Huang, *J. Non-Cryst. Solids* **227**, 1168 (1996).
4. K. J. Chen, X. F. Huang, J. Xu, and D. Feng, *Appl. Phys. Lett.* **61**, 2069 (1992).
5. U. Banin, Y. W. Cao, D. Katz, and O. Millo, *Nature* **400**, 542 (1999).
6. A. D. Yoffe, *Advanced in Physics* **50**, 1 (2001).
7. Y. Wakayama, T. Tagami, and S. Tanaka, *Thin Solid Films* **350**, 300 (1999).
8. C. C. Striemer, R. Krishnan, and P. M. Fauchet, *Nano Lett.* **1**, 643 (2001).
9. B. Dahlheimer, U. Karrer, C. E. Nebel, and M. Stutzmanm, *J. Non-Cryst. Solids* **227–230**, 916 (1998).
10. M. Heintze, P. V. Santos, C. E. Nebel, and M. Stutzmanm, *Appl. Phys. Lett.* **64**, 3148 (1994).
11. C. E. Nebel, *Mat. Res. Soc. Symp. Proc.* **420**, 117 (1996).
12. K. J. Chen *et al.*, *J. Non-Cryst. Solids* **227–230**, 934 (1998).
13. X. F. Huang, Z. F. Li, Z. G. Liu, and K. J. Chen, *J. Non-Cryst. Solids* **198–200**, 821 (1996).
14. X. F. Huang *et al.*, *J. Non-Cryst. Solids* **266–269**, 1015 (2000).
15. M. Jiang, M. X. Wang, and K. J. Chen, *Chinese J. Lasers B* **8**, 142 (1999).
16. G. X. Chen, K. J. Chen, and X. K. Zhang, *Phys. Stat. Sol. A* **129**, 421 (1992).
17. L. Wang, J. Li, X. F. Huang, W. Li, and K. J. Chen, *Appl. Surf. Sci.* **165**, 85 (2000).

This page is intentionally left blank

International Journal of Nanoscience, Vol. 1, Nos. 5 & 6 (2002) 611–616

DEEP UV PHOTOPATTERNING OF SELF-ASSEMBLED MONOLAYER AND ITS APPLICATION IN BIOELECTRONIC DEVICE

SE YOUNG OH*, HANG SOK JIE, HYUNG SEOK CHOI, and JEONG WOO CHOI
Department of Chemical Engineering, Sogang University, Seoul, 121-742, Korea
**syoh@sogang.ac.kr*

Received 27 November 2002
Revised 17 December 2002

The photopatterning process of self-assembled monolayer has been used as template for fabricating biomolecular microstructures. Alkanethiolates formed by the adsorption of 1-octanethiol molecules on a gold substrate were oxidized by the irradiation of deep UV light and then developed with deionized water. The resulting positive patterned substrate was immersed into a dilute ethanolic solution of 11-mercaptoundecanoic acid (11-MUDA). Cytochrome c monolayers were immobilized onto the patterned gold substrate by self-assembly technique and their electrochemical properties were investigated through the measurements of cyclic voltammetry. Also, I–V characteristics of biomolecular multilayers consisting of cytochrome c and green fluorescent protein (GFP) were studied with a scanning tunneling microscope (STM).

Keywords: Photopatterning; self-assembled monolayer; cytochrome c; GFP; electrochemical property; I–V characteristics.

1. Introduction

Self-assembled monolayers (SAMs) can potentially give a robust method for fabricating protein multilayers. Moreover, the affinity of thiol moiety for gold surface makes alkanethiol suitable for the preparation of modified electrode.[1] The micro array pattern formation of self-assembled protein is an important factor in the fabrication of molecular device composed of biomolecules. Thus, the ability to generate fine pattern of protein on a solid surface has attracted considerable interest in bioelectronic technology and fundamental study of biophysics, especially, the studies on the characteristics for patterning and modification of solid surface at molecular level, and the use of these patterns to control the immobilization of protein have been widely progressed. In this study, we have fabricated the submicro array of biophotodiode consisting of alkanethiolate/cytochrome c/GFP/gold by using alkanethiolate SAMs as a very simple photoresist utilizing photochemical conversion of alkanethiolates to alkanesulfonates.[2] The physical and electrochemical properties of self-assembled protein multilayers were studied through the measurements of cyclic voltammetry (CV), photoluminescence (PL) and atomic force microscopy (AFM).

The photodiode property using a scanning tunneling microscope (STM) was also investigated.

2. Materials and Experiment

2.1. *Materials*

Ethyl alcohol anhydrous (99.99%), 11-mercaptoundecanoic acid (11-MUDA) and decanethiol were purchased from Aldrich Chemical Co. (Milwaukee, USA). 1-Octanethiol was purchased from TCI Co. (Japan). Cytochrome c (extracted from horse heart muscle) and GFP (rEGFP protein) were purchased from Sigma Chemical Co. (St. Louis, USA) and Clontech Co. (Palo Alto, USA), respectively. Au (111) substrate was purchased from INOSTEK Inc. (Korea). Other reagents were purchased from Aldrich Chemical Co. and used without further purification.

2.2. *Fabrication of SAMs and protein multilayers*

Gold substrate was pretreated by a *piranha* solution for 5 min, rinsed with deionized water. The gold substrate was immersed into 1 mM octanethiol ethanolic solution for 18 h. Following the removal from the thiol solution, the substrate was washed with degassed ethanol, and then dried in a stream of nitrogen. The photopattering of alkanethiol monolayer was carried out with an exposure system of Spectral Energy Co. equipped with a 500 W high-pressure mercury lamp in conjunction with a narrow band pass filter for 254 nm.[3] The self-assembled octanethiol monolayer on a gold substrate was oxidized by deep UV irradiation, and then developed with deionized water. The resulting positive patterned substrate was immersed into ethanolic solution of 1 mM 11-MUDA. Cytochrome c was sequentially immobilized onto the modified substrate.[4] The carboxylic group of 11-MUDA allowed the cytochrome c to form SAM. Finally, GFP molecules were adsorbed onto the self-assembled cytochrome c monolayer.

2.3. *Characterizations*

Static secondary ion mass spectrometer (SSIMS) was investigated with a PHI 7200 TOF-SIMS/SALi. The topographies of self-assembled cytochrome c on the photopatterned monolayer were observed by AFM (AutoProbe CP, Park Scientific Instruments, USA). Cyclic voltammetry measurements were carried out with a potentiostat measurement analyzer (IM6 system, Zahner Elektrik Co., Germany). The Ag/AgCl (3.0 M KCl) reference electrode, a gold substrate working electrode, and a 1-cm^2 Pt-gauze counter electrode were used for all experiments. The I–V characteristics of the protein multilayers were studied by a STM (AutoProbe CP, Park Scientific Instruments, USA) technique. The set point for Au tip approaching was 0.5 nA and the scan range for conductivity measurement was $-0.5 \sim 0.5$ V.

3. Results and Discussion

Figure 1 shows SSIMS spectra of SAM of 1-octanethiol on a gold substrate before and after exposure to deep UV light for 60 min. The spectrum of SAM exhibited a peak corresponding to 1-octanethiol at m/z 145. After the irradiation of deep UV light, a peak corresponding to the sulfonate species, RSO_3^- was observed at m/z 193.

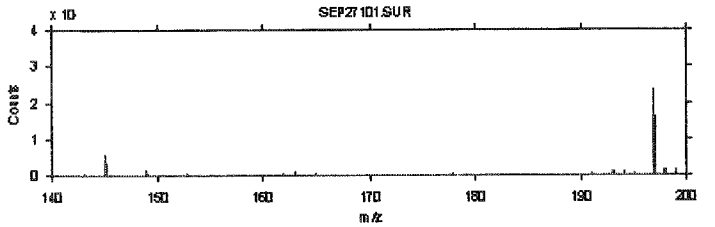

(a)

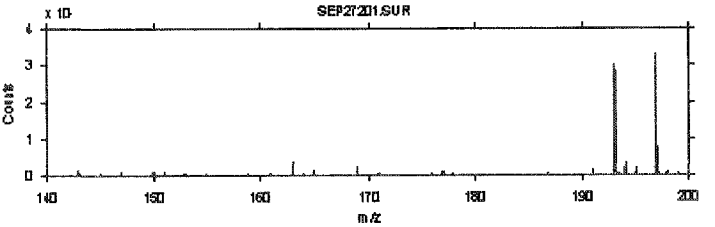

(b)

Fig. 1. SSIMS spectra of 1-octanethiol SAM (a) before and (b) after exposure to deep UV light.

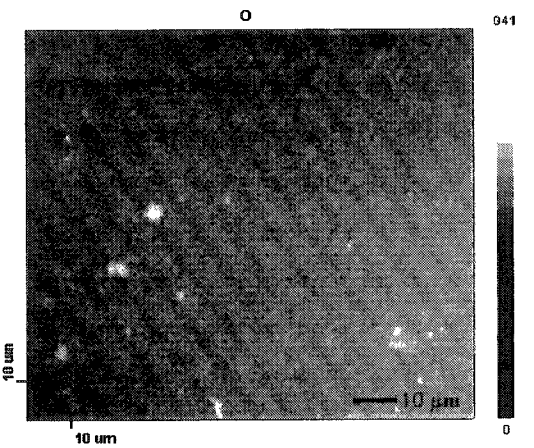

Fig. 2. SSIMS image of photopatterned SAM formed by mapping O^- intensity.

The ratios of these peak areas were used to calculate the extent of oxidation.[5] It can be found that 99% conversion of octanethiolates to octanesulfonates occurred by the irradiation of deep UV light. Figure 2 shows a SSIMS mapping of 1-octanethiol SAM and SAM of 11-MUDA adsorbed onto the patterned gold substrate. The carboxylic acid terminated regions exhibited bright contrast by mapping the oxygen intensity, while methyl terminated regions exhibited dark contrast.

Figure 3 shows AFM images of bare gold and self-assembled cytochrome c monolayer immobilized onto the 11-MUDA molecules. It is indicated that the head moiety

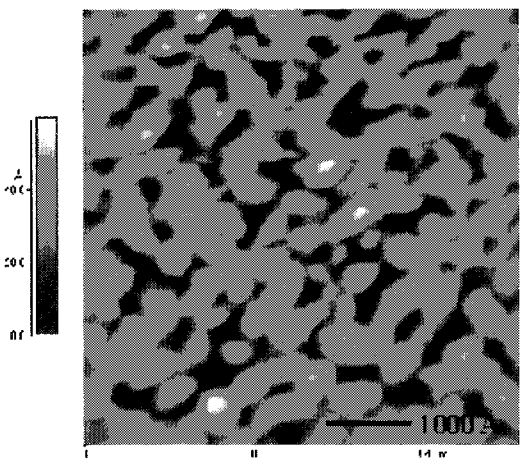

(a)

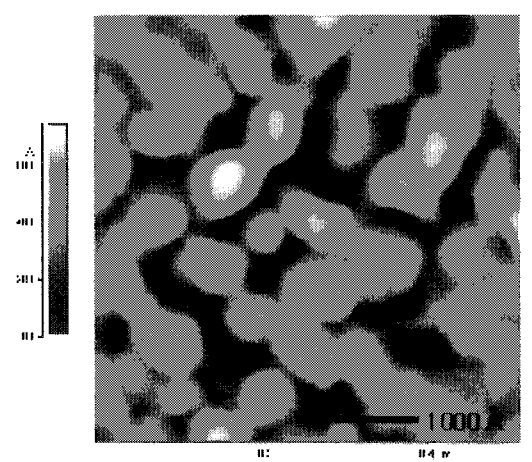

(b)

Fig. 3. AFM images of (a) bare gold and (b) cytochrome c monolayer.

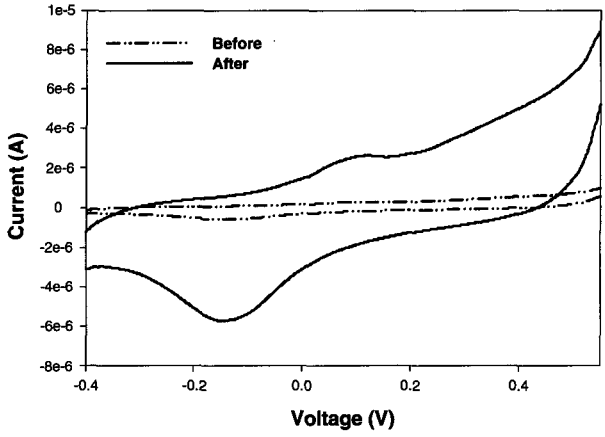

Fig. 4. Cyclic voltammogram of cytochrome c monolayer before (-···-) and after (—) immobilization of cytochrome c.

of cytochrome c molecule and methyl-terminated alkanethiolates exhibited bright and dark spots, respectively. The size and height of bright spot domain were 600 Å and 50 Å. The redox current of the cytochrome c monolayer was observed from the measurement of cyclic voltammetry as shown in Fig. 4. It has been noted that uniform cytochrome c molecules were well immobilized onto the patterned 11-MUDA molecules. To explore the rectifying property of hetero self-assembled multilayers of cytochrome c and GFP, the current–voltage characteristics were measured by a STM technique.

4. Conclusions

The submicro pattern of self-assembled 1-octanethiol monolayer on a gold substrate was fabricated by photochemical oxidation using a 700 ~ 800 nm mask. 11-MUDA molecules were well self-assembled onto the positive patterned gold substrate. It has been found that the patterned biomolecular photodiode consisting of cytochrome c–GFP multilayers was successfully obtained by using the simple photopatterning of SAM.

Acknowledgment

This work was supported by Korea Research Foundation Grant (KRF-2002-005-D0000 2).

References

1. L. Jiang, A. Glidle, A. Griffith, C. J. McNeil, and J. M. Cooper, *Bioelectrochem.* **42**, 15 (1997).
2. M. J. Tarlov, D. R. F. Burgess, and G. Gillen, *J. Am. Chem. Soc.* **115**, 5305 (1993).

3. S. Y. Oh, J. K. Park, J. W. Choi, and C. M. Chung, *Mol. Cryst. Liq. Cryst.* **370**, 169 (2001).
4. S. Y. Oh, J. K. Park, J. W. Choi, and C. M. Chung, *Mol. Cryst. Liq. Cryst.* **377**, 241 (2002).
5. M. J. Tarlov and J. G. Newman, *Langmuir* **8**, 1398 (1992).

International Journal of Nanoscience, Vol. 1, Nos. 5 & 6 (2002) 617–620

PREPARATION OF HOLLOW STRUCTURES COMPOSED OF TITANIA NANOCRYSTAL ASSEMBLY

SHIGENORI FUJIKAWA and TOYOKI KUNITAKE

Topochemical Design Laboratory, Frontier Research System, RIKEN
2-1 Hirosawa, Wako-shi, Saitama 351-0198, Japan

Received 9 January 2003
Revised 11 January 2003

A novel procedure to fabricate nanoarchitectures of crystalline titania hollow shells was developed by using assembled latex particles as templates. Latex particles were assembled on the surface of solid substrates and covered with ultrathin titania films by the surface sol–gel process. When the titania-covered latex particle was subjected to oxygen plasma treatment, hollow titania spheres were formed at the original site of particle deposition. Following calcination of the amorphous, titania hollow shells induced their crystallization to titania nanocrystals (anatase).

Keywords: Nanocrystal; titania; 3D structure; ultrathin film.

1. Introduction

Surface fabrication for the construction of 3D nanoarchitectures is a key feature of nanotechnology. The design and preparation of dispersed hollow structures is considered as one of the most interesting topics, because of its many potential applications such as drug delivery. The template approach has been widely utilized to prepare hollow structures in most of the previous studies. Unfortunately, the shape of the hollow structure is rather restricted in this approach, because it is still difficult to freely design 3D nanosized templates which can be dispersed in solution. In contrast, the shape of nanometer-sized objects, if they are placed on solid surface, can be designed by the conventional fabrication technique, such as photo- and electron-lithographies, micro contact printing and nanoparticle arrangement. The morphology of the hollow structure, however, would be limited by such approaches. Thus, we proposed the use of nano-objects as template for preparation of surface-bound hollow structures, and successfully obtained interconnected titania hollow structures from the 2D-assembled latex particles.[1] In this case, the shell component of the hollow structure is composed of ultrathin layers of amorphous titania. It is known that titania assumes two crystalline types, anatase and rutile, and the particular crystalline state is responsible for unique functions such as a photo-catalytic activity.[2] The well-designed shape of titania crystal would offer a great potential as functional material. For example, a hollow structure composed of

titania crystal may be expected as effective photo-catalyst because of its large surface area. In this report, we examined conversion of amorphous titania hollow shells to the corresponding crystalline state without changing the unique morphological characteristics.

2. Experimental Procedure

The latex particle we employed (Polyscience: Polybeads carboxylate) has carboxyl groups on its surface. The diameter is 500 nm, and it is supplied as 2.61 wt% aqueous dispersion. It was used after dilution to 1/10 by ion-exchanged water. Silicon wafer (Tokyo Ohka Kogyo) and silicon oxide-coated TEM gold grid (Ted Pella: Silicon Monoxide Type-A) were used as solid substrates. In order to prepare a positively-charged surface, these solid substrates were immersed in an aqueous solution of poly(diallyldimethylammonium chloride) (PDDA, Polymer Source: MW = 240 000, 1 mg/ml) and in ion-exchanged water for 1 min each. It was then immersed in an aqueous solution of poly(sodium styrene-4-sulfonate) (PSS, Polymer Source: MW = 127 600, 1 mg/ml) and in ion-exchanged water for 1 min each. These successive operations were repeated three times, and the modified substrate was further immersed in aqueous PDDA. Latex particles were adsorbed by dipping the substrate for 10 min in their aqueous dispersions. It was then soaked in ion-exchanged water for 1 min, and the substrate was dried by flushing nitrogen gas. The surface sol–gel process was conducted by dipping the substrate in 100 mM of titanium (IV) iso-propoxide (Azmax) in ethanol for 1 min, rinsing by ethanol and ion-exchanged water for 1 min each, and drying by flushing nitrogen gas. This process was repeated five times. Oxygen plasma treatment (South Bay Technology: PE-2000 Plasma Etcher) was carried out by placing the sample directly on the RF electrode. The applied radio frequency (RF) was 13.56 MHz and the base pressure in the reactor was 75 mTorr. The oxygen (industrial grade) pressure during plasma treatment was about 180 mTorr and the RF power dissipated to the sample was 20 W for 1 h at room temperature. Subsequently, the substrate was placed on a bench inside a muffle furnace (Denken, KDF S-70) for calcination and the temperature was raised from room temperature to 600°C in 5 h, kept at 600°C for 4 h, and finally allowed to cool to room temperature.

SEM images were obtained by using a Hitachi S-5200 scanning electron microscope, operated at an acceleration voltage of 1.0 kV, without sample coating. TEM observation was conducted on a JEOL JEM-2000EX instrument. The sample prepared on silicon oxide grid was subjected without staining to TEM observation with an acceleration voltage of 100 kV and an original magnification of 10 000. In the measurement of electron diffraction, the camera length was 80 cm at the same acceleration voltage.

3. Results and Discussion

The latex samples on which the surface sol–gel process was repeated for five cycles (Fig. 1(b)) were exposed to oxygen plasma for 1 h (Fig. 1(c)), and subjected to

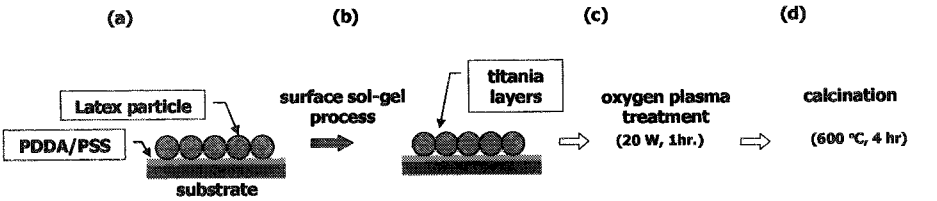

Fig. 1. Preparation of the hollow structure composed of assembled titania nanocrystals by oxygen plasma treatment and calcination from latex-titania core/shell structure.

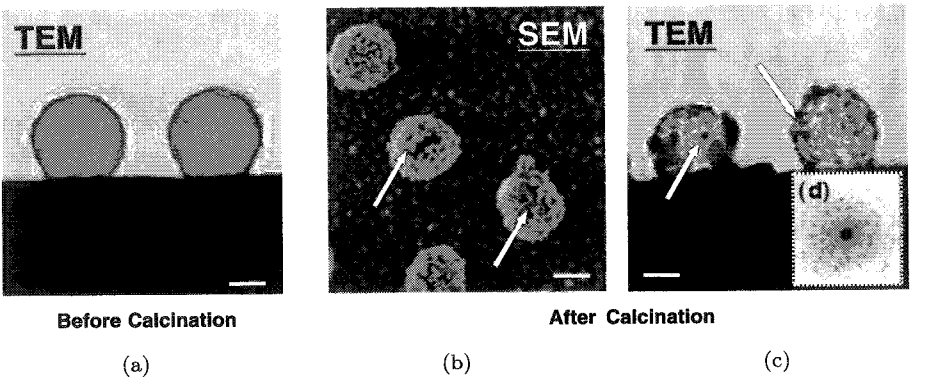

Fig. 2. SEM and TEM images of the titania hollow structures before and after calcination. (a) Before calcination, (b) and (c) after calcination, and (d) diffraction pattern of the micro crystal in (c). Scale bar corresponds to 200 nm.

TEM observation. Figure 2(a) shows a TEM image of the plasma-treated sample, in which spherical structures are clearly observed. The diameter of the sphere is about 500 nm and the thickness of the shell is estimated to be about 10 nm. There is no material left inside the sphere, showing that the original latex particle was completely removed by oxygen plasma treatment. This situation was also confirmed in our previous report.[1]

Titania can be converted from amorphous state to crystalline anatase by calcination. Thus, the oxygen plasma treated hollow structure of ultrathin titania shell was subjected to calcination. The oven temperature was raised to 600°C from room temperature at a rate of 2°C/min, and was held at this temperature for 4 h (Fig. 1(d)). SEM observation of the calcined sample proved that the spherical shell was totally preserved even after calcination (Fig. 2(b)). Direct calcination of titania film-coated latex particle without pre-treatment of oxygen plasma underwent collapse of the hollow structures and only flattened titania disk was formed (data not shown). In short, once a hollow structure is formed by oxygen plasma treatment, it is not destroyed by calcination. Oxygen plasma treatment is indispensable for maintaining the hollow structure of ultrathin titania shell.

In the surface sol–gel reaction alone, the condensation reaction does not proceed to completion and unreacted alkoxide moieties still remain in the oxide layer.[3] The mechanical strength of the as-prepared ultrathin titania shell appears not strong enough to preserve the spherical structure during calcination. Oxygen plasma promotes decomposition of the organic moiety and further condensation of titanium oxide, surface morphology of the spheres after calcination is not smooth nor continuous, in contrast to the smooth surface before calcination (Figs. 2(a) and 2(c)). It has a skeleton-like structure, which is composed of small blocks of titania with sizes of 10 to several tens nm (Fig. 2(b): indicated by arrows). The TEM observation clearly shows that the skeleton-like structure is composed of micro blocks of titanium oxide (Fig. 2(c): indicated by arrows). The electron diffraction of the blocks shows a distinct pattern (Fig. 2(d)) of the anatase crystal.[4–6] Since the crystal phase has a higher density than the amorphous phase,[7] the titania layer upon calcinations should shrink due to crystallization and the original titania shell becomes less continuous, creating defects. The nanocrystals of anatase are tightly connected to each other, maintaining the three-dimensional structure (Figs. 2(b) and 2(c)). The shape of the titania nanocrystal assembly is readily designed on the basis of the structure of the original template. In the current study, we used rather simple templates in order to test the feasibility of our approach. More complex patterns and the corresponding functions would be derived from more complex templates. We should emphasize the role of the oxygen plasma treatment for maintaining three-dimensional structures which have not been put to proper use in the past. In conclusion, it is clear that the current approach offers a great potential for surface fabrication of hollow structures composed of nanosized metal oxide crystals.

References

1. S. Fujikawa and T. Kunitake, *Chem. Lett.* **11**, 1134 (2002).
2. A. Fujishima and K. Honda, *Nature* **37**, 238 (1972).
3. I. Ichinose, H. Senzu, and T. Kunitake, *Chem. Mater.* **9**, 1296 (1997).
4. T. Kasuga, M. Hiramatsu, A. Hoson, T. Sekino, and K. Niihara, *Langmuir* **14**, 3160 (1998).
5. L. Wang, T. Sasaki, Y. Ebina, K. Kurashima, and M. Watanabe, *Chem. Mater.* **14**, 4827 (2002).
6. S.-Z. Chu, K. Wada, S. Inoue, and S. Todoroki, *Chem. Mater.* **14**, 266 (2002).
7. J. Huang, I. Ichinose, T. Kunitake, and A. Nakao, *Langmuir* **18**, 9048 (2002).

International Journal of Nanoscience, Vol. 1, Nos. 5 & 6 (2002) 621–625

MICRO-PHASE SEPARATION IN BINARY MIXED LANGMUIR MONOLAYERS: CORRELATION BETWEEN MOLAR FRACTION AND AREA FRACTION

TATSUYA SHIRAKU, KEN-ICHI IIMURA, and TEIJI KATO

Department of Applied Chemistry, Faculty of Engineering, Utsunomiya University 7-1-2 Yoto, Utsunomiya 321-8585, Japan

Received 27 November 2002
Revised 24 December 2002

Correlation between molar fraction and area fraction in micro-phase separated structures formed in binary mixed Langmuir monolayers of arachidic acid (C20) and a perfluoropolyether amphiphile (PFPE) has been examined. On the water surface, C20 and PFPE separate into fully condensed micro-domains and a largely expanded phase, respectively. The area fraction of the condensed phase domains is estimated by two different ways: one is by analyzing atomic force microscope (AFM) images and the other is calculated from π–A isotherm data assuming complete immiscibility of the film components in the monolayers. Two area fractions are in agreement with each other, and increase exponentially with increase in molar fraction. Our results ensure the complete phase separation of the two film components on the water surface, the monolayer transfer without any structural changes, and the fruitfulness of digital image analysis for the evaluation of two-dimensional organized structures.

Keywords: Mixed Langmuir monolayer; two-dimensional phase separation; π–A isotherm; atomic force microscope (AFM); area fraction.

1. Introduction

Two-dimensional phase separation in binary mixed Langmuir monolayers are of great interest in surface engineering. In particular, phase-separated monolayers of long-chain silanes are advantageous as a versatile system because of their chemisorption to give robust films on hydroxylic solid surfaces.[1–3] However, the formation mechanism of the phase-separated morphology has not been well understood. Apparently, this is not only the case of silane compounds but also of usual amphiphiles, although such knowledge is of significant important for controlled construction of patterned functional surfaces.

In previous work, we have shown the systematic variation of phase-separated structures in binary mixed Langmuir monolayers of n-alkyl fatty acid (Cn) and PFPE.[4] The final goal of our work is to find out the fundamental principles, which control the phase-separated morphologies formed in mixed monolayers of a variety of amphiphiles. Cn is the most suitable film material for this investigation because of

its unique characteristics and widespread usage, even though it has less monolayer stability on solid substrates than chlorosilane.

In this paper, we report correlation between the area fraction and the molar fraction in mixed monolayers of arachidic acid (C20) and PFPE. AFM images revealed that C20 forms circular domains at 20°C irrespective of the mixing ratio, however, the number of the domains increased with increasing mixing ratio. Area fraction of C20 domains (ϕ_{AFM}), estimated from AFM images, was correlated with molar fraction of C20 (ϕ) in mixtures and was compared with the area fraction ($\phi_{\pi-A}$) calculated from π–A isotherm data.

2. Experimental

Highly purified arachidic acid (C20) and perfluoro-2,5,8-tirimethyl-3,6,9-trioxadodecanoic acid (PFPE) were used as film materials without further purification. Chloroform was employed as the spreading solvent. C20 and PFPE were mixed in the spreading solution under defined molar ratios to give a total concentration of 2.5 mM. The subphase was a 0.5 mM aqueous solution of cadmium acetate dehydrate adjusted to pH 7.0 with potassium hydrogen carbonate. Monolayers were compressed after 30 min of spreading at a constant strain rate of 10%/min. The monolayers were transferred onto silicon wafer substrates at 20 mNm^{-1} pressure by the horizontal scooping-up method. AFM observation was performed using Nanoscope III (Digital Instruments Inc.) with tapping mode. The images were obtained with a spatial resolution of 512 × 512 pixels and binarized to estimate area fraction of C20 phase using a digital image analysis software, Win ROOF (MITANI Corp.).

3. Results and Discussion

Figure 1 shows (a) π–A isotherms and (b) AFM images of C20/PFPE mixed monolayers at 20°C. The isotherm shifts regularly with the change in the mixing ratio, giving a linear relation between the molar fractions of C20 and the average molecular areas at 10, 20, and 30 mNm^{-1} (the plots are not shown). It is well known that the average molecular area becomes a linear function of composition when two components are ideally miscible or completely immiscible in their mixed monolayers. Considering the fact that the phase separation occurred in the mixed monolayers as seen in the AFM images in Fig. 1(b), it is clear that the two components are completely immiscible in the present system. Independent contribution of the film components to the monolayer behavior was observed in the isotherm of C20/PFPE (8/2) monolayer, in which two collapses appear at about 40 mNm^{-1} and above 60 mNm^{-1} corresponding to collapses of PFPE and C20 phase, respectively. This observation indicates that a higher molecular area region in the isotherm is governed by PFPE component, and after the collapse of PFPE component, the feature of C20 component emerges at a lower molecular area. The AFM images in Fig. 1(b)

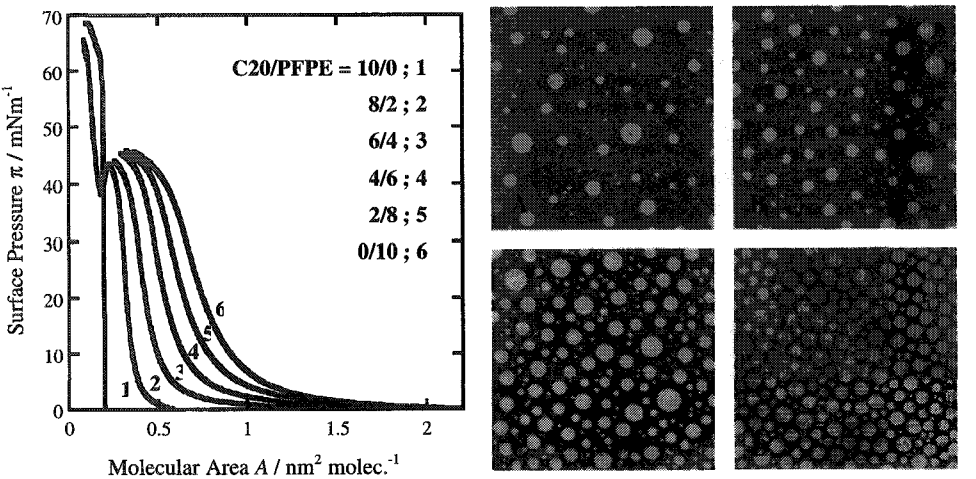

(a) π–A isotherms (b) AFM images (30×20 μm^2)

Fig. 1. Mixing ratio dependency of (a) π–A isotherm and (b) AFM image of C20/PFPE mixed monolayers at 20°C. In AFM images, the mixing ratios of C20/PFPE are (A) 2/8, (B) 4/6, (C) 6/4, and (D) 8/2. Deposition pressure was 20 mNm^{-1} for all monolayers.

imply that C20 and PFPE form island-like condensed phase domains and a surrounding sea-like region in the mixed monolayers, respectively. The number of C20 domains increase with the increase in the molar fraction of C20, while the domain shape remained circular regardless of the mixing ratio.

Area fraction of C20, $\phi_{\pi-A}$, was calculated by the following equation when two film components are mutually immiscible in their mixed monolayer,

$$\phi_{\pi-A} = \frac{\phi A_{\mathrm{C20}}}{\phi A_{\mathrm{C20}} + (1-\phi) A_{\mathrm{PFPE}}}, \tag{1}$$

where ϕ is the molar fraction of C20 in the mixtures, and A_{C20} and A_{PFPE} are the molecular area of C20 and PFPE, respectively. From π–A isotherms of single component monolayers, one obtains $A_{\mathrm{C20}} = 0.199$ nm^{2}molec.$^{-1}$ and $A_{\mathrm{PFPE}} = 0.749$ nm^{2}molec.$^{-1}$ at 20 mNm^{-1}, and hence can calculate the values of $\phi_{\pi-A}$ for different mixing ratios. On the other hand, we can also estimate the area fraction of C20 by analyzing AFM images of the phase-separated monolayers. In this case, the area fraction, ϕ_{AFM}, was calculated by dividing the area of C20 domains in the image by the total image area. Data of ϕ_{AFM} shown hereafter is the average of the values obtained from at least ten macroscopically separate areas on at least two samples.

Values of ϕ, $\phi_{\pi-A}$, and ϕ_{AFM} were summarized in Table 1. It should be noted here that the molar fraction is not consistent with the area fractions since C20 and PFPE occupy largely different molecular areas on the water surface. The relation between the area fractions and molar fraction was shown in Fig. 2. It becomes clear

Table 1. Molar fraction (ϕ) and area fractions (ϕ_{AFM}, $\phi_{\pi-A}$) of C20 in mixed monolayers at 20°C.

Molar fraction of C20, ϕ	Area fraction of C20 calculated by Eq. (1), $\phi_{\pi-A}$	Area fraction of C20 determined from AFM images, ϕ_{AFM}
0	0	—
0.2	0.062	0.080 ± 0.010
0.4	0.151	0.121 ± 0.021
0.6	0.285	0.246 ± 0.026
0.8	0.516	0.409 ± 0.024
1	1	—

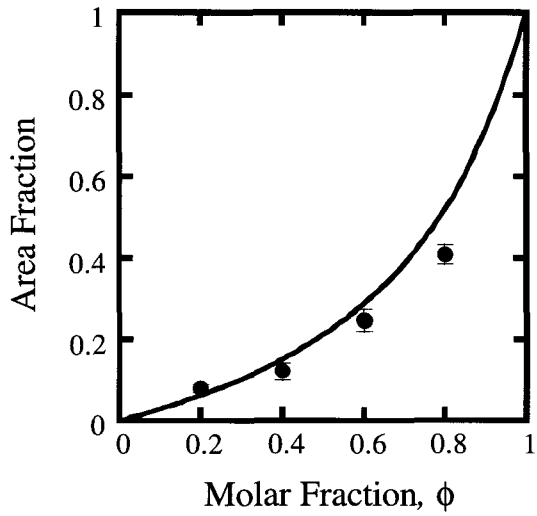

Fig. 2. A plot of area fraction of C20 at 20 mNm^{-1} versus molar fraction of C20 (ϕ) in the mixtures: ϕ_{AFM} determined from AFM images (•), $\phi_{\pi-A}$ calculated by Eq. (1) (—).

that $\phi_{\pi-A}$ and ϕ_{AFM} almost coincide with each other, and exponentially increase with the increase of ϕ. The good agreement between two area fractions indicates that two film components are completely phase-separated, and the monolayers are transferred on the solid supports without any structural changes from the water surface. Moreover, the results suggest the fruitfulness of the digital image analysis for the evaluation of monolayer structures.

Acknowledgments

The authors thank Prof. N. Suzuki (Utsunomiya University, Japan) for helpful discussion. Part of this work was supported by the Satellite Venture Business Laboratory of Utsunomiya University and by Grant-in-Aid for Scientific Research (12555240) in 2000–2002 from the Ministry of Education, Culture, Sports, Science, and Technology.

References

1. S. Ge, A. Takahara, and T. Kajiyama, *Langmuir* **11**, 1341 (1995).
2. M. Fujihira and Y. Morita, *J. Vac. Sci. Technol. B* **12**, 1609 (1994).
3. K. Iimura, K. Ito, and T. Kato, *Mol. Cryst. Liq. Cryst.* **322**, 117 (1998).
4. K. Iimura, T. Shiraku, and T. Kato, *Langmuir*, in press.

This page is intentionally left blank

International Journal of Nanoscience, Vol. 1, Nos. 5 & 6 (2002) 627–630

PRESSURE EFFECT ON CONDUCTIVITY IN Au(dmit)$_2$ LANGMUIR–BLODGETT FILMS

YASUHIRO F. MIURA*, SHIN-ICHI MORITA,
SHIN-HACHIRO SAITO, and MICHIO SUGI

Department of Functional Chemistry, Toin University of Yokohama
1614 Kurogane-cho, Aoba-ku, Yokohama, 225-8502, Japan
**yfmiura@cc.toin.ac.jp*

MASATO HEDO and YOSHIYA UWATOKO

Institute for Solid State Physics, University of Tokyo
5-1-5 Kashiwanoha, Kashiwa, 277-8581, Japan

Received 27 November 2002
Revised 26 December 2002

The resistance of the Langmuir–Blodgett films of ditetradecyldimethylammonium-Au(dmit)$_2$ ($2C_{14}$-Au(dmit)$_2$) salt has been measured under hydrostatic pressure up to 0.7 GPa. The room-temperature resistance decreases with increasing pressure, reaching a 0.6-times smaller value compared to that at ambient pressure. The film under the pressure shows a clear resistance decrease below 1.4 K on cooling, while that under ambient pressure shows a blunt decrease below 0.85 K and it turns to increase below 0.65 K. These results suggest the existence of the pressure-induced superconducting phase together with the earlier results of the ac magnetic susceptibility measurement.

Keywords: Langmuir–Blodgett techniques; superconductivity; electrochemical doping.

1. Introduction

The fabrication of a superconducting Langmuir–Blodgett (LB) film is one of the long-standing goals among various trials for fabricating LB films with electronic and opto-electronic functions. Since the LB technique allows us to assemble organic molecules, amphiphilic ones typically, into organized two-dimensional molecular sheets, the realization of superconductivity will open up the possibility for a variety of applications in the field of nanomolecular electronics.[1]

We have been interested in the metal(dmit)$_2$ systems as the film-forming materials for the LB films and have reported that the LB film of ditetradecyldimethylammonium-Au(dmit)$_2$ ($2C_{14}$-Au(dmit)$_2$, Fig. 1) shows an in-plane conductivity of 40–50 S/cm at room temperature with a metallic temperature dependence in the range 230–300 K.[2] Recently, we have also reported that the ac

*Corresponding author.

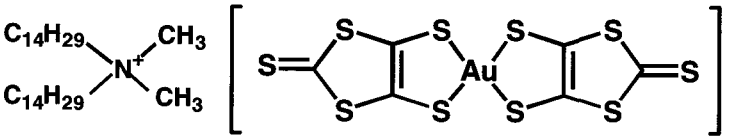

Fig. 1. Chemical structure of $2C_{14}$-Au(dmit)$_2$ salt.

magnetic susceptibility suggests the existence of superconducting phase below 4 K.[3] While the diamagnetic shift of the ac magnetic susceptibility can be reproducibly seen, the resistance decrease upon cooling cannot be seen for the majority of the sample batches in the measurement down to 1.2 K.[4]

It is well-known that the parameter, "pressure", often induces superconductivity in a variety of materials that includes molecular conductors. In particular, superconducting states in the bulk metal(dmit)$_2$ (metal = Ni, Pd) systems are mostly induced by hydrostatic pressure.[5] We postulate that the pressure is also an important parameter for the LB systems based on charge-transferred salts and we report here the effect of hydrostatic pressure upon the resistance of the $2C_{14}$-Au(dmit)$_2$ LB films.

2. Experimental

The $2C_{14}$-Au(dmit)$_2$ salt was synthesized following the procedure of Steimecke *et al.*[6] and spread at the air/water interface using a 1:1 mixture of acetonitrile and benzene. The horizontal lifting method was utilized and the $2C_{14}$-Au(dmit)$_2$ film at the air/water interface was transferred onto a 0.1-mm-thick poly(ethylene terephthalate) (PET) sheet. Prior to the LB film deposition, the substrate was precoated with five layers of cadmium arachidate and four gold electrode strips with a gap of 0.5 mm were vacuum-deposited on it. The as-deposited LB film was rendered to be conductive by electrochemical doping in an aqueous solution of $LiClO_4$. The details of the sample preparation are in our previous papers.[2–4]

The resistance was measured along the film plane by the four electrode strips deposited underneath the LB layers. A dc four-probe method and an ac four-probe method were used for measuring the room-temperature resistance and the temperature dependence of the resistance, respectively. The resistance was measured for the 20-layered $2C_{14}$-Au(dmit)$_2$ LB films unless otherwise stated. As the hydrostatic pressure medium, a hydrocarbon oil (Daphne Oil 7373, Idemitsu, Co. Ltd.) was used. The details of the high pressure apparatus will be described elsewhere.[7]

3. Results and Discussion

The resistance of the $2C_{14}$-Au(dmit)$_2$ LB film decreases with increasing pressure, reaching a 0.6-times smaller value at 0.7 GPa. Then the pressure cell was clamped at 0.7 GPa and cooled down to 0.5 K. A different sample strip cut from the same

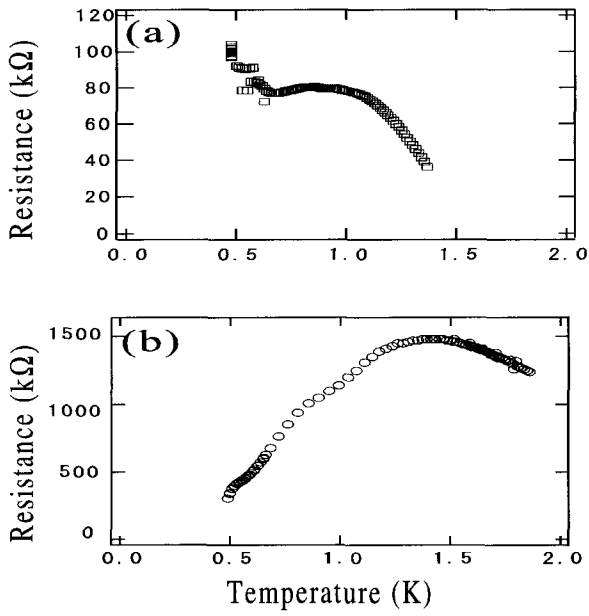

Fig. 2. The resistance of the 20-layered $2C_{14}$-Au(dmit)$_2$ LB film at (a) ambient and at (b) 0.7 GPa.

sample batch was also set outside the pressure cell and the ambient resistance was measured as the reference.

We have already reported that some sample batches of the $2C_{14}$-Au(dmit)$_2$ LB system show resistance decrease on cooling below 3.9 K, however, this sample batch did not show any resistance decrease in the measurement down to 1.5 K. The temperature dependence of the resistance at 1 bar and at 0.7 GPa are shown in Figs. 2(a) and 2(b), respectively. As shown in Figs. 2(a), a blunt decrease is seen below 0.85 K, but it turns to increase below 0.65 K on cooling, which is possibly interpreted as a re-entrant state. On the other hand, as shown in Fig. 2(b), a distinct resistance decrease is seen below 1.4 K. The vast difference in the magnitude of the resistance between the sample at 1 bar (Fig. 2(a)) and that at 0.7 GPa (Fig. 2(b)) is mostly due to the sample size. Since the thickness of the 20-layered LB films is ca. 10^2 nm, resistivities at 1 bar and at 0.7 GPa at around 1.4 K are both as low as 10^1 Ω cm.

We have already reported that the ac magnetic susceptibility suggests the existence of the Meissner state below 4 K.[3] The pressure-induced decrease of the resistance on cooling is possibly caused by the emergence of superconducting phase. The measurements at higher pressure and under dc magnetic fields are now underway.

Acknowledgments

We thank Mr. Takamasa Hasegawa, Mr. Ayumu Kato, and Ms. Emi Saito for technical assistance. This work was supported in part by Grant-in-Aid for Scientific

Research of Ministry of Education, Culture, Sports, Science and Technology (Japan) under Grant No. 12750019, and Kanagawa Academy of Science and Technology (Japan) under Grant No. 0012011. This work was also carried out in part by the Visiting Researcher's Program of the Institute for Solid State Physics, the University of Tokyo.

References

1. A. Ulman, *An Introduction to Ultrathin Organic Films: From Langmuir–Blodgett Films to Self-Assembly* (Academic Press, San Diego, 1991).
2. Y. F. Miura, Y. Okuma, H. Ohnishi, T. Kawasaki, and M. Sugi, *Jpn. J. Appl. Phys.* **37**, L1481 (1998).
3. Y. F. Miura, M. Horikiri, S.-H. Saito, and M. Sugi, *Solid State Commun.* **113**, 603 (2000).
4. Y. F. Miura, M. Horikiri, S. Tajima, T. Wakaita, S.-H. Saito, and M. Sugi, *Synth. Met.* **120**, 727 (2001).
5. T. Ishiguro, K. Yamaji, and G. Saito (eds.), *Organic Superconductors, Springer Ser. in Solid-State Sci.*, Vol. 51, 2nd edition (Springer-Verlag, Berlin, 1998).
6. G. Steimecke, H. J. Sieler, P. Kirmse, and E. Hoyer, *Phosphorus Sulfur* **7**, 49 (1979).
7. Y. Uwatoko, private communication.

International Journal of Nanoscience, Vol. 1, Nos. 5 & 6 (2002) 631–635

SYNTHESIS OF NOVEL NANOMETER SIZE RUTHENIUM COMPLEXES FOR SINGLE ELECTRON CHARGING DEVICES AND THEIR ELECTROCHEMICAL PROPERTIES

HIROAKI ENDO* and TAKUJI OGAWA†

Department of Chemistry, Faculty of Science, Ehime University
2-5 Bunkyocho, Matsuyama, Ehime 790-8577, Japan
†*Precursory Research for Embryonic Science and Technology*
Japan Science and Technology Corporation
1-8 Honcho, Kawaguchi, Saitama 332-0012, Japan
**endo@chem.sci.ehime-u.ac.jp*
†*ogawat@dpc.ehime-u.ac.jp*

Received 27 November 2002
Revised 9 January 2003

With the aim of studying single charging phenomena of individual molecules that have clear redox states, a series of ruthenium complexes surrounded by dendrimers were prepared. The structure and electronic characteristics of them were studied by ^{1}H NMR, MALDI TOF-MS, UV-vis absorption spectra and electrochemical methods. The electrochemical results revealed that the clear redox states were retained even with the surrounding dendrimers, and the molecules can be good candidates for nanometer size charging pools.

Keywords: Ruthenium complex; single electron transistors; Coulomb blockade phenomena.

1. Introduction

The Coulomb blockade is an essential phenomena in nanoscale electronics, and is utilized for single electron transistors using silicon particles as the charging islands.[1,2] The charging energies (U_c) of metal particles are definitely determined by the size of the particles (r) as follows; $U_c = e^2/8\pi\varepsilon r$. The size should not be more than 1 nm in order to observe the Coulomb blockade at room temperature. It is not easy to make this size of metal or semiconductor particles with little size distributions. In contrast, most organic molecules have the size of this region and there are essentially no distributions. In addition, their electronic states are determined not only by their sizes but also by the constituting elements and molecular structures. Thus, the studies of the Coulomb blockade with using organic molecules are

*Corresponding author.

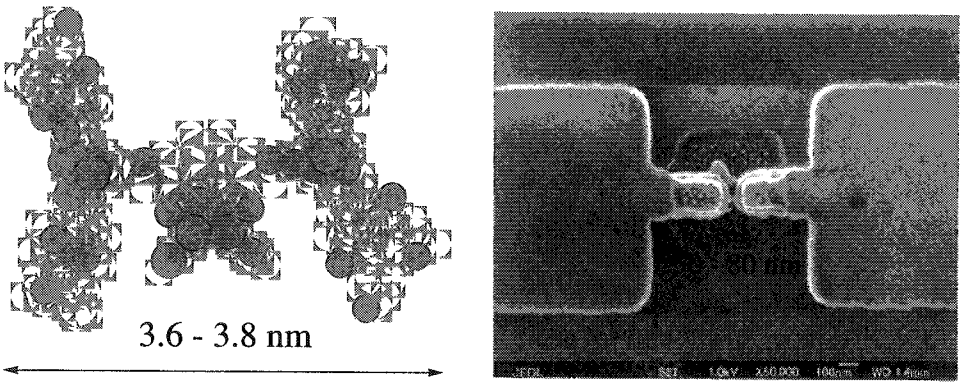

(a) (b)

Fig. 1. (a) Molecular modeling structure of the ruthenium complex protected by dendrimer moieties (**4**). The size of the molecule was calculated to be ca. 3.6–3.8 nm. (b) Scanning electron microscopic image of the nanogap electrode. The gap sizes were about 50–80 nm.

promising because of the low size distributions and the high designability. However, when charges are injected into usual organic molecules they become ion radicals or multi ions, which are usually very unstable in arbitrary conditions. However, metal complexes are usually stable even in the charged states, because the metal atom can serve as a good electron pool. Thus, we designed and synthesized ruthenium complexes, as stable and low size distributed nanoparticles. In Fig. 1, the molecular modeling structure of the target molecule and the SEM image of the nanogap electrode were exhibited. Since the size of the molecule was calculated to be ca. 3.6–3.8 nm, the electrode gap will be filled up with about 10–20 molecules. With this number of particles, quantized electronic phenomena could be measurable.

Here we described the synthetic procedure, strucuture identification and the electrochemical behavior of the molecules. Electrochemical reversibility is a good index for the stability of the charged species and the molecules with high electrochemical reversibilities can be free from the instability in the charged states, being adequate as nanosize charge pools.

2. Results and Discussion

2.1. *Synthesis of the ruthenium complexes*

We have synthesized a series of ruthenium complexes surrounded by the first, the second, and the third generation dendrimers as shown in Scheme 1 and Table 1.[3,4]

The ruthenium complex PF_6 salt protected by dendrimers of the first generation (**4a** $(PF_6)_2$) did not dissolved in chloroform indicating the relatively strong ionic character of the complex. The ruthenium complexes protected by dendrimers of the second (**4b** $(PF_6)_2$) or the third generation (**4c** $(PF_6)_2$) were soluble in chloroform, which suggests that the ionic ruthenium atoms were surrounded by the

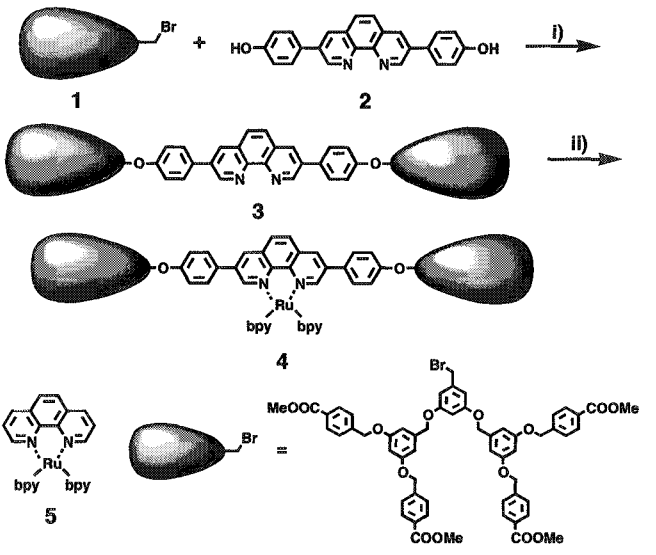

Scheme 1. A typical synthetic scheme of the ruthenium complexes bearing dendrimers. In the scheme, the third generation dendrimer was depicted as an example. *Reagents*: (i) K_2CO_3, 18-Crown-6-ether/dry-DMSO and (ii) $Ru(bpy)_2Cl_2$/dry-DMF.

Table 1. Yields of the compounds **1**, **3** and **4**.

		Yields/%		
	Entry	**1**	**3**	**4**
1st Generation	**a**	not determined	54	76
2nd Generation	**b**	97	46	54
3rd Generation	**c**	quant.	31	44

dendrimers to exhibit hydrophobic nature. The relatively low yield of the third generation ruthenium complex **4c** may be attributed to the steric hindrance between the dendrimer part and the ruthenium bipyridyl moiety.

2.2. *Spectroscopic analyses of the ruthenium complexes*

The newly-prepared ruthenium complexes **4a**, **4b** and **4c** were identified by ^{1}H NMR, MALDI-TOF-MS, and UV-vis absorption spectra. In the ^{1}H NMR, the two major peaks at 8.02 and 7.46 ppm were those of the aryl part of the dendrimers. Phenanthroline protons exhibited at 9.29 ppm (2H, d), 8.19 ppm (2H, d) and 7.69 (2H, s). A singlet peak at 9.29 ppm shown in the starting ligands **3c** and **3b** disappeared in those of the corresponding ruthenium complexes **4c** and **4b**, probably because of the electronic effect of the ruthenium metal. The MALDS TOF-MS data were consistent with the structures **4a**, **4b** and **4c**. As shown in Table 2, in all

Table 2. UV-vis data of the ruthenium complexes.

Compounds	λ_{max}/nm
5	449
4a	452, 364
4b	454, 370
4c	450, 370

the UV-vis absorption of the ruthenium complexes, the MLCT transitions and the $d\pi^*$ transitions were observed at almost identical wavelength, revealing that the electronic states of the molecules were not affected by the surrounding dendrimers.

2.3. *Electrochemical analyses of the ruthenium complexes*

In Fig. 2, the cyclic voltammographs of the ruthenium complexes **4c** and **5** were depicted, and the electrochemical data of **5**, **4a**, **4b** and **4c** were tabulated in Table 3. The first generation dendrimer protected ruthenium complex **4a** showed similar

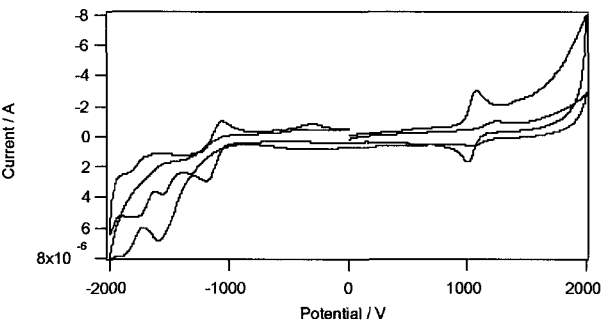

Fig. 2. Cyclic voltammograph of the ruthenium complexes **4c** (—) and **5** (- - -). The solvent for **5** was CH_3CN and for **4c** is CH_2Cl_2. Working electrode, glassy carbon; counter electrode, platinum; supporting electrolyte, tetrabutylammonium perchlorate.

Table 3. Redox potentials determined by cyclic voltammogram.

	Redox potentials/mV[a]		
Ruthenium complex	Anodic peak	Cathodic peak	Difference
5	1068	1008	60
4a	1074	1012	62
4b	1277	1111	166
4c	1240	1038	202

[a]Redox potentials were those of $Ag/AgNO_3$ in CH_3CN.

values with those of **5** that bear no dendrimers. However, the higher generation dendrimer protected ruthenium complexes **4b** and **4c** showed different electrochemical behaviors. The peak around 1000 mV shifted about 200 mV to the positive potential for these compounds when compared with that of **5**, and the differences between anodic and cathodic peaks were enlarged. These behavior could be attributed to the hindrance of the electron transfer from the electrode to the ruthenium complex by the dendrimer protecting groups. In spite of it, the reversible redoxes were retained in these dendrimer protected ruthenium complexes.

3. Conclusion

With the aim to prepare nanoparticles which have clear redox states, a series of ruthenium complexes surrounded by dendrimers have been synthesized, identified, and measured the electrochemical properties in solution. Although the electrochemical behaviors of these ruthenium complexes were affected by the dendrimer, they still exhibited reversible redoxes around 1000 mV versus $Ag/AgNO_3$. These results revealed that the molecules are good candidates for the nanoparticles bearing clear redox states which can be defined by the molecular structure. We are now making the nanodevices with the molecule and studying the solid-state electronic properties of them.

References

1. L. P. Kouwenhoven, N. C. van der Vaart, A. T. Johnson, W. Kool, C. J. P. M. Harmans, J. G. Williamson, A. A. M. Staring, and C. T. Foxon, *Condensed Matter* **85**, 367 (1991); L. P. Kouwenhoven, A. T. Johnson, N. C. van der Vaart, A. van der Enden, C. J. P. M. Harmans, and C. T. Foxon, *Condensed Matter* **85**, 381 (1991).
2. J. Park, A. N. Pasupathy, J. I. Goldsmiths, C. Chang, Y. Yaish, J. R. Petta, M. Rinkoski, J. P. Sethna, H. D. Abrunas, P. L. McEuen, and D. C. Ralph, *Nature* **417**, 722 (2002).
3. T. Yamamoto, T. Maruyama, Z.-H. Zhou, T. Ito, T. Fukuda, Y. Yoneda, F. Begum, T. Ikeda, S. Sasaki, H. Takezoe, A. Fukuda, and K. Kubota, *J. Am. Chem. Soc.* **116**, 4832 (1994).
4. C. J. Hawker and J. M. J. Frechet, *J. Am. Chem. Soc.* **112**, 7638 (1990); G. L'abbe, B. Forier, and W. Dehaen, *Chem. Commun.*, 143 (1996).

This page is intentionally left blank

International Journal of Nanoscience, Vol. 1, Nos. 5 & 6 (2002) 637–640

NANOSURFACE MODIFICATION USING REACTIVE LANGMUIR–BLODGETT FILMS

Y. KADO, A. AOKI, and T. MIYASHITA

Institute of Multidisciplinary Research for Advanced Materials (IMRAM)
Tohoku University, Katahira 2-1-1
Aobaku, Sendai 980-8577, Japan

Received 10 December 2002
Revised 13 December 2002

We describe a simple and effective approach to the introduction of a functional group into polymer nanofilms on the solid surface using reactive Langmuir–Blodgett films. *N*-Dodecylacrylamide copolymers containing a terminal amino group in the side chains as a reactive moiety form a stable monolayer on a water surface, and the monolayer was transferred onto a solid support with a transfer ratio of unity. The LB films were characterized by various spectroscopic methods. The reactivity of the terminal amino group incorporated in the LB films was investigated in detail using fluorescein isothiocyanate (FITC) as a fluorescent probe. The chemical reaction between the amino group in the LB films and FITC in the bulk solution was completed within approximately 30 min and the chemical bond formation was confirmed by FT-IR spectroscopy. Furthermore, the ability as a pH sensor was observed with fluorescent microscopy.

Keywords: Surface modification; reactive LB film; pH sensor.

1. Introduction

Recently, various techniques for the preparation of organic ultrathin films have been studied. Organic thin films are attractive materials for their processability, ease of functionalization, their light weight, flexibility, and so on. Various organic films, for example, a spin-coating film,[1] self-assembled monolayers (SAM),[2] and layer-by-layer,[3] have been investigated. Most applications of these films have been extended to optics, microelectronics devices,[3] sensors,[1] optical memory devices,[4] and so on. The Langmuir–Blodgett (LB) technique is an excellent one providing organized molecular assemblies with controlled molecular orientation and well-defined molecular arrangement.[5] The method can prepare a flat surface in molecular scale and the resulting assemblies are applied for micro- and nanodevices with a bottom–up method. A high performance sensor can be constructed because dense packing of molecules achieves a high intensity of the signal. If a sensor is constructed by LB films and homogeneously introduced various functional groups in a sensor, it is possible to obtain two-dimensional (2D) information and use for 2D mapping.

In this paper, we report a simple and effective approach to introduce a functional group into polymer film on a solid surface using reactive polymer LB films. Furthermore, the ability of the thin film as a pH sensor was observed.

2. Experimental

2, 2′-(Ethylenedioxy)bis(ethylamine) (DADOO) and fluorescein isothiocyanate (FITC) isomer I were purchased from Aldrich. Octadecyltrichlorosilane was purchased from ShinEtsu Chemical Co. Ltd. Na_2CO_3 and $NaHCO_3$ were purchased from Nacalai Tesque. *N*-Dodecylacrylamide (DDA) and the copolymers (pDDA-DADOO; Fig. 1) were prepared as described in previous papers.[6,7] FITC solution was dissolved in an aqueous buffer solution of 0.1 M Na_2CO_3–$NaHCO_3$ (pH 9.6).

Measurement of surface pressure (π)–area (A) isotherms and the deposition of monolayers was carried out with a computer-controlled Langmuir trough system (FSD-50, 51 USI). The copolymers were dissolved in chloroform at a concentration of about 1 mM (monomer unit) and spread onto a pure water (Milli-Q grade water; resistivity >17 M$\Omega \cdot$cm). The compression speed was 1400 mm^2/min. The polymer monolayers were transferred onto solid substrates by the vertical dipping method at a dipping speed of 10 mm/min under surface pressure of 35 mN/m at 20°C. Glass substrates were cleaned using an O_3 cleaner, and were treated with octadecyltrichlorosilane to make the surface hydrophobic. PDDA LB films with 10 layers were precoated on substrates and then pDDA-DADOO LB films were deposited on them.

Fluorescence spectra were measured with Hitachi U-4000 spectrometer. The reactive LB films on the substrates were immersed in an FITC solution, and rinsed with the buffer and water to remove unreacted species from the LB film surface. Finally, they were dried with pure N_2 gas. The fluorescent images of the LB films reacted with FITC were observed with a fluorescence microscope (Olympus Vanox). Fluorescence images were taken through a 380–490 nm excitation filter with a 200 W high pressure mercury lamp.

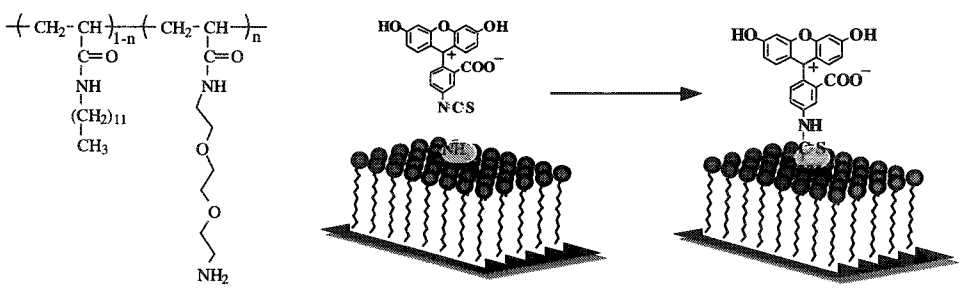

Fig. 1. (a) The chemical structure of pDDA-DADOO copolymer and (b) the scheme of the reaction between the amino group in the pDDA-DADOO and FITC.

3. Results and Discussion

pDDA-DADOO LB films containing terminal amino group in the side chains as a reactive moiety (Fig. 1(a)) were prepared and characterized with some spectroscopies.[6] The reactivity of the LB films was investigated in detail using FITC as a fluorescent probe. The amino group of the LB film is allowed to react with FITC as shown in Fig. 1(b). The time profile of the reaction in the LB films was measured by monitoring the fluorescent intensity as a function of immersing time. The intensity increased rapidly in the initial 10 min, and became saturated after 30 min, indicating the completion of the reaction of amino groups with FITC. In addition, the chemical attachment of amino groups with FITC was confirmed with FT-IR spectra. Furthermore, we tried to introduce FITC into the LB films with more than two layers. A two-layer LB film was deposited onto a glass surface and then contacted with FITC solution. The fluorescence spectra were measured and the intensities at 530 nm were plotted as a function of the number of depositions of the two layers. As the result, the fluorescent intensity increased with the number of layers and FITC was homogeneously introduced into the LB film. Therefore, this coating method is effective for tailoring functional organic ultrathin films on solid substrates.

It is known that FITC changes its chemical structure, solubility and optical properties with pH.[8] We tried to investigate the ability of pH sensor using the pDDA-DADOO LB film treated with FITC. The pDDA-DADOO (12%) LB films with two layers were deposited on the substrate (precoated with pDDA LB film) and FITC was introduced into the LB film. Then the resulting substrates were immersed in pure water within 10 min and their fluorescent spectra were measured. These fluorescent intensities at 530 nm were defined as I_0. Next, the samples were

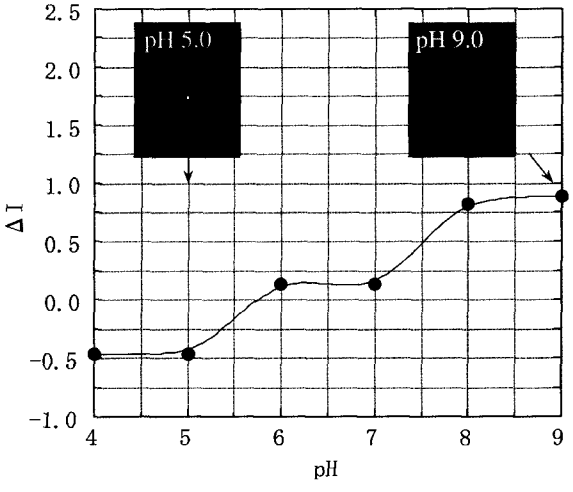

Fig. 2. Fluorescent microscopic images at pH 5 and 9, and the change of ΔI as a function of pH.

immersed in buffer solutions at pH 4–9 and their fluorescent spectra were measured. These fluorescent intensities at 530 nm were defined as I. Therefore, the change of fluorescent intensity, ΔI, was defined as following:

$$\Delta I = \frac{I - I_0}{I_0} . \tag{1}$$

The ΔIs were plotted as a function of pH (Fig. 2). Between pH 5 and 9, they changed drastically. This performance agrees with the literature.[8] The value of pKa of free fluorescein has also been reported around 6.8. Furthermore, it was observed that the fluorescent images of the film at pH 5 and 9 had a fine contrast (inset in Fig. 2). Conclusively, the pDDA-DADOO LB film treated with FITC has an excellent ability as a pH sensor between pH 5 and 9, and it is useful for 2D sensors.

References

1. S.-H. Lee, J. Kumar, and S. K. Tripathy, *Langmuir* **16**, 10482 (2000).
2. Y. Xia and G. M. Whitesides, *Angew. Chem. Int. Ed.* **37**, 550 (1998).
3. E. J. Calvo and A. Wolosiuk, *J. Am. Chem. Soc.* **37**, 550 (1998).
4. R. K. Lammi, R. W. Wagner, A. Ambroise, J. R. Diers, D. F. Bocian, D. Holten, and J. S. Lindsey, *J. Phys. Chem. B* **150**, 5341 (2001).
5. T. Miyashita, Y. Mizuta, and M. Matsuda, *Langmuir* **37**, 4839 (2002).
6. Y. Kado, A. Aoki, and T. Miyashita, *J. Mater. Sci.* **37**, 4839 (2002).
7. K. Arisumi, F. Feng, T. Miyashita, and H. Ninomiya, *Langmuir* **14**, 5555 (1998).
8. M. Carvell, I. D. Robb, and P. W. Small, *Polymer* **39**, 393 (1998).

International Journal of Nanoscience, Vol. 1, Nos. 5 & 6 (2002) 641–644

PHOTOBRIGHTENING AND PHOTODARKENING IN CdSe NANOCRYSTAL/POLYMER THIN FILMS

HARUMI ASAMI*,†,‡,§, ITARU KAMIYA†,‡, and MASAHIKO HARA*,‡

*Tokyo Institute of Technology, 4259 Nagatsuta, Midori-ku, Yokohama 226-8503, Japan
†Mitsubishi Chemical Corporation, 1000 Kamoshida-cho, Aoba-ku, Yokohama, 227-8502, Japan
‡The Institute of Physical and Chemical Research (RIKEN)
2-1 Hirosawa, Wako, Saitama 351-0198, Japan
§1104329@cc.m-kagaku.co.jp

Received 28 November 2002
Revised 24 December 2002

The change in the photoluminescence intensity of CdSe nanocrystal/polymer thin films with duration of illumination is investigated. The choice of polymer has an influence on photobrightening and photodarkening. In particular, photodarkening in CdSe nanocrystal/poly(vinyl carbazole) thin film occurs immediately upon illumination, in contrast to the slow changes observed with polystyrene and poly(2-vinylpridine). We discuss the mechanisms of this phenomenon in comparison with interaction between surface of CdSe nanocrystals and polymer side chain.

Keywords: CdSe nanocrystals; nanocrystal/polymer thin film; photobrightening; photodarkening.

1. Introduction

Chemically synthesized semiconductor nanocrystals (NCs) are small molecular clusters whose size is ca. 1 to 10 nm in diameter and exhibit unique optical properties arising from three-dimensional quantum confinement of carriers, which are different from the bulk crystals.[1] Quantum confinement leads to formation of discrete and blue-shifted absorption emission bands, whose wavelengths can be changed by simply controlling the nanocrystal size. The optical properties of CdSe NCs are being extensively investigated.[2,3] It has been reported that a single CdSe NC shows intermittent emission or blinking, which is not observed in ensembles of CdSe NCs.[4] In the ensembles of CdSe NCs, several groups recently reported that CdSe NC thin films show photobrightening,[5–7] where photoluminescence (PL) intensity of CdSe thin films increases with duration of illumination with UV excitation light, followed by photodarkening, where PL intensity gradually decreases. It is considered that photobrightening and photodarkening observed in the ensemble of CdSe NCs depend on the structure of the ensembles and the interaction between the surface of NCs and local environment. In this report, we investigate the PL intensity change in CdSe NC/polymer thin films as a function of duration of excitation with blue

light. To clarify the influence of the local environment in which the CdSe NCs is embedded on the PL intensity change, we varied the choice of the polymer matrix.

2. Experimental Procedures

Tri-*n*-octylphosphine oxide (TOPO) capped CdSe nanocrystals used in the present study were prepared by injecting organometallic precursors that nucleated and grew in TOPO, which was heated up to 300–350°C.[8] Absorption and PL peaks are observed at 535 nm and 555 nm, respectively. The diameter of CdSe NCs used in this study is about 3.5 nm. As polymer matrices, polystyrene (PS), poly(vinyl carbazole) (PVK) and poly(2-vinylpyridine) (P2VP) were used. The CdSe nanocrystals were dispersed in $CHCl_3$ along with either PS, PVK or P2VP, with a NC to polymer ratio of 0.02:1 in weight. The NC and NC/polymer solutions were cast onto a glass substrate. A fluorescence microscope equipped with an optical multichannel analyzer was used to measure the PL intensity change of CdSe NC/polymer thin films with 470–490 nm continuous-waves excitation, whose power density was about 4 W/cm^2. All measurements were perfomed at room temperature in air.

3. Results

Figures 1(a) and 1(b) show PL spectra and their transients of CdSe NC thin film without a polymer matrix as a function of duration of illumination in air, respectively. Figure 1(a) shows the PL spectra after various illumination time: (1) 0 s, (2) 360 s and (3) 1785 s. In Fig. 1(b), squares show the PL intensity change and triangles show the peak wavelength change. The PL intensity increased during the first 360 s and then gradually decreased, which indicates that photobrightening and photodarkening occurred with this excitation intensity. The peak position shifted to shorter wavelength by 9 nm during the illumination. A gradual blue shift of CdSe

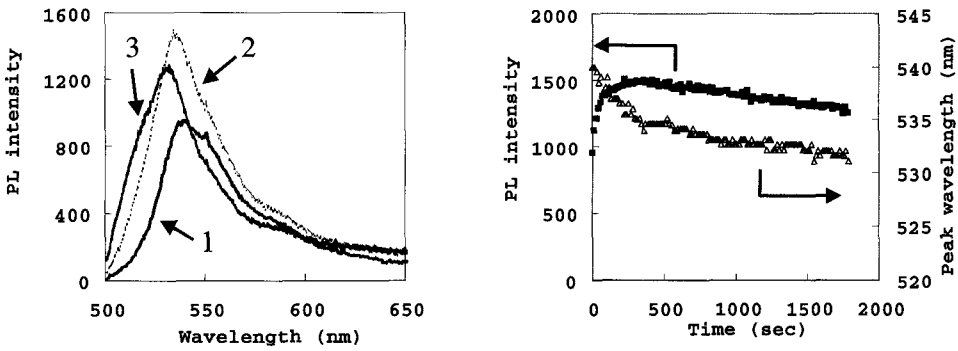

Fig. 1. (a) PL spectra of CdSe NC thin film after different illumination time: (1) 0 s, (2) 360 s, and (3) 1785 s. The sample was excited at 470–490 nm at an intensity of about 4 W/cm^2. (b) PL intensity (■) and peak wavelength change (△) plotted as a function of illumination time.

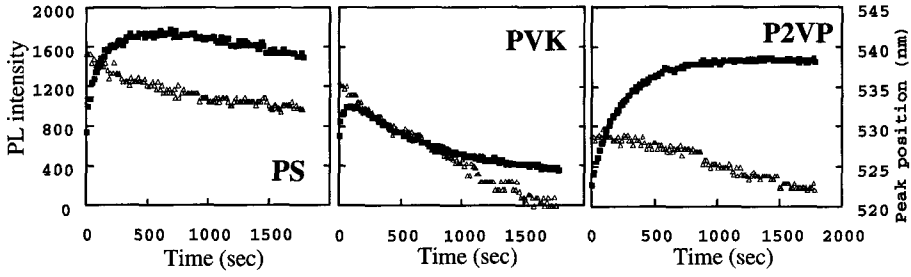

Fig. 2. PL intensity change (■) and peak position shift (△) in CdSe NC/polymer thin films as a function of illumination time. As a polymer matrix, PS, PVK and P2VP were used.

NCs illuminated in air has been previously observed at room temperature luminescence from ensemble of NCs and single NCs, which no blue shift was observed in a nitrogen atmosphere, which is attributed to a shrinkage of the CdSe core by photo-oxidation.[4,6]

The three panels in Fig. 2 show PL intensity change and peak position shift in CdSe NC/polymer thin films when the polymer matrix was varied between PS, PVK and P2VP, respectively. The PL intensity in CdSe/PS thin film increased during the first 600 s and then gradually decreased, whose behavior is almost identical to the CdSe NC thin film. PL intensity in CdSe NC/PVK thin film increased during the first 130 s and then decreased at a decay constant of about −1000 s, while that in CdSe NC/P2VP thin film increased monotonically and with no photodarkening observed up to 2000 s although further illumination of more than 3600 s did induce photodarkening. Peak positions in all cases shifted to blue during the illumination, which again is attributed to photo-oxidation. However, we observed that the peak position before illumination depends strongly on the choice of polymer matrix, even when the same lot of NCs was used. The initial peak positions of the NC thin film and the NC/PS thin film were almost the same. For PVK and P2VP, the peak positions are shorter than for NC and NC/PS thin films. These results indicate that dispersity in polymers or local surrounding environment may has an influence on photophysical properties of the NCs.

4. Discussions

We have shown that the choice of polymer has a strong influence on photobrightening and photodarkening in CdSe NC/polymer thin films during illumination. Although the mechanisms of photobrightening observed in CdSe NCs are not yet clear, Cordero *et al.* suggested that light-induced passivation of the surface trap states following adsorption of water resulted in increased luminescence.[6] Light-induced surface state modification such as photo-oxidation, surface passivation by water molecule, and/or adsorption states of ligands might be deeply correlated with photobrightening and photodarkening. From the results obtained, the behavior of photobrightening and photodarkening observed in NC/polymer thin films can be

classified into two types: the first is represented by the case of NC, NC/PS and NC/P2VP and the second NC/PVK depending on the degree of photodarkening. For photodarkening, the following two factors should be considered. One is dispersity of NCs in polymer and the other is interaction between surface of NCs and polymer side chain.

To eliminate the effect of the dispersity of NCs in polymer, thin films where individual NCs are sufficiently separated from each other in the polymer matrix (PS, PVK or P2VP) were fabricated. Intermittent emission or blinking of luminescence of NCs upon Ar laser excitation (continuous wave) was observed, which indicates that each NCs are sufficiently separated. Photodarkening of NCs in PVK also occurred more significantly compared to PS and P2VP, which means that the dispersity of NCs in polymer has little influence on luminescence transient as mentioned above. Another explanation for the difference in luminescence change is the interaction between surface of NCs and polymer side chain. It is reported that there is an interaction between the pyridine group of polymer and surface Cd atoms of NCs.[9,10] One possible explanation is that charge transfer between PVK and NC occurs when NC is excited by light. Ionization potential (IP) and electron affinity (EA) of PVK are about 5.3 eV and 2.2 eV, respectively. IP and EA of CdSe NC are 6.5 eV and 4.4 eV, respectively. One possibility for photodarkening is that exciton is formed upon excitation by light, which is followed by hole transfer from NC to PVK. For the benzene and pyridine group of large IP, no hole transfer occurs. This subject is currently under investigation.

References

1. S. V. Gaponenko, *Optical Properties of Semiconductor Nanocrystals* (Cambridge University Press, Cambride, 1998).
2. B. O. Dabbousi, J. Rodriguez-Viejo, F. V. Mikulec, J. R. Heine, H. Mattoussi, R. Ober, K. F. Jensen, and M. G. Bawendi, *J. Phys. Chem. B* **101**, 9463 (1997).
3. S. Empedocles and M. G. Bawendi, *Acc. Chem. Res.* **32**, 389 (1999).
4. M. Nirmal, B. O. Dabbousi, M. G. Bawendi, J. J. Macklin, J. K. Trautmann, T. D. Harris, and L. E. Brus, *Nature* **383**, 802 (1996).
5. S. Maenosono, E. Ozaki, and Y. Yamaguchi, *Jpn. J. Appl. Phys.* **40**, L638 (2001).
6. S. R. Cordero, P. J. Carlson, R. A. Estabrook, G. F. Strouse, and S. K. Buratto, *J. Phys. Chem. B* **104**, 12137 (2000).
7. B. C. Hess, I. G. Okhrimenko, R. C. Davis, B. C. Stevens, Q. A. Schulzke, K. C. Wright, C. D. Bass, C. D. Evans, and S. L. Summers, *Phys. Rev. Lett.* **86**, 3132 (2001).
8. C. B. Murray, D. J. Norris, and M. G. Bawendi, *J. Am. Chem. Soc.* **115**, 8706 (1993).
9. H. Asami, S. Saita, I. Kamiya, and K. Yoshie, *Mater. Res. Soc. Symp. Proc.* **636**, D9.52/1 (2001).
10. E. Hao, L. Wang, J. Zhang, B. Yang, X. Zhang, and J. Shen, *Chem. Lett.*, 5 (1999).

International Journal of Nanoscience, Vol. 1, Nos. 5 & 6 (2002) 645–649

PRECISE ANALYSIS OF OPTICALLY TRAPPED PARTICLE POSITION AND INTERACTION FORCES IN THE VICINITY OF AN INTERFACE

JUN-ICHI HOTTA, HIDEHISA TAKASAKI, HIDEKI FUJIWARA, and KEIJI SASAKI

Research Institute for Electronic Science, Hokkaido University
Kita 12 Nishi 6, Kita-ku, Sapporo 060-0812, Japan

Received 27 November 2002
Revised 24 December 2002

We report precise analysis of particle position while optically manipulating a particle in solution. Three-dimensional position sensing system, which we developed for measuring femto-Newton force upon a single particle, was used to detect particle position in nanometer resolution. A laser trapping system and a total internal reflection microscope are combined. During manipulation of a microparticle in the vicinity of an interface, the position of the particle behaves as stepwise transition. The spacing of the stable position is coincident with the half wavelength of the trapping laser beam, so that we conclude the surface reflection from the interface causes the stepwise transition. The force measurement is based on a thermodynamic analysis of Brownian motion, and this system can be applied to measure the force onto a single nanoparticle.

Keywords: Laser trapping; radiation force; nanometer position sensing.

1. Introduction

Laser trapping technique based on radiation pressure of a single focused laser beam is developed by Ashkin *et al.* in 1986,[1] and applied to laser-manipulation of polymer latex, liquid droplets, and biological cells, and so forth.[2–6] Optical control of molecular associations was also achieved by use of this technique.[7–10] Nanometer-sized repulsive unimolecular micelles in aqueous solution were gathered by radiation pressure, and a single particle was formed.[10] Recently, laser-manipulated particles are used as probes of the surface physical properties.[11] In order to use the trapped particle as a probe, precise analyses of the trapped particle position in nanometer-resolution and forces upon the probe particle in femto-Newton resolution are indispensable. We developed the three-dimensional potential measurement for a trapped particle in the vicinity of an interface, which enables the nanometer-resolution position detection and the femto-Newton-resolution force measurement of a single particle.[12,13] By using this position analysis system, the radiation force acting on a particle and the surface charge density of a single microparticle, were measured.[12–14] Furthermore, Matsuo *et al.* analyzed the absorption of a single

microparticles using this optical force measurement system.[15] In this paper, we report our recent results using this position detection system.

2. Experiment

The schematic diagram of the experimental setup is shown in Fig. 1. The second harmonic pulses of a LD-pumped Q-switched Nd^{3+}: YAG laser ($\lambda = 532$ nm, 300 kHz, 70 ns), which is used as a trapping beam, is focused onto the sample by an objective (×100, NA = 1.35). A power-stabilized He–Ne laser (Neoarc NEO-5MSS, $\lambda = 633$ nm, 3.0 mW) is used as an illumination laser. The He–Ne laser beam is introduced to a prism that is optically coupled to the glass plate, and is incidence to the interface of glass and water under the total-internal-reflection condition (incident angle = 61.8°), and the evanescent field irradiates the particle in solution. A sample particle (poly(metylmetacrylate) (PMMA), diameter = 20 μm), which is trapped by the focused laser beam, is manipulated into the evanescent field. The scattered He–Ne light by the particle is imaged onto a quadrant photodiode or photomultiplier tube. The output signals from the quadrant photodiode are input to differential amplifier and converted to three-dimensional position data. The intensity of the scattered evanescent field is given as an exponential function of the distance r between the surfaces of the particle and the glass plate. The penetration depth of the evanescent field is ~ 700 nm. By use of the thermodynamic analysis of Brownian motion, the position data is converted to the potential curves of the forces. In the vicinity of an interface, the electric field is complicated. The scanning piezo-electric translation stage was scanned at constant velocity (= 20 nm/s). The focal point in sample solution moves at constant velocity, therefore the distance between the particle and surface changes continuously.

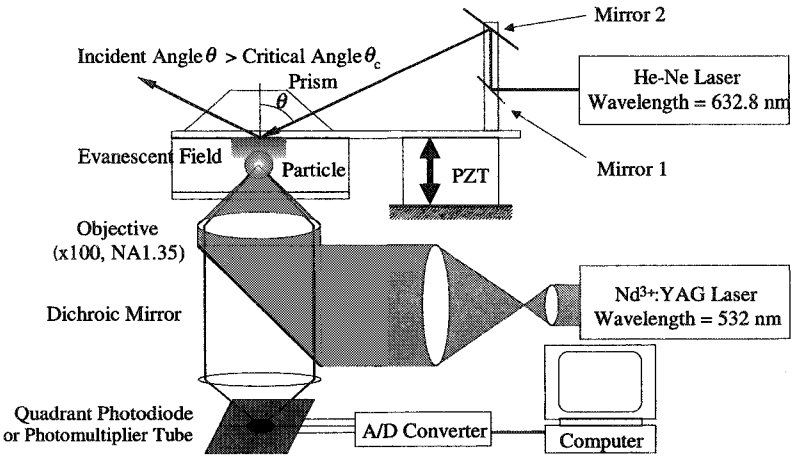

Fig. 1. A schematic diagram of the experimental setup. Mirror 1 is attached to the microscope. Mirror 2 is attached to the piezoelectric translation stage (PZT).

3. Results and Discussions

The distance between the surface of the glass and the focal point of trapping laser is increased continuously. Since the focal point of the trapping laser beam was moved continuously, we expected the position of the particle to change similarly. The distance between the surfaces of the particle and the glass plate is shown in Fig. 2.

It is clear that the particle is not smoothly manipulated. The particle has a tendency to fluctuate around a stable point and jumped to another stable point and fluctuates. The histogram, which was calculated from the time series data of the particle position, is shown in Fig. 3. There are four peaks in the histogram and the peaks are separated ~ 200 nm, which is same as the half wavelength of the trapping laser in water (refractive index = 1.33). It clearly indicates that this phenomenon is caused by interference of the second harmonics of the YAG laser.

An example of the optical force analysis achieved by the same optical set-up of Ref. 14 is shown in Fig. 4. A rhodamine B (RhB)-doped PMMA particle

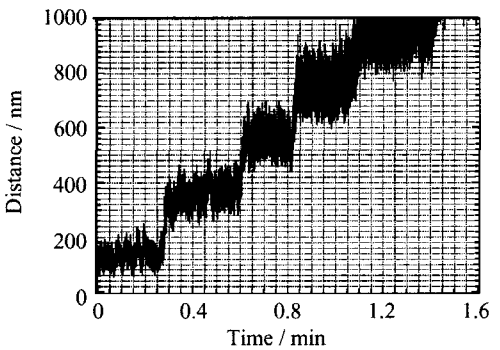

Fig. 2. The distance between the surfaces of the particle and glass plate. The power of the trapping laser beam is 180 mW.

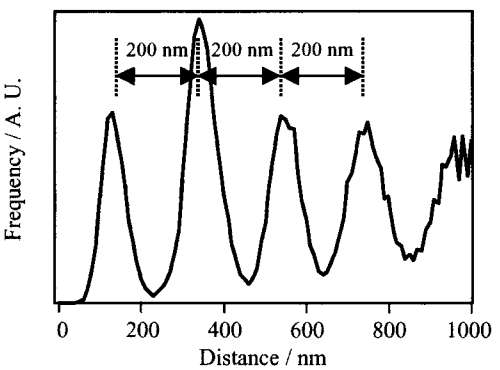

Fig. 3. The histogram of the distance.

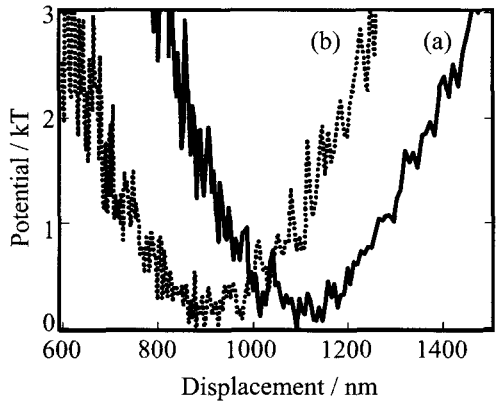

Fig. 4. (a) A potential exerted on a RhB-doped PMMA latex particle as a function of the separation distance. (b) A potential curve for the same particle but under irradiation of 532-nm laser beam.

(diameter = 5.0 μm, 10^{-2}mol/l) was used as a sample. The particle was trapped with 1064-nm laser beam, and (a) with and (b) without irradiation of 532-nm beam with the power of 2.0 MW/m^2. A potential profile of absorption-induced radiation pressure is given by subtracting Fig. 4(a) from Fig. 4(b). The potential profile can be fitted to linear function and gradient (absorption-induced radiation pressure) is 60 fN.

4. Conclusion

Optically trapped particle motion in the vicinity of an interface was precisely analyzed by the nanometer resolution position detection system. The focal point of the trapping laser beam was continuously scanned, and the Brownian motion of the particle was confined by radiation force. However, interference effect of the trapping laser beam was also observed as stepwise motion of the trapped particle. This phenomenon obstructs the smooth manipulation, but it might be good for tracking at a certain distance.

Acknowledgment

The present work was partly supported by a Grant-in-Aid on Scientific Research from the Ministry of Education, Science, Sport, and Culture of Japan (12750032).

References

1. A. Ashkin, J. M. Dziedzic, J. E. Bjorkholm, and S. Chu, *Opt. Lett.* **11**, 288 (1986).
2. K. Sasaki, M. Koshika, H. Misawa, N. Kitamura, and H. Masuhara, *Opt. Lett.* **16**, 1463 (1991).
3. H. Misawa, M. Koshioka, K. Sasaki, N. Kitamura, and H. Masuhara, *J. Appl. Phys.* **70**, 3829 (1991).

4. H. Misawa, K. Sasaki, M. Koshioka, N. Kitamura, and H. Masuhara, *Appl. Phys. Lett.* **60**, 310 (1992).
5. A. Ashkin, J. M. Dziedzic, and T. Yamane, *Nature* **330**, 769 (1987).
6. K. Svobda, C. F. Schmidt, B. J. Schnapp, and S. M. Block, *Nature* **365**, 721 (1993).
7. J. Hofkens, J. Hotta, K. Sasaki, H. Masuhara, H. Faes, and F. De Schryver, *Mol. Cryst. Liq. Cryst.* **283**, 165 (1996).
8. J. Hotta, K. Sasaki, and H. Masuhara, *J. Am. Chem. Soc.* **118**, 11968 (1996).
9. J. Hotta, K. Sasaki, and H. Masuhara, *Appl. Phys. Lett.* **71**, 2085 (1997).
10. J. Hotta, K. Sasaki, H. Masuhara, and Y. Morishima, *J. Phys. Chem. B* **102**, 7687 (1998).
11. T. Sugiura, T. Okada, Y. Inouye, O. Nakamura, and S. Kawata, *Opt. Lett.* **22**, 1663 (1997).
12. K. Sasaki, M. Tsukima, and H. Masuhara, *Appl. Phys. Lett.* **71**, 37 (1997).
13. K. Sasaki, J. Hotta, K. Wada, and H. Masuhara, *Opt. Lett.* **25**, 1385 (2000).
14. Y. Matsuo, H. Takasaki, J. Hotta, and K. Sasaki, *J. Appl. Phys.* **89**, 5438 (2001).
15. K. Wada, K. Sasaki, and H. Masuhara, *Appl. Phys. Lett.* **81**, 1768 (2002).

This page is intentionally left blank

International Journal of Nanoscience, Vol. 1, Nos. 5 & 6 (2002) 651–655

NONLINEAR OPTICAL PROPERTIES OF SEVERAL π-CONJUGATED SYSTEMS INCLUDING NITROGEN ATOMS

SATORU YAMADA*, MASAYOSHI NAKANO,
MASAHIRO TAKAHATA, and KIZASHI YAMAGUCHI

Department of Chemistry, Graduate School of Science, Osaka University
Toyonaka, Osaka 560-0043, Japan
**yamada@chem.sci.osaka-u.ac.jp*

Received 27 November 2002
Revised 24 December 2002

Static second hyperpolarizability (γ) of 1,4-phenylendiamine and 4,4′-diaminodiphenylamine in neutral and dicationic states are investigated as model systems of dendritic structure. Expansion of π-conjugation is found to significantly enhance the γ value of the neutral model system. Charged defect in the present system is found to have a remarkable influence on the magnitude and sign of static γ in the direction of π-conjugation.

Keywords: Nonlinear optical property; dendrimer; charged π conjugated system.

1. Introduction

The nonlinear optical (NLO) properties for organic compounds have been actively studied because of their large nonlinearity and fast responses, which originate in π-electron.[1–3] One of the topics in this field is NLO property of dendrimers. Dendrimer is a new class of polymeric systems having high light-harvesting property.[4,5] Dendrimers are characterized by a large number of terminal groups originating in a focal point with at least one branch at each repeat unit. Such unique features of π-conjugation in fractal structures are also expected to provide a remarkable influence on the NLO properties since the π-conjugation is known to sensitively affect the NLO properties for such systems. Some dendrimer systems have charged defects. We have pointed out that a system having charge defects shows strong structure-correlations on NLO property and importance for electron-correlation effect, based on detailed *ab initio* molecular orbital (MO) calculations for second hyperpolarizability (γ), which is the origin of the macroscopic third-order nonlinear optical response.[6]

In this study, third-order NLO properties and effects of existence of charged defect are investigated for several π-conjugated systems including nitrogen atoms by using *ab initio* MO calculation. Figures 1(a) and 1(b) show the molecules investigated in this study. The model system shown in Fig. 1(b) has a form in which two anilines are connected with a nitrogen atom. Since a fractal structure is constructed

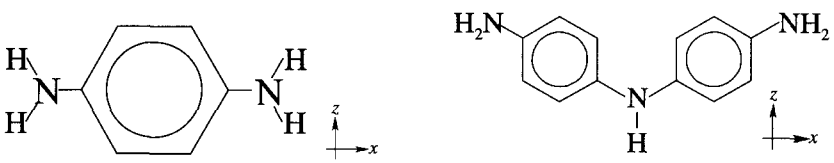

(a) (b)

Fig. 1. Examined π-conjugated systems and coordinate systems: (a) 1,4-phenylendiamine (model-A) and (b) 4,4′-diaminodiphenylamine (model-B). These geometry are optimized using MP2 method with 6-31G** basis set.

by recursive substitution of hydrogen atoms connected with nitrogen in the model system by model-A, the model-B system can be considered as one of the smallest models of a dendrimer.

2. Calculation

The γ value is calculated by the fourth-order numerical differentiation of the total energy $E(\mathbf{F})$ with respect to the applied field $\mathbf{F}$. This numerical differential method is called finite-field method.[7] In order to avoid numerical errors, we try several field strengths from 0.001 to 0.003 a.u. (1 a.u. = 3.50950×10^{10} MW/cm^2) as the minimum finite field and adopt a numerically stable γ.

The effects of electron-correlation on γ values are examined by the second-order Møller–Plesset perturbation (MP2) method. In order to examine the basis set dependence of γ values for the systems, we use 6-31G, 6-31G*, 6-31 + G and 6-31G + d basis sets for the present *ab initio* calculations. The "*" and "+" mean augmentation of polarization and diffuse function, respectively, for C and N atoms.[8] Orbital exponents for d-function in 6-31G + d ($\xi_C = 0.0523$, $\xi_N = 0.0582$) are chosen by the even-temper method. All the *ab initio* MO calculations are performed using *Gaussian 98* program package.[8]

3. Results and Discussion

3.1. γ values of 1,4-phenylendiamine (model-A)

Table 1 shows the calculated values of γ_{xxxx}, γ_{yyyy} and γ_{zzzz} components for model-A. As shown in Table 1, γ_{yyyy} and γ_{zzzz} components calculated with 6-31 + G or 6-31G + d basis set, which includes diffuse function, are much larger than those with 6-31G or 6-31G* basis set in every system. The improvement on γ corrected by using the basis set including diffuse function is not considered to be negligible for the systems studied here. Although electron-correlation effects give positive contribution to γ values, the order of γ values at the MP2 level are the same as those at the HF level. We predict that the electron-correlation effect at the MP2 level on the γ values is sufficient to provide qualitatively reliable γ values of model-A in neutral (model-A) and dicationic (model-A′) states. As shown in Table 1, γ

Table 1. Comparison of calculated γ components of model-A in neutral and dicationic states (unit: a.u.).

Basis set	Method	Neutral			Dication		
		γ_{xxxx}	γ_{yyyy}	γ_{zzzz}	γ_{xxxx}	γ_{yyyy}	γ_{zzzz}
6-31G	HF	2074	10	188	−2981	10	427
	MP2	3129	9	203	−1575	8	579
6-31G*	HF	1994	7	185	−2190	7	395
	MP2	2419	6	210	−1901	7	463
6-31 + G	HF	3251	2227	1662	−2829	754	619
	MP2	4275	2508	2039	−2051	798	750
6-31G + d	HF	4965	1683	1325	−2207	489	621
	MP2	6441	2018	1549	−1440	532	744

1 a.u. = 5.03670×10^{-40} esu.

values of model-A′ are much differ from those of neutral system. The reduction in magnitude γ_{yyyy} and γ_{zzzz} of model-A′ are considered to be reasonable, since reduction in γ values of several positive charged systems are reported.[9,10] Charged defects in molecules are usually known to decrease the positive contribution to γ in the off resonant region. However, the change in sign of γ_{xxxx} component of model-A′ seems to be caused by the increase in negative contribution to γ. In our previous paper, we proposed a structure-property correlation rule based on the time-dependent perturbation theory.[11] In this rule, the symmetric resonance structure with invertible polarization (SRIP) plays an important role on γ. A system whose ground state has a large contribution of SRIP tends to exhibit negative γ. We infer that the ground state of model-A in dicationic state has some SRIP contributions originating in charged defects.

3.2. γ *values of* 4,4′*-diaminodiphenylamine (model-B)*

Table 2 shows calculated γ values for neutral and dicationic states of model-B. The basis set and electron-correlation dependencies on γ values of neutral state is shown to similar to those of model-A. Therefore, the calculated γ values with 6-31 + G or 6-31G + d basis set at the MP2 level is predicted to be qualitatively reliable. The magnitudes of γ_{yyyy} and γ_{zzzz} of model-B are about two to three times as large as those of model-A. The enhancement in γ value is considered to be reasonable since the model-B structure contain two model-A systems (see Fig. 1). On the other hand, the magnitude of γ_{xxxx} for model-B in neutral state is remarkably larger than that of model-A. As shown in Fig. 1, model-B has a structure, in which two π-conjugation system (model-A) is connected with a nitrogen atom in x direction. Therefore, enhancement in γ_{xxxx} value of model-B in neutral state is predicted to be caused by an expansion of π-conjugation.

As shown in Table 2, basis set and electron-correlation dependencies of γ_{yyyy} and γ_{zzzz} values for model-B in dicationic state (model-B′) are similar to the neutral state of model-B and the neutral and dicationic state of model-A. The reduction in

Table 2. Comparison of calculated γ components of model-B in neutral and dicationic states (unit: a.u.).

Basis set	Method	Neutral			Dication		
		γ_{xxxx}	γ_{yyyy}	γ_{zzzz}	γ_{xxxx}	γ_{yyyy}	γ_{zzzz}
6-31G	HF	23096	18	433	−864520	18	1380
	MP2	42402	16	470	1367448	15	1314
6-31G*	HF	23742	12	425	−875290	12	1271
	MP2	44124	10	495	1813105	11	1205
6-31 + G	HF	29483	4057	2845	−956165	1978	2151
	MP2	56911	5127	4172	1511834	2293	2528
6-31G + d	HF	30359	2836	3146	−953611	1389	2250
	MP2	57449	3921	4568	1558819	1721	2645

γ_{yyyy} and γ_{zzzz} values of model-B′ is also similar to model-A. On the other hand, the effect of electron-correlation and charged defect on γ_{xxxx} value of model-B′ is very different from those on γ_{yyyy} and γ_{zzzz}. Although the γ_{xxxx} value of model-B′ at the HF level is negative in sign and its magnitude is more enhanced than those of model-A′, the γ_{xxxx} value at the MP2 level become extremely large positive. The electron-correlation effect at the MP2 level on the γ_{xxxx} value seems to be somewhat overestimated and higher electron-correlation method, e.g., coupled-cluster method, should be necessary to obtain converged γ_{xxxx} value of model-B in dicationic state.

4. Conclusion

It was found that extreme enhancement of γ values caused by the expansion of π-conjugation for the system in which two small π-conjugation systems are connected by nitrogen atom. Since this connected molecule can be considered to be the smallest model system of dendrimer, a large enhancement of NLO property is expected for large dendrimer systems with extended π-conjugation.

Acknowledgments

This work was supported by Grant-in-Aid for Scientific Research (No. 14340184) from Japan Society for the promotion of Science (JSPS) and a Grant from the Ogasawara Foundation for the Promotion of Science and Engineering.

References

1. D. J. Williams (ed.), *Nonlinear Optical Properties of Organic and Polymeric Materials — ACS Symposium Series*, Vol. 233 (American Chemical Society, Washington DC, 1984).
2. P. N. Prasad and D. J. Williams, *Introduction to Nonlinear Optical Effects in Molecules and Polymers* (Wiley, New York, 1991).
3. M. Nakano and K. Yamaguchi, *Trends in Chemical Physics*, Vol. 5 (Research Trends, Trivandrum, India, 1997), p. 87.
4. J. M. J. Fréchet, *Science* **263**, 1710 (1994).

5. S. K. Grayson and J. M. J. Fréchet, *Chem. Rev.* **101**, 3819 (2001).
6. M. Nakano, I. Shigemoto, S. Yamada, and K. Yamaguchi, *J. Chem. Phys.* **103**, 4175 (1995).
7. H. D. Cohen and C. C. J. Roothaan, *J. Chem. Phys.* **S34**, 43 (1965).
8. M. J. Frisch *et al.*, *Gaussian 98*, Revision A.6 (Gaussian, Inc., Pittsburgh PA, 1998).
9. S. Yamada, M. Nakano, and K. Yamaguchi, *J. Phys. Chem. A* **103**, 7105 (1999).
10. S. Yamada, K. Yamaguchi, and K. Ohta, *Mol. Phys.* **100**, 1839 (2002).
11. M. Nakano, S. Yamada, I. Shigemoto, and K. Yamaguchi, *Chem. Phys. Lett.* **251**, 381 (1996).

This page is intentionally left blank

International Journal of Nanoscience, Vol. 1, Nos. 5 & 6 (2002) 657–661

RESONANT LIGHT TRANSMISSION IN METALLIC PHOTONIC CRYSTAL SLABS

XIANGANG LUO and TERUYA ISHIHARA*
Frontier Research System, RIKEN, Wako 351-0198, Japan
**terish@postman.riken.go.jp*

Received 27 November 2002
Revised 6 January 2003

Light transmission through an opaque nanoscale metallic photonic crystal slabs (MPCS) are investigated. The experimental results show that it is possible to get the extraordinary transmission in visible region even without the presence of holes, which is different from the perforated nanoholes or nanoslits in metallic system. The observed phenomenon can be understood in terms of surface plasmon-enhanced resonant emission of light through a metal structure with a nanoscale corrugation rather than light penetration through tiny holes. It is the periodicity of the interface corrugation that is important for the plasmon as a radiative channel rather than loss. The study suggests that a wide range of photonic applications is possible for such system.

Keywords: Nanometal structure; transmission; plasmon.

1. Introduction

By virtue of recent development of nanofabrication and nanocharacterization techniques, we are now able to produce nanoholes or nanoslits. Generally speaking, the transmission efficiency of light through subwavelength holes or slits is exceedingly low.[1] So the application of nanoscale holes or slits was limited in the past years. However, extraordinary optical transmissions through subwavelength hole or slits arrays have been reported in recent experimental and theoretical reports, which have re-promoted discussions on the properties of metal fine structure.[2] It has been proposed that the effect is due to the resonant excitation of surface plasmon (SP) modes or guided modes in the channels (holes or slits) engraved through the metal.[3]

Here we explore the experimental study of resonant transmission of light through a periodically corrugated nanometal structure on a glass substrate. There is a major difference between a nanostructure with unperforated periodic modulation in our study and a structure with an array of subwavelength size holes or subwavelength width slits of others: propagating channel modes or evanescent waves along the

*Corresponding author.

direction perpendicular to the structure plane cannot exist in the opaque unperforated metallic structure while they survive in a nanostructure with subwavelength width slits or holes.[4] Absorption in the metal indicates that energy coupled to SP is usually lost in the form of heat, thus quenching optical emission, so SP are often regarded as a problem owing to their nonradiative nature. Here we ascribe the enhanced light in the transmission direction to plasmon resonance between the opposite surfaces. There are three parts in the following of this paper. In the second part, we describe our experimental study. In the third part, we discuss the physical process of optical response in unperforated metallic MPCS. Finally, we give out some conclusion.

2. Experimental Study

The MPCS are prepared by evaporating a layer of Ag on glass grating substrates patterned by e-beam lithography. Then a layer of polystyrene is spincoated on the metal surface in order to protect Ag from oxygenized. Thus the metal structure is unperforated, which differentiate our system from others (with holes or slits).

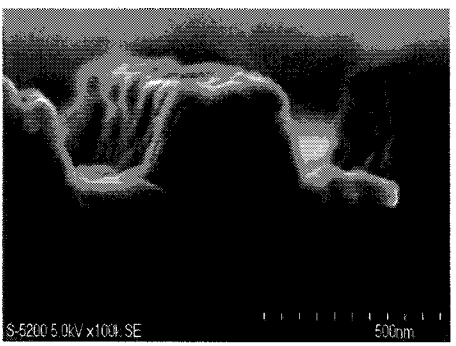

Fig. 1. SEM image of the MPCS.

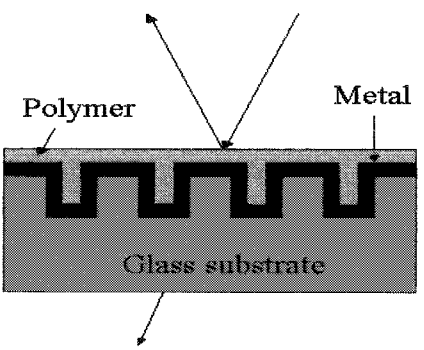

Fig. 2. Experimental scheme.

Figure 1 shows our sample structure. The periodicity of the 1D structure are 700 nm. The thickness of the Ag structure on the glass substrate is 40 nm.

In our experiments the coupling of light with SP is observed both in transmission and reflection (Fig. 2), in contrast with previous work on SP in reflection[5] or transmission[2–4] only. The control variables of the SP resonance are the period and thickness of Ag structure. With TM-polarized incident light, transmission spectra are shown in Fig. 3(a). Surprisingly, resonance transmission enhancement was observed just as that in perforated holes or slits metallic system.[2] A flat 40-nm-thick Ag film has a small transmission around 0.001 in visible range. However, with the corrugation, prominent transmission enhancement is seen at particular wavelength (in Fig. 3(a)). Figures 3(a) and 3(b) show the measured transmission and reflection

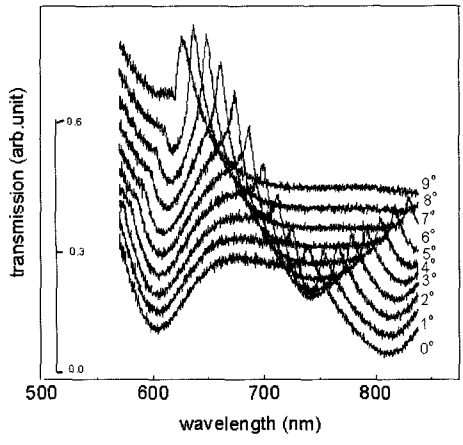

(a)

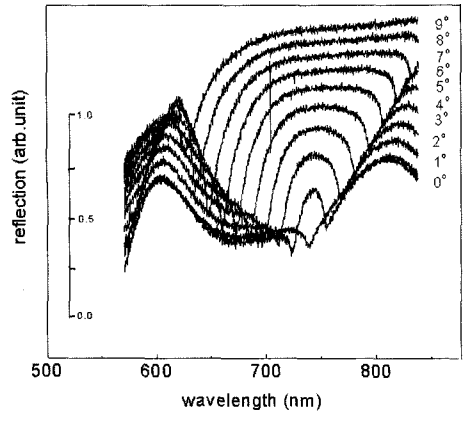

(b)

Fig. 3. (a) Transmission spectra and (b) reflection spectra for different angles.

spectra with different angles for incident p-polarized radiation (H field parallel to the grooves) on the top side of the metallic photonic crystals slabs. The absolute value is shown only for $\theta = 0°$. Other curves are shifted for clarity. As expected Fig. 3 shows that a peak in transmission curve always corresponds to a minimum in the reflection curve at the same frequency. The dispersion curves of resonant transmission are shown in Fig. 4.

Figure 5 shows the p-polarized reflectivity and transmission spectra for a fixed azimuthal angle $\Phi = 0°$ at $\theta \sim 7°$. The reflectivity drops to a minimum at 650 nm, where the in-plane wave vector of the incident beam and the SP mode are equal, which enables the incident beam to excite the SP mode. The peak of the transmission spectra at 650 nm is due to the radiation from SP mode via G_x scattering. The intensity coupled out in this way is negligible unless the incident beam is at an

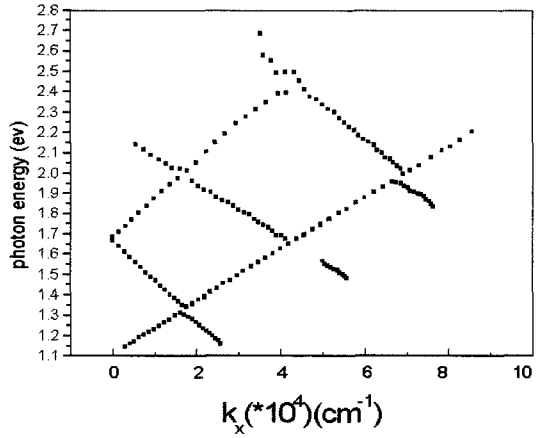

Fig. 4. The dispersion of transmission light.

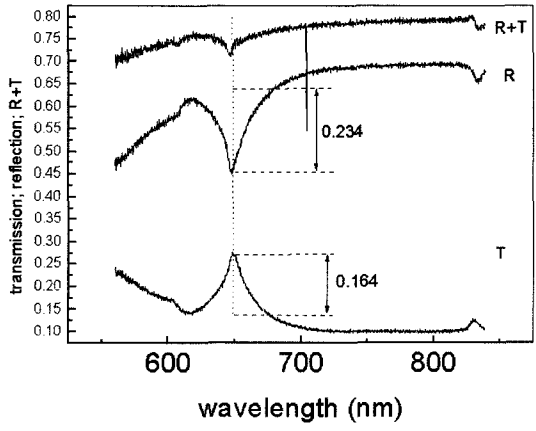

Fig. 5. Reflection and transmission spectra for $\theta = 7°$.

angle appropriate for SP mode excitation. The intensity coupled from the incident beam to the SP mode was evaluated from reflection data shown in Fig. 5. The coupling efficiency 70% is estimated as the ratio of the height of the transmission to the depth of the reflection at 650 nm, for this azimuthal angle. We anticipate this may be improved by optimizing the surface profile of the metallic MPCS. We have thus demonstrated that SP mode can be considered as a radiative channel rather than a loss. This opens up many interesting possibilities, notably the extraction of light from structured optical sources containing corrugated metallic layers.

3. Discussion

The penetration depth of light into silver in visible range is approximately 10 nm, that means only a fraction of the structure with a thickness below 10 nm can be considered as a transparent region or holes. The separation between the grooves on the opposite surfaces in our case is much larger than this value. Therefore there should be no propagating electromagnetic modes between the top and the bottom surfaces, that is a situation much different from the previous experiment by Ebbesen *et al.* In our case, there are SP modes strongly localized in the grooves on both sides of the unperforated nanostructure, which contribute to the enhancement of transmission. The channel mode in the holes or slits cannot be supported in the structure of this work, but SP resonant modes in our structure have the similar properties as the channel mode in their structures: both are highly localized in the holes, slits or the grooves and both have broad spectra peaks in the transmission direction.

4. Conclusion

In conclusion, we have demonstrated a different mechanism for strong optical transmission through metallic structures. We have shown an example which can be understood in terms of surface plasmon-enhanced resonant emission of light through a metal structure with a corrugation rather than light penetration through tiny holes. The physical emission process can be used to explain the extraordinary transmission through holes or slits system. Our results not only bring insight on an alternative physical mechanism of the unexpected strong light transmission through metal structures with subwavelength hole arrays or groove arrays, but they may also lead to micro- and nanophotonics applications such as polarizers, filters, plasmon radiative channel devices, etc.

References

1. H. A. Bethe, *Phys. Rev.* **66**, 163 (1944).
2. T. W. Ebbesen *et al.*, *Nature* **391**, 667 (1998).
3. L. Martin-Moreno *et al.*, *Phys. Rev. Lett.* **86**, 1114 (2001).
4. J. A. Porto, F. J. Garcia-Vidal, and J. B. Pendry, *Phys. Rev. Lett.* **83**, 2845 (1999).
5. I. R. Hooper and J. R. Sambles, *Phys. Rev. B* **66**, 205408 (2002).

This page is intentionally left blank

International Journal of Nanoscience, Vol. 1, Nos. 5 & 6 (2002) 663–666

DEVELOPMENT OF AN EVANESCENT FIELD SYSTEM FOR REAL-TIME DETECTION OF DNA HYBRIDIZATION

DO-KYUN KIM* and YOUNG-SOO KWON

Department of Electrical Engineering, Dong-A University
840, Hadan-2dong, Saha-gu, Busan, 604-714, Korea
**kdk-mail@hanmail.net*

EIICHI TAMIYA

School of Materials Science, Japan Advanced Institute of Science & Technology
1-1, Asahidai, Tatsunokuchi, Ishikawa, 923-1292, Japan

Received 27 November 2002
Revised 31 December 2002

In this research, we report the characterization of the probe and target oligonucleotide hybridization reaction using the evanescent field microscopy. For detection of DNA hybridization assay, a high-density array of sensor probes were prepared by randomly distributing a mixture of particles immobilized with oligonucleotides for DNA chip applications. With the evanescent field excitation and real-time detection method, we suggest that a very sharp discrimination of bulk fluorescence against surface excitation in combination with high excitation intensities can be achieved.

Keywords: Evanescent field system; DNA hybridization; DNA chip microarray.

1. Introduction

The purpose of our research is the development of the high function, sensitivity system that can analyze various biomaterials in real-time.[1] In this research, 5′-biotinylated probes oligonucleotides were immobilized on the surface of patterned particles as template for DNA chip microarray via biotin-avidin bridge. Hybridization reactions with fluorescence conjugated target sequences (be involved mismatching sequences) were studied *in vitro* by evanescent field microscopy excited fluorescence generated on the surface of patterned particles. This result can identify a single base mismatch in the hybridized duplex under the experimental conditions. Hybridization of surface immobilized oligonucleotides at various concentrations of target oligonucleotides in solution performance was studied.

*Corresponding author.

2. Experimental

2.1. *Materials*

All oligonucleotide sequences of the verotoxin II subunit A gene in *E.coli* O157:H7 strain used in this study were synthesized and HPLC purified by Nisshinbo Co. in Japan. Biotin phosphoramidite and fluorescent phosphoramidite (Rhodamine) were used in the synthesis of 5′-biotinylated oligonucleotides and 5′fluorescein conjugated oligonucleotides, respectively. The sequences of these oligonucleotides were given in Table 1. The probe and target oligonucleotides were supplied as a dry powder and were reconstituted to 100 μM with TE buffer solution (10 mM Tris, 1 mM EDTA, pH 7.4) and stored at $-20°$C. The concentration of oligonucleotides was adjusted from 1 μM to 1 pM by dilution in the aqueous buffer solution (10 mM Tris-HCl, 0.2 M MaCl, pH 7.9).

2.2. *Hybridization assay measurement*

The DNA chip microarray with immobilized probe oligonucleotides was fixed on a trapezoid glass prism of the evanescent field microscopy after dropping of immersion oil (nd = 1.516, 23°C). For the measurement of hybridization reaction, small volumes (400 μl) of fluorescent conjugated target oligonucleotides were prepared in an aqueous buffer solution at various concentrations and mismatching conditions, they were spread onto the surface of the DNA chip microarray, and signals were recorded in real-time every 1 min for up to 60 min. The hybridization assay temperature was set at room temperature (23°C). For all the hybridization assays, a new DNA chip microarray prepared from the same batch was used for each measurement. It should be noted that the optimal hybridization condition are different for different assay methods.[2]

3. Results and Discussions

Figure 1(a) shows the comparison of hybridization reaction to concentration of complementary oligonucleotides (CR-1). Here, ΔFI indicates the shift of fluorescence intensity. ΔFI was given by subtracting the measured fluorescence intensity after spreading with the measured fluorescence intensity before spreading. The concentration of probe oligonucleotides was 1 μM. As shown in this figure, the fluorescence

Table 1. Sequences of probe and target oligonucleotides.

Oligonucleotide	Base sequence	Description
Probe (PB-1)	5′ Bio-TGCAGAGTGGTATAACTG 3′	5′-biotinylated
Complementary (CR-1)	5′ CAGTTATACCACTCTGCA 3′	5′-Rhodamine conjugated
Mismatching 1 (MR-1)	5′ GGTTTCCATGACAACGGA 3′	5′-Rhodamine conjugated
Mismatching 2 (MR-2)	5′ CAGTTATGCCACTCTGCA 3′	5′-Rhodamine conjugated
Mismatching 2 (MR-3)	5′ CAGTTATACCACTCTGCG 3′	5′-Rhodamine conjugated
Mismatching 2 (MR-22)	5′ CAGTTATAGGACTCTGCA 3′	5′-Rhodamine conjugated
Mismatching 3 (MR-33)	5′ CAGTTATACCACTCTGGG 3′	5′-Rhodamine conjugated

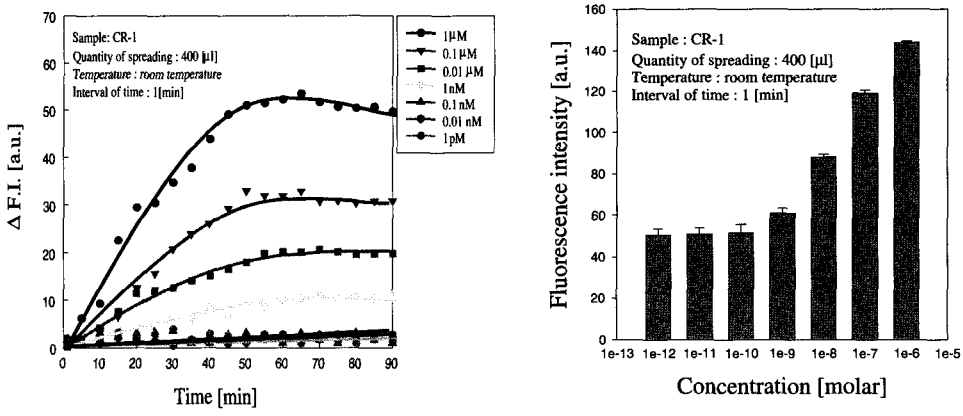

Fig. 1. Comparison of hybridization reaction as to concentration of complementary oligonucleotide (CR-1). (a) ΔFI as a function of time for various concentrations of target oligonucleotides. (b) Fluorescence response versus concentration of target oligonucleotide.

response that was measured by evanescent field microscopy was not detected gradually with decreasing of a concentration. It is considered that when the probe oligonucleotides are hybridized with target oligonucleotides until a concentration of 1 nM, it can detect the fluorescence intensity by evanescent field microscopy. However, the concentration of target oligonucleotides were essentially changed more than 0.1 nM throughout the experiment.

Figure 1(b) shows evolution of the fluorescence intensity as a function of the concentration of target oligonucleotides. The fluorescence response increased with the concentration of oligonucleotides in solution from 1 nM.

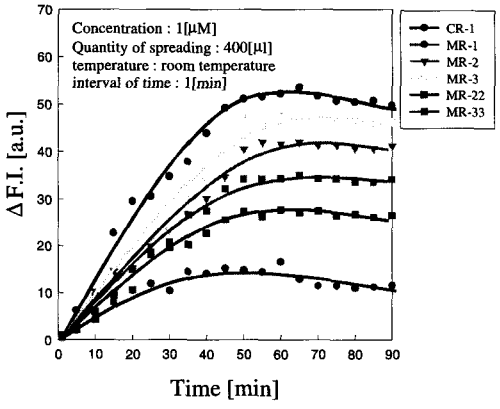

Fig. 2. Comparison of hybridization reaction as to each mismatching condition. ΔFI as a function of time for various mismatching conditions of target oligonucleotides.

The differences in the fluorescence intensity between complementary oligonucleotides and mismatching oligonucleotides as to each mismatching condition are given in Fig. 2. As a result, the complementary oligonucleotides (CR-1) shown most stable state to the fluorescence intensity, which were respectively measured by the DNA sensors by using the evanescent field microscopy showed to be similar to 1-mer terminal mismatching oligonucleotides (MR-3). The MR-2, MR-3, MR-22 and MR-33 have each mismatching sequence on central and terminal. With this set the role of point mutations was investigated. Terminal mismatching oligonucleotides (MR-3, 33) is shown more stable state than central mismatching oligonucleotides (MR-2, 22), and 1-mer mismatching oligonucleotides (MR-2 or 3) is shown more stable state than 2-mer mismatching oligonucleotides (MR-22 or 33).

4. Conclusion

We order to investigate the possible development of a high sensitivity system that can analyze various biomaterials in real-time, we have proceeded as follows: first, DNA chip microarray were fabricated. Then, the particles on which probe oligonucleotides were immobilized were arranged by random fluidic self-assembly on the pattern chips, through hydrophobic interaction. Finally, detection of DNA hybridization was carried out under various conditions using evanescent field microscopy. In the results, the image detection technique of evanescent field microscopy was shown to be able to distinguish between probe and target oligonucleotides regions on the surface at various concentration and mismatching condition.

Acknowledgment

This work was supported by the KOSEF through the CIIPMS at Dong-A University.

References

1. J. A. Steyer and W. Almers, *Nat. Rev. Mol. Cell Biology* **2**, 268 (2001).
2. J. V. Ness and W. E. Hahn, *Nucl. Acids Res.* **10**, 8061 (1982).

International Journal of Nanoscience, Vol. 1, Nos. 5 & 6 (2002) 667–671

MOLECULAR RECOGNITION OF NUCLEOBASES ATTACHED TO SELF-ASSEMBLED MONOLAYERS DETECTED BY CHEMICAL FORCE MICROSCOPY AND QUARTZ CRYSTAL MICROBALANCE

HIROSHI SUNAMI

Graduate School of Science, Hokkaido University
N12 W6, Kita-Ku, Sapporo 060-0812, Japan

KUNIHARU IJIRO

PRESTO, Japan Science and Technology Corporation (JST)
Research Institute for Electronic Science, Hokkaido University
N12 W6, Kita-Ku, Sapporo 060-0812, Japan

MASATSUGU SHIMOMURA

Nanotechnology Research Center, Research Institute for Electronic Science
Hokkaido University, N12 W6, Kita-Ku, Sapporo 060-0812, Japan

Received 27 November 2002
Revised 24 December 2002

In order to develop a new DNA sequencing method by using chemical force microscopy (CFM), we have investigated the interaction of the hydrogen bonding between surfaces of nucleobase self-assembled monolayers (SAMs) and AFM-tips modified with the nucleobases. The two different adhesion forces, the jump-in force and pull-off force, between the AFM-tip modified with cytosine-SAM and the surfaces of four kinds of nucleobase SAMs were measured in water (20°C) by CFM. The adsorption of poly (C) onto a nucleobase-SAM on a gold electrode of quartz crystal microbalance (QCM) was measured as resonance frequency changes. The relative relation among four bases showed similar tendency in the adhesion force measured by the cytosine AFM-tip and in the adsorption amount of poly (C) on the QCM electrode as well as in the theoretically calculated interaction energies between two nucleobases.

Keywords: AFM; CFM; SAM; DNA; adhesion force; hydrogen bonding; molecular recognition.

1. Introduction

Maxam–Gilbert method and Sanger method are mainly used for the DNA sequence determination. However, certain amount of the DNA sample and complicated procedures are required for those methods. If scanning probe microscopy can be used to detect the complimentary base-pairing, the base-sequence of a single DNA molecule can be achieved by scanning the probe tip along the DNA molecule like the recording

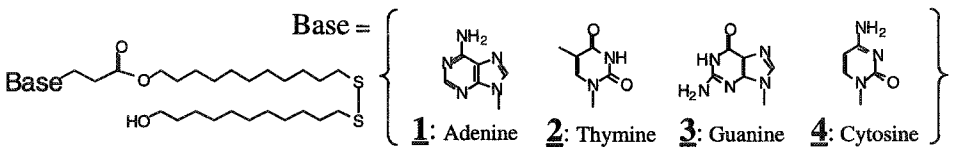

Scheme 1. Chemical formulae of nucleobase disulfide derivatives.

tape. For this purpose, we have developed a chemical force microscope (CFM) which can measure a force mapping with a nucleobase-immobilized AFM-tip. We reported that the disulfide derivatives of nucleobases **1**–**4** (Scheme 1) formed self-assembly monolayers (SAMs) on the gold surface. When the pull-off force mapping of nucleobase SAMs on the gold substrates were measured with an AFM gold-tip covered with thymine disulfide (**2**), the pull-off force on the adenine SAM (**1**) was stronger than that on the thymine SAM. It was expected that nucleobase of the SAMs on the AFM-tip could form a specific base-pair with those on the substrates.[1,2]

In this report, in order to investigate the molecule recognition between nucleobase-SAMs on the AFM-tip and the substrates in detail, the following two approaches were performed. First, the jump-in and pull-off forces mapping on four kinds of SAMs (**1**–**4**) were carried out by AFM-tips modified with cytosine disulfide (**4**) in water (Fig. 1(a)). Second, the adsorption of poly (C) onto four kinds

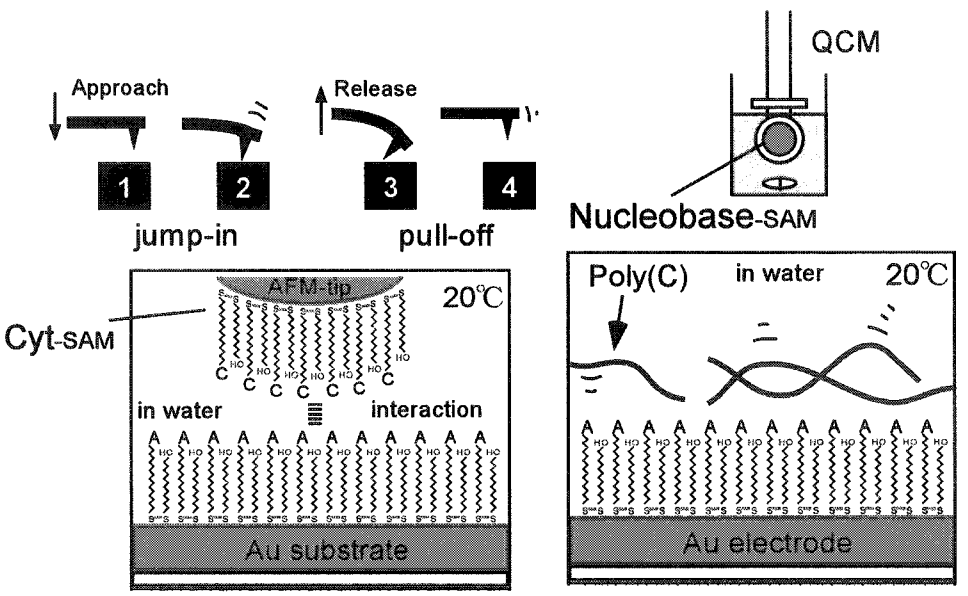

Fig. 1. (a) Schematic illustration of the jump-in and pull-off force measurements between cytosine SAM on the AFM tip and adenine SAM on the Au substrate. (b) Schematic illustration of the measurements of adsorption of poly (C) on the nucleobase SAM on Au electrode of QCM.

of nucleobase SAMs on gold electrodes of the quartz crystal microbalance (QCM) was measured as resonance frequency change (Fig. 1(b)). The results were compared with those obtained by CFM and theoretical values of interaction energy, respectively.

2. Experimental Section

Nucleobase disulfides **1**–**4** were synthesized. The QCM experiments revealed that the nucleobases (**1**–**4**) formed densely-packed monolayers on the gold substrates from those ethanol solutions. Gold-coated AFM tips (spring constant: 0.18 N/m) and Au substrates were modified with cytosine-SAM (**1**). Tips and substrates were soaked in 100 μM ethanol solutions of nucleobase disulfides for 12 h at room temperature, and rinsed with ethanol at 60°C to remove the excess adsorption. Adhesion force curves were measured in pure water at 20°C by using OLYMPUS-NV2500 AFM (Olympus. Co., Tokyo, Japan). The adhesion forces, both in jump-in and pull-off, were mapped as 32 × 32 dots images.

AT-cut quartz crystals (9 MHz, diameter: 4.5 mm, thickness: 300 nm) were purchased from USI systems (Fukuoka, Japan). Gold electrodes of QCM were cleaned with piranha solution (7:3 mixture of conc. H_2SO_4:H_2O_2) for 3 min and soaked in 100 μM ethanol solutions for 12 h at room temperature. The adsorption processes of poly (C) on the nucleobase SAMs were traced in stirred 0.16 mg/L Milli-Q water at 20°C as frequency changes of the QCM (Q-200, USI systems, Japan).

3. Results and Discussion

The average jump-in and pull-off forces at 256 points on nucleobase SAMs were shown in Fig. 2. Optimized interaction energies between two nucleobases calculated with an atomic dipole approximation using CNDO-Cl by Kudritskaya and Danilov[3] were shown in Fig. 2(c). Although the interaction energy and adhesion force cannot be directly compared, the interaction energies can be used as references for the discussion about the molecular recognition of the CFM. The jump-in forces varied depending on the nucleobase (guanine-SAM > cytosine-SAM > adenine-SAM > thymine-SAM) (Fig. 2(a)). The pull-off force measurements showed the similar pattern (guanine-SAM > cytosine-SAM > adenine-SAM > thymine-SAM) (Fig. 2(b)). There is no difference between jump-in and pull-off forces. It was suggested that the molecular recognition of the tip was identified for jump-in and pull-off motions by using cytosine modified AFM-tip. These adhesion forces (Figs. 2(a) and 2(b)) were compared with the theoretically calculated interaction energies contributed by hydrogen bonding (Fig. 2(c)). The relative relations among four bases in adhesion force histograms (Figs. 2(a) and 2(b)) were similar to that of the theoretically calculated interaction energies (Fig. 2(c)).

Adsorption amounts of poly (C) on nucleobase SAM prepared on Au-coated quartz tips were calculated from the frequency changes of QCM by Sauerbrey's

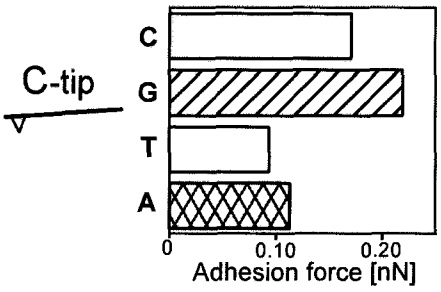

(a) jump-in force

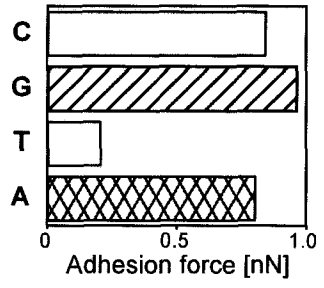

(b) pull-off force

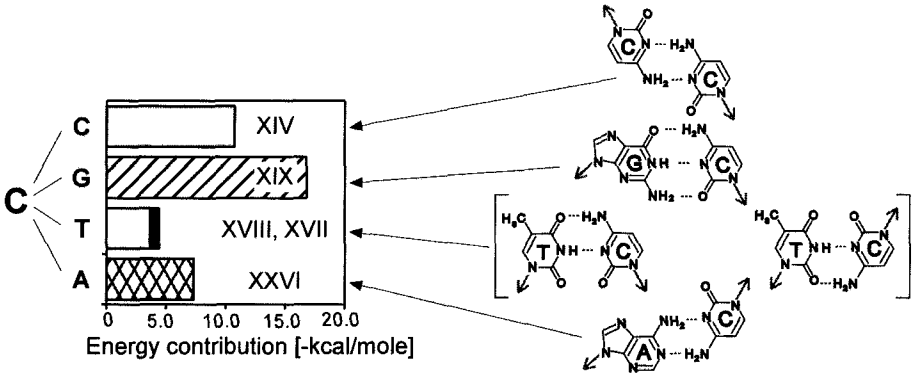

(c) interaction energy

Fig. 2. (a) and (b) Adhesion forces between the cytosine-modified AFM-tip and four nucleobase SAMs on Gold substrates in pure water. These forces were measured at load = 0.1 nN, release-rate = adhesion-rate = 200 nm/s. (c) Optimized interaction energies of some selected base-pairs calculated by quantum chemical methods.[3]

equation.[4] The adsorption amount (unit nmol) of poly (C) decreases as follows: on guanine-SAM > cytosine-SAM > adenine-SAM > thymine-SAM (Fig. 3). Adhesion forces (jump-in) between nucleobase-SAMs and cytosine-modified AFM-tip (Figs. 2(a) and 2(b)), and the interaction energies contributed by hydrogen bonding (Fig. 2(c)) and adsorption amounts of poly (C) on the nucleobase-SAMs (Fig. 3) show a similar tendency.

Since the tendency of adhesion forces (jump-in) and adsorption amounts are similar to the interaction energies, it is considered that the specific hydrogen bonding is dominant in the adhesion force between the nucleobase-SAMs in water. The adhesion forces (pull-off) were not only attributed to hydrogen bonding, because many interactions should exist between the nucleobase-SAMs of the AFM-tips and the substrates in water. The molecular numbers of nucleobases, which form hydrogen bonds between the AFM tip and the sample, cannot be estimated accurately,

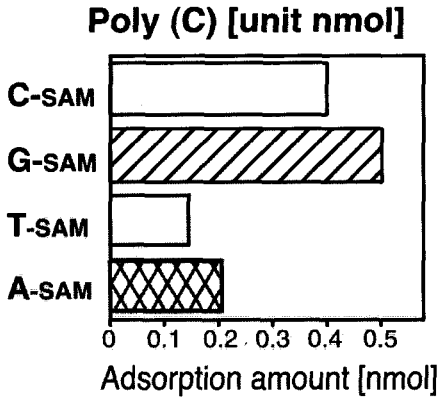

Fig. 3. Adsorption amounts of poly (C) on the nucleobase-SAM in water.

because the contact area between the SAMs is unknown. It is important that strong adhesion force was detected for the complementary combination, although the densities of the nucleobase on SAM are almost identical.

4. Summary

These results lead us to the conclusion that the mapping of base pair formation between nucleobases is possible by using CFM, even if the oligo- and polynucleic acid are not used. It was elucidated that nucleobase-SAMs can recognize not only nucleobase-SAM, but also polynucleic acid in water.

References

1. H. Sunami, K. Ijiro, O. Karthaus, S. Kraemer, S. Mittler, W. Knoll, and M. Shimomura, *Molecular Crystals & Liquid Crystals* **371**, 151 (2001).
2. K. Ijiro, H. Sunami, K. Arai, J. Matsumoto, O. Karthaus, S. Kraemer, S. Mittler, N. Nishi, B. Juskowiak, S. Takenaka, W. Knoll, and M. Shimomura, *Colloids and Surfaces A* **198–200**, 677 (2002).
3. W. Saenger, *Principles of Nucleic Acid Structure* (Springer-Verlag, 1983), pp. 132–140.
4. Z. G. Sauerbrey, *Z. Phys.* **206**, 155 (1959).

This page is intentionally left blank

International Journal of Nanoscience, Vol. 1, Nos. 5 & 6 (2002) 673–676

FABRICATION OF ORGANIC/INORGANIC HYBRID MESO-STRUCTURES BY SELF-ORGANIZATION

HIROSHI YABU*

Graduate School of Science, Hokkaido University
North 10 West 8, Sapporo, 060-0812, Japan

MASATSUGU SHIMOMURA*,†

Nanotechnology Research Center, Research Institute for Electronic Science
Hokkaido University, North 12 West 6, Sapporo, 060-0812, Japan

Received 27 November 2002
Revised 24 December 2002

The honeycomb patterned titania films with submicron pores were prepared by a sol–gel reaction. Self-organized 2D arrays of water droplets were formed on surfaces of reaction solution as a template. Polystyrene particles were embedded into the micropores of the honeycomb films by casting dispersion of the particles. The arrangement of aggregated particles was controlled by changing pore sizes.

Keywords: Titania; honeycomb patterned films; polystyrene particles; organic/inorganic hybrid.

1. Introduction

Titanium oxide (Titania) has high refractive index and photo-catalytic properties. It was reported that nano- or microporous honeycomb films were prepared from titania by sol–gel reaction of titan alkoxide sol with amphiplile.[1] To combine the microporous titania film and colloidal particles, it was expected that a novel type of organic/inorganic hybrid materials with photo-catalysts and photonic band gap (PBG) properties was prepared. We showed the preparation of highly-ordered titania porous membranes. Furthermore, the composite formation of the titania films and polystyrene microparticles by self-organization was reported. The arrangements of embedded particles were discussed.

2. Experimental

Honeycomb patterned films were prepared according to the literature.[1] By the analogy of honeycomb films from polymer materials,[2–5] chloroform solution of 3.51 M of

*Frontier Research System, Institute of Physical and Chemical Research (RIKEN Institute).
†Corresponding author.

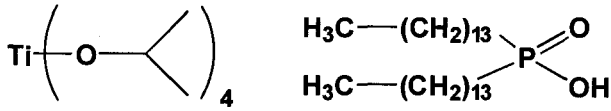

1 2

Fig. 1. Chemical formulae of used compounds. **1** and **2** were purchased from TCI, Japan and Sogo Pharmaceuticals, Japan, respectively.

titanium isopropoxide **1** and 0.246 M of ditetradecyl-phosphate **2** (Fig. 1) was prepared. After casting of 20 μl $\sim$ 500 μl of the solution on horizontal glass substrate, solvent chloroform was evaporated by applying humid air. The relative humidity of applied air was controlled c.a. 60%. Evaporation heat allowed condensing water droplets on the reaction solution. The condensed water droplets were stabilized by amphiphile **2** and then regular arrays of water droplets were formed. After evaporation of solvent and water, the polymer film with hexagonal-arranged pores was remained on the substrate.

Pyrolysis was performed under N_2 atmosphere by hot-stage at 400°C (RINKAM-600, Japan-hitech, Japan). Polystyrene particles, diameter of 1.5 μm and 3.2 μm were obtained from Scientific Polymer Products Inc., USA. After pyrolysis, 20 μl of 1.0 g/l particle dispersions were cast on prepared honeycomb films and dried at room temperature. The prepared patterns were imaged by optical microscopy (Olympus BH-2), equipped with a CCD camera and a video recording system and by scanning electron microscopy (S-3500, Hitachi).

3. Results and Discussion

3.1. *Titania honeycomb films*

Metal alkoxides are known to form metal oxides in a sol–gel process when it contacts water. After completely solvent evaporation, titanium oxide films with hexagonally-arranged pores were prepared. The pore size from 800 nm to 5.0 μm, was controlled by changing the casting volume.[5] Scanning electron micrograph of typical honeycomb structure was shown in Fig. 2(a). The concentration of solution changed the thickness of the films. After pyrolysis at 400°C for 3 h, the film shrank and the average pore size changed from 800 nm to 500 nm. The white gel films turned to black because of thermal decomposition of amphiphile and other organic compounds. These grimes were washed away by chloroform and ethanol. The honeycomb structure was kept even after pyrolysis (Fig. 2(b)). The cross-section of honeycomb structures showed that the pores kept original shape of template water droplets (inset of Fig. 2(b)).

3.2. *Combination of honeycomb films and polystyrene particles*

There are some approaches to combine micropatterns and colloidal clusters. It was reported that the colloidal clusters usually fixed by electrostatic interactions

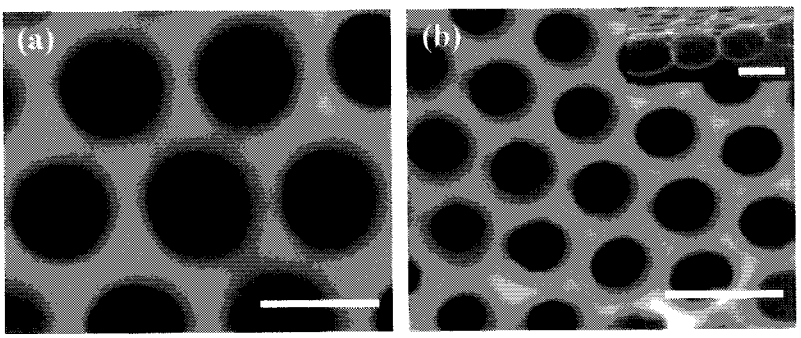

Fig. 2. Scanning electron micrograph of titania honeycomb films. (a) Honeycomb film of titania before pyrolysis. (b) Honeycomb film of titania after pyrolysis. Inset micrograph shows cross-section of the film. Each white bar indicates 1.0 μm.

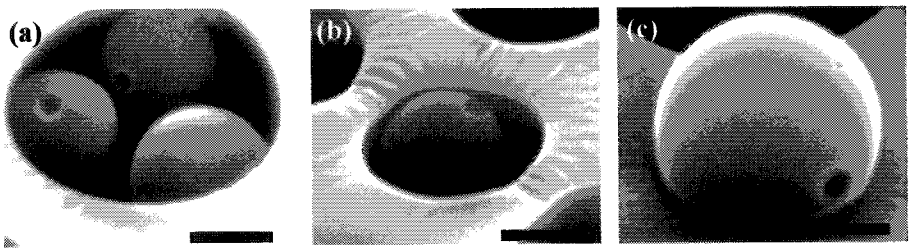

Fig. 3. Scanning electron micrographs of the combination of PS particles and titania honeycomb films. (a) 1.5 μm PS particles in a 3.3 μm honeycomb pore. (b) A single 1.5 μm PS particle in a 2.7 μm honeycomb pore. (c) A 3.2 μm PS particles capped over a 2.7 μm honeycomb pore. Each black bar indicates 1.0 μm.

between self-assembled monolayers (SAMs) and the surface charges on the colloids.[6] But here we show the procedure to form organic/inorganic hybrid materials without surface modification. An aqueous dispersion of polystyrene (PS) particles (1.0 g/l, average diameter was c.a. 1.5 microns) was cast on the honeycomb films and water was evaporated under ambient condition. After complete evaporation of water, the films were observed by SEM. When the dispersion was cast on the honeycomb film having pores of 3.3 μm diameter, three PS microparticles were trapped in the honeycomb pores by the advection and capillary force (Fig. 3(a)). PS particles were arranged in a triangle in the pores. When the particles aggregate in a small dimension, lateral capillary force allowed PS particles to close-packed arrangements. In case of the smaller pore honeycomb film (2.7 μm diameter), only one particle was kept in each pores (Fig. 3(b)). Moreover, when larger PS particles (3.2 μm) were cast on the same honeycomb film, particles were not trapped in the pores but some of them capped over the pores (Fig. 3(c)). These results show that the size of honeycomb pores and particles dominate the number of particles embedded in the pores.

4. Conclusion

We showed the preparation of composite of titania honeycomb films and PS particles by self-organization. The pore sizes of titania honeycomb film were controlled from 500 nm to 5 μm. PS particles were embedded in the pores. Number and aggregation arrangements of particles were controlled by changing of the pore and particle size. The organic/inorganic hybrid meso-structures can be utilized for novel type of photonic band gap materials and photo-catalysts.

References

1. O. Karthaus, X. Cieren, N. Maruyama, and M. Shimomura, *Mater. Sci. Eng. C* **10**, 103 (1999).
2. O. Karthaus, N. Maruyama, X. Cieren, M. Shimomura, H. Hasegawa, and T. Hashimoto, *Langmuir* **16**(15), 6071 (2000); N. Maruyama, O. Karthaus, K. Ijiro, M. Shimomura, T. Koito, S. Nishimura, T. Sawadaishi, N. Nishi, and S. Tokura, *Supramol. Sci.* **5**, 331 (1998).
3. M. Shimomura and T. Sawadaishi, *Curr. Opn. Colloid and Interface Sci.* **6**, 11 (2001).
4. S. A. Jenekhe and X. L. Chen, *Science* **283**, 372 (1999).
5. T. Nishikawa, R. Ookura, J. Nishida, K. Arai, J. Hayashi, N. Kurono, T. Sawadaishi, M. Hara, and M. Shimomura, *Langmuir* **18**(15), 5734 (2002).
6. I. Lee, H. Zheng, M. F. Rubner, and P. T. Hammond, *Adv. Mater.* **14**(8), 572 (2002).

International Journal of Nanoscience, Vol. 1, Nos. 5 & 6 (2002) 677–681

CIRCULAR ARRANGEMENT OF AZOBENZENE CHROMOPHORES IN THE NUCLEOAMPHIPHILE MONOLAYER BY BASE-PAIRING WITH CYCLIC DNA

JIN NISHIDA*, JIN MATSUMOTO*, MITSUHIKO MORISUE†, and KUNIHARU IJIRO*,†

*Precursory Research for Embryonic Science and Technology
Japan Science and Technology Corporation (PRESTO, JST)
†Research Institute for Electronic Science
Hokkaido University, N12W6 Kita-ku, Sapporo 060-0812, Japan

MASATSUGU SHIMOMURA

Nanotechnology Research Center, Research Institute for Electronic Science
Hokkaido University, N12W6 Kita-ku, Sapporo 060-0812, Japan

Received 27 November 2002
Revised 24 December 2002

In order to construct chromophores arrays that precisely controlled their arrangement, monolayers of an azobenzene bearing nucleoamphiphile were prepared on various oligoDNA solutions. Monolayers of the amphiphilic adenine derivative bearing an azobenezene moiety ($C_{12}AzoC_5Ade$) were prepared on thymidylic acid tetramer (dT4) and octamer (dT8) solutions, and UV-vis reflection absorption spectra of the monolayers were measured to investigate aggregation structures of the azobenzene. The absorption maximum of the monolayer was blue-shifted on the dT4 solution and red-shifted on the dT8 solution. It shows that azobenzene groups in the monolayer have parallel orientation (H aggregate) on the dT4 solution. Though, azobenzene groups have head-to-tail orientation (J aggregates) on the dT8 solution. When monolayers of $C_{12}AzoC_5Ade$ were prepared on the synthesized cyclic oligonucleotides, the absorption spectra were totally different from those of the corresponding linear oligonucleotides.

Keywords: Cyclic DNA; azobenzene; monolayer; nucleoamphiphile; base pair.

1. Introduction

Natural biological systems such as proteins express high functions, due to precise arrangement of functional groups. In the case of light-harvesting complex (LH2) composed in photosynthesis system, cyclic arrangement of chromophores with nanometer scale has been revealed by X-ray crystallographic analysis.[1] This specific structure of the chromophores may be important for efficient and fast energy transfer. Therefore various attempts have been carried out to construct chromophore arrays prepared by covalent[2] and coordinate[3] bond.

We have attempted to use DNA as scaffold for arranging chromophores. DNA stores and replicates genetic informations, and plays the critical role in the life

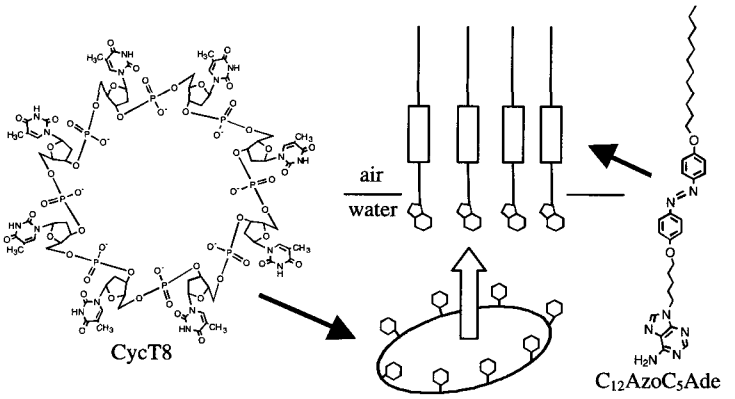

Schematic illustration of the $C_{12}AzoC_5Ade$ monolayer on the aqueous solution of CycT8.

system. DNA is an anionic polymer composed of two pairs of nucleobases, which complementarily recognize each other. According to this feature, DNA is attractive for using as scaffold to construct nanoscale structures.[4] We already reported that amphiphilic nucleobase derivatives formed complementary base pairs and base trimers with nucleic acid dissolving in the subphases at the air–water interface.[5] Controlled polymerization of diacetylene groups in a nucleoamphiphile monolayer have been achieved by formation of complementary base pair and base trimer with oligonucleotides at the air–water interface.[6]

In this paper, we described attempts to control azobenzene aggregates in monolayers by complementary base-pairing between nucleoamphiphiles having azobenzene and oligonucleotides dissolved in subphase.

2. Experimental

Oligonucleotides, dT4 and dT8 were purchased from Takara Bio Inc. Cyclic thymidylic acid tetramer (CycT4) and cyclic thymidylic acid octamer were synthesized followed by H. C.-Y. Jenny *et al.*[7] and E. de Vroom *et al.*[7] $C_{12}AzoC_5Ade$[8] was spread from the chloroform/ethanol (9:1, v/v) solution on the surface of 10 mM Tris-HCl buffer solution (pH = 7.8) containing 750 nM (monomer unit) of the nucleotides. Water was purified to 18 MΩ · cm by a Milli-Q SP reagent system (Millipore Co.). Surface monolayer experiments were carried out by a computer controlled Langmuir film balance (FSD-300, USI System) with a Wilhelmy pressure sensor at 20°C. The absorption spectra of the monolayers were measured by a fiber-optics reflection UV-vis absorption spectroscopy (LB-100, JASCO).

3. Results and Discussion

Effect of chain length of linear oligonucleotides on aggregate structures of azobenzene in monolayer of $C_{12}AzoC_5Ade$ was investigated. $C_{12}AzoC_5Ade$ monolayers

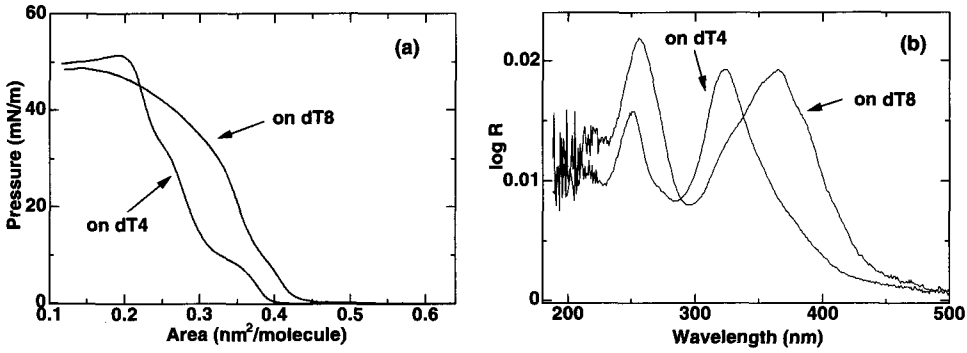

Fig. 1. (a) Surface pressure–area isotherms of the $C_{12}AzoC_5Ade$ monolayers on dT4 and dT8 solutions at 20°C. (b) Reflection UV-vis absorption spectra of $C_{12}AzoC_5Ade$ monolayers on dT4 and dT8 solutions at 20 mN/m.

were prepared on aqueous dT4 and dT8 solutions respectively, and surface pressure–area isotherms and reflection UV-vis absorption spectra at 20 mN/m were measured. The results of surface pressure–area isotherms showed that the monolayer on dT8 solution was expanded more than that on the dT4 solution (Fig. 1(a)). It is known that the absorption maximum of isolated azobenzene is 355 nm. The absorption spectrum of the monolayer on dT4 showed that absorption maximum was shifted to 325 nm. On the other hand, the absorption maximum of the monolayer on dT8 was shifted to 366 nm (Fig. 1(b)).

According to Kasha's molecular exiton theory,[9] systematic X-ray crystallographic studies[10] and absorption spectra of two-dimensional molecular assemblies of single-chain ammonium amphiphiles containing an azobenzene chromophore,[11] chromophore orientation in the assemblies can be estimated by the spectral shift of azobenzene.

Therefore the blue shift of the absorption maximum on dT4 shows that the parallel azobenzene orientation (so-called H aggregate) was formed. The red shift of the absorption maximum on dT8 shows the head-to-tail azobenzene orientation (so-called J aggregate) was formed.

Then, cyclic oligonucleotides were adopted to interact with the nucleobase amphiphile for the cyclic arrangement of azobenzene. The surface pressure–area isotherms of $C_{12}AzoC_5Ade$ monolayers on CycT4 and CycT8 solutions showed that monolayer was expanded on octamer solution more than on tetramer (Fig. 2(a)). Both absorption spectra of monolayers on CycT4 and CycT8 were completely different from those on corresponding linear oligonucleotide subphases. Spectral splitting observed in the cyclic oligomer cases indicated that coexistence of two aggregation structures (H and J aggregates) or another specific aggregate structure was formed on the cyclic oligomer subphases.

The reason why H and J aggregates of azobenzene were formed on dT4 and dT8 solutions has been unsolved until now. Oligonucleotide is expected to be flexible in

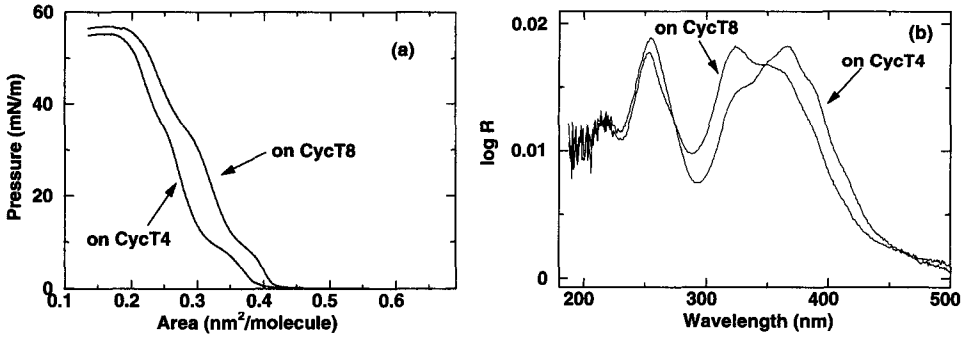

Fig. 2. (a) Surface pressure–area isotherms of the $C_{12}AzoC_5Ade$ monolayers on CycT4 and CycT8 solutions at 20°C. (b) Reflection UV-vis absorption spectra of $C_{12}AzoC_5Ade$ monolayers on CycT4 and CycT8 solutions at 20 mN/m.

water. Intra- and inter-molecular electrostatic repulsion of oligonucleotides bound to the monolayers might influence the aggregate structure. Splitting of the absorption spectra of the monolayers on the cyclic oligonucleotide solutions is interesting. Now futher structural analysis of the azobenzene aggregates in the monolayer is in progress.

4. Conclusion

The monolayers of $C_{12}AzoC_5Ade$ were prepared on various oligonucleotides solutions. Aggregate structures of azobenzene in the monolayer depend on the kinds of complimentary oligonucleotides. H or J aggregates of azobenzene were formed on dT4 or dT8 solutions, respectively. On cyclic oligonucleotides solutions, split absorption spectra of azobenzene were obtained.

References

1. G. McDermott, S. M. Prince, A. A. Freer, A. M. Hawthornthwalte-Lawless, M. Z. Papiz, R. J. Cogdell, and N. W. Isaacs, *Nature* **374**, 517 (1995).
2. A. Nakano, A. Osuka, I. Yamazaki, T. Yamazaki, and Y. Nishimura, *Angew. Chem. Int. Ed.* **37**, 3023 (1998); J. Li, A. Ambroise, S. I. Yang, J. R. Diers, J. Seth, C. R. Wack, D. F. Bocian, D. Holten, and J. S. Jindsey, *J. Am. Chem. Soc.* **121**, 8927 (1999); O. Mongin, A. Schuwey, M.-A. Vallot, and A. Gossauer, *Tetrahedron Lett.* **40**, 8347 (1999); M.-S. Choi, T. Aida, T. Yamazaki, and I. Yamazaki, *Angew. Chem. Int. Ed.* **40**, 3194 (2001).
3. J. Fan, J. A. Whiteford, B. Olenyuk, M. D. Levin, P. J. Stang, and E. B. Fleischer, *J. Am. Chem. Soc.* **121**, 2741 (1999); R. A. Haycock, A. Yartsev, U. Michelsen, V. Sundström, and C. A. Hunter, *Angew. Chem. Int. Ed.* **39**, 3616 (2000); K. Chichak and N. R. Branda, *Chem. Commun.* **1211** (2000).
4. J. J. Storhoff and C. A. Mirkin, *Chem. Rev.* **99**, 1849 (1999).
5. M. Shimomura, F. Nakamura, K. Ijiro, H. Taketsuna, M. Tanaka, H. Nakamura, and K. Hasebe, *J. Am. Chem. Soc.* **119**, 2341 (1997); F. Nakamura, K. Ijiro, and

M. Shimomura, *Thin Solid Films* **327–329**, 603 (1998); M. Morisue, K. Ijiro, and M. Shimomura, *Stud. Surf. Sci. Catal.* **132**, 549 (2001).
6. J. Matsumoto, K. Ijiro, and M. Shimomura, *Chem. Lett.*, 1280 (2000); J. Matsumoto, K. Ijiro, and M. Shimomura, *Mol. Cryst. Liq. Cryst.* **371**, 33 (2001); K. Ijiro, J. Matsumoto, and M. Shimomura, *Stud. Surf. Sci. Catal.* **132**, 481 (2001).
7. C.-Y. J. Hsu, D. Dennis, and R. A. Jones, *Nucleosides Nucleotides* **4**, 377 (1985); E. de Vroom, H. J. G. Broxterman, L. A. J. M. Sliedregt, G. A. der Marel, and J. H. van Boom, *Nucleic Acids Res.* **16**, 4607 (1988).
8. M. Morisue, Ph.D. Thesis, Hokkaido University, Sapporo, 2001.
9. M. Kasha, *Spectroscopy of the Excited State*, ed. B. D. Bartolo (Plenum Press, 1976), p. 337.
10. K. Okuyama, H. Watanabe, M. Shimomura, K. Hirabayashi, T. Kunitake, T. Kajiyama, and N. Yasuoka, *Bull. Chem. Soc. Jpn.* **59**, 3351 (1986).
11. M. Shimomura, R. Ando, and T. Kunitake, *Ber. Bunsenges. Phys. Chem.* **87**, 1134 (1983).

This page is intentionally left blank

International Journal of Nanoscience, Vol. 1, Nos. 5 & 6 (2002) 683–688

DISEASED RED BLOOD CELLS STUDIED BY ATOMIC FORCE MICROSCOPY

YONG CHEN* and JIYE CAI

Department of Chemistry, Jinan University, Guangzhou 510632 Guangdong, P. R. China
**Anhui Institute of Optics and Fine Mechanics, Chinese Academy of Sciences Hefei 230031, Anhui, P. R. China*

JINGXIAN ZHAO

Laboratory for Tissue Transplantation and Immunology Jinan University, Guangzhou 510632, Guangdong P. R. China

Received 3 December 2002
Revised 30 December 2002

In recent years, many mammalian cells, especially erythrocytes because of simpleness of their membrane surfaces, were widely studied by atomic force microscopy. In our study, diseased erythrocytes were taken from patients of lung cancer, myelodisplastic syndrome (MDS), and so on. We obtained many clear topographical images of numerous erythrocytes, single erythrocyte, and ultramicrostructure of erythrocyte membrane surfaces from normal persons and patients. By studying the red cells of lung cancer patients, we found that many erythrocytes of lung cancer patient have changed into echinocytes. One erythrocyte has 10–20 short projections, most of which, with a mean width of 589.0 nm and a length of 646.7 nm, are on the edge of cell. The projections in the center of echinocytes are lodged and embedded, but in conventional model of echinocytes, the projections in the center stretch outside cell membrane, so a novel model of erythrocytes was designed in our paper. After observation of microstructure of MDS patient's erythrocyte membrane surface, we found that many apertures with different diameters of tens to hundreds nanometers appeared on the surface of cell membrane. It can be concluded that AFM may be widely applied in clinic pathological inspection.

Keywords: Diseased red blood cells; atomic force microscopy; lung cancer; myelodisplastic syndrome; echinocytes; projections.

1. Introduction

Normal mature red blood cells are biconcave disks that lack internal organelles and transcellular filament systems. Therefore, no new proteins will add to membrane in erythrocytes' lifetime. On the membrane surface of erythrocytes, only several membrane proteins, mainly including band 3 proteins and glycophorins, can be found. Therefore, in past decades, many researches on red blood cells by atomic force microscopy (AFM) have been conducted, including normal erythrocytes,[1–5] hypotonic hemolysis erythrocytes,[6] Gadolinium-induced

erythrocytes,[7] mechanically-traumatized erythrocytes,[8,9] Babesia bovis-infected erythrocytes,[10] malaria-infected erythrocytes,[11] and so on. In those papers, most abnormal erythrocytes were artificially induced. In our study, diseased human erythrocytes were taken from patients of lung cancer, myelodisplastic syndrome, and so on. By studying these diseased erythrocytes, we try to apply AFM in clinic pathological inspection.

2. Materials and Methods

In this paper, erythrocyte samples from normal, lung cancer patients and myelodisplastic syndrome patients were investigated. Fresh human blood samples were taken and mixed with an anticoagulant (EDTA). The freshly-extracted human bloods were diluted (80 times) in phosphate-buffered saline (PBS). 5 μl aliquot of these solutions were introduced respectively to the freshly-clear cover slip surfaces and were then air-fixed rapidly by vigorously waving the slide. The film was examined under the optical microscope, and then was performed in air on the blood film using a commercial AFM (AutoProbe CP Research, Thermomicroscopes, USA) in tapping mode. Microfabricated silicon cantilevers (Park Scientific Instruments) of sharp tips with a tip radius of curvature 10 nm and a force constant of approximately 2.8 N/m were used. The scan speed of the tip was 1 Hz. The AFM images were planar-leveled using the software (Thermomicroscopes Proscan Image Processing Software Version 2.1) provided with the instrument. Using the line analysis function of the software, the average width and the average height of the regions of interest were determined.

3. Results

3.1. *Observation of many red blood cells*

Figure 1 is the relatively low-resolution images of tens of diseased red blood cells. In Fig. 1(a) (90 cells) and 1(b) (20 cells), many erythrocytes of lung cancer patient have changed into echinocytes with a diameter of around 8 μm, a thickness of around 1 μm, an average volume of 72.19 μm^3, a surface area of 155.33 μm^2, and a surface area/volume ratio of about 2.223 $\mu m^2/\mu m^3$. The erythrocytes of MDS patient are still biconcave in shape (Fig. 1(c)), with a diameter of around 8.697 μm, a thickness of around 777.5 nm, an average volume of 69.67 μm^3, a surface area of 185.6 μm^2, and a surface area/volume ratio of about 2.409 $\mu m^2/\mu m^3$.

3.2. *Observation of single echinocyte*

Imaging several ehinocytes and parts of them (Figs. 2(a)–2(d)), we found that one echinocyte has 10–20 short projections, most of which, with a mean width of 589.0 nm and a length of 646.7 nm, are on the edge of cell. The projections in the center of echinocytes are lodged and embedded (just as Fig. 2(f)), but in conventional model of echinocytes, the projections in the center stretch outside cell

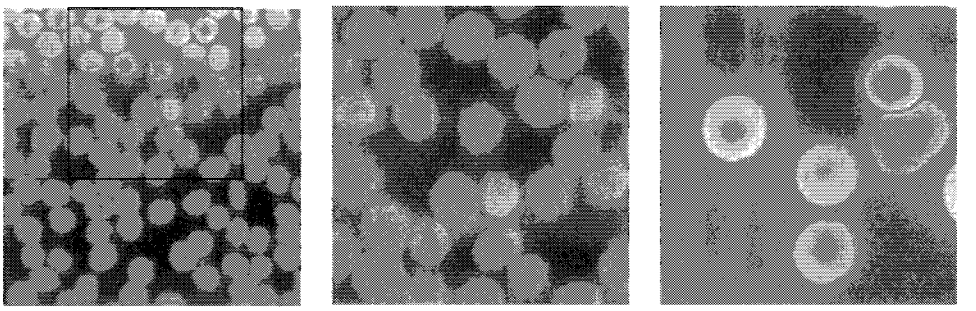

(a) (b) (c)

Fig. 1. AFM topographic images of erythrocytes at large range. (a) Echinocytes of lung cancer (90 μm), (b) enlarged image of the black box in (a) (50 μm), and (c) erythrocytes of MDS patient (40 μm).

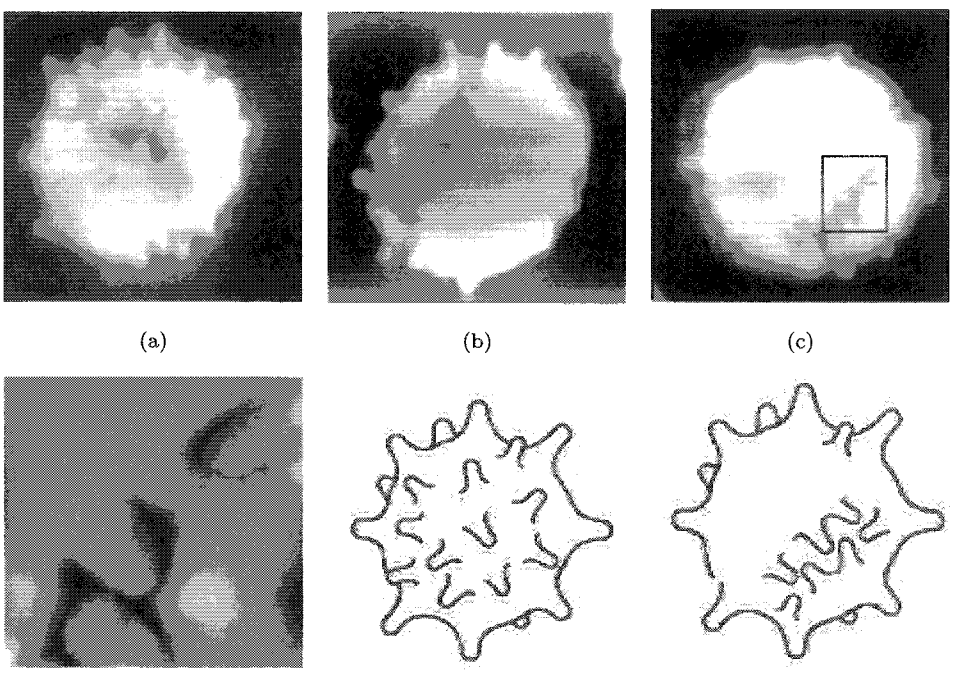

(a) (b) (c)

(d) (e) (f)

Fig. 2. AFM topographic images of the whole and parts of single echinocyte. Scanning size: 10 μm (a), (c); 11 μm (b); 2 μm (d). (d) is the enlarged image of (c) (showed by black box). (e) and (f) are the schematic representation of echinocyte shape. (e) Traditional model and (f) our model.

membrane (Fig. 2(e)).[12] In general, echinocytes are speculated red cells with regular, short and uniform projections on their surfaces. In our study, we found that the projections in the center were longer in length but less in width than those on the edge. Different projection has different length and width. Various disorders

may cause echinocytic transformation of red cells, including abnormal plasma lipid metabolism, low red cell ATP, increased concentration of intracellular Ca++, pyruvate kinase deficiency, heparinization, extensive burns, uraemia, liver disorders, and so on.[13] But in our paper, the reason causing echinocytes in lung cancer patients is unknown, and more researches will be done to deal with the problem. We think that various disorders will induce different type of echinocytes, the conventional model or the model we constructed. All these results will be important in the clinic pathological inspection.

3.3. *High-resolution imaging comparisons of membrane surface ultrastructures of erythrocytes of MDS patients with normal mature erythrocytes*

After the observation of microstructure of MDS patient's erythrocyte membrane surface, we found that many apertures with different diameters of tens to hundreds nanometers appeared on the surface of the cell membrane (Figs. 3(b) and 3(c)). On

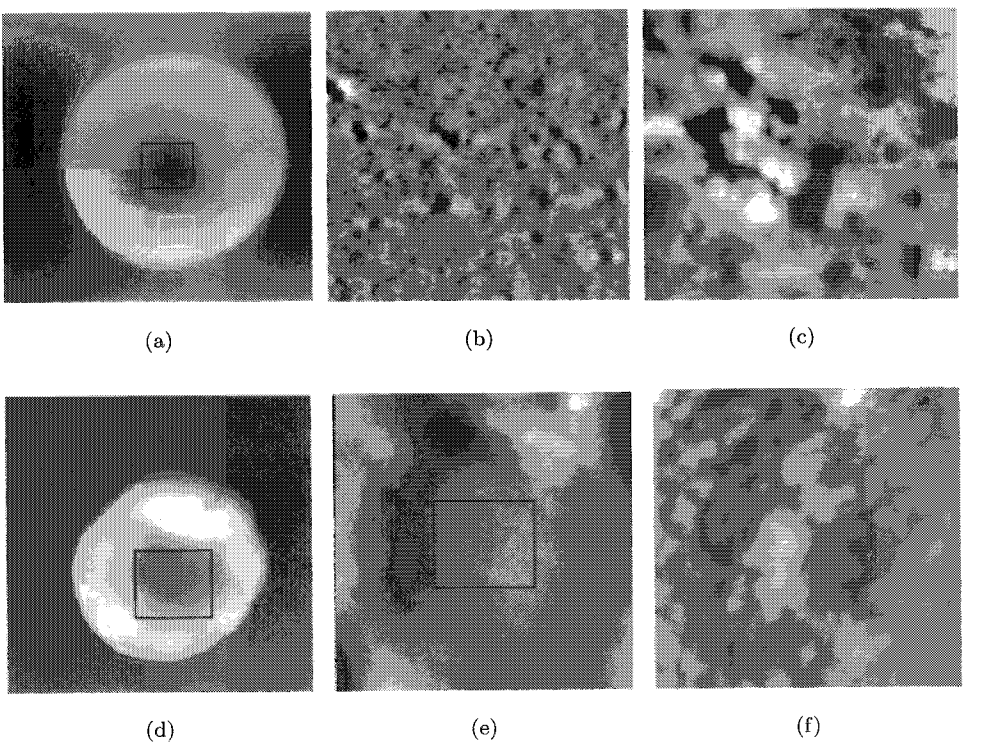

Fig. 3. Comparison of AFM topographic images of membrane surface microstructures between normal and MDS patient's erythrocytes. (a) A single MDS erythrocyte (10 μm), (b) the enlarged image of the black box in (a) (2 μm), (c) the enlarged image of the white box in (a) (1 μm), (d) a single natural biconcave erythrocyte (10 μm), (e) the enlarged image of the black box in (d) (3 μm), and (f) the enlarged image of the black box in (e) (1 μm).

the membrane surface of the normal mature erythrocyte, no aperture was found (Figs. 3(e) and 3(f)). The high-resolution imaging comparisons of membrane surface ultrastructures maybe used to diagnose the MDS.

4. Discussion

In recent years, AFM has been widely applied in biology, mainly because of its advantages, such as convenient preparation of sample, various (air, liquid or physiological) work environments, resolution of around 1 nm, and so on. It will become a routine method in the research of life science and clinic pathological inspection. This paper preliminarily described the application of AFM in clinic pathological inspection by AFM observation of red blood cells, which is an important parameter in clinic inspection. One of the elementary functions of AFM applied in clinic pathological inspection is to scan interested regions at a large range. In present, xy-range of commercial AFM is around 100 μm, and z-range is about 10 μm. Those ranges are enough for observation of tens of cells and statistical analysis. In general, the thickness of cells is 0.1–50 μm. In order to investigate most kinds of cells, AFM with a z-range of larger than 100 μm has been developed.[14] Comparing with traditional clinic inspection of blood, using AFM can get the data of numbers and volumes of blood cells, as well as the topographical images, diameter, thickness, surface, surface area/volume ratio, and so on. What's more, more analysis of those data can be made. Take the average of heights and surface area/volume ratio among the 20 cells in Fig. 1(b) for example, results can be shown in Table 1, which will be useful in the diagnosis of disease in different phase.

Investigation of projections or particles on membrane surface of single cell is another function of AFM, which make AFM beauty compare with electron microscopy (EM). For EM, samples must be dried or treated with chemicals; low-temperature and ultrahigh vacuum techniques are important for high-resolution EM to ensure stability and minimal beam damage. For AFM, those disadvantages disappeared. What's more, AFM observation can be finished in a short time (generally in one hour). All these advantages make AFM become a useful technique in the clinic pathological diagnosis.

Most importantly, resolution to around 1 nm made AFM be widely applied to study ultrastructures of membrane surface of cells. As we all know, the

Table 1. Statistic analysis of average heights and surface area/volume ration among the 20 cells in Fig. 1(b).

Average height	Quantity of cells	Surface area/volume ratio	Quantity of cells
< 0.8 μm	3	1.7–2 $\mu m^2/\mu m^3$	7
0.8–1 μm	2	2–2.5 $\mu m^2/\mu m^3$	10
1–1.2 μm	11	> 3 $\mu m^2/\mu m^3$	3
> 1.2 μm	4		

ultrastructures of membrane surface among cells of various kinds or between normal and diseased cells are different (just as shown in Fig. 3). Furthermore, many cells have their special cell surface markers, by which we can identify some cells. So, it is possible for clinic diagnosis to reach molecular level by AFM technique.

AFM can be used to study blood, stem cells and tumor cells. Besides topographical images, the physical properties, including charge density, adhesion, stiffness, and the force required to break specific ligand–receptor bond, can be examined.[15–18] Besides the static cell structures, dynamic structures of cells with time lapse can be investigated. In other word, the development of AFM technique will drive the application of AFM in clinic pathological inspection.

5. Conclusions

AFM can be widely applied in clinic pathological inspection, including quantification of cells, obtainment and comparison of many parameters, such as diameter, thickness, volume, surface, surface area/volume ratio, and so on, observation of topograph of single cell, and observation and comparison of membrane surface microstructure of cells, and so on.

Acknowledgments

The experiments in this study were carried out with an Autoprobe CP AFM in the experiment analysis center at Jinan University of Guangzhou. The authors thank the reviews for their helpful suggestions on improving the manuscript. This research was performed with a support from the national 973 program of China.

References

1. P. Zachee, *Am. J. Nephrol.* **14**, 197 (1994).
2. P. C. Zhang, *Scanning Microsc.* **9**, 981 (1995).
3. M. Grandbois, *J. Histochem. Cytochem.* **48**, 719 (2000).
4. R. Nowakowski, *Biochim. Biophys. Acta* **1514**, 170 (2001).
5. U. Salzer, *Blood* **99**, 2569 (2002).
6. Y. Sato, *Biol. Pharm. Bull.* **16**, 506 (1993).
7. Y. Cheng, *Biochim. Biophys. Acta* **1421**, 249 (1999).
8. M. Girasole, *J. Microsc.-Oxford* **204**, 46 (2001).
9. Y. Ohta, *Artif. Organs* **26**, 10 (2002).
10. M. Aikawa, *Parasitol. Int.* **46**, 241 (1997).
11. E. Nagao, *J. Electron Microsc.* **49**, 453 (2000).
12. A. Iglic, *J. Biomechanics* **30**, 35 (1997).
13. B. Agroyannis, *Clinica. Chimica. Acta* **261**, 185 (1997).
14. P. P. Lehenkari, *Ultramicroscopy* **82**, 289 (2000).
15. F. H. William, *Tibtech. April.* **17**, 143 (1999).
16. T. E. Fisher, *TIBS.* **24**, 379 (1999).
17. H. Haga, *Ultramicroscopy* **82**, 253 (2000).
18. M. H. Robert, *Am. J. Physiol. Renal.* **278**, F689 (2000).

International Journal of Nanoscience, Vol. 1, Nos. 5 & 6 (2002) 689–693

PREPARATION OF THE HONEYCOMB PATTERNED POROUS FILM OF BIODEGRADABLE POLYMER FOR TISSUE ENGINEERING SCAFFOLDS

KATSUHISA SATO and KIYOSHI HASEBE

Graduate School of Environmental Earth Science
Hokkaido University, N10 W5, Kita-ku Sapporo, Hokkaido 060-0810, Japan

MASARU TANAKA, MASAFUMI TAKEBAYASHI,
KAZUTAKA NISHIKAWA, and MASATSUGU SHIMOMURA

Research Institute for Electronic Science
Hokkaido University, N12 W6, Kita-ku Sapporo, Hokkaido 060-0812, Japan

TOMOAKI KAWAI, MICHIAKI MATSUSHITA, and SATORU TODO

Hokkaido University School of Medicine
N15W7, Kita-ku,Sapporo, Hokkaido 060-8648, Japan

Received 27 November 2002
Revised 14 January 2003

Fabrication and surface modification of a cell scaffold are very important in tissue engineering. In this study, the effects of pore size and surface wettability on hepatocyte adhesion and morphology was studied, using the porous poly-ε-caprolactone (PCL) film prepared by a simple casting technique. The degree of spreading of hepatocyte was enhanced with the decrease of the pore size (~ 10 μm). Hepatocyte motility and spreading were restricted on the patterned film having cellular-sized pores (ca. 20 μm). Partial hydrolysis of the film surface enhanced the migration and spheroid formation of the cultured hepatocyte.

Keywords: Tissue engineering scaffolds; biodegradable polymer; hepatocyte.

1. Introduction

In the field of Tissue Engineering,[1] scaffolds are used to direct the growth of cells migrating form surrounding tissue or the growth of cells seeded within the porous structure formed in the scaffold. It is recognized that the behavior of the adhesion and proliferation of different types of cells on polymeric materials depend on the surface characteristics such as wettability, chemistry, charge, rigidity, and topography. The scaffold must provide a suitable substrate for cell attachment, proliferation, and differentiated function. Biodegradable polymers have been one of the candidate materials of scaffolds. The present study describes the fabrication of highly-regular-patterned poly-ε-caprolactone (PCL) (Fig. 1(a)) films by simple

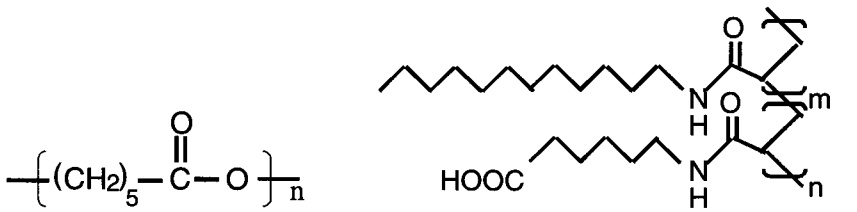

(a) (b)

Fig. 1. Chemical structures of (a) poly-ε-caprolactone (**PCL**) and (b) an amphiphilic polymer **Cap** (m:n = 4 : 1).

casting technique,[2,3] and pore size and surface wettability effects on hepatocyte adhesion and morphology.

2. Materials and Methods

Honeycomb-patterned PCL (MW = 100 000) films were prepared by casting polymer solution in a petri dish with 10 cm diameter under moist air flow. Evaporative cooling leads to the formation of hexagonally-packed water droplets on the surface of polymer solution. The pore size of the PCL-patterned films can be controlled from 1 μm to 50 μm by changing the evaporation time of the polymer solution. A chloroform solution of PCL and copolymer of dodecylacrylamide and co-carboxyhexyl acrylamide (Cap) (10:1 w%) (Fig. 1(b)) was used. The PCL-patterned films were partially hydrolyzed by soaking in aqueous NaOH solution (1 N). The hydrolyzed films (pore size ca. 5 μm, thickness ca. 8 μm) were characterized by the measurement of water contact angle and scanning electron microscopy (SEM).

Hepatocytes were isolated from 6–7-week-old male Wistar rats weighing 200–300 g by a modified two-step *in situ* collagenase perfusion technique.[4] The obtained cells were washed by four times centrifugation at 50 × g for 1 min. The hepatocyte viability were determined by trypan blue exclusion. Hepatocyte were cultivated in serum-free Williams' E medium supplemented with 0.1 μM $CuSO_4 \cdot 5H_2O$ (Wako Pure Chemical Industries Ltd., Osaka, Japan), 25 nM Na_2SeO_3 (Wako), 1.0 μM $ZnSO_4 \cdot 7H_2O$ (Wako), 0.1 μM insulin (Sigma Chemical Co., St. Louis, MO), 1.0 μM dexamethasone (Sigma), 20 ng/mL epidermal growth factor (Sigma), 100 μg/mL ascorbic acid di-phosphate (Sigma), 5 KIE/mL aprotinin (Bayer, Germany), 48 μg/mL gentamicin (Schering-Plough, USA), and 100 ng/mL Chloramphenicol (Sankyo, Japan). Cell suspension of Hepatocytes were adjusted to the cell density of 2.0×10^5 cells/well (24 well plate) in Williams' E medium. Hepatocytes were seeded onto polymer substrates that immersed with the medium over 6 h. Hepatocytes were incubated at 37°C in 95% air containing 5% CO_2. The culture medium exchange was carried out every 24 h. Hepatocyte morphology on each polymer substrate was observed by SEM 72 h after seeding.

3. Results and Discussion

The hepatocyte cultured on the flat film can spread well (Fig. 2(a)). On the other hand, cells cultured on the patterned-PCL film with subcellular size pores ($\sim$10 μm) formed aggregates whose size increased with increasing pore size (Figs. 2(b) and 2(c)). The patterned films with cellular size pores (ca. 20 μm) gave restricted hepatocyte motility and spreading (Figs. 3(a) and 3(b)). On the other hand, the

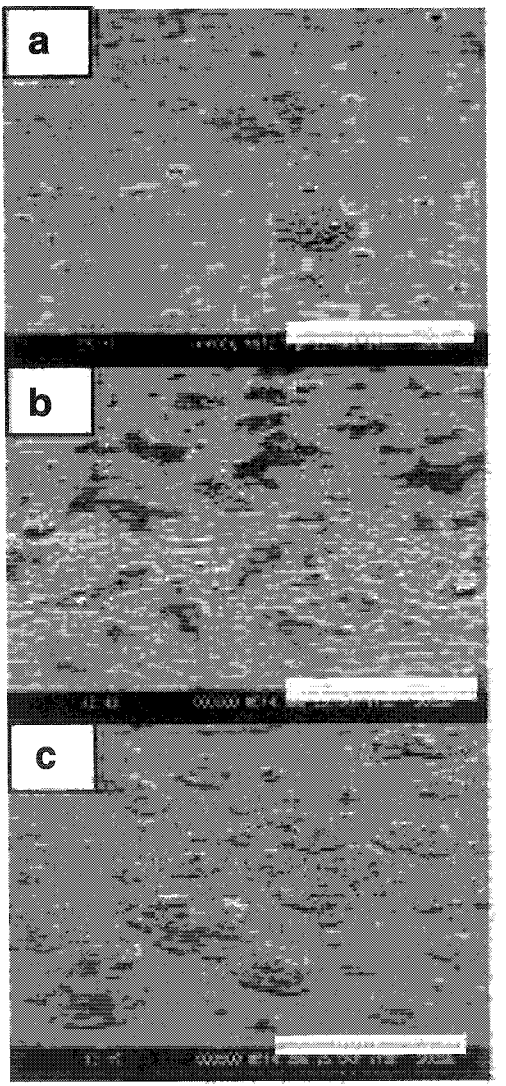

Fig. 2. SEM images of hepatocyte on PCL films. (a) Flat film, (b) patterned film of ca 5 μm and (c) ca. 10 μm pore size. Bar: 500 μm.

hepatocyte can spread on the film when cells contact with each other (Fig. 3(c)). These results indicate that both the surface topography and the pore size strongly affect the cell adhesion and spreading.

The surfaces of PCL are hydrophobic to reduce cell compatibility in the initial stage of contact. So, it is desirable to change its surface character or property of scaffold from hydrophobic to hydrophilic.[5] The changes of water contact angle of

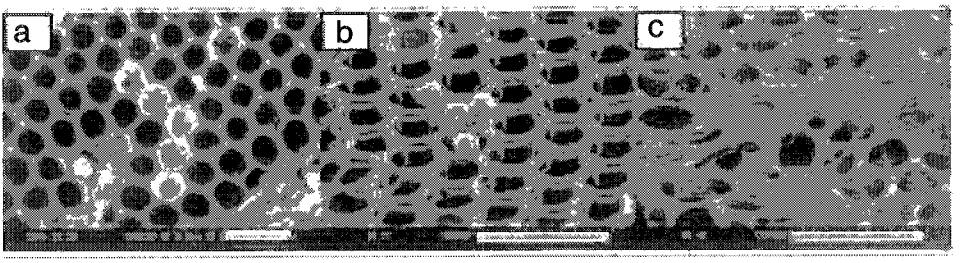

Fig. 3. SEM images of hepatocyte on PCL-patterned films. Pore size: ca. 20 μm. Bar: 50 μm.

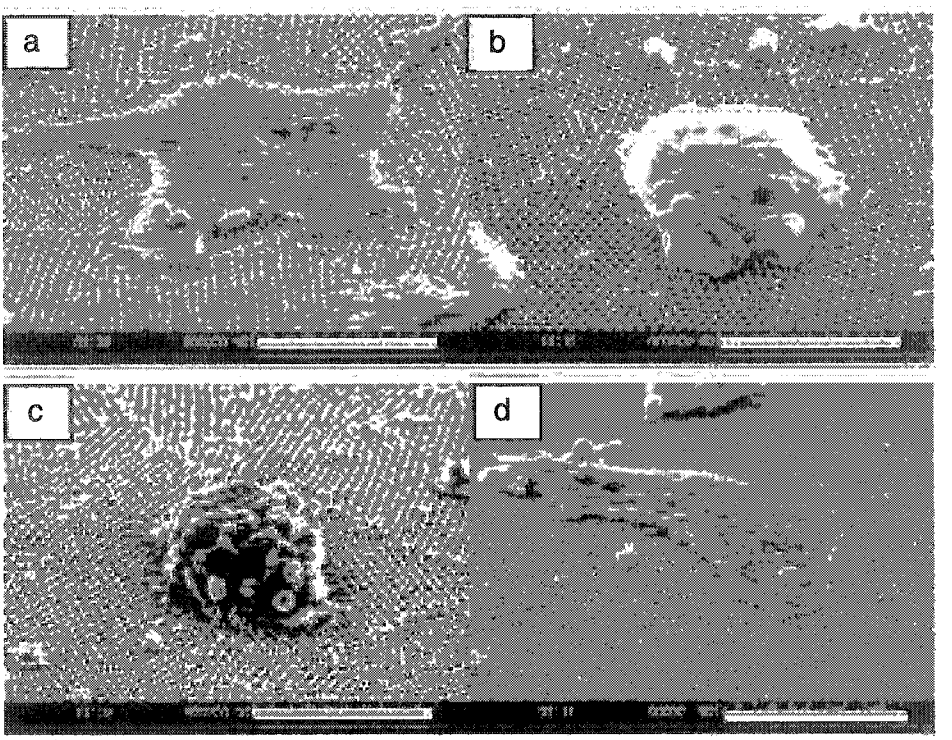

Fig. 4. SEM images of hepatocyte on PCL-patterned films. Pore size: ca. 5 μm. Hydrolysis time: (contact angle). (a) 0 min (ca. 115°), (b) 1 min (ca. 92°), (c) 5 min (ca. 75°), and (d) 12 h (ca. 20°). Bar: 100 μm.

polymer surface gradually declined with increasing hydrolyzed time, owing to the oxygen-based functional groups generated on the surface by hydrolysis.[6,7]

Short hydrolysis time (~5 min) enhanced the cell migration and spheroid formation of the cultured hepatocyte (Figs. 4(a)–4(c)). With further hydrolysis (12 h), however, the hepatocytes spread well (Fig. 4(d)). In this study, cell–surface interactions have dominated on hydrophilicity of the PCL films. We assume that the proper wettability and surface topography might reflect increased preference for cell–cell interactions. To further characterize cell–surface and cell–cell interactions, it is required to investigate the expression of focal adhesion contacts and tight junctions, respectively.

In conclusion, the PCL-patterned films with controlled pore size and surface wettability have a strong influence on the hepatocyte attachment and morphology. These results indicate that the patterned films are powerful candidate of the scaffold with functional regulation of cultured cells for tissue engineering.

References

1. R. Langer and J. P. Vacanti, *Science* **260**, 920 (1993).
2. T. Nishikawa, R. Ookura, J. Nishida, K. Arai, J. Hayashi, N. Kurono, T. Sawadaishi, M. Hara, and M. Shimomura, *Langmuir* **18**, 5734 (2002).
3. N. Maruyama, T. Koito, J. Nishida, T. Sawadaishi, X. Cieren, K. Ijiro, O. Karthaus, and M. Shimomura, *Thin Solid Films* **327–329**, 854 (1998).
4. P. Seglen, *Methods Cell Biol.* **13**, 29 (1976).
5. J. H. Lee, S. J. Lee, G. Khang, and H. B. Lee, *J. Biomater. Sci. Polymer Ed.* **10**, 283 (1999).
6. S. J. Lee, G. Khang, and Y. M. Lee, *J. Biomater. Sci. Polymer Ed.* **13**, 197 (2002).
7. I. K. Kwon, K. D. Park, S. W. Choi, S. H. Lee, E. B. Lee, J. S. Na, S. H. Kim, and Y. H. Kim, *J. Biomater. Sci. Polymer Ed.* **12**, 1147 (2001).

This page is intentionally left blank

International Journal of Nanoscience, Vol. 1, Nos. 5 & 6 (2002) 695–699

STRETCHING OF SINGLE DNA MOLECULES BY LANGMUIR–BLODGETT METHOD

YASUTAKA MATSUO and KUNIHARU IJIRO*

Precursory Research for Embryonic Science and Technology
Japan Science and Technology Corporation
4-1-8, Honcho, Kawaguchi, Saitama 332-0012, Japan
**Research Institute for Electronic Science, Hokkaido University*
N12W6 Kita-ku, Sapporo, Hokkaido 060-0812, Japan

MASATSUGU SHIMOMURA

Nanotechnology Research Center, Research Institute for Electronic Science
Hokkaido University, N12W6 Kita-ku, Sapporo
Hokkaido 060-0812, Japan
shimo@poly.es.hokudai.ac.jp

Received 27 November 2002

We propose a new method that double-stranded DNA molecules can be stretched and immobilized on the clean glass substrate by using a lipid monolayer at the air–water interface. This method is based on the substrate lifting of Langmuir–Blodgett method. We observed fluorescence images of polyion complex films with a scanning near-field optical microscope (SNOM). As a result, straight fluorescent lines aligned parallel to the lifting direction were observed and it was considered that isolated single DNA molecules were extended to align on the substrate. This method is applied to various DNA molecules.

Keywords: DNA; Langmuir–Blodgett films; polyion complex; scanning near-field optical microscope.

1. Introduction

DNA molecules have received considerable attention due to the genetic information in modern biology. Double-stranded DNA (dsDNA) has a double helical structure composed of complementary base-pairs between adenine–thymine or cytosine–guanine. In recent years DNA has been focused as a high functional polymer. In particular, the applications of molecular recognition devices using complementary nucleic acid base pairing, based on hydrogen bonding and nanometer-scale molecular electronic devices utilizing the electrical transport through stacking π-electrons of base pairs, are expected.[1–4]

As DNA molecules are flexible polymer in an aqueous solution and have high-order structures (random coil, supercoil and globule), it is difficult to fabricate one-dimensionally straightening molecular wire of dsDNA. Therefore it is necessary to

develop the technique to stretch and immobilize isolated single DNA molecules on a solid substrate.

Some methods of stretching DNA were reported. Schwartz *et al.* have already found alignment of DNA molecules in gel by electrophoresis.[5] However DNA molecules cannot be immobilized on a solid substrate by electrophoresis. Bensimon *et al.* have discovered a new method, called "molecular combing", that DNA were stretched and immobilized on solid substrates by an action of receding meniscus.[6] In order to efficiently immobilize DNA the "molecular combing" method requires chemically-treated glass substrates.

In this paper, we propose a new method for stretching and immobilization of single dsDNA molecules on substrates. This method is based on Langmuir–Blodgett (LB) method. We have reported that a monomolecular film of DNA can be prepared by using a polyion complex technique.[7] When a chloroform solution of a cationic amphiphile was spread on an aqueous dsDNA subphase, a polyion complex film of the cationic amphiphile and dsDNA was formed by electrostatic interaction at the air–water interface. This film was transferred on a clean glass substrate by a vertical lifting method. We investigated stretched and immobilized DNA molecules on the substrate by SNOM.

2. Experimental

Dioctadecyldimethylammonium bromide ($2C_{18}N^{+}2C_1$) was purchased from Sogo Pharmaceutical Co. Ltd. DNA (λ-phage, Nippon Gene Co.) was used without further purification. Chloroform (spectrophotometric grade, Wako pure chemical industries) was used as a spreading solvent. A dilute solution of DNA was prepared at a concentration of 10 nM in base pair (bp) with TE buffer (pH 7.8). DNA molecules were labeled with the intercalating fluorescent dye YOYO-1 (molecular probes) at a dye/bp ratio 1/10.

Cationic amphiphile $2C_{18}N^{+}2C_1$ was spread on the DNA subphase. DNA molecules were expected to adsorb to the cationic monolayer by electrostatic interaction and form a polyion complex film at the air–water interface. After 5 min, the formed monolayer was compressed at the rate of 0.02 nm^2/molecule/min by a film balance system FSD-50 (USI System, Japan). The surface pressure was measured by a Wilhelmy plate. The subphase temperature was maintained at $20 \pm 0.2°C$. When the surface pressure reached 5 mN/m, the glass substrate immersed under the subphase before monolayer spreading was lifted up at a speed of 2 mm/min to transfer the polyion complex film on the glass substrate. (Fig. 1)

Fluorescence images of the polyion complex film on glass substrates were measured by dynamic force mode commercial SNOM (SPA300, Seiko Instruments). An Ar ion laser (488 nm, Stabilite2017, Spectra-Physic) was coupled to optical fiber to illuminate samples. The emission from the sample was collected by objective lens (100× oil immersion type, N.A. 1.4, Olympus) and was detected by an avalanche photodiode (APD, SPCM-ARQ-14, EG&G) for observation of the fluorescence images.

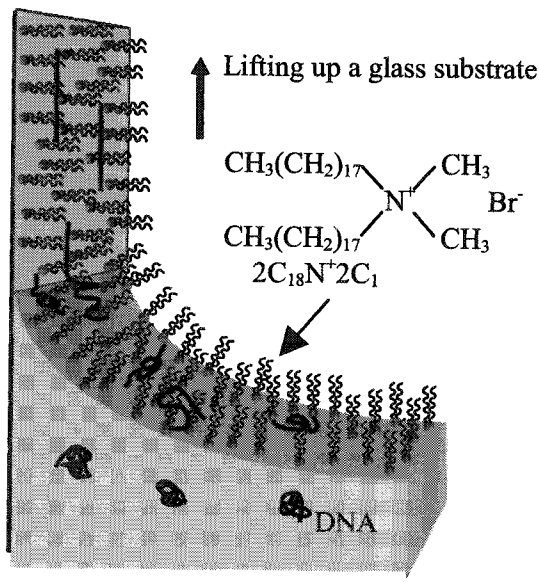

Fig. 1. Schematic illustration of deposition of a DNA-amphiphile polyion complex monolayer on a solid substrate.

3. Results and Discussion

Figure 2 shows fluorescence images of the polyion complex film transferred on the glass substrate. Fluorescent lines aligned parallel to the lifting direction were observed. The average length of fluorescent lines was about 16 μm. A calculated length of B-formed λ-phage DNA is 16.5 μm, therefore good agreement between average length of fluorescent lines and calculated length (16.5 μm) of λ-phage DNA indicates that the fluorescence image could be attributed to stretched single DNA molecules. We could not measure the corresponding topographic images of fluorescent lines. On the glass substrates DNA molecules are covered with the amphiphile monolayer. At the surface pressure of 5 mN/m the monolayer is in the fluid state at the air–water interface.[8] It is considered that the topographic imaging of the DNA in the monolayers was not easy due to the soft surface.

The maximum length of fluorescent lines reached about 21.5 μm and was approximately 1.25 times longer than calculated one as B-formed DNA. DNA molecules bound to the amphiphile monolayer were in random coil state at air–water interface before the transfer on the substrate. Thus DNA molecules were stretched by the lifting process. It turns out that the force exerted on dsDNA molecules was strong enough to elongate them but too weak to break the molecules during lifting process. Uniform fluorescent profile of DNA molecule suggests that the single DNA molecule was uniformly stained by YOYO-1 (Fig. 2(a)).

As shown in Fig. 2(b), high fluorescence intensities were observed at the both ends of the DNA molecule. This line is shorter than 21.5 μm and fluorescence

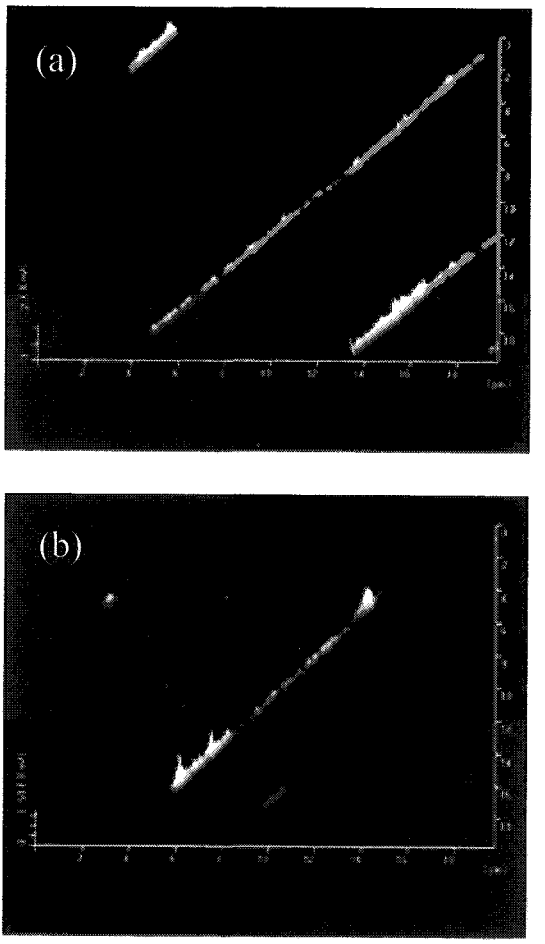

Fig. 2. Fluorescence images of λ-phase DNA stained with YOYO-1. Scan area is 20 μm × 20 μm.

intensity in the middle part is uniform. Some single DNA molecules were not fully stretched and that ends were aggregated. The "molecular combing" method requires a specific binding of DNA via its ends on an appropriately treated substrate.[6] It is not necessary to anchor DNA molecules by binding of the end on the substrate in our method, thus the LB method can be applied to circular DNA molecules such as a plasmid.

4. Conclusion

We have shown that isolating single dsDNA molecules can be stretched and immobilized on the glass substrate by the LB method. This method can be applied to various dsDNA molecules, a wide range of length and different types (linear or circular). This method is expected to lead to new development of DNA devices.

Acknowledgments

This work was financially supported by the Precursory Research for Embryonic Science and Technology project (PRESTO) (Conversion and Control by Advanced Chemistry) of Japan Science and Technology Corporation (JST) and also by a Grant-in-Aid on Scientific Research from the Ministry of Education, Science, Sport, and Culture of Japan.

References

1. C. A. Mirkin, R. L. Letsinger, R. C. Mucic, and J. J. Storhoff, *Nature* **382**, 607 (1996).
2. S. J. Tans, A. R. M. Vershueren, C. Dekker, and M. Tinkham, *Nature* **393**, 49 (1998).
3. D. Porath, A. Bezryadin, S. Vries, and C. Dekker, *Nature* **403**, 635 (2000).
4. Y. Okahata, T. Kobayashi, K. Tanaka, and M. Shimomura, *J. Am. Chem. Soc.* **120**, 6165 (1998).
5. D. C. Schwartz *et al.*, *Science* **262**, 110 (1993).
6. A. Bensimon, A. Simon, A. Chiffaudel, V. Croquette, F. Heslot, and D. Bensimon, *Science* **265**, 2096 (1994).
7. K. Ijiro, M. Shimomura, M. Tanaka, H. Nakamura, and K. Hasebe, *Thin. Solid Films* **284/285**, 780 (1996).
8. M. Shimomura, R. Mitamura, J. Matsumoto, and K. Ijiro, *Synthetic Metals*, in press.

This page is intentionally left blank

International Journal of Nanoscience, Vol. 1, Nos. 5 & 6 (2002) 701–705

PREPARATION AND CHARACTERISTICS OF SANDWICHED POLYMER/MAGNETIC PARTICLES/POLYMER MAGNETIC NANOMICROSPHERES

XIA HONG, XINTONG ZHANG, XIN CHEN, LI XU, YANMEI LIU, FENGQI LIU, and YUBAI BAI*

Department of Chemistry, Jilin University, Changchun
Jilin Province 130023, P. R. China
**yubai@mail.jlu.edu.cn*

Received 27 November 2002
Revised 13 December 2002

A template polymerization approach is reported to prepare uniform functional sandwiched magnetic composite nanomicrospheres with polymer core, magnetic Fe_3O_4 mezzanine and multicomponent polymer shell. The fine superparamagnetic properties, thermostability and stability in a wide pH range of aqueous solution made the composite mirospheres had the potential applications in biology and medicine.

Keywords: Template polymer process, sandwiched structure, superparamagnetism.

1. Introduction

Even though magnetic composites have long been under study, interest in nanometer-scale magnetic composites has recently increased owing to the development of nanotechnology. Nowadays these materials have been widely used as immunoassay,[1] drug delivery,[2] magnetic resonance contrast agent,[3] separation of the biological reagent,[4] etc.

Extensive efforts to synthesize efficient microspheres with fine magnetic properties have been carried out. Two major ways have been described. One is that the magnetic solid cores are coated with inorganic materials,[5] polymers[6] or biomacromolecules.[7] The other is that magnetic particles are adsorbed or precipitated onto surface of matrix.[8] However, the above magnetic particles still suffer from a few major disadvantages: (a) Most of the particles synthesized using these methods are of micron- or submicron-sized, which might limit their applications.[6] (b) Most of the available particles are somewhat polydispersed. (c) The available magnetic microspheres usually can only be used in a neutral aqueous media. Application of acidic, alkaline solutions, or many organic solvents, often leads to agglomeration process. (d) Some systems limited the choice of functional groups as well as the range of reactions that carried out efficiently on the surface of the magnetic particles.

In the present paper, we addressed a novel "template polymerization method" to synthesize a kind of sandwiched magnetic multicomponent polymer nanomicrospheres containing polymer core, Fe_3O_4 mezzanine and polymer shell. This multicomponent polymer shell was easier to introduce functional groups by the particles surface modification than polysaccharide or silica shell. In addition, we employed a technique of high gradient magnetic fields (HGMF) to quantitatively separate magnetic products from the nonmagnetic impurities.

2. Experimental Section

Copolymer latex was prepared by batch emulsion copolymerization according to the literature.[9] Monomers (styrene:butyl acrylate:acrylic acid = 6:5:1, wt. %), sodium dodecyl sulfate (0.8 g), triton-100 (1.33 g), potassium persulfate (0.37 g) and Na_2CO_3 (0.3 g) were dissolved in 140 ml of deionized water and reacted for 4.5 h at 78°C, 370 rpm.

Magnetite nanoparticles were prepared by Massart's method.[10] In a typical experiment, a mixed aqueous solution of ferric chloride (50 ml, 1 M) and ferrous chloride (10 ml, 2 M, in 2 M HCl) was slowly added into ammonia solution (500 ml, 0.7 M) with vigorous stirring for 30 min at room temperature. The resulting black precipitate was collected by magnet. An aqueous solution of 2 M perchloric acid was added to the precipitate, and was then isolated by centrifugation. The precipitate was dispersed in water. A brown suspension of 0.01 M was finally obtained.

The sandwiched functional magnetic nanocomposites were prepared by the seed polymerization method. The copolymer emulsion was diluted to one hundred times and adjusted to pH 2.5 with hydrochloric acid. Fe_3O_4 hydrosols (2 ml) were added into the above solution and the pH value was adjusted to 4.2 with sodium acrylate. Then, monomers (2 g), emulsifiers (53 mg) and initiator (9 mg) were added with stirring at 370 rpm. The reaction lasted for 1.5 h at 78°C. Unbound copolymer was removed by washing in a HGMF, which is performed in steelwool columns (1 × 10 cm) and placed in a magnetic field of 4210 gauss. The magnetic composites were stained in the column. After the column was removed from the external magnetic field, the composites were eluted with distillated water.

The particle size and shape of the dispersions were measured by transmission electron microscope (TEM) operating at 200 kV. X-ray diffraction patterns were recorded with a Rigaku D/Max model with Cu Kα radiation. Thermogravimetric analysis (TGA) was carried out using a Perkin-Elmer TGA/DTA. Magnetic property of the composites was measured by Quantum Design SQUID magnetometer.

3. Results and Discussion

There are many reports on preparing magnetite (Fe_3O_4) nanoparticles by the coprecipitation of ferrous and ferric salts. As described by Massart,[10] magnetite nanoparticles prepared were easily peptized when ferric salt was excess. In our work, we

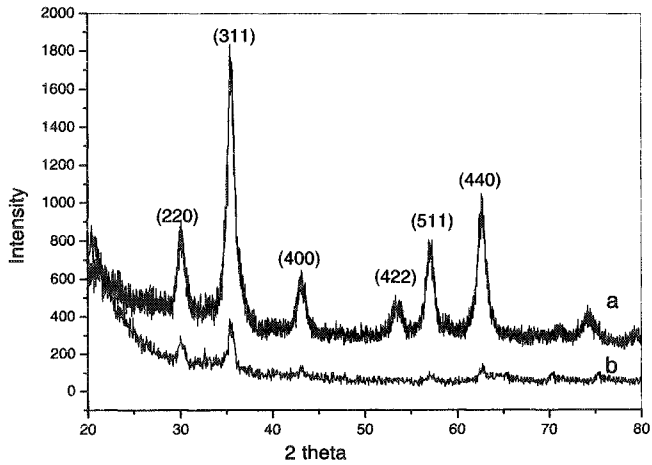

Fig. 1. XRD spectra of (a) magnetite nanoparticles and (b) sandwiched magnetic composite.

selected a Fe II/Fe III ratio of 0.4. Figure 1 showed the XRD patterns of the magnetic nanoparticles and composites prepared. The peaks in Fig. 1(a) agreed well with the ICDD data card of magnetite, which exhibited the inverse spinel structure. No other crystalline phase coexisted with the spinel in a detectable amount. In Fig. 1(b), almost all of the same peaks appeared in the same position and the similar relative intensity, except that the whole intensity was much weaker than that in Fig. 1(a) due to the small quantity of Fe_3O_4 in the composites. The peaks were all broaden due to the small particle size. By the Deby–Scherrer formula,[11] the size of the magnetic particles was calculated from the (311) peak as 8.5 nm.

The sandwiched core–shell structure could be directly visualized by TEM. Figure 2(a) was the TEM image of the polymer core. They were spherical shape and exhibited a smooth surface with diameter of 45 nm. The image in Fig. 2(b) indicated that magnetic particles were adhering to the polymer cores. The black

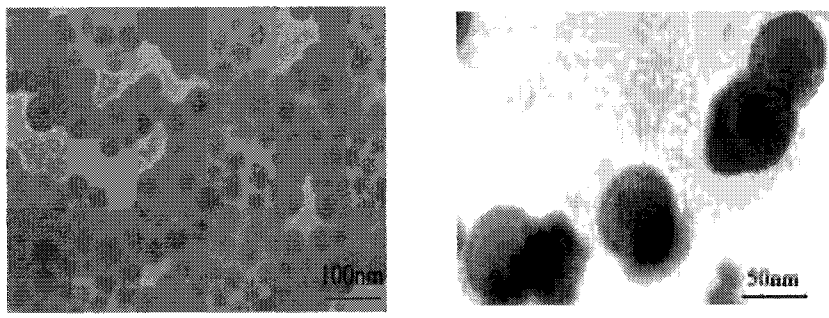

(a) (b)

Fig. 2. TEM images of magnetic nanocomposite: (a) polymer and (b) magnetic composite.

dots were magnetic particles and their sizes were about 9 nm, which was consistent with the XRD results. The whole composite microspheres were about 65 nm.

The isoelectric point of Fe_3O_4 is around pH 4.9.[12] However, the isoelectric point of the sandwiched composite microsphere was shifted to pH 2.5. This indicated that the composite magnetic microspheres had high-dispersed stability in aqueous medium of a wide range of pH value due to the electrostatic repulsion. In fact, our composites were stable when pH value was between 3.0 and 12.0. TGA was carried out to obtain information on the thermostability of the polymer and the magnetic composites. The pure polymer disintegrates from 300°C to 510°C, while the magnetic composite material was stable only up to 230°C. A possible reason might be that magnetite particles weaken the van der Waals interaction between the polymer chains, which affects the three-dimensional structure of the polymer. We also calculated the composition of the micropheres approximately by the TGA results. The amount was to be 91% latex and 9% magnetic particles by wt. %.

A magnetization curve as a function of field at room temperature was studied. The initial susceptibility showed no hysteresis at room temperature, that is, both the retentivity and coercivity were zero, consistent with superparamagnetic behavior and the nanoscale dimensions of the particles. At 10 kOe, the composite had a magnetic saturation moment of 69.69 emu/g. In fact, when employed to facilitate biochemical separations and immunoassay, these magnetic particles must have the property of being superparamagnetic, meaning that they are only magnetic when placed in a very strong magnetic field. If the individual particles possessed a remnant magnetic field, each particle would act as a small dipole magnet, resulting in aggregates, destabilization and precipitation of the composites. So superparamagnetism is critical to success.

4. Conclusion

We used a template polymerization approach to prepare sandwiched magnetic multicomponent nanomicrospheres. This approach resulted in the formation of particles of very narrow size distribution and adsorbed fine abundant magnetic particles. TEM images showed that the composite microspheres were about 65 nm in diameter with 45 nm core and 10 nm mezzanine. The surface of these microspheres yielded an abundant of functional groups, i.e., carboxyl, which could be further coupled with biomolecular by carbodi-imide method.[13] Also, the good dispersed stability obtained in aqueous medium and superparamagnetic properties made the sandwiched micropheres a promising candidate in biological separation and detection.

Acknowledgment

The authors thank the National Natural Science Foundation of China (NNSFC) for the financial assistance.

References

1. J. L. Guesdon and S. Avrameas, *Methods Enzymol.* **73**, 471 (1981).
2. T. K. Jain, I. Roy, T. K. De, and A. Maitra, *J. Am. Chem. Soc.* **120**, 11092 (1998).
3. C. H. Reynolds, N. Annan, K. Beshah, J. H. Huber, S. H. Shaber, R. E. Lenkinski, and J. A. Wortman, *J. Am. Chem. Soc.* **122**, 8940 (2000).
4. S. S. Airapetyan, G. G. Balayan, and A. G. Khachatryan, *Russian J. Appl. Chem.* **74**, 519 (2001).
5. P. Philipse, M. P. B. Bruggen, and C. Pathmamanoharan, *Langmuir* **10**, 92 (1994).
6. S, Miltenyi, W. Multer, W. Meichel, and A. Radbruch, *Cytometry* **11**, 231 (1990).
7. D. P. E. Dickson, S. A. Walton, S. Mann, and K. Wong, *Nanostruct. Mater.* **9**, 595 (1997).
8. H. Shiho, Y. Manabe, and N. Kawahashi, *J. Mater. Chem.* **10**, 333 (2000).
9. H. Du, S. Kan, G. Zhang, F. Liu, X. Tang, and T. Li, *Chem. J. Chin. Univ.* **16**, 33 (1995).
10. R. Massart, *IEEE Trans. Magn.* **17**, 1247 (1981).
11. A. Guinier, *X-Ray Diffraction* (Freeman, San Francisco, CA, 1963), p. 142.
12. G. D. Mendenhall, Y. Geng, and J. H. Wang, *J. Colloid Interface Sci.* **184**, 519 (1996).
13. M. Suzuki, M. Shinkai, M. Kamihira, and T. Kobayashi, *Biotechnol. Appl. Biochem.* **21**, 335 (1995).

This page is intentionally left blank

International Journal of Nanoscience, Vol. 1, Nos. 5 & 6 (2002) 707–711

ELECTRIC CONDUCTIVITY OF NUCLEIC ACID POLYMER MONOLAYER

YUICHI HASHIMOTO
Graduate School of Science, Hokkaido University
N10W8 Kita-ku, 060-0810 Sapporo, Japan

KUNIHARU IJIRO
Research Institute for Electric Science, Hokkaido University
N12W6 Kita-ku, 060-0812 Sapporo, Japan
PRESTO, Japan Science and Technology Corporation (JST)
N12W6 Kita-ku, 060-0812 Sapporo, Japan

TETSURO SAWADAISHI and MASATSUGU SHIMOMURA*
Frontier Research System, RIKEN, Hirosawa
Wako, 351-0198 Saitama, Japan
**Nanotechnology Research Center, Research Institute for Electric Science*
Hokkaido University, N12W6 Kita-ku, 060-0812 Sapporo, Japan
**shimo@poly.es.hokudai.ac.jp*

Received 27 November 2002
Revised 24 December 2002

We investigated electric conductivities of poly nucleic acid-amphiphile polyion complex monolayers. The polyion complex monolayers were prepared by spreading of dialkylammonium salt on aqueous solutions of various poly nucleic acids. The complex monolayers were compressed at the air–water interface and transferred on comb-shaped Au-electrode substrates by vertical lifting method. I–T plots of the complex monolayers, which were measured under applying direct voltage, suggested that the complex monolayers were dielectric substances. The I–V plots indicated that the conductivity of the monolayer depended on the species of poly nucleic acids. Based on the ac impedance analysis of those monolayers, the bulk resistance of those monolayers was estimated from the complex impedance plane plots.

Keywords: Poly nucleic acid; polyion complex monolayer; conductivity.

1. Introduction

It is suggested that DNA can act as a π–electron medium for the electron transfer because of its close stacking of base pairs. An electronic application of DNA has attracted attentions of many researchers. Many studies have been reported on the

*Corresponding author.

conductivity of DNA. However, the electric character of DNA has not yet been concluded.[1,2]

DNA is an anionic polyelectrolyte having phosphate residues. When DNA is mixed with a cationic amphiphile, polyion complex can be formed through the electrostatic interaction between DNA and the amphiphile. Okahata *et al.* reported that a stretched cast film of the DNA–amphiphile polyion complex showed an anisotropic electric conductivity. However, DNA molecules in the polyion complex were covered with insulating amphiphiles and could not directly contact with the electrode.[3]

In order to make direct contact of DNA to the electrode, we report here the conductivity experiments of the DNA monolayer. We have already prepared Langmuir–Blodgett (LB) films of the DNA–amphiphile polyion complex monolayers.[4,5] When cationic amphiphiles were spread on the aqueous DNA solution, the polyion complex was formed at the air–water interface. When octadecylacridine orange ($C_{18}AO$), as a photosensitizer, was mixed with the cationic amphiphile, the acridine moiety of $C_{18}AO$ was intercalated in DNA complexed with the amphiphile.[5] Then photoconductivity of DNA–amphiphile polyion complex monolayer containing $C_{18}AO$ is expected.

Prior to the photoconductivity measurement, we investigated the dark-conductivities of the polyion complex monolayers transferred on the comb-shaped electrodes. DNA is expected to directly attach onto the electrode surface in the first up-stroke of the vertical dipping process.

2. Experiment

Double-stranded DNA (sodium salts from salmon testes, Wako chemicals, Japan), double-stranded poly(G)·poly(C) sodium salts, poly(A)·poly(U) sodium salts (Sigma, USA), and carboxymethylcellulose (CMC, sodium salts, Daicel chemicals, Japan) for a control experiment were used without further purification. Chloroform for a spreading solvent was of spectroscopic grade (Dojindo chemicals, Japan). Dihexadecyl-dimethylammonium bromide, $2C_{16}N^{+}2C_1$, was purchased from Sogo Pharmaceutical Company, Japan. 10-Octadecyl acridine orange iodide ($C_{18}AO$) was prepared.[5]

A comb-shaped Au electrode (the distance between electrodes was 5 μm, the width of the electrode was 10 μm and the number of the electrode pairs was 65 on a quartz substrate, BAS, Japan) was used. DC conductivity was measured by an ampere meter (R8349A, Advantest, Japan) applying certain dc voltage. An ac impedance analyzer (1296/1260, Solartron, United Kingdom) was used to measure impedance of the monolayer.

A mixture of two cationic amphiphiles ($2C_{16}N2C_1$ and $C_{18}AO$, the molar ratio was 10:1) was spread on various aqueous solutions of nucleic acid polymers. The nucleic acid polymer can be electrostatically bound to the cationic amphiphile at the air–water interface to form the polyion complex (Fig. 1). The formed monolayer

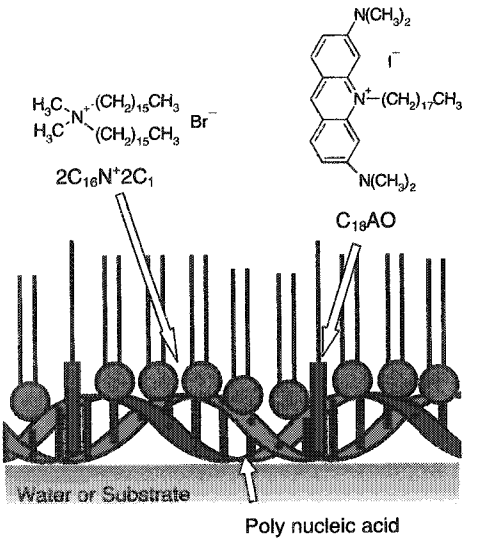

Fig. 1. A schematic illustration of poly nucleic acid–amphiphile polyion complex monolayer.

was compressed to surface pressure of 5 mN/m and deposited on the comb-shaped Au electrode by vertical lifting method with lifting speed of 2 mm/min.

3. Result and Discussion

For dark-current measurement, direct voltage was applied. The inset of Fig. 2 shows the plot of current versus time (I–T plot) of the poly(G) · poly(C)-amphiphile

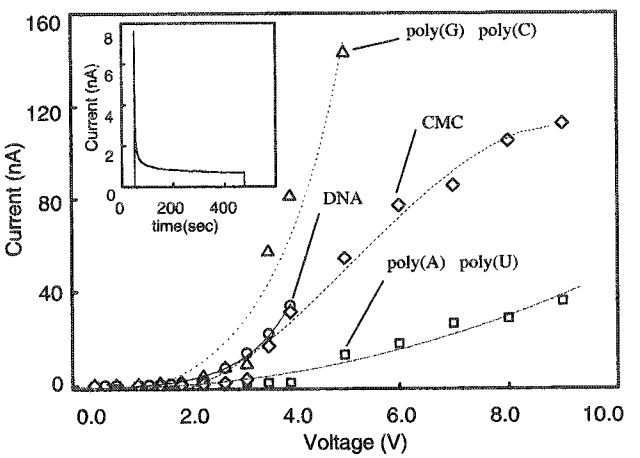

Fig. 2. I–V plots of polyion complex monolayers. DNA (○), poly(G) · poly(C) (△), poly(A) · poly(U) (□), and CMC (◇). Inset shows the I–T plot of poly(G) · poly(C)–amphiphile complex at 1.4 V.

complex monolayer at dc voltage of 1.4 V at room temperature and under 30% relative humidity. By applying voltage, a current peak and a steady-state current were observed. This indicates the poly nucleic acid–amphiphile polyion complex monolayers are conductive and capacitive materials. All of four complex monolayers carried out in this experiment show the similar I–T profile. Plots of steady-state currents versus applied voltage in dark (I–V plots) were shown in Fig. 2. Slopes of I–V plots depended on the species of polymers. Poly(G) · poly(C) gave the lowest resistance in this experiment.

However CMC is the anionic polymer without nucleobases, the CMC–amphiphile polyion complex monolayer showed certain resistance. This indicates that the conduction of the monolayers is related to an ionic conduction.

In order to elucidate the conduction mechanism of the monolayers, impedance measurements were carried out by applying ac voltage in the frequency range of 10 MHz to 0.1 Hz for poly(G) · poly(C) and poly(A) · poly(U) monolayers. The complex impedance plane plots of complex monolayers consisted of two different semicircle parts (Fig. 3). Small (left part) and large (right part) semicircles was corresponded to the bulk and the monolayer/electrode interface resistances, respectively. An equivalent circuit supposed from the plots is shown in Fig. 3.

The conductivities of various complex monolayers calculated from Figs. 2 and 3 are summarized in Table 1. The dc conductivity of poly(G) · poly(C) monolayer was 67 times higher than that of the poly(A) · poly(U) monolayer. On the other hand, the ac conductivities of the bulk parts of both monolayers were almost identical. This indicates that a difference in the ac conductivities of the monolayer/electrode interface may be responsible for the difference in the dc conductivities of the poly(G) · poly(C) and poly(A) · poly(U) monolayers. Unfortunately, the

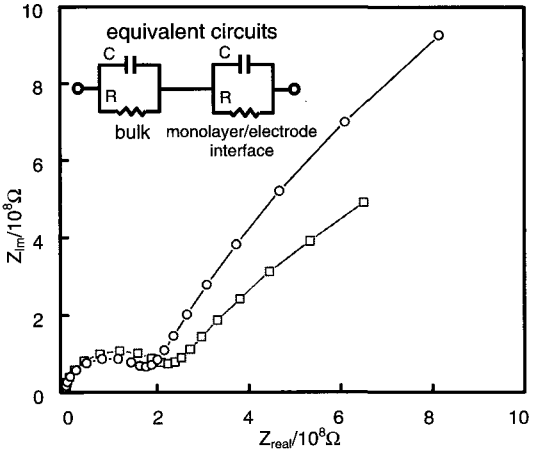

Fig. 3. Complex impedance plane plots of complex monolayers. Poly(G) · poly(C) (○) and poly(A) · poly(U) (□). The inset illustration shows equivalent circuits of poly nucleic acid polymers.

Table 1. The conductivities of monolayers (S/cm).

	Dc measurement	Ac measurement (bulk parts)
DNA from salmon testes	8×10^{-7}	—
poly(G) · poly(C)	20×10^{-7}	6×10^{-7}
poly(A) · poly(U)	0.3×10^{-7}	5×10^{-7}
CMC	8×10^{-7}	—

ac conductivities of the monolayer/electrode interfaces could not be estimated from Fig. 3 due to the insufficient data at the lower frequency range.

It is supposed that the ac conductivities of the monolayer/electrode interface part were contributed by redox chemical reactions of the monolayers at the surfaces of the electrodes. The difference of both monolayers is the species of nucleic acids. Ionization potential of guanine (7.75 eV) is the smallest, next to adenine (8.24 eV), in other nucleic acids.[6] The redox reaction of guanine of the poly(G) · poly(C) monolayer is expected to occur more easily than the poly(A) · poly(U) monolayer at the electrodes. The difference of the dc conductivities can be assumed to reflect the difference of ionization potentials of nucleobases.

In conclusion, the dc conductivities of the polyion complex monolayers measured in this experiments might be derived from both the ionic conduction and the electron transfer by chemical reaction of nucleobase. The dc conductivity was influenced on the species of nucleic acids contacted with the monolayer/electrode interface. Thus electron transfer between the electrode and the complex monolayer would be important for the whole conductivity of the monolayer.

Acknowledgment

This work was partly supported by a Grant-in-Aid from the Ministry of Education, Culture, Sports, Science, and Technology, Japan.

References

1. C. J. Murphy, M. R. Arikin, Y. Jenkins, N. D. Ghatlia, S. H. Bossmann, and J. K. Barton, *Science* **262**, 1025 (1995).
2. P. J. de Pablo, F. M. Herrero, J. Colchero, J. G. Herrero, P. Herrero, A. M. Baró, and P. Ordejón, *Phys. Rev. Lett.* **85**, 4992 (2000).
3. Y. Okahata, T. Kobayashi, K. Tanaka, and M. Shimomura, *J. Am. Chem. Soc.* **120**, 6165 (1998).
4. K. Kago, H. Matsuoka, R. Yoshitome, H. Yamaoka, K. Ijiro, and M. Shimomura, *Langmuir* **15**, 5193 (1999).
5. M. Shimomura, J. Matsumoto, F. Nakamura, T. Ikeda, T. Fukasawa, K. Hasebe, T. Sawadaishi, O. Karthaus, and K. Ijiro, *Polym. J.* **31**, 1115 (1999).
6. H. Sugiyama and I. Saito, *J. Am. Chem. Soc.* **118**, 7063 (1996).

This page is intentionally left blank

International Journal of Nanoscience, Vol. 1, Nos. 5 & 6 (2002) 713–717

THEORETICAL STUDY OF EXCITON–EXCITON CORRELATION EFFECT ON EXCITON MIGRATION IN MOLECULAR AGGREGATE

MASAHIRO TAKAHATA, MASAYOSHI NAKANO,
SATORU YAMADA, and KIZASHI YAMAGUCHI

Department of Chemistry, Graduate School of Science, Osaka University
Machikaneyama 1-1, Toyonaka, Osaka 560-0043, Japan

Received 27 November 2002
Revised 9 January 2003

Two-exciton migration dynamics of a molecular aggregate is performed using the density matrix approach. Exciton–exciton correlation is shown to cause an oscillatory behavior in the one-exciton population dynamics. Such a feature is found to be well explained by the bypass transition from the ground to a one-exciton forbidden state via a two-exciton state.

Keywords: Exciton dynamics; molecular aggregate; exciton–exciton correlation.

1. Introduction

Excitation energy transfer has attracted much attention from the scientific and technological points of view.[1] For example, phenylacetylene dendrimers have been investigated theoretically and experimentally on the light-harvesting properties.[2–4] In our theoretical study, the overlaps of exciton distributions between exciton states are found to be important for realizing the unique migration.[4,5] However, exciton–exciton correlation effects on exciton migrations have not been investigated. This study aims to clarify the exciton–exciton correlation effects on the migrations in a molecular aggregate. In the one-exciton model, only a excitation is assumed to exist on any monomer unit, while in the two-exciton model, we consider two excitations on different monomer units. We perform the two-exciton migration dynamics of a dendritic molecular aggregate D4, which is modeled after the smallest phenylacetylene dendrimer, using the quantum Liouville equation with phenomenological relaxation parameters.

2. Calculation Method

We consider a molecular aggregate composed of two-state monomers (dipoles) with an excitation energy (38 000 cm^{-1}) and a transition moment (5 D) (see Fig. 1). The

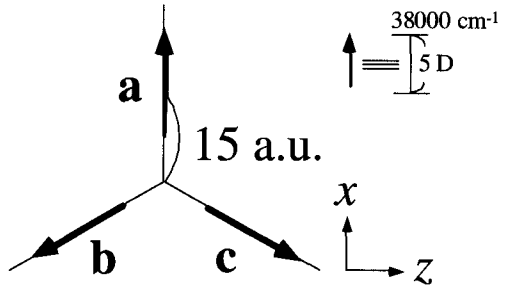

Fig. 1. Structure of a molecular aggregate.

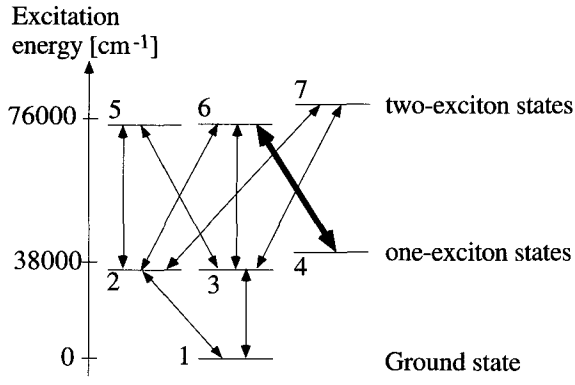

Fig. 2. Schematic energy states with the transition among exciton states.

monomers are assumed to be coupled by the dipole–dipole interaction. The Hamiltonian (H_S) for the molecular aggregate is diagonalized using molecular-aggregate bases which satisfy the completeness relation:

$$1 = |0\rangle\langle 0| + \sum_{i}^{N} |i\rangle\langle i| + \sum_{i,j}^{N} |ij\rangle\langle ij| \,, \tag{1}$$

where, $|0\rangle$, $|i\rangle$ and $|ij\rangle$ represent the ground-state, one-exciton and two-exciton bases, respectively. N indicates the number of monomers. Exciton states $\{|\psi_m\rangle\}$, which are numbered from **1** to **7** (see Fig. 2), with energies $\{E_m\}$ satisfy the following eigenvalue equation:

$$H_S|\psi_m\rangle = E_m|\psi_m\rangle \,. \tag{2}$$

The time evolution of exciton population ($\rho(t)$) is described by the quantum Liouville equation:

$$i\hbar\frac{\partial}{\partial t}\rho = [H(t),\, \rho(t)] - i\Gamma\rho(t) \,, \tag{3}$$

where the second term on the right-hand side of Eq. (3) represents a relaxation term in the Markov approximation.[3] The total Hamiltonian ($H(t)$) is expressed by

the sum of the Hamiltonian (H_S) for the molecular aggregate and the interaction ($V(t)$) between aggregate system and an external field:

$$H(t) = H_S + V(t) = \sum_{m}^{M} E_m |\psi_m\rangle\langle\psi_m| + \sum_{m,n}^{M} \mu_{mn}(F\cos\omega_{\text{ext}}t)|\psi_m\rangle\langle\psi_n|\,, \qquad (4)$$

where ω_{ext} and F are an external-field frequency (37 992 cm^{-1}) and an amplitude (corresponding to 100 MW/cm^2) in the direction of x axis (see Fig. 1). μ_{mn} is the magnitude of the transition moment from the state m to n. The number of states, M, is equal to $1 + N + N(N-1)/2$ for the two-exciton model.

The relaxation term in Eq. (3) can be considered as two types of mechanism:

$$(-\Gamma\rho(t))_{mm} = -\Gamma_{mm}\rho_{mm}(t) + \sum_{m\neq n}^{M} \gamma_{nm}\rho_{nn}(t) \qquad (5)$$

and

$$(-\Gamma\rho(t))_{mn} = -\Gamma_{mn}\rho_{mn}(t)\,. \qquad (6)$$

The relations among damping (Γ_{mn}) and feeding parameters (γ_{mn}) are represented in details in Ref. 3. The feeding parameters are assumed to satisfy the following condition:

$$\gamma_{mn} = C(E_m - E_n)\,, \qquad (m > n) \qquad (7)$$

where C is fixed to be 0.01 when both of exciton states m and n are one-exciton states or two-exciton states, while C is fixed to be 0.0 for otherwise.

3. Results and Discussion

Figure 2 shows the schematic energy states with the transition among exciton states. Two pairs of exciton states ((**2**, **3**) and (**5**, **6**)) are degenerate to each other, respectively. The energy difference between states **3** and **4** is 254 cm^{-1}, and that between **6** and **7** is 255 cm^{-1}. Exciton states **2** and **3** are allowed to excite to all two-exciton states (states **5**, **6** and **7**). On the other hand, the ground state is forbidden to excite to exciton state **4**, while state **4** is allowed to excite only to state **6** (as shown by a thick line in Fig. 2). It is noted that the ground state is allowed to excite to one-exciton state **4** via two-exciton state **6**.

Figure 3 shows the change of exciton population ((I), (II) and (III)) at each monomer (**a**, **b** and **c**) using two-exciton model as well as that (IV) using one-exciton model. Figures 3(I) and 3(II) show the contributions of one- and two-exciton populations at each monomer, respectively. Figure 3(III) shows the sum of one- and two-exciton contributions at each monomer. At $t = 0$, the ground-state population is assumed to be 1. After 10 optical cycles, the external field is cut off. As seen from Fig. 3(I), one-exciton population is found to spatially oscillate between monomers ((**a** $\leftrightarrow$ **b**) and (**a** $\leftrightarrow$ **c**)). In the case of one-exciton model, however, such an oscillation is not observed (see Fig. 3(IV)). In general, exciton population is known to

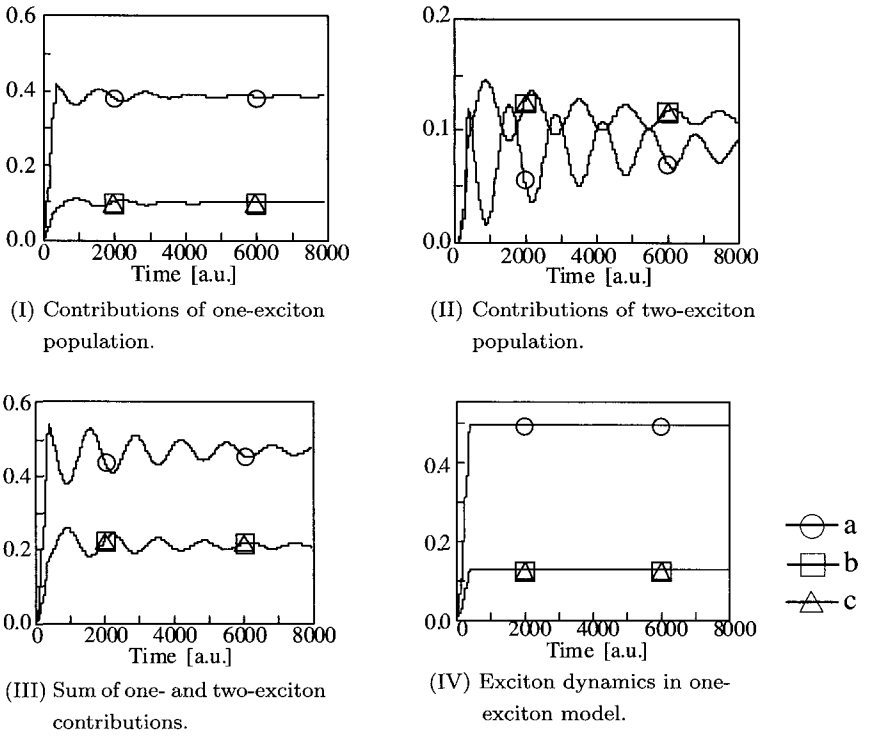

(I) Contributions of one-exciton population.

(II) Contributions of two-exciton population.

(III) Sum of one- and two-exciton contributions.

(IV) Exciton dynamics in one-exciton model.

Fig. 3. Change of exciton population ((I), (II) and (III)) at each monomer (**a**, **b** and **c** shown in Fig. 1) using two-exciton model, and that (IV) using one-exciton model. a.u. is an abbreviation for the atomic unit.

oscillate between monomers only when exciton population is induced in the exciton states with different energies from each other. In this study, exciton oscillation does not occur in one-exciton model since only two degenerate one-exciton states **2** and **3** are populated. In contrast, in the case of two-exciton model, exciton state **4** is populated by the transition via a two-exciton state **6**. This feature leads to a spatially oscillation behavior of one-exciton population shown in Fig. 3(I).

As seen from Fig. 3(II), two-exciton population is found to oscillate between monomers. This is caused by the fact that low-lying degenerate two-exciton states (**5** and **6**) and a high-lying two-exciton state (**7**) are all populated due to the existence of transitions from one-exciton states.

4. Concluding Remarks

We investigated the exciton dynamics in a dendritic molecular aggregate D4 using two-exciton model as well as that using one-exciton model. It was found that exciton–exciton correlation causes an oscillatory behavior in the spatial one-exciton distributions. This unique behavior originates in the bypass transition (via a two-exciton state) from the ground state to a one-exciton forbidden state.

Such exciton correlation effects obtained by including two-exciton configurations are expected to provide significant changes in the one-exciton migration pathway, the feature of which will be useful for the control of exciton dynamics in the nanostructured dendritic systems.

Acknowledgments

This work was supported by Grant-in-Aid for Scientific Research (No. 14340184) from Japan Society for the promotion of Science (JSPS), a Grant from the Ogasawara Foundation for the Promotion of Science and Engineering.

References

1. L. Charbonneau (ed.), *Polymeric Materials: Science & Engineering* **84** (2001).
2. C. Devadoss, P. Bharathi, and J. S. Moore, *J. Am. Chem. Soc.* **118**, 9635 (1996).
3. M. Nakano, M. Takahata, H. Fujita, S. Kiribayashi, and K. Yamaguchi, *Chem. Phys. Lett.* **323**, 249 (2000).
4. M. Takahata, M. Nakano, H. Fujita, and K. Yamaguchi, *Chem. Phys. Lett.* **363**, 422 (2002).
5. M. Takahata, M. Nakano, and K. Yamaguchi, *Synthetic Metals*, in press.

This page is intentionally left blank

International Journal of Nanoscience, Vol. 1, Nos. 5 & 6 (2002) 719–723

MICROSTRUCTURE AND RESISTIVITY OF CARBON NANOTUBE AND NANOFIBER/EPOXY MATRIX NANOCOMPOSITE

JIN-HONG DU, ZHE YING, SHUO BAI, FENG LI, CHAO SUN, and HUI-MING CHENG*

Shenyang National Laboratory for Materials Science
Institute of Metal Research, Chinese Academy of Sciences
72 Wenhua Road, Shenyang 110016, China
**cheng@imr.ac.cn*

Received 27 November 2002

Single-walled carbon nanotubes (SWNTs), multiwalled carbon nanotubes (MWNTs) and vapor-grown carbon nanofibers (VGCNFs)/epoxy matrix nanocomposites were prepared, respectively. The microstructure of the nanocomposites was observed by SEM and the resistivities of the nanocomposites with different concentration of CNTs/VGCNFs were measured. Based on the experimental results, the dispersion of SWNTs and MWNTs were relatively poor but that of VGCNFs is uniform within the matrix. The resistivitiy of pure epoxy is about $10^{10.5}\ \Omega \cdot$ cm and several orders of magnitude higher than those of SWNT, MWNT and VGCNF/epoxy nanocomposites. The resistivities of the nanocomposites drop with the increase of the CNTs/VGCNFs content in the matrix and the resistivity of VGCNFs/epoxy nanocomposites was much lower than that of CNT/epoxy nanocomposites.

Keywords: Carbon nanocomposite; resistivity.

1. Introduction

Much interest has been paid to producing polymer composites using carbon nanotubes and nanofibers as fillers. Such nanocomposites would presumably exhibit superior performance owing to the high strength, high aspect ratio, high flexibility, high electrical conductivity, and other special functional properties of nanotubes and nanofibers. In particular, the high electric conductivity of carbon nanotube and nanofiber, combined with their low density, will enlarge their application in industrial and commercial fields. For example, they can be used as electronics, electromagnetic interface (EMI) shielding and microwave absorption, and electrostatic discharge materials. However, the key problem, dispersion of carbon nanotubes and nanofibers in polymer matrix and its influence on the resistivity, must be studied and solved before they can be practically used.

*Corresponding author.

In this study, we prepared the nanocomposites by embedding single-walled carbon nanotubes (SWNTs), multiwalled carbon nanotubes (MWNTs) and vapor-grown carbon nanofibers (VGCNFs) in an epoxy matrix, respectively. The dispersion of CNTs and VGCNFs in the epoxy matrix and its effect on the resistivity of the nanocomposites were studied.

2. Experimental

In the experiments, the SWNTs were synthesized by the hydrogen arc discharge method.[1] The MWNTs with a diameter of about 50 nm and VGCNFs with a diameter of about 100 nm were obtained at 1423–1473 K in the presence of sulfur by the floating catalyst method using benzene as the carbon source.[2,3] The as-prepared CNTs and VGCNFs are film-like and foam-like black block, respectively, in which the CNTs and VGCNFs are tangled with one another. Therefore, the as-prepared products must be broken up firstly so that they can be easily and uniformly embedded in the matrix. Secondly the products were mixed with epoxy (WSR618) and polyamide, which was used as curing agent, and then the mixture was continuously agitated for 30 min for the good distribution of CNTs/VGCNFs in the matrix. Lastly, the mixture was molded in a mold and then hardened in a vacuum oven at 60°C for 6 h to obtain a composite specimen. The fracture surface morphologies of the SWNT, MWNT, and VGCNF/epoxy composites were observed by scanning electron microscopy (SEM) and their resistivities were measured by the four-point method. The size of the specimens is 40 mm × 5 mm × 1 mm for measurements of their resistivity.

3. Results and Discussion

From Fig. 1(a), it can be seen that the SWNT product is composed of many SWNTs bundles, and the bundles are interlaced with each other to form a web. Figures 1(b) and 1(c) show that the as-prepared MWNTs and VGCNFs are relatively straight and they simply overlapped with each other. The diameter distribution of the nanotubes and nanofibers is in a small range but their purity is very high.

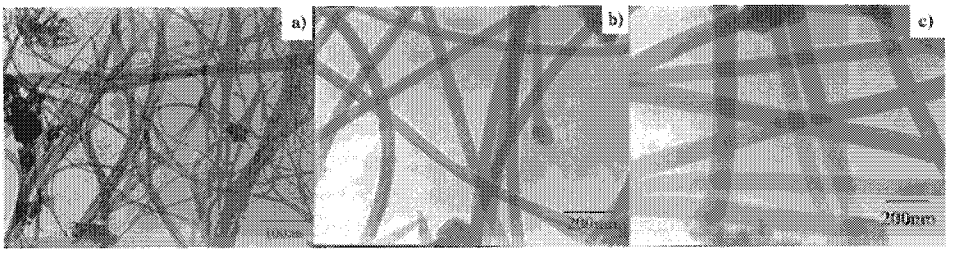

Fig. 1. TEM images of (a) SWNTs, (b) MWNTs with an average diameter of about 50 nm and (c) VGCNFs with an average diameter of about 100 nm.

Figure 2 shows the fracture surface of the SWNT/epoxy nanocomposites. It can be seen that the SWNTs are not well distributed in the matrix. There are few SWNTs in some regions, while large amounts of SWNTs aggregate in some other region within the matrix. Figure 3 shows that the dispersion of MWNTs in the matrix is better than that of SWNTs, but some MWNTs also aggregate in some region and become web-like. On the other hand, VGCNFs can be separated from each other and well distributed within the epoxy matrix (Fig. 4). These results indicate that it is much more difficult for CNTs with smaller diameter to be separated and dispersed uniformly in the matrix than for the VGCNFs with larger diameter.

In general, in the preparation of the CNT and VGCNF/epoxy nanocomposites, respectively, several factors that will influence the dispersion of the CNTs/VGCNFs in the epoxy matrix have to be considered.[4,5] The CNTs/VGCNFs tangled with one another during space growth process, and the attraction between CNTs/VGCNFs by van der Waals force also tends to make them aggregate. These factors prevent the CNTs/VGCNFs dispersed well in the epoxy. On the other hand, the mechanical stirring will force the dispersion of the CNTs and VGCNFs in the epoxy through the adhesive action between the CNTs/VGCNFs and epoxy, and

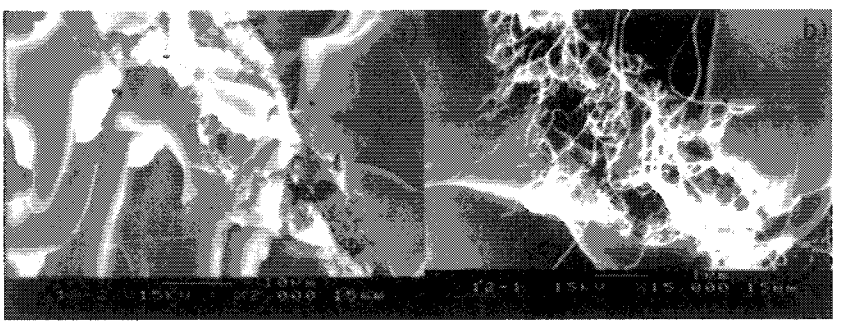

Fig. 2. Fracture surface SEM images of SWNT/epoxy nanocomposites: (a) low resolution and (b) high resolution.

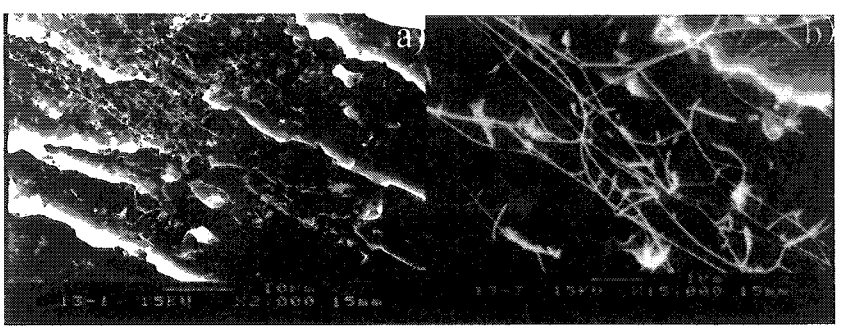

Fig. 3. Fracture surface SEM images of MWNT/epoxy nanocomposites: (a) low resolution and (b) high resolution.

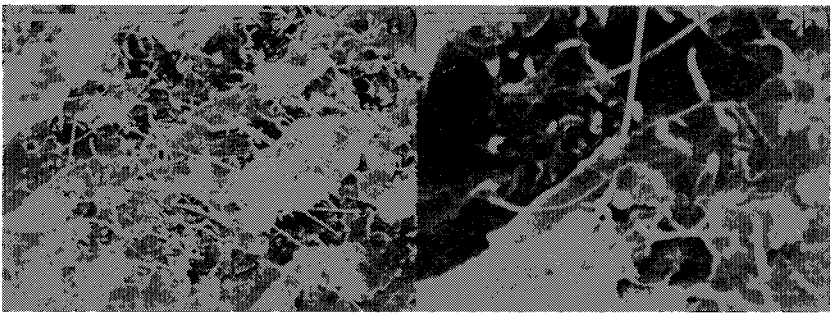

Fig. 4. Fracture surface SEM images of VGCNF/epoxy nanocomposites: (a) low resolution and (b) high resolution.

the adhesive force will keep the CNTs/VGCNFs from aggregating with one another again during the curing of the nanocomposite. According to the observation results of TEM and the theoretical estimate, we can find that the smaller the diameter of the CNTs and VGCNFs, the stronger the attractive force between the CNTs/VGCNFs.[4,5] Moreover, the surface area and microstructure defects on the surface of a single CNT or VGCNF will increase with the increasing in the diameter of CNTs/VGCNFs, which will make the adhesive force between CNT/VGCNF and matrix increase. Therefore, separation of VGCNFs from each other by the same external force through mechanical stirring is easier and have less chance to aggregate again during the curing of their composite than that of SWNTs and MWNTs, so that VGCNF/epoxy nanocomposite can be relatively more uniformly dispersed than CNT/epoxy nanocomposites.

The logarithmic electric resistivity of SWNT, MWNT and VGCNF/epoxy nanocomposites with different CNTs/VGCNFs concentrations is shown in Fig. 5. It shows that the resistivitiy of pure epoxy is quite high at about $10^{10.5}\,\Omega \cdot \mathrm{cm}$ and is several orders of magnitude higher in comparison with those of CNT and VGCNF/epoxy nanocomposites. The resistivities of nanocomposites sharply drop with the increase of the CNTs/VGCNFs concentration in the matrix. This is because a conductive path throughout the epoxy matrix can be provided by CNTs/VGCNFs, which can form a three-dimensional conducting network due to their high electric conductivity and aspect ratio.[6] Moreover, the increase of CNTs/VGCNFs concentration can enhance the connection among CNTs/VGCNFs so that the resistivity will decrease with the increase of CNTs/VGCNFs concentration in the matrix. However, it can be found that SWNT/epoxy nanocomposite has the highest resistivity and VGCNF/epoxy nanocomposite has the lowest resistivity in three kinds of nanocomposites with the same concentration, even though SWNTs have the highest theoretical conductivity and aspect ratio. The resistivity of VGCNF/epoxy nanocomposite can drop to about 200 $\Omega \cdot \mathrm{cm}$ at 2.8 wt%, whereas that of SWNT/epoxy nanocomposite to 7000 $\Omega \cdot \mathrm{cm}$ at 10.3 wt%. It is possibly due to the uniform dispersion of VGCNFs and well-distributed conducting

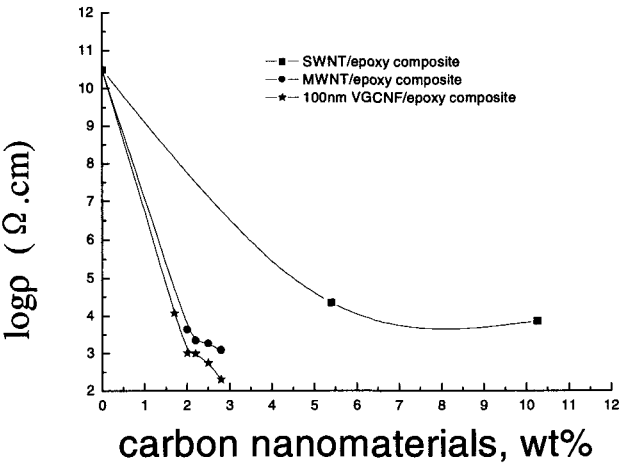

Fig. 5. Logarithmic resistivity of SWNT, MWNT and VGCNF/epoxy nanocomposites at different CNTs/VGCNFs concentrations.

electric web formed in the matrix comparing with the SWNTs and MWNTs. The results indicate that the dispersion of CNTs and VGCNFs in the matrix is one of the most important factors influencing the resistivity of CNT and VGCNF/epoxy nanocomposite.

4. Conclusion

The dispersion of VGCNFs in the epoxy matrix is relatively uniform while it is relatively poor in the SWNTs and MWNTs. The resistivities of CNT and CNF/epoxy nanocomposites decrease with the increase of the CNTs/VGCNFs concentration in the matrix and the resistivity of VGCNF/epoxy nanocomposites is much lower than that of the SWNT/epoxy nanocomposites. The experimental results indicate that the dispersion of the CNTs and VGCNFs in the epoxy matrix is one of the most important factors influencing the resistivity of nanocomposites.

Acknowledgments

This work was supported by the National Natural Science Foundation of China (Nos. 50025204 and 50102007) and by Chinese Academy of Sciences.

References

1. C. Liu *et al.*, *Carbon* **37**, 1865 (1999).
2. Y. Y. Fan *et al.*, *Carbon* **38**, 789 (2000).
3. Y. Y. Fan *et al.*, *J. Mater. Res.* **13**, 2342 (1998).
4. V. Lordo and N. Yao, *J. Mater. Res.* **15**, 2770 (2000).
5. R. Schueler *et al.*, *J. Appl. Polymer Sci.* **63**, 1741 (1997).
6. J. Sandler *et al.*, *Polymer* **40**, 5967 (1999).

This page is intentionally left blank

International Journal of Nanoscience, Vol. 1, Nos. 5 & 6 (2002) 725–730

REAL-TIME VISUALIZATION OF MORPHOLOGICAL EVOLUTION OF N, N'-di(naphthalene-1-yl)-N, N'-diphthalbenzidine THIN FILMS: VARIABLE TEMPERATURE ATOMIC FORCE MICROSCOPY STUDY

M. S. XU*, J. B. XU†, and J. AN

Department of Electronic Engineering
The Chinese University of Hong Kong, Shatin, NT, Hong Kong
**msxu@ee.cuhk.edu.hk*
†jbxu@ee.cuhk.edu.hk

Received 27 November 2002
Revised 26 December 2002

Variable temperature tapping mode atomic force microscopy is exploited to *in situ* visualize the morphological evolution of N, N'-di(naphthalene-1-yl)-N, N'-diphthalbenzidine (NPB) thin film. The *apparent glass* transition of the NPB thin film initially occurred at 60°C, proceeded until 95°C, and crystallization from the glassy state quickly appeared at 135°C. The NPB thin film gradually melted and disappeared when the temperature was above 175°C, revealing the underlying layer. These observations are technically helpful and significant to gauge the temperature dependent lifetime and luminance of organic light-emitting diodes.

Keywords: Variable temperature atomic force microscopy; morphological change; NPB.

1. Introduction

Organic light-emitting diodes (OLEDs) have great potential applications to hand-held electronics and large-area flat panel display.[1–3] Thermal stability of OLEDs has been improved by adopting high glass transition temperature (T_g) hole transport materials,[4–6] and a few investigations of the temperature-dependent luminance were carried out.[5–9] However, the relationship between luminance and temperature or the Joule heating remains unclear.[2,6–13] Furthermore, there is no detailed investigation of the morphological change or phase transition due to the Joule heating and there is no report on the thermally-activated degradation pathways of OLEDs though Han *et al.* observed crystallization of N, N''-diphenyl-N,N''-bis(3-methylphenyl)-1,1′-biphenyl-4,4′-diamine (TPD) stored in air at room temperature or elevated temperature by using atomic force microscopy (AFM).[14,15] It is known, by the replacement of TPD with T_g of 60°C,[5] N, N'-di(naphthalene-1-yl)-N, N'-diphthalbenzidine (NPB) with T_g of around 95°C,[6,16] as a hole transport

†Corresponding author.

material in OLEDs, shows better device performance. Therefore, *in situ* study on the temperature-induced phase transition or morphological evolution of the thin films is of technological significance in understanding the Joule heating effect on the operation of OLEDs. The development of variable temperature tapping mode atomic force microscopy (VT-AFM) makes it possible to visualize the thermally-activated morphological change in nanoscale level.[17] To use this technique, the tip temperature can be extremely important in the organic phase transition because the organic film at elevated temperature can act as a contamination source of the tip and would cause significant variation of the phase transition conditions and formation of artificial morphological features if there is no tip temperature control during imaging.

In this article, the phase transition or morphological evolution of NPB (from Kodak) thin films will be sifted by exploiting VT-AFM (Digital Instruments). The initial morphological alteration of NPB thin films occurred at ~60°C, proceeded until 95°C, and crystallization suddenly took place at 135°C.

2. Experiments

The intended NPB thin films were placed on the indium tin oxide (ITO)/copper phthalocyanine (CuPc) (Aldrich) underlying layer, which is commonly used as anode/hole injection layer/hole transport layer configuration in OLEDs. The ITO substrate was cleaned according to an appropriated procedure involving ultrasonication in acetone, ethanol and deionized water, and then treated by using UV-ozone. The organic thin films purified by gradient sublimation were deposited on the substrate remained at room temperature, under a base pressure of 1×10^{-6} Torr. During the deposition of the different organic layers, the underlying layers were shortly exposed to ambient less than 2 min in order to change the source materials. The thicknesses of the CuPc and NPB layers were about 11 and 40 nm with the growth rates of around 0.2 and 1.0 Å/s, respectively. During the VT-AFM experiments, the temperature variation would cause a shift of the AFM tip position with respect to the surface region of interest because of thermal expansion and/or contraction. Also, temperature changes lead to a shift of the resonant frequency of the Si cantilever, making it necessary to retune the driving frequency.

3. Results and Discussion

Typical VT-AFM images in Fig. 1 demonstrate the morphological evolution of the NPB thin film on the ITO/CuPc underlying layer from 25 to 125°C. These images were acquired in the same area if the thermal drift were neglected. At room temperature, the fresh film exhibits ripple-like morphological feature (see Fig. 1(a)). Morphological change can be more closely examined when the temperature was up to 60°C (see Fig. 1(b)), and obviously, the evolution was almost completed at 95°C (see Fig. 1(d)), and such scenario remained stagnant as the temperature was up to 125°C as shown in Fig. 1(e). The morphology is very smooth and flat. Note that

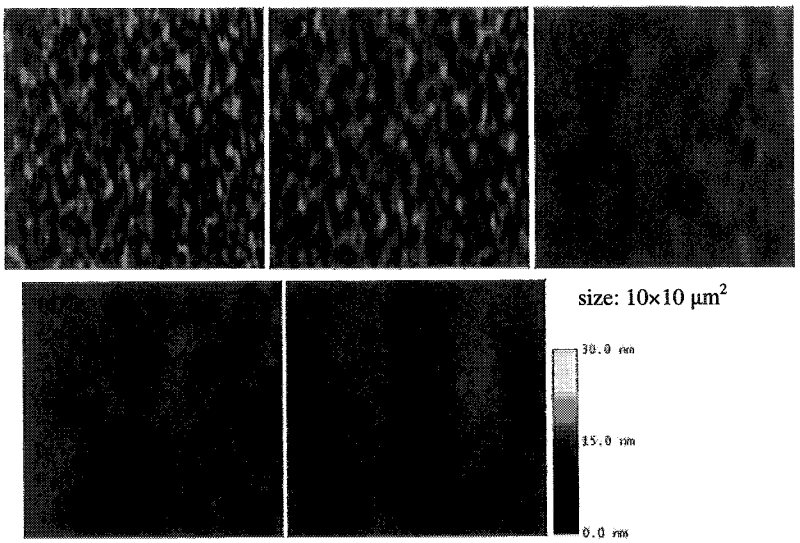

Fig. 1. VT-AFM images of the NPB thin film on the ITO/CuPc underlying layer to exhibit the apparent glass transition acquired at (a) 25°C, (b) 60°C, (c) 90°C, (d) 95°C, and (e) 125°C.

the present morphological evolution is very similar to the characteristics of glass transition that is typically a second-order transition, and generally occurs over a sizable temperature range rather than in an abrupt alteration.

To the best of our knowledge, this is the first real-time observation of the morphological variation of the NPB film at elevated temperatures. Since the dependence of the morphological variation on temperature shows the similar behavior in the glass transition of NPB, we believe that the morphological change is associated with the glass transition. It is generally reported that the T_g of NPB is around 95°C.[6,16] The observed morphological change, however, initially occurred at 60°C and progressed until 95°C. This observation is in reasonable agreement with the fact that a glass transition is a relaxation of certain physical parameters. The reported glass transition temperature of the organic materials in OLEDs is generally measured by differential scanning calorimetry (DSC).[12,18] The use of this technique to determine a reasonable T_g is not trivial. But usually the middle of the incline of the DSC signal versus temperature is assumed to be T_g.[18] In the present study, the middle of the morphological evolution versus temperature (60–125°C) is ~95°C, very identical to the reported T_g of NPB.[6] Other related techniques are also employed to ascertain T_g of polymer materials.[19,20] However, the acquired results are relatively controversial.[19,20] Also, it is found, by comparing to the bulk phase, that the polymer thin films exhibit a much lower T_g and are more dependent on thickness.[20] Therefore, it is sensible to define ~60°C as the *apparent* glass transition temperature (T_g^*). In contrast to the other techniques, the present VT-AFM technique can easily illustrate how and at which temperature the apparent glass transition occurs on a submicron scale.

As demonstrated in Fig. 2(a), a sudden change of the NPB morphology took place as the temperature had been raised for only 13 min at 135°C, whereas the glassy state on the whole remains more than 150 min from 95 to 125°C. As the temperature further increased, the crystalline NPB structures became melting and liquate (Fig. 2(b)), and the underlying surface is gradually discerned. This appeared surface is the top surface of ITO/CuPc underlying layer, because the features of the surface is exactly the same as that observed on the temperature-induced morphological change of the CuPc thin film on ITO substrate (not shown here). Above 185°C, the NPB structures gradually became gas species to evaporate or decompose and eventually disappeared (Fig. 3(a)). The ITO/CuPc underlying layer is almost completely seen, as shown in a zoom-in image (Fig. 3(b)). The cross-section profiles along line "1" in Fig. 2(a) and line "2" in Fig. 3(a) are depicted in Figs. 4(a) and 4(b), respectively. The height of the crystalline NPB structures with respect to the appeared surface is almost 100 nm. This uneven surface would cause the OLEDs failure due to the local electrical inhomogeneity in OLEDs.[2]

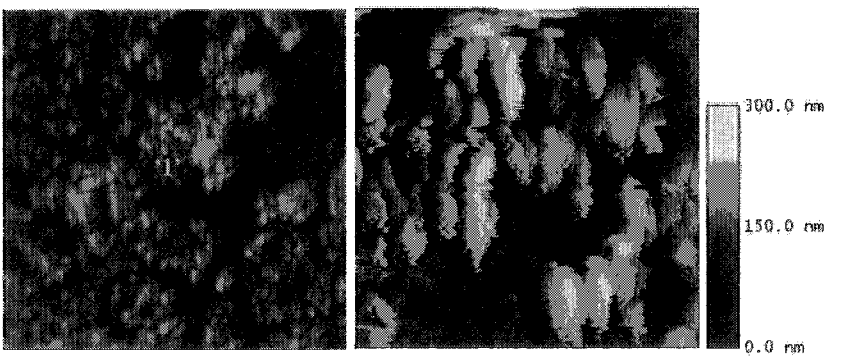

Fig. 2. Morphological evolution of the NPB thin film on ITO/CuPc underlying layer. (a) 135°C (10×10 μm^2) and (b) 175°C (5×5 μm^2).

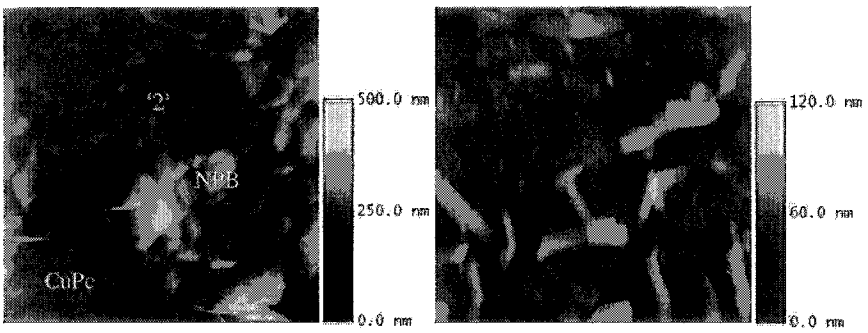

Fig. 3. (a) VT-AFM image of the top surface of ITO/CuPc/NPB structure acquired at 185°C (5×5 μm^2) along with (b) a zoom-in image of the appeared surface (2×2 μm^2).

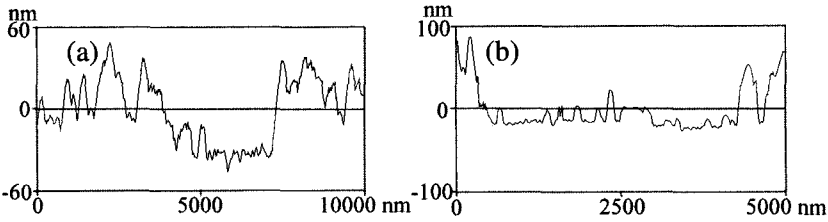

Fig. 4. AFM cross-section profiles along with (a) line "1" in Fig. 2(a) and (b) line "2" in Fig. 3(a).

4. Conclusions

In summary, the temperature-induced apparent phase transition of the NPB thin films on the ITO/CuPc underlying layer has been studied by using VT-AFM in detail. The *apparent glass* transition of the NPB thin films initially occurred at 60°C and finished at about 95°C, and crystallization from the glassy state quickly appeared at 135°C. The NPB thin films gradually melted at 175°C, and disappeared when the temperature was above 185°C, completely revealing the ITO/CuPc underlying layer. These findings are technically helpful and significant to gauge the temperature-dependent lifetime and luminance reduction of OLEDs. Furthermore, variable-temperature tapping mode atomic force microscopy has proved to be a powerful technique to study the temperature-induced phase transition or morphological evolution of organic/polymer films.

Acknowledgment

This work is partly funded by the Research Grant Council of Hong Kong, particularly, via Grant No. CUHK 4372/02E.

References

1. C. W. Tang and S. A. VanSlyke, *Appl. Phys. Lett.* **51**, 913 (1987).
2. J. R. Sheats, H. Antoniadis, and M. Hueschen, *Science* **273**, 884 (1996).
3. http://www.universaldisplay.com.
4. S. Tokito, H. Tanaka, K. Noda, A. Okada, and Y. Taga, *Appl. Phys. Lett.* **70**, 1929 (1997).
5. X. Zhou, J. He, L. S. Liao, M. Lu, X. M. Ding, X. Y. Hou, X. M. Zhang, X. Q. He, and S. T. Lee, *Adv. Mater.* **12**, 265 (2000).
6. D. F. O'Brien, P. E. Burrows, S. R. Forrest, B. E. Koene, D. E. Loy, and M. E. Thompson, *Adv. Mater.* **10**, 1108 (1998).
7. M. Ishii and Y. Taga, *Appl. Phys. Lett.* **80**, 3430 (2000).
8. I. D. Parker, Y. Cao, and C. Y. Yang, *J. Appl. Phys.* **85**, 2441 (1999).
9. H. Aziz, Z. D. Popovic, and N. X. Hu, *Appl. Phys. Lett.* **81**, 370 (2002).
10. J. R. Sheats and D. B. Roitman, *Synth. Met.* **95**, 79 (1998).
11. D. E. Loy, B. E. Koene, and M. E. Thompson, *Adv. Funct. Mater.* **12**, 245 (2002).
12. M. Ishii and Y. Taga, *Appl. Phys. Lett.* **80**, 3430 (2002).
13. V. Choong, J. Shen, J. Curless, S. Shi, J. Yang, and F. So, *J. Phys. D: Appl. Phys.* **33**, 760 (2002).

14. E. M. Han, L. M. Do, Y. Niidome, and M. Fujihira, *Chem. Lett.* **5**, 969 (1994).
15. E. M. Han, L. M. Do, N. Yamamoto, and M. Fujihira, *Thin Solid Films* **273**, 202 (1996).
16. S. A. VanSlyke, C. H. Chen, and C. W. Tang, *Appl. Phys. Lett.* **69**, 2160 (1996).
17. D. A. Ivanov, Z. Amalou, and S. N. Magonov, *Macromolecules* **34**, 8944 (2001).
18. http://www.psrc.usm.edu/macrog/dsc.htm.
19. R. M. Overney, C. Buenviaje, R. Luginbuhl, and F. Dinelli, *J. Therm. Anal. Cal.* **59**, 206 (2000).
20. H. Fischer, *Macromolecules* **35**, 3592 (2002).

International Journal of Nanoscience, Vol. 1, Nos. 5 & 6 (2002) 731–735

NANOSCALE FRICTION AND RELATED TRIBOLOGICAL PHENOMENA AT SOLID INTERFACES

TAKAAKI KAWAGUCHI

Department of Technology, Faculty of Education, Shimane University
1060 Nishikawatsu, Matsue 690-8504, Japan

HIROSHI MATSUKAWA

Department of Physics, Osaka University
1-1 Machikaneyama, Toyonaka 560-0043, Japan

Received 27 November 2002

Nanoscale friction and related tribological phenomena are studied by a numerical simulation. It is found that the kinetic friction is caused by some resonating phonon excitations. The contribution from the surfaces and lubricant to the kinetic friction is clarified.

Keywords: Friction; tribology; solid interfaces.

1. Introduction and Model of Friction

Nanoscale tribological phenomena at solid interfaces have been attracting much attention in several fields concerning nanotechnology.[1] In nanoscale tribology, interfacial friction at nanoscale plays essentially important roles. In this study, to understand the nanoscale tribology, we investigate nanoscale friction and related phenomena using a numerical simulation based on an atomic lattice model, which is an extended one of previous studies.[2–7] We discuss some peculiar features of the model at solid interfaces on the nanoscale.

We consider here a simple one-dimensional model that describes a nanoscale interface. It consists of two solids and lubricant. As shown in Fig. 1, for each solid, the bulk and surface parts are expressed by a rigid plate and an elastic atomic layer, respectively.

We explain in brief parameters used in the present model. The layers A, B and C have N_a, N_b and N_c atoms, respectively. The neighbor atoms in layers A, B and C are interacting via a harmonic spring with the elastic strengths K_a, K_b and K_c, respectively. The top (bottom) plate and the atoms in layer A (C) are interacting via a harmonic spring with the elastic strength K_{sa} (K_{sb}). The mean atomic spacing in layers A, B and C are denoted by c_a, c_b and c_c, respectively. The atoms between layers A and B (B and C) are interacting with an interlayer atomic

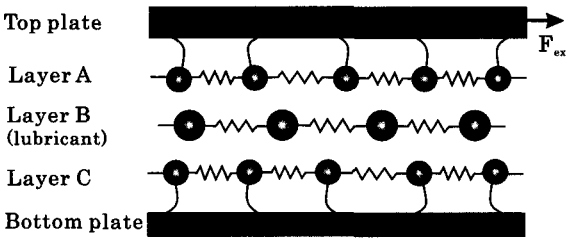

Fig. 1. Schematic illustration of solid interface with a lubricant layer.

force F_{Iab} (F_{Ibc}). The top plate is driven by an external force F_{ex}, and the bottom one is fixed.

The equations of motion of the model are expressed as follows: for the top plate

$$M\ddot{U} = F_{ex} - K_{sa}\sum_{i\in a}^{N_a}(U + ic_a - u_a^i)\,, \tag{1}$$

for the layer A

$$m_a\ddot{u}_a^i + \gamma_{ab}(\dot{u}_a^i - \langle\dot{u}_b^i\rangle_i) = K_a(u_a^{i+1} + u_a^{i-1} - 2u_a^i) - K_{sa}(u_a^i - ic_a - U) + \sum_{j\in b}^{N_b} F_{Iab}(u_a^i - u_b^j)\,, \tag{2}$$

for the layer B

$$m_b\ddot{u}_b^i + \gamma_{ab}(\dot{u}_b^i - \langle\dot{u}_a^i\rangle_i) + \gamma_{bc}(\dot{u}_b^i - \langle\dot{u}_c^i\rangle_i) = K_b(u_b^{i+1} + u_b^{i-1} - 2u_b^i) + \sum_{j\in a}^{N_a} F_{Iab}(u_b^i - u_a^j) + \sum_{j\in c}^{N_c} F_{Ibc}(u_b^i - u_c^j)\,, \tag{3}$$

and for the layer C

$$m_c\ddot{u}_c^i + \gamma_{bc}(\dot{u}_c^i - \langle\dot{u}_b^i\rangle_i) = K_c(u_c^{i+1} + u_c^{i-1} - 2u_c^i) - K_{sc}(u_c^i - ic_c) + \sum_{j\in b} F_{Ibc}(u_c^i - u_b^j)\,, \tag{4}$$

where M is the mass, U the position of the top plate, $u_{a,b,c}^i$ the position of the ith atom, $m_{a,b,c}$ the atomic mass in the corresponding layer, and $\gamma_{ab,bc}$ the damping parameter due to energy dissipation between neighboring two layers. We adopt here a Gaussian interlayer potential: $U_I = (K_I/2)\exp(-4x^2)$, where K_I is the potential strength. Then, the interlayer force is given by $F_{Iab} = F_{Ibc} = \underline{-dU_I/dx}$. The frictional force per atom of layer A, F, is given by $F = F_{ex}/N_a - \gamma_{ab}(\langle\dot{u}_a^i\rangle_i - \langle\dot{u}_b^i\rangle_i)$, where a viscous term is subtracted.

In this study we consider an incommensurate system because most sets of two solid surfaces become incommensurate. In numerical simulations, under periodic

boundary conditions, we set the values of model parameters as follows: $N_b = 55$, $N_a = N_c = 89$, $c_a = c_c = 1$, $c_b = 89/55 = 1.618\ldots$, $M = 89$, $m_a = m_b = m_c = 1$, $\gamma_{ab} = \gamma_{bc} = 0.7$, and $K_a = K_b = K_c = K_{sa} = K_{sc} = 1$. Only K_I is varied. Numerical simulations based on Eqs. (1)–(4) are performed using a fourth-order Runge–Kutta formula.

2. Kinetic Frictional Forces and Phonon Excitations

First, we consider the kinetic frictional force working on the top plate and calculate its dependence on the sliding velocity. In Fig. 2, the kinetic frictional forces for $K_I = 0.2$ and 0.5 are plotted against the velocity difference between layers A and B, where the time-averaged velocities of layers A and B are denoted by V_a and V_b, respectively.

The kinetic frictional force curve shows a smooth peak structure for $K_I = 0.2$. For $K_I = 0.5$, however, the largest peak becomes discontinuous and has a large gap and noisy peaks appear in a high velocity regime. The gap structure means the occurrence of dynamical instability in the lubrication at the corresponding velocity regimes because the velocity–kinetic frictional force characteristic has a negative slope in the gap regime. Using a perturbation theory of kinetic frictional force,[5,8] the appearance of the peak structure is understood as a phonon excitation effect due to superharmonic resonance. The condition on the resonance peaks in Fig. 2 is given by

$$n\frac{2\pi}{c_b}V_{dif} = \Omega\left(n\frac{2\pi}{c_b}\right), \tag{5}$$

where n is an integer ($\geq$1), V_{dif} the velocity difference between layers A and B (or between layers B and C), and $\Omega(q)$ the phonon frequency of layer A (or C). The velocity at which the largest peak appears in Fig. 2 corresponds to V_{dif} with $n = 1$. Another phonon process is parametric resonance, which corresponds to multi-phonon processes. For two-phonon processes, the resonance condition is given

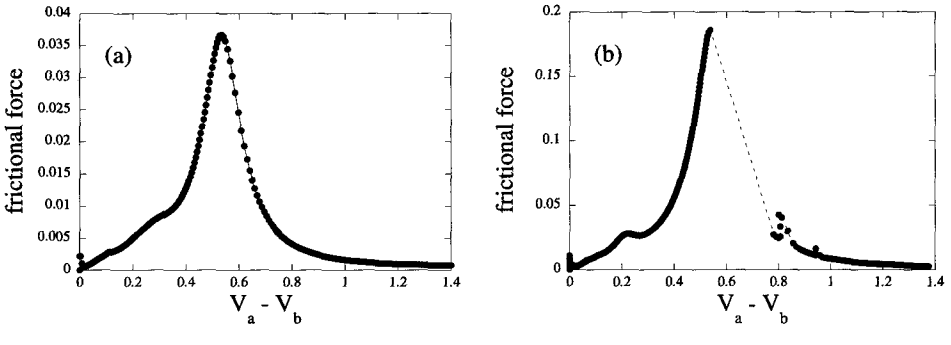

Fig. 2. Kinetic frictional force versus velocity difference $V_a - V_b$. (a) $K_I = 0.2$ and (b) $K_I = 0.5$.

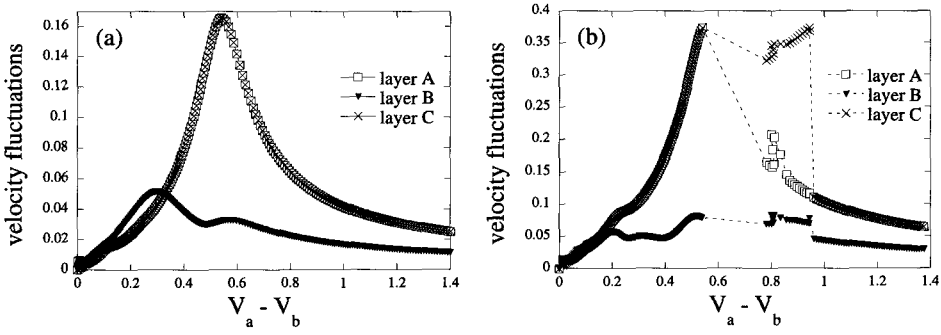

Fig. 3. Velocity fluctuations in layers A, B and C. (a) $K_I = 0.2$ and (b) $K_I = 0.5$.

by

$$n\frac{2\pi}{c_b}V_{dif} = \Omega(k) + \Omega\left(n\frac{2\pi}{c_b} - k\right). \tag{6}$$

The noisy peaks in Fig. 2(b) are caused by this parametric resonance with $n = 1$. Note here that, in the present system, the dominant contributions to the kinetic friction come from the phonons in layers A and C. The contribution from layer B is rather weak.

To clarify this point further and see the role of each layer in the resonances, we calculate the velocity fluctuations which are given by

$$\delta\dot{u}_{a,b,c} = \sqrt{\overline{\langle(\dot{u}^i_{a,b,c})^2\rangle_i} - \overline{\langle\dot{u}^i_{a,b,c}\rangle_i^2}}\,. \tag{7}$$

The velocity fluctuations reflect the strengths of energy dissipations, i.e., contributions to kinetic friction. In Fig. 3, $\delta\dot{u}_a$, $\delta\dot{u}_b$ and $\delta\dot{u}_c$ are plotted against the velocity difference $V_a - V_b$ for $K_I = 0.2$ and 0.5. For $K_I = 0.2$, both the fluctuations in layers A and C are equivalent in strength, and the fluctuations in layer B make only small contribution in the whole velocity regime. For $K_I = 0.5$, in the parametric resonance regime, the fluctuation in layer C is significantly strengthened. This means that the parametric resonance occurs dominantly in layer C.

3. Conclusions

Using a three-layer model which describes surfaces of two solids and lubricants at the nanoscale, we have found that the kinetic frictional forces show both superharmonic and parametric resonance behaviors in the sliding velocity dependence under certain conditions on the interlayer interaction.

In previous studies,[6,7] it was found that, when the surfaces of solids are rigid and therefore do not excite phonons, lubricants have dominant contribution to kinetic friction. When surfaces are also elastic, as shown in the present study, it is possible that phonons excited in surfaces make dominant contributions to the kinetic friction.

Acknowledgments

This work was financially supported by the Kinki-chihou Hatsumei Center and Grants-in-Aid for Scientific Research of the Ministry of Education, Culture, Sports, Science and Technology.

References

1. B. N. J. Persson and E. Tosatti (eds.), *Physics of Sliding Friction* (Kluwer Academic Publishers, Dordrecht, 1996); B. N. J. Persson, *Sliding Friction* (Springer, Berlin, 1998).
2. H. Matsukawa and H. Fukuyama, *Phys. Rev. B* **49**, 17286 (1994).
3. H. Matsukawa and H. Fukuyama, *Physics of Sliding Friction* (Ref. 1), p. 139.
4. T. Kawaguchi and H. Matsukawa, *Phys. Rev. B* **56**, 4261 (1997); *ibid. B* **58**, 15866 (1998); *ibid. B* **61**, R16366 (2000).
5. T. Kawaguchi and H. Matsukawa, *Phys. Rev. B* **56**, 13932 (1997).
6. T. Kawaguchi and H. Matsukawa, *Surf. Rev. Lett.* **8**, 447 (2001).
7. T. Kawaguchi and H. Matsukawa, *Mol. Phys.* **100**, 3161 (2002).
8. T. Strunz and F. J. Elmer, *Physics of Sliding Friction* (Ref. 1), p. 149; M. Weiss and F. J. Elmer, *ibid.*, p. 163.

This page is intentionally left blank

International Journal of Nanoscience, Vol. 1, Nos. 5 & 6 (2002) 737–741

AC ELECTRIC-FIELD-INDUCED ORIENTATION OF POLAR ORGANIC NANOCRYSTAL IN DISPERSE SYSTEM

T. ONODERA, M. YOSHIDA, S. OKAZOE, S. FUJITA, H. KASAI, S. OKADA, H. OIKAWA*, and H. NAKANISHI†

Institute of Multidisciplinary Research for Advanced Materials
Tohoku University, 2-1-1 Katahira, Aoba-ku, Sendai, 980-8577 Japan
**Nanomaterials Laboratory, National Institute for Materials Science*
1-2-1 Sengen, Tsukuba, Ibaraki, 305-0047 Japan
†*hnakanis@tagen.tohoku.ac.jp*

Received 27 November 2002

Monodispersed DAST nanocrystals have almost been successfully fabricated by means of the inverse reprecipitation method. By employing AC electric field, high electric field of above ca. 1.0 $kVcm^{-1}$ could be applied to polar DAST nanocrystals dispersed in decahydronaphthalene, so as to avoid electrophoresis of nanocrystals under DC electric field. The response of DAST nanocrystal dispersion to applied AC electric field was analyzed phenomenologically by fitting Langevin function, which provided a large permanent dipole moment of DAST nanocrystal. In addition, we have succeeded in *in situ* observation of AC electric-field-induced orientational motion of DAST crystals by using an optical microscope. The present DAST nanocrystal dispersion system will be expected as an optical device like display monitor.

Keywords: DAST; nanocrystal; inverse reprecipitation method; electric-field-induced orientation; dipole moment.

1. Introduction

An alignment of nanoparticles induced by external fields such as electric, magnetic and flow field is a key technology in novel optical and electronic devices. If nanocrystals dispersed in liquid could respond sensitively to applied external fields, the dispersion system would be easily converted from a random phase to an anisotropic phase, which might lead to the changes of optical properties such as transmittance and refractive index. We have already established the reprecipitation method for fabrication of organic nanocrystals.[1] The most striking characteristic of this method is that organic nanocrystals are obtained as a dispersed state. In fact, we have successfully prepared nanocrystals of 4′-dimethylamino-*N*-methylstilbazolium *p*-toluenesulfonate (DAST) in disperse state, and observed the reversible absorbance changes based upon the orientation of DAST nanocrystals

†Corresponding author.

induced by applying DC electric field under 300 Vcm^{-1}.[2] In the present study, AC electric-field-induced orientation of DAST nanocrystals dispersed in liquid will be discussed to overcome electrophoresis problem in the case of DC electric field.

2. Experiment

DAST used in the present research was synthesized as described in the literature.[3] By the inverse reprecipitation method,[2] DAST nanocrystals were fabricated as follows: 100 μl of DAST-ethanol solution (5 mM) was injected into 10 ml of vigorously stirred decahydronaphthalene, and then retained for 1 h at room temperature. *N*-dodecyltrimethylammonium chloride (DTMAC) was previously added as a disperse stabilizer into DAST-ethanol solution. All procedures were performed in dry air.

Scanning electron microscopy (SEM; JEOL, JSM-6700F) and dynamic light scattering (DLS; Ootsuka Electronic Co., DLS-7000) measurements have been carried out to determine the crystal size and shape. Before SEM observation, gold was sputtered onto filtrated DAST nanocrystals. In addition, the absorbance at the absorption maximum wavelength (λ_{max} = 555 nm) in DAST nanocrystal dispersion has been monitored by using UV-vis spectrometer (JASCO, V-550DS). The paired ITO electrodes were equipped with quartz cell (cell length = 10 mm), and were connected with variable high-voltaged power supply (Towa Instrumentation Co., AKT-015KP).

3. Results and Discussions

3.1. *SHG-active DAST nanocrystals*

DAST nanocrystal was a rectangular plate as shown in Fig. 1. The average crystal size was about 500 nm, was almost equal to that evaluated by DLS measurement. In addition, the resulting DAST nanocrystals were confirmed to be SHG-active both by the powder test and powder X-ray diffraction perttern,[4] which implied that

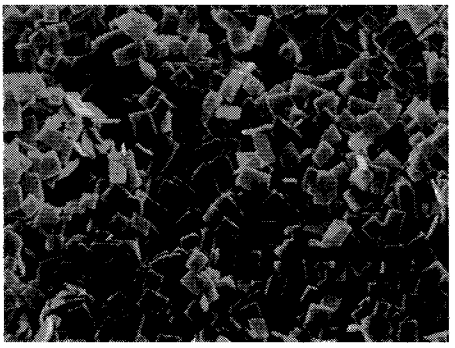

Fig. 1. SEM image of DAST nanocrystals.

DAST nanocrystal took noncentrosymmeric crystal structure having permanent dipole moment.

3.2. *AC electric-field-induced orientation of DAST nanocrystals in dispersion*

When the absorbance changes induced by applying electric field to DAST nanocrystals in dispersion were monitored, the two kinds of configurations were employed as described elsewhere.[2,4] One is the perpendicular configuration between directions of applied electric field and prove light to measure the absorbance ($E \perp h\nu$), and the other is the parallel one ($E \parallel h\nu$).

The reversible absorbance changes were observed with applying DC 300 Vcm^{-1} or below.[2] However, the electrophoresis of nanocrystals may happen to some extent at more than DC 300 Vcm^{-1}, and then the response has become irreversible. So, AC electric field was employed instead of DC electric field, so that the reversible absorbance changes were successfully achieved by higher electric field of above ca. 1.0 $kVcm^{-1}$. Figure 2 shows the dependence of absorbance change ratios on applied DC and AC (50 Hz) electric fields. As discussed previously,[2,4] the absorbance change ratio ($R = (A - A_0)/A_0$) takes the plus sign at $E \perp h\nu$ while the minus sign at $E \parallel h\nu$. The permanent dipole moment of seven of order of 10^6 D per one DAST nanocrystal evaluated by fitting Langevin function[5] was smaller than theoretically predicted value (7.1×10^8 D; supposing 500 nm $\times$ 500 nm $\times$ 50 nm in

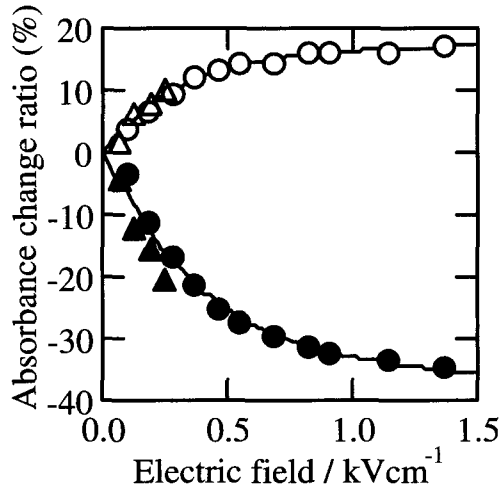

Fig. 2. Dependence of absorbance change ratios R on applied DC (triangular symbols) and AC (50 Hz, circular symbols) electric fields. Open symbols indicate the data in the perpendicular configuration ($E \perp h\nu$), and the closed symbols show the data in the parallel one ($E \parallel h\nu$). R is defined as $(A - A_0)/A_0$, in which A and A_0 are the absorbance with or without applied electric field. The solid curves were the calculated one by fitting Langevin function: $R/R(x \to \infty) = L(x)$, $x = \mu E/k_B T$, where μ, E, k_B and T are dipole moment, an applied electric field, Boltzmann constant and temperature, respectively.

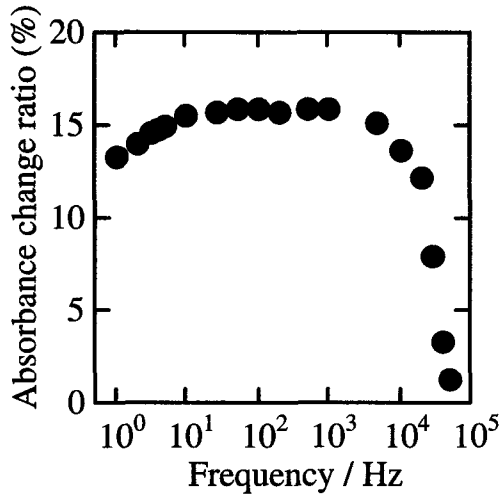

Fig. 3. Relationship between absorbance change ratio and frequency of AC electric field at 0.9 $kVcm^{-1}$ in the perpendicular configuration ($E \perp h\nu$).

size and dipole moment per one DAST molecule of $\mu = 30$ D). This discrepancy seems to be due to ignorance of local field, theoretically overestimated dipole moment of DAST nanocrystal, and so on. Anyway, the electric-field-induced orientation of DAST nanocrystals was realized at the much lower electric field, compared with ordinary liquid crystal molecules.

3.3. *Effect of AC frequency*

Figure 3 indicates the plots of the absorbance change ratio versus frequency of AC electric field. The ratio slightly increased up to ca. 10 Hz, almost constant over the range of about three orders of magnitude, and drastically decreased at more than 10^3 Hz. Although the degree of orientation of DAST nanocrystals seems to be determined by both the strength of applied electric field and thermal fluctuation, presumably the thermal fluctuation of nanocrystals is influenced and coupled with the frequency of AC. At high frequency, the dipole moment of DAST nanocrystals could not respond to the rapid inversion of AC electric field, mainly due to hydrodynamic factor. With decreasing the frequency, the orientational motion of DAST nanocrystals may follow the modulation of AC electric field. At extremely low frequency below 10 Hz, the thermal fluctuation becomes gradually dominant, and then the absorbance change ratio decreased to some extent.

3.4. *In situ observation of electric-field-induced orientation of DAST crystal*

Electric-field-induced orientation of DAST crystal dispersed in decahydronaphthalene was *in situ* observed under optical microscope as shown in Fig. 4. The crystal

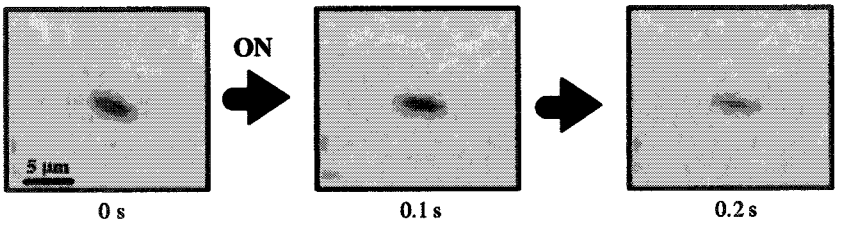

Fig. 4. *In situ* observation of orientation of DAST crystal. The response time was of sub-second order at AC 0.9 $kVcm^{-1}$, 1 Hz.

size was about 3 μm in the present case. The response time for orientation was of order of sub-second, which was roughly similar to that evaluated from absorbance changes after applying AC electric field.

4. Conclusions

AC electric field was much available to control the "Liquid and Crystal system"[2,4] of polar DAST nanocrystals dispersion system, which is expected as a large surface display monitor and so on.

References

1. H. Kasai, H. S. Nalwa, H. Oikawa, S. Okada, H. Matsuda, N. Minami, A. Kakuta, K. Ono, A. Mukoh, and H. Nakanishi, *Jpn. J. Appl. Phys.* **31**, L1132 (1992).
2. S. Fujita, H. Kasai, S. Okada, H. Oikawa, T. Fukuda, H. Matsuda, S. K. Tripathy, and H. Nakanishi, *Jpn. J. Appl. Phys.* **38**, L659 (1999).
3. H. Nakanishi, H. Matsuda, S. Okada, and M. Kato, *MRS Int. Mtg. Adv. Mater.* **1**, 97 (1989).
4. H. Oikawa, S. Fujita, H. Kasai, S. Okada, S. K. Tripathy, and H. Nakanishi, *Colloids Surf. A* **169**, 251 (2000).
5. P. J. W. Debye, *Topics in Chemical Physics* (Elsevier, Amsterdam, 1962).

This page is intentionally left blank

International Journal of Nanoscience, Vol. 1, Nos. 5 & 6 (2002) 743–747

USING EMISSION QUENCHING TO STUDY THE INTERACTION BETWEEN ZnO NANOCRYSTALS AND ORGANIC LIGANDS

JUN LI, KUI ZHAO, RUOKUN JIA, YANMEI LIU, YUBAI BAI*, and TIEJIN LI

Department of Chemistry, Jilin University
ChangChun 130023, People's Republic of China
Yubai@mail.jlu.edu.cn

Received 27 November 2002
Revised 14 December 2002

Colloidal ZnO nanocrystals with strong green luminescence were prepared. When ZnO nanocrystals were modified with different organic ligands, the emission quenching was measured and used to study the interaction between ZnO nanocrystal and organic ligands. Efficiency of emission quenching relates to the chemical structures of the ligands, and metal-thiolate bond was formed between nanocrystals and thiol ligands. The relative strength of the binding and the surface concentration of the adsorbed species could be determined using this method.

Keywords: ZnO nanocrystals; green luminescence; emission quenching; interaction.

1. Introduction

Colloidal semiconductor nanocrystals have been of great interest for fundamental research and industrial development in recent years due to their flexible processibility and unique properties.[1–3] Many of organic ligands, especially the thiols, have been utilized for both stabilizing semiconductor nanocrystals and fine-tuning their desired surface properties.[4–6] Colloidal nanocrystals are metastable species in comparison to the corresponding bulk crystals/solids and have to be kinetically-stabilized. The stability of nanocrystals is essential to their various applications. At the same time, the ligands provide nanocrystals with the water solubility, surface charge desired and useful function group for conjugation. In addition, the use of organic ligands as chemical treatments holds great promise for controlling the surface electronic properties of semiconductor. But not much is known regarding the nature and chemical properties of the binding between nanocrystals and their ligands.

ZnO was chosen because it is an important large band gap semiconductor that has wide applications in electronic, display and catalytic devices,[7,8] and because it can serve as a representative example of the important class of oxidic nanoparticles. This semiconductor has an added advantage that it emits quite strongly in the visible region.[9]

In this work, the ZnO nanocrystals were modified with three different organic ligands. The emission quenching was measured and used to study the interaction between nanocrystals and organic ligands. The apparent equilibrium constants of the reactions were calculated. Our results further supported the choice of ZnO nanocrystals as a smart nanomaterial for sensing organic molecules in solutions.

2. Experimental Section

The preparation of colloidal ZnO nanocrystals was similar to those previously reported by Meulenkamp.[10] Some modifications were made in our experiments.

The colloidal ZnO nanocrystals was modified with three kinds of organic molecules, including 4-mercaptobenzoic acid (MBA), 4-mercaptophenylamine (MPA) and benzoic acid (BA), respectively. The concentration of ZnO nanocrystals was 2×10^{-3} M in all systems (according to Zn^{2+}). Each organic molecule with different concentrations was added to the colloidal ZnO nanocrystals.

3. Results and Discussion

The colloidal ZnO has been proved to be pure nanocrystalline materials with wurtzite structure by XRD (Fig. 1). The TEM image (Fig. 2) shows that the ZnO nanocrystals are nearly monodisperse and the average size is about 3 nm.

The excitation spectrum recorded by monitoring the visible emission (520 nm) shows an onset at 342 nm. A well-resolved absorption maximum of the first electronic transition indicates a sufficiently narrow size distribution. The emission spectrum shows that the green emission is very strong, while the excitonic emission band cannot be observed in our steady-state emission measurements. As has been

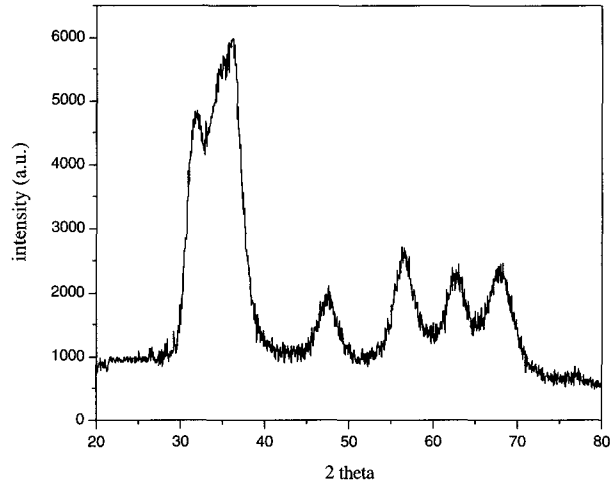

Fig. 1. Powder X-ray diffraction (XRD) patterns of precipitates obtained by addition of hexane to ZnO sols.

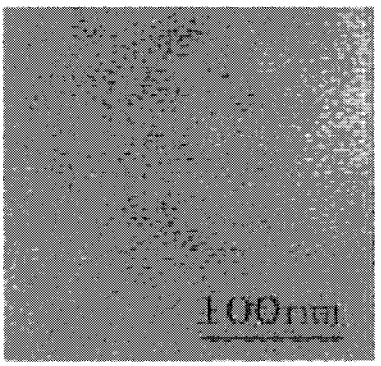

Fig. 2. TEM image of ZnO nanocrystals.

characterized in earlier studies with ZnO colloids and nanostructure films, the visible emission in ZnO arises from the oxygen vacancies.[11,12] Because of the high surface-to-volume rates of colloidal nanocrystals, the oxygen vacancies are abounding on the ZnO surface. As a result, the excitonic emission band is too weak to be observed. On the other hand, the surface of ZnO nanocrystals provides chemically binding platforms for organic ligands.

When MBA molecule was added into colloidal ZnO nanocrystals, the strong green emission was quenched. Moreover the emission yield decreased with increasing concentration of the MBA. Figure 3 shows that the emission spectra of ZnO–MBA systems at different MBA concentrations. However, when BA molecule was added into colloidal ZnO nanocrystals solution, as above conditions, the emission yield did not changed within the experimental error. It was obvious that the -SH group played a crucial role in the emission quenching.

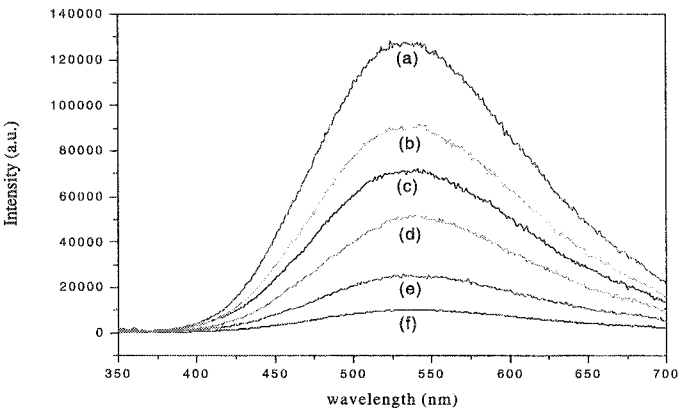

Fig. 3. Emission spectra of ZnO nanocrystals at different MBA concentrations. (a) No MBA, (b) 1×10^{-2}, (c) 2×10^{-2}, (d) 4×10^{-2}, (e) 8×10^{-2}, and (f) 1×10^{-1} mM.

In the ZnO–MBA systems, the -SH of MBA can react with the surface of ZnO nanocrystals to form a metal–thiolate bond. The S–H vibrations (ca. 2556 cm^{-1}) in MBA were not detectable after the MBA was added into the systems, which was a proof of covalent binding of MBA to the nanocrystals surface. Oxygen vacancies, the centers responsible for green luminescence, were occupied by MBA molecules when the MBA molecule was chemically-adsorbed efficiently onto ZnO surface. The surface concentration of the adsorbed species and the energetics determine the rate and efficiency of hole–electron transfer and recombination at the semiconductor interface, in other words, determine the efficiency of the emission quenching.

Then we have done another experiment in the same conditions, with MPA instead of MBA. The change of emission quenching in MPA systems was similar to that in MBA systems, but decreased more efficiently.

We further analyzed the emission quenching data by considering adsorption equilibrium between ZnO and thiols illustrated as Eq. (1):

$$\mathrm{ZnO} + \mathrm{MSH} \overset{\mathrm{Ka}}{\rightleftharpoons} [\mathrm{ZnO{-}SM}]\,. \tag{1}$$

The observed emission yield ($\Phi_{f(\mathrm{obs})}$) can then be related to the emission yields of ZnO nanocrystals that are unassociated (Φ_f^0) and associated (Φ'_f) with thiols (MSH), by Eq. (2),[11]

$$\frac{\Phi_f^0}{\Phi_f^0 - \Phi_{f(\mathrm{obs})}} = \frac{\Phi_f^0}{\Phi_f^0 - \Phi'_f} + \frac{\Phi_f^0}{\mathrm{Ka}(\Phi_f^0 - \Phi'_f)[\mathrm{MSH}]}\,. \tag{2}$$

The results (Fig. 4) fit the linear relationship between $\Phi_f^0/(\Phi_f^0 - \Phi_{f(\mathrm{obs})})$ and $1/[\mathrm{MSH}]$. From the intercept and slope of the straight-line plot we can obtain reaction equilibrium constants (Ka). The value of Ka in MBA self-assembly system was 3.26×10^4, while that in MPA self-assembly system was 6.78×10^4.

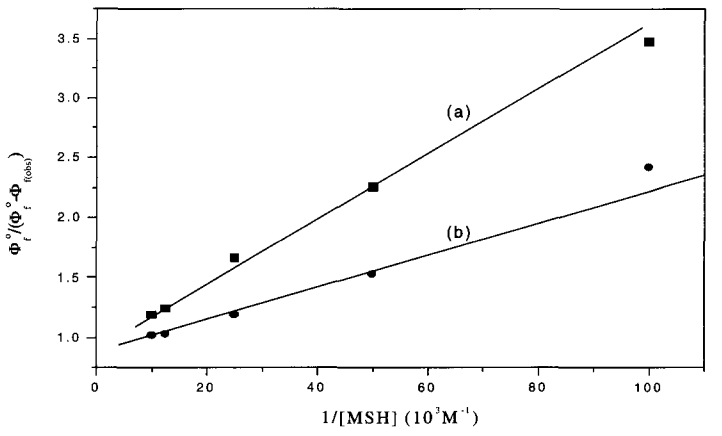

Fig. 4. Plot of $\Phi_f^0/(\Phi_f^0 - \Phi_{f(\mathrm{obs})})$ versus $1/[\mathrm{MSH}]$. (a) [MSH] = [MBA] and (b) [MSH] = [MPA].

From the structures of two thiols, the amino group of MPA is an electron pushing substituent, while the carboxyl group of MBA is an electron withdrawing substituent. The S atom of MPA is more negative than that of MBA, and more favorable to forming metal–thiolate bond. As a result, the value of Ka in MPA self-assembly system is larger, and the MPA molecules are chemically-adsorbed more efficiently onto the surface of ZnO nanocrystals.

4. Conclusions

Colloidal ZnO nanocrystals with strong green luminescence were prepared. The ZnO nanocrystals have been modified with three kinds of organic ligands: MBA, MPA and BA. Both MBA and MPA made the emission of ZnO quenched, while the BA did not affect the emission. The emission quenching was closely related to their chemical structure. Metal–thiolate bond was formed between the ZnO nanocrystals and thiols. The relative strength of the binding between the ZnO nanocrystals and organic ligands could be compared using emission quenching. The relative strength decreased in the following order: MPA > MBA $\gg$ BA.

The linear relationship between $\Phi_f^0/(\Phi_f^0 - \Phi_{f(\mathrm{obs})})$ and $1/[\mathrm{MSH}]$ can be used to determine the surface concentration of the adsorbed species. Quite high values of Ka ($> 10^4$) in two thiols self-assembly system indicated that ZnO nanocrystals are potentially useful in sensing some low concentrations of organic or bio-molecules in solutions.

Acknowledgments

The authors thank the National Natural Science Foundation of China (NNSFC) and 973 project for the financial assistance.

References

1. X. G. Peng, L. Manna, W. D. Yang, J. Wickham, E. Scher, A. Kadavanich, and A. P. Alivisatos, *Nature* **404**, 59 (2000).
2. A. P. Alivisatos, *Science* **271**, 933 (1996).
3. W. W. Yu and X. G. Peng, *Angew. Chem., Int. Ed. Engl.* **114**, 2474 (2002).
4. W. C. W. Chan and S. M. Nie, *Science* **281**, 2016 (1998).
5. M. Bruchez, M. Moronne, P. Gin, S. Weiss, and A. P Alivisatos, *Science* **281**, 2013 (1998).
6. S. Bharathi, M. Nogami, and S. Jkeda, *Langmuir* **17**, 1 (2001).
7. T. K. Gupta, *J. Am. Ceram. Soc.* **73**, 1817 (1990).
8. K. L. Chopra, S. Major, and D. K. Pandya, *Thin Solid Film* **102**, 1 (1983).
9. P. V. Kamat, R. Huehu, and R. J. Nicolaescu, *J. Phys. Chem. B* **106**, 788 (2002).
10. E. A. Meulenkamp, *J. Phys. Chem. B* **102**, 5566 (1998).
11. P. V. Kamat and B. Patrick, *J. Phys. Chem.* **96**, 6829 (1992).
12. K. Vanheusden, W. L. Warren, C. H. Seager, D. R. Tallant, J. A. Voigt, and B. E. Gnade, *J. Appl. Phys.* **79**, 7983 (1996).